



TU WIEN  
DEPARTMENT OF GEODESY  
AND GEOINFORMATION  
RESEARCH UNIT  
GEOPHYSICS

## DISSERTATION

# The joint inversion of seismic refraction and electrical resistivity data: A quantitative approach to estimate hydrogeological parameters in an imaging framework

Ausgeführt zum Zwecke der Erlangung des akademischen Grades eines Doktors der technischen Wissenschaften unter der Leitung von

Prof. Dr. Adrián Flores Orozco

E120-3

Department für Geodäsie und Geoinformation

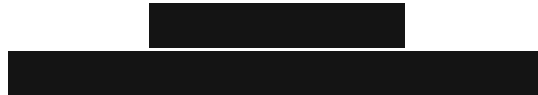
Forschungsbereich Geophysik

eingereicht an der Technischen Universität Wien

Fakultät für Mathematik und Geoinformation

von

Matthias Steiner



Wien, November 2022

---

Matthias Steiner

(Verfasser)

---

Adrián Flores Orozco

(Betreuer)





TU WIEN  
DEPARTMENT OF GEODESY  
AND GEOINFORMATION  
RESEARCH UNIT  
GEOPHYSICS

## DISSERTATION

# The joint inversion of seismic refraction and electrical resistivity data: A quantitative approach to estimate hydrogeological parameters in an imaging framework

Carried out for the purpose of obtaining the degree of Doctor technicae (Dr. techn.)  
under the supervision of

Prof. Dr. Adrián Flores Orozco

E120-3

Department of Geodesy and Geoinformation  
Research Unit of Geophysics

submitted at TU Wien

Faculty of Mathematics and Geoinformation

by

Matthias Steiner



Vienna, November 2022

---

Matthias Steiner  
(Author)

---

Adrián Flores Orozco  
(Supervisor)



*Examination committee:*

**Prof. Dr. Adrián Flores Orozco**

TU Wien

Department of Geodesy and Geoinformation

Research Unit of Geophysics

**Prof. Dr. Andreas Kemna**

University of Bonn

Institute of Geosciences

Geophysics Section

**Prof. Dr. Frédéric Nguyen**

University of Liege

Argenco Department

Applied Geophysics



### *Affidavit*

I declare in lieu of oath, that I wrote this thesis and performed the associated research myself, using only literature cited in this volume. If text passages from sources are used literally, they are marked as such.

I confirm that this work is original and has not been submitted elsewhere for any examination, nor is it currently under consideration for a thesis elsewhere.

Vienna, November 2022

---

Matthias Steiner

This work received funds of the Austrian Academy of Science through the project "Atmosphere-permafrost relationship in the Austrian Alps" (ATMOperm) and was supported by the Swiss National Science Foundation (grant no. 200021L\_178823).

# Abstract

Geophysical methods have proven to be suitable for complementing traditional point-wise direct investigations in environmental and engineering studies, as they provide information regarding the subsurface properties with high spatio-temporal resolution in a non-invasive manner. In near-surface investigations, electrical resistivity tomography (ERT) and seismic refraction tomography (SRT) methods are commonly applied due to their sensitivity to variations in the hydrogeological or chemical properties of the subsurface materials. In particular, the joint application of these geophysical techniques with complementary sensitivities is a common approach to mitigate the effect of uncertainties associated with data collection, processing and inversion on the consistency in the obtained results.

A careful processing of the geophysical data is critical for the estimation of reliable subsurface models. In case of the ERT, the data processing can be automatized to a high degree due to the availability of well-established guidelines and algorithms. In contrast, the SRT data processing refers to an interactive procedure controlled by user experience commonly relying on commercial software solutions. Accordingly, the geophysical modeling and processing library proposed in this thesis addresses the justified demand for open-source tools facilitating transparent and more automatized SRT processing workflows.

Due to the non-uniqueness of the geophysical inversion problem the interpretation of the resolved subsurface models is also associated to uncertainties, which might be further amplified if the geophysical images are transformed to quantitative estimates of the actual parameters of interest. The combination of complementary imaging results aims at a more reliable interpretation, yet inconsistencies in the models obtained from independently inverted data sets might limit the applicability of such approach.

To overcome these limitations of joint interpretation approaches, petrophysically-coupled joint inversion (PJI) schemes based on ERT and SRT data have emerged as innovative tools due to their ability to directly solve for subsurface models expressed in terms of the actual target parameters, e.g., hydrogeological properties. However, the parameterization of the underlying petrophysical model might also be affected by uncertainties. Hence, this thesis explores the possibility to impose structural and petrophysical constraints on the PJI to enhance the consistency in the resolved sub-

## *Abstract*

surface models.

In fine-grained environments or in presence of organic matter, neglecting the effect of the surface conduction on the observed electrical response results in biased estimates for the hydrogeological target parameters. Accordingly, this study extends the PJI scheme to consider surface conductivity during the parameter estimation by leveraging upon the frequency-dependence of the surface conductivity obtained through ERT data collected at a low and a high frequency.

In summary, the results presented in this thesis demonstrate: (i) the ability to build modeling and processing tools for seismic refraction data based on open-source python libraries; (ii) that imposing a porosity model as constraint in the PJI compensates for the lack of contrast in the physical properties of different media and can also act as a time-lapse constraint in the PJI; (iii) that the frequency-dependent effect of the surface conduction can be taken into account during the PJI parameter estimation based on conductivity magnitude data collected at a high and a low frequency; (iv) the applicability of the PJI to solve for hydrogeological parameters, e.g., water content and hydraulic conductivity, in different environments ranging from frozen conditions in alpine regions, to landfills, landslides and undisturbed natural media; and (v) the possibility to adapt the PJI framework with regard to both input data and target parameters, which lays the foundation for future incorporation of other geophysical methods and petrophysical relationships.

## Kurzfassung

Im Rahmen von umweltbezogenen bzw. ingenieurtechnischen Untersuchungen werden die Eigenschaften des Untergrunds traditionell mit direkten Messmethoden erfasst. Jedoch sind die gewonnenen Daten in ihrer räumlichen Auflösung begrenzt, da direkte Untersuchungen meist nur punktuell durchgeführt werden können (z.B. in Bohrlöchern). Im Gegensatz dazu sind geophysikalische Methoden in der Lage, Informationen über die Beschaffenheit des Untergrunds in nicht-invasiver Weise und mit hoher räumlicher und zeitlicher Auflösung zu bestimmen, und haben sich daher als geeignete Ergänzung von direkten Methoden erwiesen. Die elektrische Widerstandstomographie (electrical resistivity tomography; ERT) und die seismische Refraktionstomographie (seismic refraction tomography; SRT) sind in der Lage Veränderungen der hydrogeologischen bzw. chemischen Eigenschaften des Untergrunds zu detektieren und werden daher häufig für oberflächennahe Untersuchungen eingesetzt. Die Kombination dieser komplementären geophysikalischen Methoden ist ein gängiger Ansatz, um den Einfluss von Unsicherheiten bzw. Fehler im Zusammenhang mit der Datenerfassung, -verarbeitung und -inversion auf die Ergebnisse zu vermindern.

Das sorgfältige Prozessieren der geophysikalischen Daten ist von zentraler Bedeutung, um verlässliche Modelle der Untergrundeigenschaften zu erhalten. Insbesondere die Prozessierung von ERT-Datensätzen kann basierend auf etablierten Richtlinien und Algorithmen weitestgehend automatisiert werden. Im Gegensatz dazu handelt es sich bei der Prozessierung von SRT-Daten um einen interaktiven Vorgang, der maßgeblich von der Erfahrung der auswertenden Person beeinflusst wird und zudem oftmals den Einsatz von kommerziellen Softwarelösungen erfordert. Dementsprechend besteht begründeter Bedarf an der Entwicklung von lizenzfreien bzw. open-source Lösungen, die transparente und automatisierte Abläufe im Zusammenhang mit der Prozessierung von SRT-Daten ermöglichen.

Bei der Inversion von geophysikalischen Daten handelt es sich um ein mehrdeutiges Problem, wodurch insbesondere die Interpretation der Inversionsergebnisse mit Unsicherheiten behaftet sein kann, die zusätzlich verstärkt werden, wenn die geophysikalischen Parameter in andere Größen umgerechnet werden (z.B. die von direkten Methoden erfassten Untergrundeigenschaften). In dieser Hinsicht ist eine verbesserte Interpretation durch die Kombination komplementärer Inversionsergebnisse möglich,

jedoch setzt dies voraus, dass die durch unabhängige Inversionen erhaltenen Untergrundmodelle in sich konsistent sind.

Um diese Nachteile zu beheben, hat sich die petrophysikalisch gekoppelte Inversion (petrophysical joint inversion; PJI) von ERT- und SRT-Daten als ein geeignetes Verfahren erwiesen, welches die direkte quantitative Bestimmung der relevanten Untergrundeigenschaften (z.B. hydrogeologische Parameter) ermöglicht. Jedoch erfordert die Anwendung solcher PJI-Verfahren eine adäquate Parametrisierung des zugrundeliegenden petrophysikalischen Modells, die wiederum von Unsicherheiten betroffen sein kann. Daher untersucht diese Arbeit die Möglichkeit, strukturelle und petrophysikalische Randbedingungen in der petrophysikalisch gekoppelte Inversion zu berücksichtigen, um konsistente Untergrundmodelle zu erhalten.

Bei einem hohen Anteil von tonigen Sedimenten oder organischem Material ist es essentiell, dass das dem PJI-Verfahren zugrundeliegende petrophysikalische Modell den Einfluss der Oberflächenleitfähigkeit auf die beobachteten elektrischen Eigenschaften des Untergrunds berücksichtigt. Wird dieser Einfluss bei der PJI vernachlässigt, führt dies zu einer fehlerhaften quantitativen Bestimmung der hydrogeologischen Untergrundeigenschaften. Dementsprechend wird in dieser Arbeit das eingesetzte PJI-Verfahren erweitert, um den Einfluss der Oberflächenleitfähigkeit im Zuge der Inversion, d.h., bei der Parameterschätzung, zu berücksichtigen. Dieses modifizierte PJI-Verfahren quantifiziert die Oberflächenleitfähigkeit basierend auf ERT-Daten, die bei einer niedrigen und einer hohen Frequenz gemessen werden.

Die im Rahmen dieser Arbeit erzielten Resultate lassen sich wie folgt zusammenfassen: (i) Entwicklung einer Softwarelösung für die Modellierung und Prozessierung von SRT-Daten basierend auf open-source python-Bibliotheken; (ii) die Verwendung eines Porositätsmodells als Randbedingung in der PJI kompensiert einen etwaigen geringen Kontrast in den physikalischen Eigenschaften verschiedener Untergrundmaterialien und kann darüber hinaus als zeitliche Randbedingung fungieren; (iii) der frequenzabhängige Effekt der Oberflächenleitfähigkeit kann im Zuge der PJI basierend auf Leitfähigkeitsmessungen bei einer hohen und einer niedrigen Frequenz berücksichtigt werden; (iv) das erweiterte PJI-Verfahren ermöglicht die quantitative Bestimmung hydrogeologischer Parameter (insbesondere Wassergehalt und hydraulische Leitfähigkeit) in unterschiedlichen Untersuchungsgebieten, z.B. gefrorener Untergrund in alpinen Regionen, Deponien, Hangrutschungen und ungestörte natürliche Sedimente; (v) das verwendete PJI-Verfahren kann sowohl hinsichtlich der zu invertierenden Datensätze als auch der Zielparameter individuell angepasst werden, wodurch zukünftige Erweiterungen basierend auf weiteren geophysikalischen Methoden und petrophysikalischen Beziehungen möglich sind.

# Acknowledgment

*We do not make mistakes, just happy little accidents.*

— Bob Ross

---

The pursuit of new discoveries, developing novel solutions and the gain of knowledge are some of the reasons I set of on this adventure. Yet, there are also negative results, setbacks or rejections one might not be prepared for. Having received outstanding scientific guidance I learned embracing the latter ones as opportunities to evolve both as a scientist and a person.

*Nothing ever came from a life that was a simple one.*

— Devil's Dancefloor *by* Flogging Molly

---

From a young age I have always had the privilege to follow my interests without my decisions being influenced or questioned by my family. Having been raised not to be afraid by the tougher path gave me the perseverance that has helped me to get further than imagined in the very beginning.

*We are only as strong as we are united, as weak as we are divided.*

— Albus Dumbledore

---

Over the years I shared offices and experiences with such remarkable personalities, whose open ears, moral support and friendship were and still are invaluable to me. The experienced togetherness of this heterogeneous group of people brought together by coincidence is one of its biggest assets. Especially the *vegan recipes* I will never forget.

## Acknowledgment

*You pretend badly in front of those who love you, and in front of others it is not worth the effort.* — Ernst Lothar

---

Recapping the past few years a roller-coaster ride comes to mind inevitably—both from a professional and an emotional point of view. There is one special person who unconditionally absorbed the raw emotions from the shiny ups as well as the bleak downs; whose support I could always rely on; and who somehow managed to keep me going even during the toughest downs (figuratively and literally).

Deserved or not—I would not have managed otherwise.

# Contents

<b>1</b>	<b>Introduction</b> . . . . .	<b>1</b>
1.1	Personal motivation . . . . .	1
1.2	Scientific background and state of research . . . . .	1
1.3	Research aim and objectives of this thesis . . . . .	5
1.4	Structure of this thesis . . . . .	6
<b>2</b>	<b>Basic principles of the employed methods</b> . . . . .	<b>9</b>
2.1	Electrical methods for environmental applications . . . . .	9
2.1.1	The electrical resistivity method . . . . .	9
2.1.2	Complex conductivity measurements . . . . .	16
2.1.3	Frequency-dependent electrical properties of the subsurface materials . . . . .	19
2.2	The seismic refraction method for near-surface applications . . . . .	20
2.3	Combined application of seismic and electric methods . . . . .	26
2.3.1	Inversion of a single geophysical data set . . . . .	27
2.3.2	Joint interpretation of independently resolved subsurface models . . . . .	29
2.3.3	Joint inversion of multiple geophysical data sets . . . . .	31
<b>3</b>	<b>formikoj: A flexible library for data management and processing in geophysics - Application for seismic refraction data</b> . . . . .	<b>35</b>
3.1	Introduction . . . . .	35
3.2	Design and structure of the formikoj library . . . . .	37
3.2.1	Generation of seismic waveform data for synthetic subsurface models: The <code>SeismicWaveformModeler</code> . . . . .	37
3.2.2	Managing and processing of seismic refraction data sets: the <code>SeismicRefractionManager</code> . . . . .	43
3.3	Exemplary use cases . . . . .	53
3.3.1	Modeling and use of synthetic seismic waveform data . . . . .	53
3.3.2	First break travel time picking for a 2D roll-along field data set: the Danube island example . . . . .	56
3.3.3	Processing of a 3D seismic refraction data set: the soda lake example . . . . .	62

3.4	Conclusions and Outlook . . . . .	64
<b>4</b>	<b>Improved estimation of ice and water contents in alpine permafrost through constrained petrophysical joint inversion: The Hoher Sonnblick case study . . . . .</b>	<b>67</b>
4.1	Introduction . . . . .	67
4.2	Materials and Methods . . . . .	71
4.2.1	PJI solving for water, ice, air, and rock content . . . . .	71
4.2.2	The study area at Hoher Sonnblick (Austria) . . . . .	74
4.2.3	Acquisition and processing of geophysical data sets . . . . .	74
4.3	Results . . . . .	78
4.3.1	Assessing the reconstruction capabilities of different inversion approaches . . . . .	78
4.3.2	Subsurface structures resolved at Hoher Sonnblick through joint interpretation . . . . .	81
4.3.3	Quantifying the subsurface ice-water content at Hoher Sonnblick . . . . .	85
4.4	Discussion . . . . .	87
4.4.1	Benefits and limitations of different PJI approaches . . . . .	87
4.4.2	Improving the estimates for ice and water content at Hoher Sonnblick . . . . .	88
4.4.3	Outlook . . . . .	91
4.5	Conclusion . . . . .	92
<b>5</b>	<b>Quantitative water content estimation in landfills through joint inversion of seismic refraction and electrical resistivity data considering surface conduction . . . . .</b>	<b>93</b>
5.1	Introduction . . . . .	93
5.2	Materials and methods . . . . .	96
5.2.1	Study area: The Heferlbach landfill (Vienna, Austria) . . . . .	96
5.2.2	Geophysical survey - Basic principles, experimental setup and data processing . . . . .	98
5.2.3	Quantitative estimation of subsurface properties through petrophysical joint inversion . . . . .	100
5.3	Geophysical and hydrogeological characterization of the Heferlbach landfill . . . . .	105
5.3.1	Longitudinal section through the landfill . . . . .	105
5.3.2	Cross section through a MSW unit . . . . .	106

5.3.3	Cross section through a CDW unit . . . . .	108
5.3.4	Independent verification based on the observed polarization re- sponse . . . . .	109
5.3.5	Evaluation of the resolved water content . . . . .	112
5.4	Conclusion . . . . .	113
<b>6</b>	<b>Application of induced polarization imaging across different scales to understand surface and groundwater flow at the Hofermuehle landslide . . . . .</b>	<b>115</b>
6.1	Introduction . . . . .	115
6.2	Material and methods . . . . .	119
6.2.1	The complex conductivity as an expression of the electrical con- ductivity and polarization properties of the subsurface . . . . .	119
6.2.2	Hydraulic conductivity ( $K$ ) estimations based on IP measure- ments . . . . .	121
6.2.3	Time-domain and frequency-domain IP measurements at the Hofermuehle site . . . . .	122
6.2.4	Analysis in soil samples: grain size analysis and SIP measurements	125
6.2.5	Complementary data: field-scale seismic refraction tomography (SRT) . . . . .	127
6.2.6	Processing and inversion of TDIP, FDIP, SRT data . . . . .	128
6.3	Results . . . . .	130
6.3.1	Time-domain IP surveys: the effect of the pulse length and a first map of the study area . . . . .	130
6.3.2	Frequency-domain imaging results for data collected at line L1 .	133
6.3.3	The frequency dependence of the SIP measurements . . . . .	135
6.3.4	Joint inversion of electrical resistivity and seismic refraction to- mography . . . . .	139
6.4	Discussion . . . . .	141
6.4.1	Quantification of the hydraulic conductivity based on different IP methods . . . . .	141
6.4.2	Independent quantification of the hydraulic conductivity through a joint inversion scheme . . . . .	143
6.4.3	3D subsurface model of study area . . . . .	147
6.5	Conclusion . . . . .	147

<b>7</b>	<b>Geophysical imaging of the spatial variability in the pore space connectivity: A field-scale application in undisturbed natural soils</b>	<b>151</b>
7.1	Introduction . . . . .	151
7.2	Materials and Methods . . . . .	152
7.2.1	Quantitative estimation of the cementation exponent $m$ . . . . .	152
7.2.2	Application of the modified PJI scheme to field data . . . . .	154
7.3	Results and Discussion . . . . .	156
7.3.1	Interpretation of the resolved subsurface models . . . . .	156
7.3.2	Deriving further soil properties from the PJI imaging results . . . . .	158
7.3.3	Evaluation of the modified PJI scheme through independent geophysical methods and direct information . . . . .	159
7.4	Conclusions . . . . .	163
<b>8</b>	<b>Conclusions and perspectives</b> . . . . .	<b>165</b>
8.1	Modeling and processing of geophysical data sets . . . . .	165
8.2	PJI - advantages, limitations and the way forward . . . . .	167
8.2.1	Quantitative estimation of hydrogeological parameters in different environments . . . . .	167
8.2.2	Perspectives for future research activities . . . . .	171
8.3	Concluding remarks . . . . .	178
	<b>List of Abbreviations, Acronyms and Symbols</b> . . . . .	<b>179</b>
	Abbreviations and Acronyms . . . . .	179
	Electrical methods . . . . .	179
	Seismic methods . . . . .	180
	Petrophysics . . . . .	180
	Inversion . . . . .	181
	<b>Bibliography</b> . . . . .	<b>183</b>

# 1 | Introduction

## 1.1 Personal motivation

After graduating from my Master's program in Geodesy and Geophysics specializing in seismology and time-series analysis, I worked as a research assistant at the Institute for Applied Geology at the University of Natural Resources and Life Sciences in Vienna. Although my work mainly focused on the seismic monitoring of mass movements I soon became also responsible for site characterizations through applied geophysical methods. This was about the time when I got in touch with the new Head of Geophysics at my alma mater – Adrián Flores Orozco – who over time became a mentor for me. Through our collaboration I got familiar with modern applications of geophysical methods in environmental and engineering investigations. Coming from an agriculturally characterized region, I was particularly fascinated by the correlation between geophysical images and the spatial patterns observed in field crops (see Figure 1.1), as well as the ability to visualize the associated subsurface structures and processes. Eventually, after working several years on seismic monitoring, I opted for environmental geophysics and was fortunate that my mentor agreed to also take on the role as my supervisor.

## 1.2 Scientific background and state of research

As early as the last decade of the 19<sup>th</sup> century, scientists became aware of the link between the CO<sub>2</sub> concentration in the atmosphere and the Earth's surface air temperature (Arrhenius, 1896). Although such research was driven by the urge to unravel the reason for past ice ages, Svante Arrhenius and Arvid Högbom also addressed the effect of burning coal on the CO<sub>2</sub> concentration and the associated rise in temperature. Considering the coal consumption in 1896, Högborn expected that it would take millenia for the CO<sub>2</sub> concentration to reach levels causing a substantial increase in temperature; yet, only a decade later this estimate had to be corrected due to the accelerated rate at which coal was burnt, now suggesting a warming of the Earth's temperature within centuries (Arrhenius, 1908). Today, about a century after this estimate was published, people around the globe are experiencing the effects of the predicted *climate change*

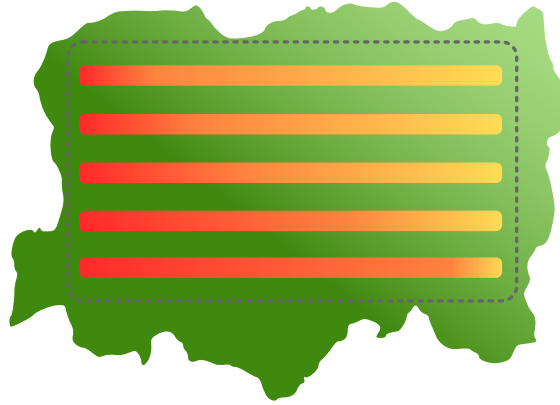


**Figure 1.1:** Schematic illustration of the qualitative correlation between field crop patterns (background) and the response observed with a generic geophysical method (horizontal lines).

in form of rising temperatures and severe weather phenomena<sup>1</sup>. Causes and effects of climate change on the environment as well as modern society are investigated by manifold academic disciplines from different points of view, such as natural, economic or social sciences (IPCC, 2022).

Climate change particularly affects the hydrological cycle causing substantial alterations, for instance, in the groundwater system and in the cryosphere (IPCC, 2022). Moreover, under certain conditions water can also act as an indirect factor contributing to climate change. For instance, in municipal solid waste (MSW) the water content refers to a key factor associated with the methanogenic fermentation of the refuse, and thus the production of the greenhouse gas (GHG) methane ( $\text{CH}_4$ , e.g., Barlaz et al., 1990; Gurijala and Sufliita, 1993; Sanphoti et al., 2006). Accordingly, the assessment or monitoring of the (unfrozen and frozen) subsurface water content is of utmost importance for climate change research. In particular, the investigation of water infiltration and groundwater flow requires information regarding the hydraulic conductivity of the subsurface materials which depends on the textural properties of the soil, e.g., the connectedness of the pore space and the grain size distribution.

Traditionally, subsurface properties are resolved through direct investigations such as measurements in boreholes or laboratory analyses of soil samples. Although these techniques allow for a direct quantification of the parameters of interest, the extraction of soil samples or the drilling of boreholes is an invasive procedure, which might interfere with the subsurface conditions, and thus bias the interpretation of the collected data. As illustrated in Figure 1.2a, the spatial resolution of direct methods is

<sup>1</sup><https://www.ncei.noaa.gov/access/monitoring/monthly-report/global/202107>; last accessed December 2, 2022

limited by the number and distribution of sampling points; whereas, the application of interpolation algorithms might yield a skewed model of the spatial variability in the investigated soil properties.

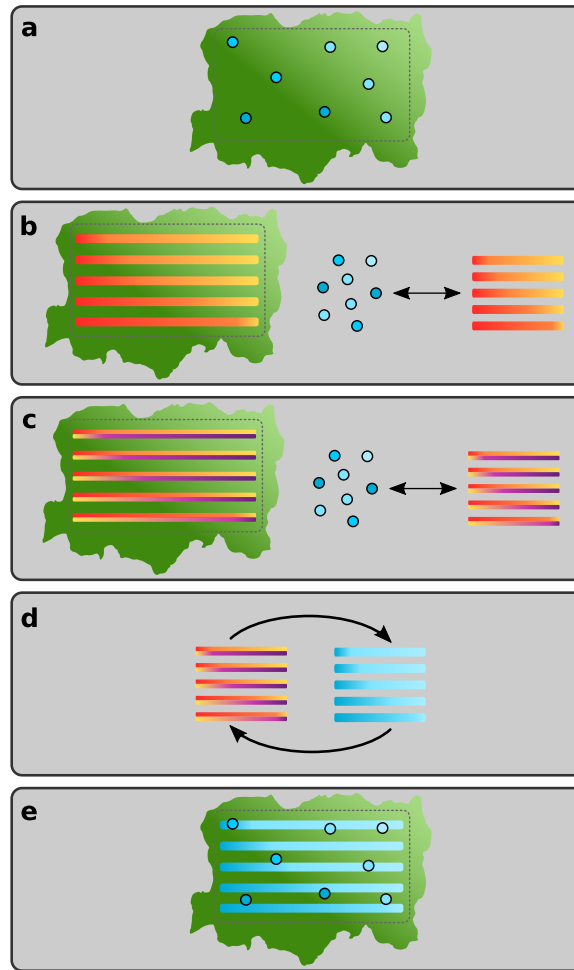


**Figure 1.2:** Schematic illustration of different aspects associated with subsurface investigations. (a) Direct assessment of subsurface properties at discrete sampling points. (b) Investigation of the subsurface through a single geophysical method sensitive to the parameter of interest. (c) Investigation of the subsurface based on two (complementary) geophysical methods. (d) Petrophysical joint inversion of two geophysical data sets to solve directly for the parameter of interest. (e) Enhanced assessment of the spatial variability in the target parameter through geophysical investigations.

Geophysical methods have proven to complement direct investigations as they provide information about subsurface properties with high spatio-temporal resolution in a non-invasive manner. Applications of geophysical methods in environmental and engineering investigations range from critical zone research (Parsekian et al., 2015) to landfill characterization (Nguyen et al., 2018) and the quantification of soil structure (Romero-Ruiz et al., 2018), amongst others. However, the information provided by

## 1 Introduction

geophysical methods is indirect as, in general, the assessed physical properties of the soil are not the actual parameters of interest.

In particular, the ability of electrical and electromagnetic methods to sense hydrogeological conditions and changes in the subsurface lead to the emergence of specialized applied geophysics branches such as hydrogeophysics (Binley et al., 2015) or agrogeophysics (Garré et al., 2021). To provide quantitative estimates of the parameters of interest the geophysical (imaging) results are often converted to hydrogeological properties through the application of petrophysical models as illustrated in Figure 1.2b. However, approaches relying on a single geophysical method and a single petrophysical relation need to be applied with caution as uncertainties related to inversion and the petrophysical model lead to substantial uncertainties in the converted water content due to error propagation (Tso et al., 2019).

Due to these uncertainties, Tso et al. (2019) suggest that the estimation of hydrological parameters should depend on more than one data source, i.e., co-located investigations with complementary geophysical methods as illustrated in Figure 1.2c. Multimethod approaches aim at overcoming the limitations of single geophysical methods through joint interpretation of the resolved model; thus, reducing the influence of the uncertainty associated with the inversion on the obtained results. Similar to single-method approaches, the complementary imaging results can be converted to the actual parameters of interest through petrophysical models. An example is the four-phase model (4PM) proposed by Hauck et al. (2011), which has been used in permafrost research for over a decade to estimate the subsurface ice and water content from independently resolved ERT and SRT imaging results. However, although the 4PM is in accordance with the suggestion of Tso et al. (2019), the inherently similar electrical and mechanical properties of rock and ice can lead to physically implausible estimates (e.g., Hauck et al., 2011; Wagner et al., 2019). This effect is amplified due to the independent inversion of the ERT and SRT data sets, i.e., due to the integration of the complementary methods at the results level.

To overcome such problems, the integration should occur at the data level to obtain more consistent and reliable models, i.e., through joint inversion schemes considering all available data sources during the parameter estimation (e.g., Linde and Doetsch, 2016). For permafrost investigations, Wagner et al. (2019) address this problem by developing a joint inversion scheme based on the 4PM and ensure physically plausible estimates by imposing a constraining interparameter relationship. In particular, such petrophysically-coupled joint inversion (PJI) schemes leverage upon the complementary sensitivities of the different data sets to directly solve for subsurface models in terms of the hydrological parameters of interest in an iterative procedure (see the

simplified illustration presented in Figure 1.2d).

The benefit of such PJI schemes is highlighted in Figure 1.2e. As the imaging results are directly obtained in terms of the actual parameters of interest, the resolved models can be easily combined with available direct information to provide a reliable characterization of the spatial variability in the target parameters with an enhanced spatial resolution. For brevity, Figure 1.2 shows geophysical surveys as 2D investigations, yet the statements provided above apply, in general, also for 3D survey geometries.

The geophysical data, the inversion process and the interpretation of the imaging results are associated with uncertainties, yet also the processing of geophysical data sets prior to the inversion can introduce further uncertainties. Accordingly, it is necessary to perform the data processing in a reproducible manner to ensure that the applied analysis is repeatable, i.e., the same results can be obtained independently (e.g., Alston and Rick, 2021). In particular, detailed information regarding uncertainties associated with the data and their processing can be considered in the inversion to reduce the uncertainty in the resolved models, and thus the interpretation. Furthermore, making data processing workflows transparent, i.e., accessible by the research community, generates an additional benefit as studies become independently reproducible and the acquired knowledge can easily ignite further developments (e.g., Alston and Rick, 2021).

### 1.3 Research aim and objectives of this thesis

The general aim of this thesis is to mitigate the effect of uncertainties associated with data collection, processing and inversion on the consistency in the imaging results obtained through the inversion of geophysical data sets. Particular focus is put on the reliable quantification of the subsurface water content (in both unfrozen and frozen state) through the joint inversion of electrical and seismic data considering that water is a critical environmental parameter related to GHG production, triggering of mass movements but also a key indicator for the effect of climate change on alpine regions. Accordingly, the central objectives of this thesis can be summarized as follows:

**Objective.** *Conceptualize and implement a light-weight and simply applicable tool based on existing open-source python libraries for the processing (and modeling) of seismic waveform data focused on seismic refraction analysis to facilitate reproducible and transparent processing workflows.*

**Objective.** *Investigate the possibility to enhance the spatial and temporal consistency in the subsurface ice and water content resolved through a petrophysical joint inversion*

*(PJI) scheme by imposing prior knowledge about subsurface conditions as structural and petrophysical constraints during the parameter estimation.*

**Objective.** *Investigate extensions of the petrophysical model underlying the considered PJI scheme to account for the effect of surface conduction during the parameter estimation aiming at a reliable quantification of the water content in presence of fine-grained materials or organic matter.*

### 1.4 Structure of this thesis

This thesis is divided into seven chapters (including this present introductory chapter), with the objectives formulated above being addressed in chapters 3 through 7 based on independent manuscripts published or under revision for publication in peer-reviewed journals. This central part of the thesis is preceded by a chapter on the fundamental theoretical basics, and followed by comprehensive conclusions and perspectives of the presented research:

**Chapter 2** I introduce the fundamental theoretical basics of the employed geophysical methods and techniques. I revisit the fundamental physical and mathematical principles of the electrical and seismic methods considered in this thesis. Moreover, I provide a formal description of deterministic inversion approaches, which reaches out from independent single method applications to the petrophysically-coupled joint inversion of different methods.

**Chapter 3** I present the open-source `formikoj` python library, which provides a framework for the development of modeling and processing solutions for different geophysical methods. In particular, I present the concept of the general framework and demonstrate its applicability through the implementation of tools for creating and managing seismic waveform data, with special emphasis on the seismic refraction analysis.

**Chapter 4** I investigate the characterization of an Alpine permafrost site, namely the Hoher Sonnblick (Austria), through a multi-method geophysical investigation. In comparison to existing studies, I use the PJI framework developed by Wagner et al. (2019) for the quantitative estimation of the subsurface water and ice contents from time-lapse data sets. I address the inherent non-uniqueness and ill-posedness of the geophysical inversion problem through the incorporation of structural and petrophysical constraints. In particular, I demonstrate

that imposing a porosity model during the parameter estimation acts as a time-lapse constraint enhancing the temporal consistency in the resolved ice content models.

**Chapter 5** I explore the possibility to widen the scope of the PJI framework aiming at an enhanced quantification of the water content within the Heferlbach landfill (Vienna, Austria). Based on existing studies I propose a modification of the existing PJI framework to account for the spatial variations in the surface conductivity during the parameter estimation. To this end, I expand the underlying petrophysical model through the formulations of the dynamic Stern layer model (e.g., Revil et al., 2017c), which makes the PJI scheme sensitive for the frequency-dependence of the observed electrical response. To evaluate the applicability of the proposed modification I compare the resolved normalized chargeability with polarization images obtained from IP investigations through complex conductivity inversion.

**Chapter 6** I present the application of the modified PJI scheme in frame of the characterization of the Hofermuehle landslide (Lower Austria). The main objective of this study is the characterization of surface and groundwater flow in terms of the hydraulic conductivity  $K$  through multi-scale IP surveys. Due to the lack of direct  $K$  measurements, I explore the applicability of the PJI imaging results to quantify the formation factor  $F$ , which is then used to obtain a model for  $K$ . In such way, the PJI scheme provides the means for a methodically different assessment of  $K$ , and thus allow for an independent evaluation of the IP-based  $K$  estimations.

**Chapter 7** I investigate a further modification of the PJI scheme aiming at an enhanced quantification of the formation factor  $F$ . In particular, I test the modified PJI scheme with data collected at the Hydrological Open Air laboratory (HOAL; Blöschl et al., 2016) and evaluate the obtained imaging results with existing ground-truth information. Based on the obtained models I show the general applicability and validity of the proposed approach, but also highlight remaining deficiencies in the underlying petrophysical model.

**Chapter 8** I provide a comprehensive summary and conclusion of the main findings presented in this thesis. Based on an objective and detailed discussion of benefits and drawbacks associated with the proposed solutions I identify and elaborate on future perspectives. In particular, I address possible applications of the formikoj library for other geophysical methods, discuss the potential of incorporating the

## 1 Introduction

IP method in the PJI scheme, and provide two possible models for an improved approximation of the seismic velocity in the petrophysical model underlying the PJI scheme.

## 2 | Basic principles of the employed methods

Geophysical methods have emerged as suitable tools for environmental and engineering studies considering their ability to complement direct investigations based on the non-invasive investigation of subsurface properties with high spatial and temporal resolution. Applications of geophysical methods range from the assessment of hydrogeological conditions (e.g., Binley et al., 2015) to the characterization of landfills (e.g., Nguyen et al., 2018), investigations of the critical zone (e.g., Parsekian et al., 2015) and the characterization and monitoring of permafrost (Hauck and Kneisel, 2008). Several studies have demonstrated the successful joint application of seismic and electrical methods, for instance, to characterize landfills (Konstantaki et al., 2015; Kondracka et al., 2021), permafrost sites (Pellet et al., 2016; Mollaret et al., 2019), or landslides (e.g., Bichler et al., 2004; Whiteley et al., 2021), as well as hydrogeological investigations (e.g., Holbrook et al., 2014; Blazevic et al., 2020; Bücken et al., 2021).

Due to the focus of this thesis on the joint application and joint inversion of electrical resistivity and seismic refraction data sets, the objective of this chapter is to present the fundamental physical, mathematical and practical principles of these geophysical methods. For completeness, this chapter provides a general introduction to the inversion of geophysical data sets following different inversion approaches, namely the independent and the joint inversion of the seismic and electrical data sets.

### 2.1 Electrical methods for environmental applications

#### 2.1.1 The electrical resistivity method

The electrical resistivity (ER) method relies on four-electrode arrays, where direct current (DC)  $I$  (given in A) is injected into the subsurface through one electrode pair and the resultant voltage  $U$  (given in V) is measured through the other pair (e.g., Everett, 2013). The resistance  $R = U/I$  can be transformed to the *apparent resistivity*  $\rho_a$  as (after Everett, 2013)

$$\rho_a = \kappa R, \tag{2.1}$$

## 2 Basic principles of the employed methods

where the *geometrical factor*  $\kappa$  is a function of the separation between the electrodes depending on the respective electrode configuration, e.g., dipole-dipole, multiple gradient or Wenner (e.g. Everett, 2013). For homogeneous subsurface conditions referring to a uniform distribution of the resistivity  $\rho$ , the computed  $\rho_a$  is constant for any combination of electrode spacing and measurement position, i.e.,  $\rho_a = \rho$  (e.g., Kearey et al., 2002; Everett, 2013). In case of an inhomogeneous subsurface, e.g., spatial variations in the  $\rho$  distribution, the computed  $\rho_a$  depends on the electrode geometry and the measurement position, i.e.,  $\rho_a \neq \rho$  (e.g., Kearey et al., 2002; Everett, 2013).

For imaging applications, the electrical resistivity tomography (ERT) method deploys several tens to hundreds of electrodes and searches for a subsurface model that can explain the measured data. This so-called *inversion* resolves the 2D or 3D variability in  $\rho$  starting from the apparent resistivity computed for an initial subsurface model, which is iteratively adapted to minimize the misfit between the measured and the computed apparent resistivity (Everett, 2013). The reciprocal of the electrical resistivity, namely the electrical conductivity  $\sigma$  defined as

$$\sigma = \frac{1}{\rho}, \quad (2.2)$$

is often the preferred measure in hydrogeological and environmental studies due to its direct relationship to material properties associated with fluid and heat transport (e.g., Binley and Slater, 2020).

Porous media are commonly described as a three-phase system consisting of a solid, a liquid and a gaseous phase (e.g., Powrie, 2018). Expanding this basic system might be necessary for specific subsurface conditions, e.g., for permafrost investigations frozen water (ice) is added as a fourth phase (four-phase model (4PM); Hauck et al., 2011). The bulk conductivity  $\sigma$  of such porous media depends on the intrinsic electrical properties, the volumetric content and the spatial distribution of the different phases, whereas the charge transport can occur through electronic or ionic conduction (Binley and Slater, 2020).

The electronic or matrix conduction  $\sigma_m$  is due to the movement of free electrons in the solid phase of porous media, and thus is only possible in metals or conductors (see Figure 2.1). However, the solids in porous media normally refer to insulators, which can become semi-conductors in presence of substantial concentrations of electron conducting minerals such as sulfides (Binley and Slater, 2020). Assuming that the solid phase impedes charge transport, the ionic conduction controls  $\sigma$  in form of electrolytic and surface conduction, respectively.

The electrolytic conduction is due to the flow of electric current through the liquid

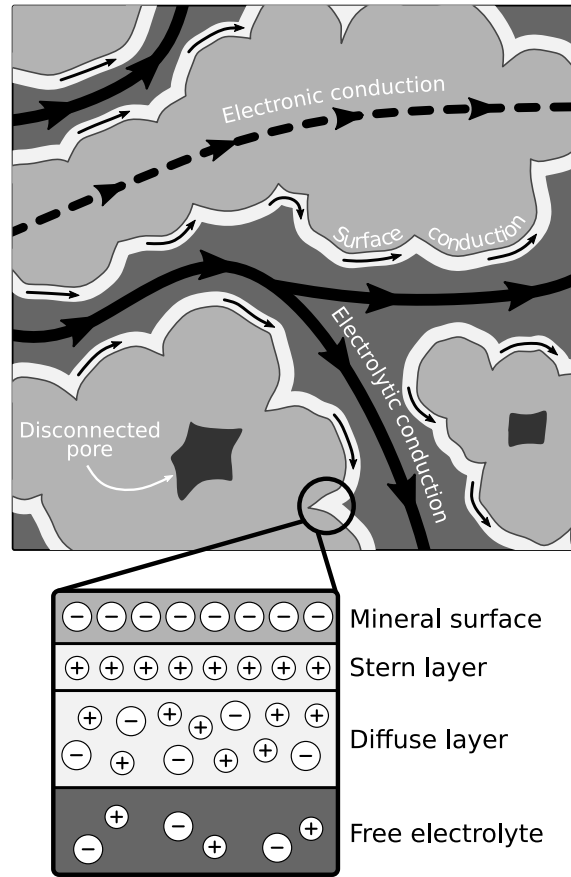


**Figure 2.1:** Schematic representation of different conduction pathways through a porous medium (modified from Glover (2015) and Binley and Slater (2020)).

phase filling the interconnected pore space of the porous medium, i.e., the transport of dissolved ions in presence of an electric field (Everett, 2013; Binley and Slater, 2020). Accordingly, the electrolytic conductivity  $\sigma_f$  is dependent on the conductivity of the fluid phase, e.g., the ground water,  $\sigma_w$ . The conductivity of such ionic solutions is given by (Binley and Slater, 2020)

$$\sigma_i = \frac{\hat{n}_i \hat{Z}_i^2 e^2}{6\pi\eta r_i}, \quad (2.3)$$

where  $\hat{n}_i$  and  $\hat{Z}_i$  are the density and the valence of a single charge carrier  $i$ , respectively;  $e$  denotes the elementary charge ( $1.6022 \times 10^{-19}$  C),  $\eta$  refers to the fluid viscosity (given in Pa s), and  $r_i$  is the radius of the hydrated ion (Binley and Slater, 2020). Equation 2.3 shows that  $\sigma_w$  and thus  $\sigma_f$  provide the link between the bulk conductivity of the porous medium and the aqueous chemistry of the pore water (Binley and Slater, 2020).

The third conduction mechanism – the surface conduction – is associated with the *electrical double layer* (EDL) formed at the interface between the solid and the fluid

## 2 Basic principles of the employed methods

phase of the porous medium (Binley and Slater, 2020). In particular, the charged surface of the solid minerals attracts counterions, i.e., oppositely charged ions, from the electrolyte, as shown in Figure 2.1. The fixed *Stern layer* consists of counterions adsorbed to the solid surface (Everett, 2013); yet, the adsorbed ions cannot balance the surface charge entirely (Glover, 2015). Accordingly, an increased concentration of counterions is found at a given distance from the solid surface (the so-called *Debye length*) where both co- and counterions form the *Diffuse layer* (Glover, 2015). In presence of an electric field, the ions in the EDL transport charge along the surface of the solid minerals, yielding the surface conductivity  $\sigma_s$ .

The empirical petrophysical relationships between electrical properties and rock properties found by Archie (1942) can be used to describe the electrolytic part  $\sigma_f$  of the bulk conductivity. Archie's first law is given as (after Glover, 2015):

$$F = \Phi^{-m} \quad (2.4)$$

Equation 2.4 shows that the electrical formation factor  $F$  is related to the porosity  $\Phi$  of the porous medium through a power law. The exponent  $m$  in Equation 2.4 is referred to as *cementation exponent*, which increases as the connectedness of the pore network decreases (Glover, 2015). Typical values for  $m$  are found to be between 1.5 and 2.5 for porous media, whereas carbonates are characterized by values higher than 2.5 (Glover, 2015). The formation factor can also be obtained from the ratio between the bulk conductivity of a fully saturated porous medium  $\sigma_o$  and the fluid conductivity as (after Glover, 2015):

$$F = \frac{\sigma_w}{\sigma_o} \quad (2.5)$$

Equations 2.4 and 2.5 can be combined to obtain Archie's first law expressed as (after Glover, 2015):

$$\sigma_o = \sigma_w \Phi^{-m} \quad (2.6)$$

Archie's second law shows that the bulk conductivity of a porous medium will increase when the pore space is filled with a conductive fluid (Glover, 2015; Binley and Slater, 2020, after):

$$I_r = S_w^{-n} \quad (2.7)$$

In Equation 2.7,  $S_w$  is the (water) saturation of the pore space, and  $I_r$  is referred to as

the resistivity index; the *saturation exponent*  $n$  is associated with changes in the electrical conductivity from partially to fully saturated rocks (e.g., Glover, 2015; Binley and Slater, 2020).  $n$  is commonly chosen as  $n = 2$  in calculations by petroleum geoscientists, whereas values of  $n = 2 \pm 0.5$  are used by hydrogeophysicists to characterize water-wet rocks (Glover, 2015; Everett, 2013). Alternatively,  $I_r$  can be expressed as the ratio between the bulk conductivity of a partially saturated porous medium  $\sigma_f$  and the bulk conductivity under fully saturated conditions  $\sigma_o$  (after Glover, 2015):

$$I_r = \frac{\sigma_o}{\sigma_f}. \quad (2.8)$$

Combining the different formulations for  $I_r$  yields the following representation of Archie's second law (after Glover, 2015):

$$\sigma_f = \sigma_o S_w^n \quad (2.9)$$

Eventually, Equations 2.6 and 2.9 can be combined to obtain the commonly used version of Archie's law (after Everett, 2013)

$$\sigma_f = \sigma_w \Phi^m S_w^n. \quad (2.10)$$

Equation 2.10 does not contain a term for the surface conductivity, and thus fails in presence of sediments associated with a substantial surface conductivity due to their large surface area (Glover, 2015). In particular, the application of Equation 2.10 to obtain  $S_w$  will result in overestimated values for  $S_w$  as the effect of the surface conduction on the observed electrical response is not taken into account (Glover, 2015). Accordingly, several mixing models have been developed for the description of the electrical properties in porous media accounting for both electrolytic and surface conduction (for more details the reader is referred to Glover, 2015). Most approaches assume a parallel conduction model where electric current is transported along the same path through the interconnected pore space in case of both electrolytic and surface conduction (Binley and Slater, 2020). In case of a negligible amount of metallic minerals in the solid phase, the bulk conductivity of the porous medium can be described as (after Binley and Slater, 2020)

$$\sigma = \sigma_f + \sigma_s = \sigma_w \frac{1}{F} + \sigma_{EDL} \frac{1}{F_{EDL}}, \quad (2.11)$$

where  $F_{EDL}$  and  $\sigma_{EDL}$  denote the formation factor and electrical conductivity of the EDL, respectively.

**Table 2.1:** Parameter values used to compute bulk conductivity based on Archie’s law and a constant surface conductivity.

$S_w$	100 %
$\sigma_w$	0.01 – 100 S m <sup>-1</sup>
$\sigma_s$	0.1 S m <sup>-1</sup>
$\Phi$	40 %
$m$	2
$n$	2

To illustrate the influence of the surface conductivity on the estimation of the saturation Equation 2.11 can be rewritten in a simplified manner as

$$\sigma = \sigma_w \Phi^m S_w^n + \sigma_s, \quad (2.12)$$

where the first term corresponds to Archie’s law and the second term refers to a constant contribution of the surface conductivity. Equation 2.12 can be used to compute the bulk conductivity based on the values for the different parameters summarized in Table 2.1. Figure 2.2 presents the obtained bulk electrical conductivity as function of the fluid conductivity for fully saturated conditions. This graph highlights how  $\sigma_w$  controls the relative importance of the different ionic conduction mechanisms. At high salinity values ( $> 5 \text{ S m}^{-1}$ ), the  $\sigma$  versus  $\sigma_w$  graph shows a linear relationship indicating that Archie’s law holds (*Archie region*), and thus the influence of  $\sigma_s$  is relatively insignificant (e.g., Binley and Slater, 2020). At low salinity values ( $\leq 5 \text{ S m}^{-1}$ ) the  $\sigma$  versus  $\sigma_w$  graph asymptotically approaches  $\sigma_s = 1 \times 10^{-1} \text{ S m}^{-1}$  as  $\sigma_w$  decreases, i.e., the relative importance of  $\sigma_s$  increases (e.g., Binley and Slater, 2020). However, the relative importance of electrolytic or surface conduction depends not only on the salinity of the pore fluid but also on the surface area of the solid minerals. In general, a high electrolytic conductivity is due to high-salinity fluids and low mineral surface area, whereas a low salinity of the pore fluid and a high mineral surface area yield a high surface conductivity (Binley and Slater, 2020). Accordingly, it is common to assume that in presence of coarse-grained materials the surface conductivity can be ignore in the interpretation of the observed electrical resistivity (Binley and Slater, 2020).

Based on Equation 2.12 it is possible to estimate  $S_w$  from the bulk conductivity  $\sigma$  as

$$S_w = \left( \frac{\sigma - \sigma_s}{\sigma_w \Phi^m} \right)^{1/n}. \quad (2.13)$$

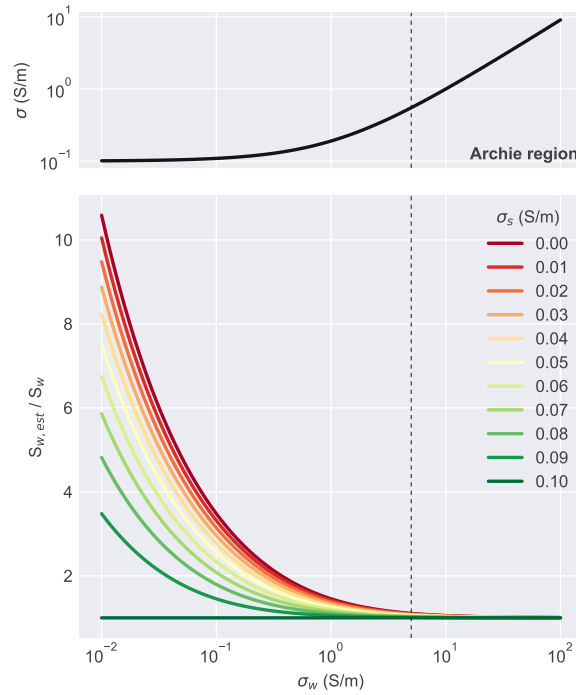


**Figure 2.2:** Influence of the surface conductivity on the estimated saturation.

To investigate the influence of the surface conductivity on the estimated saturation, Equation 2.13 is solved for  $0 < \sigma_s \leq 0.1 \text{ S m}^{-1}$ . Such estimation yields an ensemble of curves showing the ratio between the estimated ( $S_{w,est}$ ) and the true saturation ( $S_w = 100\%$ ) as a function of  $\sigma_w$ , i.e., the salinity of the pore fluid (see bottom panel of Figure 2.2). For the assumed subsurface properties (see Table 2.1, neglecting the effect of the surface conductivity (i.e.,  $\sigma_s = 0.00 \text{ S m}^{-1}$ ) Equation 2.13 severely overestimates the saturation by a factor  $\approx 10$ . As expected, the overestimation is particularly pronounced at low salinity and negligible in the Archie region where the relative importance of the surface conduction mechanism is low. Outside the Archie region a substantial overestimation is still observed for  $\sigma_s$  values approaching the true surface conductivity reported in Table 2.1. For the entire range of fluid conductivity values the true  $S_w$  value is resolved solely for  $\sigma_s = 0.10 \text{ S m}^{-1}$ . The graphs presented in Figure 2.2 demonstrate the necessity to consider the influence of the surface conductivity during the interpretation of the observed bulk electrical conductivity. Although shown here only for  $S_w$ , such erroneous estimates also have to be expected for other parameters, such as the cementation exponent (Binley and Slater, 2020).

An extensively used model to describe the surface conductivity in partially saturated porous media was proposed by Waxman and Smits (1968) and can be written as (after

Glover, 2015):

$$\sigma = \sigma_w \frac{1}{F_s} S_w^2 + \frac{1}{F_s} S_w B Q_v, \quad (2.14)$$

where  $F_s$  refers to the formation factor for shaley sand. By using a different formation factor than the Archie model, Equation 2.14 can also be applied in case the clay is dispersed throughout the solid or is part of the solid matrix (Glover, 2015). In Equation 2.14,  $B$  is the mobility of the sodium clay-exchange cations (given in  $\text{Scm}^2 \text{meq}^{-1}$ ) and  $Q_v$  denotes the volume concentration of the exchange cations, i.e., the cation exchange capacity (CEC) per unit volume given in  $\text{meq m}^{-3}$  (Glover, 2015). Accordingly, Equation 2.14 shows that the surface conductivity is controlled by the surface area instead of the volume of clay minerals as the cation exchange primarily takes place at broken bonds on the fluid-grain interface, i.e., this excess conductivity (Binley and Slater, 2020; Glover, 2015).

### 2.1.2 Complex conductivity measurements

Until this point, only a steady-state electrical flow has been considered, i.e., a constant electrical current flow due to the application of a constant electrical potential (Glover, 2015). However, the applied potential might show a transient or harmonic behavior causing two different processes: (1) the charge transport described by the electrical conductivity of a (porous) medium, i.e., the conductive properties; (2) a temporary, reversible charge storage described by the dielectric polarization of the medium, i.e., the capacitive properties (Glover, 2015; Binley and Slater, 2020). The temporary charge storage is due to different polarization mechanisms associated with the EDL, namely *Stern layer* and/or *diffuse layer polarization* as well as *membrane polarization* (e.g., Binley and Slater, 2020). Other polarization mechanisms, i.e., *Maxwell-Wagner polarization* and *electrode polarization* are not further discussed here. Assuming a narrow pore space the counterions attached to the charged surface of the solid phase mineral forming the EDL can be related to both the membrane and the Stern layer polarization (e.g., Everett, 2013). In presence of an external electrical field, the mobility of the ions dispersed in the electrolyte filling the pore space is impeded by the substantially lower mobility of the ions absorbed in the EDL (Everett, 2013). This blockage of ions causes localized excesses and deficiencies in the ion concentration in the pore space, which is referred to as membrane polarization (Binley and Slater, 2020). The Stern layer polarization is due to the tangential displacement of the ions attached to the mineral surface when an electrical field is applied, i.e., the absorbed ions are aligned according to the direction of the external electrical field (Everett, 2013; Binley and

Slater, 2020).

To gain information about the charge storage properties of the soil, *induced polarization* measurements can be conducted (Binley and Slater, 2020). As an extension of the ERT, the IP method is also based on measurements with four-electrode arrays and can be conducted in the time-domain (TDIP) or in the frequency-domain (FDIP) (e.g., Everett, 2013; Binley and Slater, 2020). Similar to the ERT, the time-domain IP (TDIP) method injects DC into the subsurface, yet at some point the current injection is switched off (Everett, 2013). In case of a polarizable subsurface, the voltage does not drop instantaneously to zero but rather decays slowly, a transient behavior referred to as the time-domain *IP effect*, which is directly related to the charge storage effect (Everett, 2013; Binley and Slater, 2020). In particular, the TDIP methods provides the resistance  $R = U/I$ , and the integral chargeability  $M$  measuring the voltage decay after the current switch-off (e.g., Binley and Slater, 2020). This thesis, primarily considers the FDIP method, which injects alternating current (AC), i.e., a harmonic sine signal, into the ground and measures the complex impedance  $Z_e^* = U^*/I^*$  in terms of the impedance magnitude  $|Z_e|$  and the impedance phase shift  $\varphi_{Z_e}$  between the injected current and the observed voltage (Binley and Slater, 2020). The inversion of  $Z_e^*$  yields models for the complex conductivity (CC)  $\sigma^*$  written as

$$\sigma^* = \sigma' + i\sigma'' , \quad (2.15)$$

where  $i = \sqrt{-1}$  is the imaginary unit (Glover, 2015). Alternatively, the complex electrical properties of the porous medium can be expressed in terms of its reciprocal, the complex resistivity (CR):

$$\rho^* = \frac{1}{\sigma^*} = \rho' - i\rho'' . \quad (2.16)$$

The real ( $\sigma'$ ) and the imaginary component ( $\sigma''$ ) of the CC refer to the charge transport and storage, respectively (Binley and Slater, 2020). Alternatively, the CC can be expressed in terms of its  $|\sigma|$  and phase  $\varphi$  as:

$$\sigma^* = |\sigma| e^{i\varphi} . \quad (2.17)$$

The constituents of Equations 2.15 and 2.17 are related as (after Binley and Slater, 2020)

$$|\sigma| = \sqrt{(\sigma')^2 + (\sigma'')^2} , \quad (2.18)$$

## 2 Basic principles of the employed methods

$$\varphi = \tan^{-1} \left( \frac{\sigma''}{\sigma'} \right), \quad (2.19)$$

and

$$\sigma' = |\sigma| \cos \varphi, \quad (2.20)$$

$$\sigma'' = |\sigma| \sin \varphi. \quad (2.21)$$

For sufficiently small phase shifts ( $\varphi < 100$  mrad) Equation 2.18 can be approximated as  $|\sigma| \approx \sigma'$ , and Equation 2.19 becomes  $\varphi \approx \sigma''/\sigma'$ .

Considering that the EDL is responsible for the surface conduction it is beneficial to express the surface conductivity also as a complex value

$$\sigma_s^* = \sigma'_s + i\sigma''_s, \quad (2.22)$$

where the real ( $\sigma'_s$ ) and imaginary component ( $\sigma''_s$ ) represent the conduction and polarization processes associated with the EDL, respectively (Binley and Slater, 2020). Based on  $\sigma_s^*$  Equation 2.11 can be extended as proposed by Vinegar and Waxman (1984) and Lesmes and Frye (2001) to account for the surface polarization (after Binley and Slater, 2020):

$$\sigma^* = \sigma_f + \sigma_s^* = \sigma_f + \sigma'_s + i\sigma''_s. \quad (2.23)$$

For low frequencies ( $< 1$  kHz) the electrolytic conductivity described by Archie's law is considered to be not associated with a polarization effect due to the weak dipolar polarization of the water molecules (Binley and Slater, 2020). Accordingly, the real and the imaginary component of the CC can be written as (following Binley and Slater, 2020):

$$\sigma' = \sigma_f + \sigma'_s, \quad (2.24)$$

$$\sigma'' = \sigma''_s. \quad (2.25)$$

Equation 2.24 is consistent with Equation 2.11 showing that the measured conductivity equals the sum of the conductivity associated with the electrolytic and surface conduction mechanisms acting in parallel (Binley and Slater, 2020). Equation 2.25 shows that the imaginary conductivity is solely sensitive to the surface conduction and not influenced by the electrolytic conduction (Binley and Slater, 2020). This highlights the relevance of the IP method for the discrimination between the electrolytic and surface conduction mechanisms allowing for an enhanced characterization of subsurface conditions.

### 2.1.3 Frequency-dependent electrical properties of the subsurface materials

So far, the electrical properties of the porous media have been assumed to be frequency-independent, with  $\sigma_f$  and  $\sigma_s$  (e.g., Equation 2.11) being treated as direct current (DC) values (Binley and Slater, 2020). However, the CC (see Equation 2.15) used to describe both the electrical conductivity and the polarization of the subsurface is actually a frequency dependent property (Binley and Slater, 2020). At IP frequencies considered here, the CC can be written as (after Lesmes and Frye, 2001)

$$\sigma^*(\omega) = \sigma'(\omega) + i\sigma''(\omega) = [\sigma_f + \sigma'(\omega)] + i\sigma_s''(\omega), \quad (2.26)$$

where  $\omega$  denotes the angular frequency. Equation 2.26 shows that the frequency-dependence of the CC is due to the surface conduction in the EDL, i.e., related to the physicochemical properties of the porous medium (Binley and Slater, 2020). To obtain information about the frequency-dependence of the CC, FDIP measurements are conducted with different frequencies referred to as *spectral induced polarization* (SIP; Binley and Slater, 2020). Such frequency-dependent measurements provide the means to obtain the characteristic relaxation time ( $\tau$ ), which defines the time-scale of the strongest polarization response, which is related to the length of the solid-fluid interface over which the ions are temporarily displaced (Binley and Slater, 2020).

A commonly used model to describe the observed dispersion in the CC is the empirical Cole-Cole model (Cole and Cole, 1941) written as:

$$\sigma^*(\omega) = \sigma_\infty - \frac{\sigma_\infty - \sigma_0}{1 + (i\omega\tau_0)^c}. \quad (2.27)$$

In Equation 2.27,  $\tau_0$  is a generalized relaxation time, which is related to the critical frequency  $f_c$  corresponding to the peak in  $\sigma''$ ; whereas  $c$  is referred to as the Cole-Cole parameter that accounts for the steepness of the dispersion (Cole and Cole, 1941;

Binley and Slater, 2020). The terms  $\sigma_\infty$  and  $\sigma_0$  refer to the DC (low frequency) and instantaneous or infinite (high frequency) values of the conductivity (Binley and Slater, 2020; Cole and Cole, 1941). The difference between  $\sigma_\infty$  and  $\sigma_0$  is a measure of the polarization strength referred to as the *normalized chargeability*  $M_n = \sigma_\infty - \sigma_0$  (Binley and Slater, 2020). Lesmes and Frye (2001) proposed that  $M_n$  is a measure of the polarization, i.e., comparable to  $\sigma''$ , and thus related to the surface conductivity (Binley and Slater, 2020).

Although empirical models such as the Cole-Cole expression are a convenient way to model the observed dispersion in the CC based on a small number of parameters, models providing a physical explanation for the frequency-dependence are required to extend the theoretical explanations from IP to SIP measurements (Binley and Slater, 2020). Such mechanistic models relate the time-dependence of the IP response to the geometric length-scales characterizing the porous medium, whereas  $\sigma_s^*$  is described based either through a grain- or pore-size-based approach, or a pore-throat models (Binley and Slater, 2020). Besides the length-scale, the mechanistic models can also be categorized based on whether surface conduction and polarization mechanisms are associated with the diffuse and/or the Stern layer of the EDL (Binley and Slater, 2020). On the one hand, some models (Schwarz, 1962; Leroy et al., 2008; Revil et al., 2017c) attribute the polarization to the Stern layer and the diffuse layer is assumed to be solely related to charge transport; whereas other models (Dukhin et al., 1974) attribute the polarization to the diffuse layer (Binley and Slater, 2020). The recently developed model from Bucker et al. (2019b) considers the polarization in the EDL to be associated with both the diffuse and the Stern layer .

## 2.2 The seismic refraction method for near-surface applications

In general, seismic methods rely on an active source, which generates elastic waves propagating through the subsurface (e.g. Everett, 2013). Due to the mechanical properties of the subsurface materials these seismic waves are reflected and refracted at interfaces between adjacent subsurface layers (also referred to as *refractors*) and eventually return to the surface (e.g., Kearey et al., 2002), where the associated ground motion is registered with geophones (e.g., Everett, 2013).

The mechanical energy transmitted into the subsurface generates different kinds of seismic waves: (i) body waves that propagate through the internal volume of an elastic medium, and (ii) surface waves propagating along the the free surface of an elastic medium (e.g., Everett, 2013; Kearey et al., 2002). The propagation velocity of

body waves is dependent on the elastic properties and the density of the subsurface materials and can be computed as (e.g., Everett, 2013)

$$v_p = \left( \frac{K_m + \frac{4}{3}\mu}{\delta_b} \right)^{1/2} \quad v_s = (\mu/\delta_b)^{1/2} \quad (2.28)$$

with  $v_p$  and  $v_s$  denoting the P-wave and S-wave velocity, respectively, and  $v_p \approx 1.7v_s$  (Kearey et al., 2002; Mavko et al., 2009). In Equation 2.28,  $K_m$  denotes the bulk modulus, i.e., the volume change due to the application of a hydrostatic pressure,  $\mu$  is the shear modulus as a measure for the shear stiffness, and  $\delta_b$  is the bulk density of the medium (e.g. Mavko et al., 2009). For a three-phase soil system,  $\delta_b$  is given as (after Bourbié et al., 1992)

$$\delta_b = \Phi (S_w \delta_w + (1 - S_w) \delta_a) + (1 - \Phi) \delta_r, \quad (2.29)$$

where  $S_w$  is the water saturation,  $\Phi$  is the porosity, and  $\delta_w$ ,  $\delta_a$  and  $\delta_r$  denote the density of the water, the air and the rock phase of the soil, respectively.

The reflection and refraction of seismic waves in the subsurface is dependent on the acoustic impedance  $Z_a$  of the different media, which can be computed as the product of density  $\delta$  and velocity  $v$ , i.e.,  $Z_a = \delta v$  (Kearey et al., 2002). As shown in Figure 2.3, a P-wave obliquely incident on an interface between two layers (angle of incidence  $i_1$ ) characterized by a contrasting acoustic impedance creates both a reflected and a refracted P-wave (the conversion to reflected and refracted S-waves is not shown here for brevity). In both cases, *Snell's Law of Refraction* applies, which shows that for the reflected P-wave ray the angle of reflection is equal to the angle of incidence (Kearey et al., 2002); whereas for the refracted ray

$$\frac{\sin i_1}{v_1} = \frac{\sin i_2}{v_2}. \quad (2.30)$$

If  $v_2 > v_1$  the ray is refracted away from the normal to the interface at the angle of refraction  $i_2 > i_1$  (Kearey et al., 2002). Moreover, in case  $v_2 > v_1$ , a P-wave incident at the critical angle  $i_c = \sin^{-1}(v_1/v_2)$  generates a *critically refracted ray*, which propagates along the interface at velocity  $v_2$ , i.e.,  $i_2 = 90^\circ$  (e.g. Everett, 2013; Kearey et al., 2002). In accordance with *Huygen's principle*, such critically refracted wave continuously transmits mechanic energy into the adjacent layers causing the so-called *head wave* in the overlying layer with the inclination of the associated ray paths being equal to the critical angle (see Figure 2.3; Kearey et al., 2002; Everett, 2013).

The basic principles of a seismic refraction survey are graphically summarized in

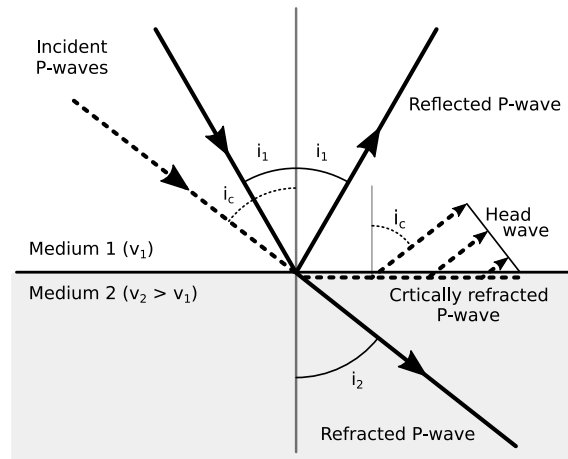


**Figure 2.3:** Reflection and refraction of a P-wave obliquely incident on an interface associated with a contrast in the acoustic impedance  $Z$  (after Everett, 2013; Kearey et al., 2002).

Figure 2.4. In particular, the example considers a model of 104 m horizontal extent without topography and three horizontal layers in the subsurface. The interfaces between these layers are parallel to the surface and found at 5 m and 15 m depth. A homogeneous seismic velocity  $v_p$  is assumed in the subsurface units, with  $v_p = 500 \text{ m s}^{-1}$ ,  $1500 \text{ m s}^{-1}$  and  $3000 \text{ m s}^{-1}$  for the top ( $v_1$ ), intermediate ( $v_2$ ) and bottom layer ( $v_3$ ), respectively.

For the subsurface model presented in Figure 2.4, the forward modeling capabilities of pyGIMLi (Rücker et al., 2017) were used to compute the ray paths associated with seismic waves radiating from a distinct shot point located at 4 m along profile direction. Moreover, the associated ground motion is registered by 12 geophones located at different offsets from the shot point along profile direction yielding the *seismograms* shown above the model. Note, that the seismogram at the shot position depicts the Ricker wavelet used to emulate the impulse generated by impact sources applied in field surveys.

Seismograms show the amplitude of the ground motion as a function of time, and thus allow for the identification of the first arrivals at the different geophone positions. In particular, the first arrival corresponds to the travel time of the seismic wave between the shot point on the corresponding geophone position, whereas the measuring of travel times in seismograms is referred to as *first break picking*. The first break travel times for this exemplary scenario are indicated by a cross overlaid on each seismogram in Figure 2.4. Connecting the crosses consecutively along the profile yields a *travel time curve*, which can be used to determine the number of interfaces in the subsurface based on the number of observed inflexion points.

As can be seen in Figure 2.4, for geophones located at small offsets from the shot point, the first arrivals correspond to the *direct wave* propagating through the top layer at velocity  $v_1$  (e.g., Kearey et al., 2002; Everett, 2013). This is due to the fact that the critically refracted wave propagating along the interface between the top and intermediate layer at velocity  $v_2$  emerges after the direct wave, and thus can be observed initially at the critical distance  $x_{crit}$  defined as

$$x_{crit} = 2z \tan i_c, \quad (2.31)$$

where  $z$  denotes the corresponding layer thickness. However, at  $x_{crit}$  the first arrivals observed in the seismograms are still related to the direct wave. The travel times of direct and critically refracted wave are equal at the crossover distance  $x_{cross}$ , which can be computed as (Kearey et al., 2002)

$$x_{cross} = 2z \left[ \frac{v_2 + v_1}{v_2 - v_1} \right]^{1/2}. \quad (2.32)$$

At  $x_{cross}$ , the critically refracted wave overtakes the direct wave, i.e., first arrivals in the seismograms are now related to the critically refracted wave propagating at velocity  $v_2$ . In the same way, the head wave generated by the critically refracted wave propagating at velocity  $v_3$  will overtake the other waves, and thus the corresponding first onsets observed in the seismograms are due to the critical refraction at the interface between intermediate and bottom layer.

As shown in Figure 2.4, the travel time curve can be used to determine the seismic velocities of the materials in the subsurface layers based on the slope of the respective segments of the curve. Moreover, by extending a travel time curve segment associated with critically refracted arrivals the intersection with time axis can be determined. The point of intersection yields the *intercept time*  $t_i$  defined as (Kearey et al., 2002)

$$t_i = \frac{2z (v_2^2 - v_1^2)^{1/2}}{v_1 v_2}, \quad (2.33)$$

which can be solved for  $z$

$$z = \frac{t_i v_1 v_2}{2 (v_2^2 - v_1^2)^{1/2}} \quad (2.34)$$

to obtain the corresponding refractor depth. Accordingly, the SR method provides a relatively simple approach to resolve the thickness of subsurface layers as well as the associated seismic velocity of the materials, assuming an increase of  $v_p$  with depth.

## 2 Basic principles of the employed methods

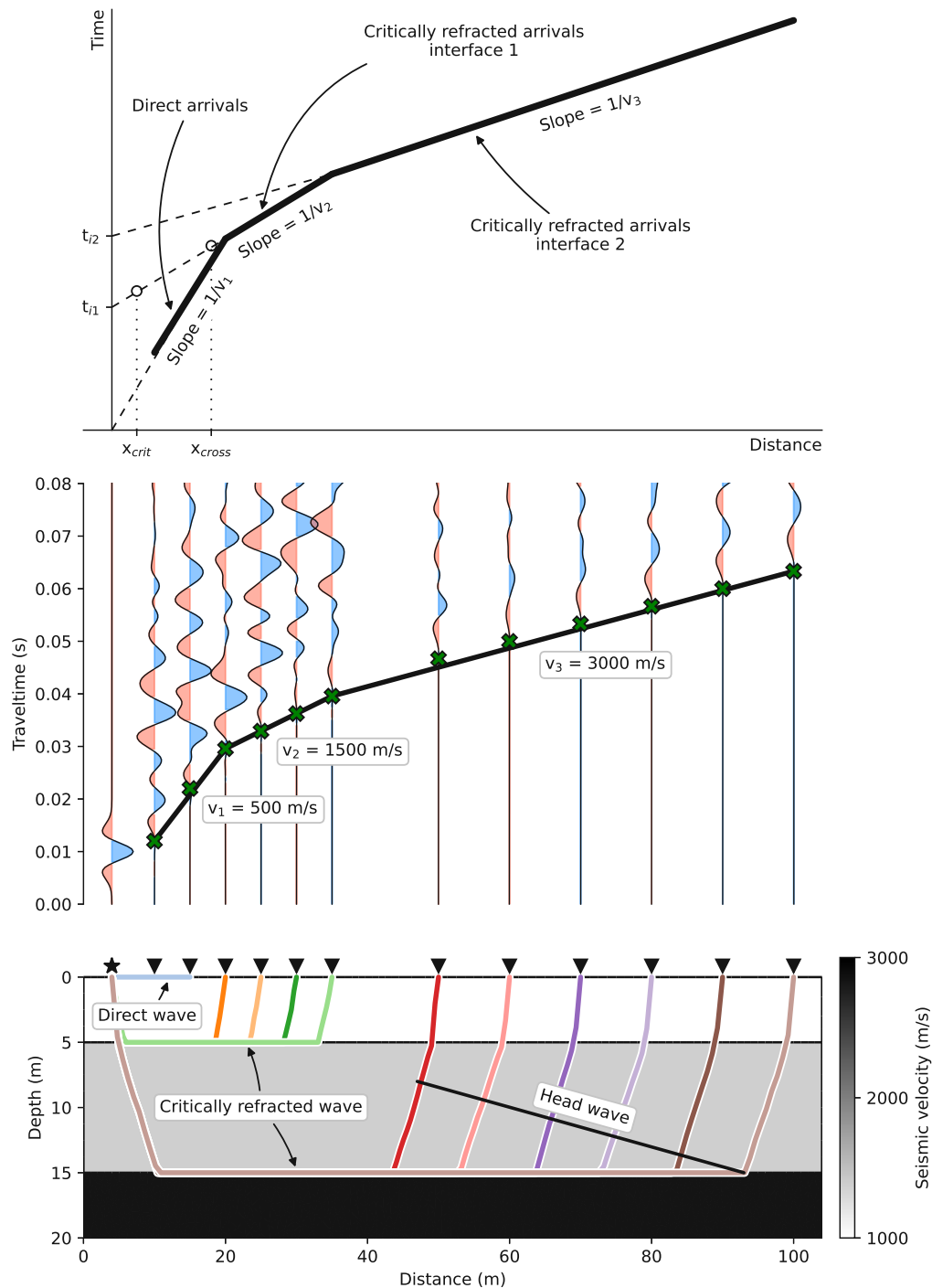


**Figure 2.4:** Schematic illustration of the key components and principles in seismic refraction investigations. In the synthetic subsurface model (bottom), the shot point is indicated by the star-shaped symbols, while filled triangles depict the geophones deployed at the ground surface. In the forward modeled seismograms shown at the positions of the geophones, the first onset of the seismic waves in the seismograms are marked with filled crosses. The top-most plot provides a geometrical interpretation of the travel time curve obtained from the first onsets.

However, if the intermediate layer is too thin or the contrast between  $v_1$  and  $v_2$  is too small, and thus the onsets associated with the head wave propagating along the interface will not be visible as first arrivals in the seismograms (hidden layer problem Kearey et al., 2002). For  $v_2 < v_1$  rays cannot be critically refracted, and thus the intermediate layer will not give rise to a head wave (blind layer problem; Kearey et al., 2002). Such scenarios have to be considered for the survey design or should be investigated during the data processing.

For field applications aiming at the characterization of the subsurface conditions, several tens to hundreds of geophones are deployed at the surface (or in boreholes) and shots are conducted at a similarly large number of positions. Most commonly, the SR measurements are conducted along straight profiles, which need to be at least five times as long as the envisaged depth of investigation (e.g., Kearey et al., 2002); yet, 3D survey designs are also possible. Considering that environmental and engineering investigations commonly require non-invasive methods the most commonly used source for such seismic surveys is a sledge hammer as it provides a fairly good repeatability and an adequate frequency content (50 Hz to 200 Hz) for near-surface applications (Everett, 2013). Mechanical energy is transmitted into the subsurface by hitting a massive plate (commonly made of plastic) with the sledge hammer. By conducting  $n$  hammer blows at a shot position the signal-to-noise ratio in the recorded seismogram can be improved by  $\sqrt{n}$  (e.g., Everett, 2013).

Following such a survey design several hundreds to thousands of first break travel times are obtained for a single profile. In the classical seismic refraction analysis these travel times can then be analyzed through different approaches, with the plus-minus method (Hagedoorn, 1959) or the generalized reciprocal method (Palmer, 1980) being most well-known (e.g., Kearey et al., 2002). In case of less distinct refractors or a gradual distribution of the seismic velocity in the subsurface, the seismic refraction tomography (SRT) is a more appropriate method. In particular, the SRT solves for the spatial variability in the seismic velocity by modeling seismic rays as the shortest path between two points (e.g., Moser, 1991), a technique known as *ray tracing* (e.g., Kearey et al., 2002). Starting from an initial subsurface model the travel times for the modeled ray paths are compared to the first break travel times and the subsurface model is iteratively adapted to minimize the misfit between modeled and observed travel times (e.g., Ronczka et al., 2017). Such inversion process yields subsurface models with high spatial resolution depending on the survey design and the available computer hardware.

In environmental and engineering investigations, the SR(T) method is the most commonly used seismic method considering its relatively simple measurement principle

and survey design (e.g., Kearey et al., 2002), although the seismic reflection method (e.g., Sloan et al., 2009), as well as methods using S-waves (e.g., Uhlemann et al., 2016) or surface waves (e.g., Barone et al., 2021) provide more information regarding the subsurface properties. However, the application of S- and surface-wave-based methods often requires increased efforts in terms of data acquisition and processing.

This thesis considers the SRT method as the resolved bulk velocity  $v$  can be related to the porosity  $\Phi$  through simple models such as the time-average equation proposed by (Wyllie et al., 1956):

$$\frac{1}{v} = \frac{1 - \Phi}{v_m} + \frac{\Phi}{v_f} \quad (2.35)$$

In Equation 2.35,  $v$  denotes the observed bulk velocity and  $\Phi$  is the porosity, whereas  $v_m$  and  $v_f$  refer to the seismic velocity of the solid phase matrix and the pore fluid, respectively. The Wyllie equation provides a simple approach to obtain the measured bulk velocity assuming it to be equal to the sum of the seismic velocity of the different soil constituents weighted by the porosity. Moreover, the Wyllie equation is similar to Archie's law (Equation 2.10), which describes the relationship between the electrical resistivity  $\rho$  and  $\Phi$ . This common sensitivity of the ER/IP and the SR methods to  $\Phi$  allows for their combined application either in joint interpretation or joint inversion approaches.

### 2.3 Combined application of seismic and electric methods

Geophysical investigations aim at characterizing the spatial variability in one or more properties of the subsurface (Binley et al., 2015). The design of surveys leveraging upon the contrasting sensitivities of different (often complementary) geophysical methods is common practice to overcome the limitations of single-method investigations (see Linde and Doetsch, 2016, and references therein). Consistencies in ERT and SRT imaging results (e.g., Meju et al., 2003) suggest that the combination of the ERT and the SRT methods can be particularly advantageous considering their contrasting sensitivities to the subsurface properties, i.e., rock composition and fluid distribution (ERT) and mechanical properties (SRT). The simplest approach is the post inversion combination of ERT and SRT imaging results referred to as *joint interpretation*; yet, the final result might be affected by uncertainties related to the independent inversion of the data sets. Alternatively, the data sets can be combined through *joint inversion*, where the data sets are inverted together leveraging upon a common sensitivity to a structural feature or a petrophysical parameter.

Traditionally, the geophysical inversion problem is solved through deterministic inversion schemes, yet stochastic approaches are becoming more common, related to both interpretation and inversion. As stated by Binley et al. (2015) the final decision regarding the inversion approach will always depend on the general setting and the focus of the geophysical investigations. This thesis considers deterministic inversion approaches, which allow for the independent and joint inversion of complementary geophysical data sets, namely electrical resistivity and seismic refraction data. Aiming at the quantification of relevant hydrogeological parameters, petrophysical joint inversion approaches are particularly suitable considering their ability to directly solve for the target parameters in a quantitative manner. Accordingly, this section revisits the formal principles of deterministic inversion approaches solving the geophysical inversion problem. In particular, the basic equations and terms are described for the independent inversion of a single geophysical data set, which are then expanded to the joint inversion of multiple geophysical data set.

### 2.3.1 Inversion of a single geophysical data set

Forward modeling and inversion of geophysical data are commonly based on a spatial discretization referred to as *mesh* in case of an irregular discretization, e.g., triangular shaped mesh cells (e.g., Rücker et al., 2017). A regular discretization (e.g., quadrangular mesh cells) is referred to as *grid* (e.g., Rücker et al., 2017), yet not further considered in this thesis. In general, such a finite-element mesh consists of  $N$  nodes,  $C$  cells and  $B$  boundaries forming the modeling domain, where nodes refer to discrete position vectors, and a collection of nodes forms a mesh cell (Rücker et al., 2017). For further details regarding meshes the reader is referred to Günther et al. (2006), Cockett et al. (2015) or Rücker et al. (2017), and the references therein.

The inversion of a geophysical data set refers to the minimization of an objective function of the form (LaBrecque et al., 1996; Günther et al., 2006)

$$\Psi(\mathbf{m}) = \Psi_d(\mathbf{m}) + \lambda\Psi_m(\mathbf{m}), \quad (2.36)$$

where the model vector  $\mathbf{m} = (m_1, m_2, \dots, m_C)^T$  holds the individual model parameters  $m_j$  for the  $C$  mesh cells, e.g., triangles in 2D or tetrahedrons in 3D (Günther et al., 2006). By minimizing the objective function (Equation 2.36) the inversion process estimates a model that can explain the observed data (e.g., Ronczka et al., 2017).

In Equation 2.36,  $\Psi_d$  is the data functional defined as

$$\Psi_d(\mathbf{m}) = \| \mathbf{W}_d(\mathbf{d} - \mathcal{F}(\mathbf{m})) \|_2^2, \quad (2.37)$$

## 2 Basic principles of the employed methods

with the data vector  $\mathbf{d} = (d_1, d_2, \dots, d_M)^T$  holding  $M$  data points; whereas the data weighting matrix  $\mathbf{W}_d$  refers to a diagonal matrix holding the reciprocals of the corresponding error  $\epsilon_i$ . For the inversion, the data errors are assumed to be normally distributed and uncorrelated (LaBrecque et al., 1996). In general, the data errors can be provided as absolute values, as a percentage of the measured data, or as an error model combining absolute and relative (percentage) error written as

$$\boldsymbol{\epsilon}(\mathbf{d}) = \epsilon_{abs} + \epsilon_{rel}\mathbf{d}, \quad (2.38)$$

where  $\epsilon_{abs}$  refers to the absolute error and  $\epsilon_{rel}$  is the relative error (following the error model proposed for the electrical resistance error, e.g., LaBrecque et al., 1996; Flores Orozco et al., 2012b; Slater et al., 2000).

The second term in Equation 2.36 refers to a model functional given as

$$\Psi_m(\mathbf{m}) = \|\mathbf{W}_m(\mathbf{m} - \mathbf{m}_0)\|_2^2, \quad (2.39)$$

with the model constraint matrix  $\mathbf{W}_m$  and the reference model  $\mathbf{m}_0$  (Günther et al., 2006; Rücker et al., 2017). In case of a constant reference model,  $\mathbf{W}_m$  controls the model characteristics, e.g., through the application of smoothness constraints (Günther et al., 2006). Alternatively,  $\mathbf{m}_0$  can be used to impose *a priori* information as constraints on the model  $\mathbf{m}$  by setting  $\mathbf{W}_m = \mathbf{I}$  or as a diagonal weighting matrix (Günther et al., 2006).

Just minimizing the misfit between observed and modeled data yields a solution that fits the data, yet the resolved models might not always be reasonable (LaBrecque et al., 1996). Accordingly, the regularization parameter  $\lambda$  in Equation 2.36 weights the relative influence of the model roughness ( $\Psi_m(\mathbf{m})$ ) versus the data misfit ( $\Psi_d(\mathbf{m})$ ) on the objective function (LaBrecque et al., 1996). The  $\lambda$  value used in the inversion depends on the length of the data vector  $\mathbf{d}$ , the data error  $\epsilon$  and the mesh properties (e.g., mesh cells between sensor nodes), and thus needs to be selected carefully as it is associated with variations over several orders of magnitude (LaBrecque et al., 1996). On the one hand, for a small  $\lambda$  value the resolved solution might be strongly affected by  $\epsilon$ , i.e., the model was probably fitted to the error instead of the signal (Calvetti et al., 2000). On the other hand, a solution obtained for a huge  $\lambda$  value is commonly associated with a large data misfit (Calvetti et al., 2000). A possible approach to determine the  $\lambda$  value is based on the so-called Tikhonov-curve (or L-curve), which is created by plotting the  $\Psi_d(\mathbf{m})$  versus  $\Psi_m(\mathbf{m})$  for a range of  $\lambda$  values (Hansen and O'Leary, 1993). In particular, the vertex of the Tikhonov-curve indicates the optimal

$\lambda$  value, which balances data misfit and error propagation (Calvetti et al., 2000).

For non-linear geophysical problems, Gauss-Newton schemes have proven to be suitable for the minimization of the objective function (Cockett et al., 2015), which yielding the model update  $\Delta \mathbf{m}_k = \mathbf{m}_k - \mathbf{m}_{k-1}$  for the  $k^{th}$  iteration by solving

$$(\mathbf{J}^T \mathbf{W}_d^T \mathbf{W}_d \mathbf{J} + \lambda \mathbf{W}_m^T \mathbf{W}_m) \Delta \mathbf{m}^k = \mathbf{J}^T \mathbf{W}_d^T \mathbf{W}_d (\Delta \mathbf{d}^k) - \lambda \mathbf{W}_m^T \mathbf{W}_m (\mathbf{m}_k - \mathbf{m}_0) \quad (2.40)$$

through a conjugate-gradient least-squares method (e.g., Kemna et al., 2000; Günther et al., 2006; Rücker et al., 2017). In Equation 2.40,  $\Delta \mathbf{d}_k = \mathbf{d} - \mathcal{F}(\mathbf{m}_k)$  (Rücker et al., 2017; Günther et al., 2006), and  $\mathbf{J}$  is the *Jacobian matrix*, which holds the changes in the model responses  $\mathcal{F}_i$  with respect to the changes in the model parameters  $m_j$  (e.g., Binley et al., 1995; Günther et al., 2006):

$$J_{i,j}(\mathbf{m}_k) = \frac{\partial \mathcal{F}_i(\mathbf{m}_k)}{\partial m_j}. \quad (2.41)$$

The inversion process stops once a data-fit criterion is reached, or the changes in  $\Psi$  remain at a stable level (e.g., LaBrecque et al., 1996; Günther et al., 2006). In this regard, a useful measure for how small  $\Psi_d$  should be is the error-weighted chi-squared fit defined as (following Günther et al., 2006; Günther and Rücker, 2015)

$$\chi^2 = \frac{\Psi_d}{M}. \quad (2.42)$$

Here,  $\chi^2 = 1$  indicates that the resolved model explains the observed data within their respective error bounds, i.e., the misfit between the observed data and the model response has reached a confidence level defined by the error model  $\epsilon$  (Günther et al., 2006; Günther and Rücker, 2015). Accordingly, in case of a least-squares approach, the inversion would finish if  $\chi^2 \approx 1$  (e.g., LaBrecque et al., 1996; Günther et al., 2006); whereas Günther et al. (2006) state that solutions for which  $1 \leq \chi^2 \leq 5$  should be considered satisfactory (Binley and Slater, 2020). Alternatively, some inversion frameworks use the root-square  $RMS = \chi = \sqrt{\chi^2}$  to quantify the data misfit (e.g., Kemna, 2000).

### 2.3.2 Joint interpretation of independently resolved subsurface models

A widely used approach to combine different – commonly complementary – geophysical methods is through the joint interpretation of the resolved (imaging) results. For the joint interpretation of ERT and SRT results, the observed apparent electrical

## 2 Basic principles of the employed methods

resistivity values ( $\rho_a$ ) and P-wave traveltimes ( $t$ ) are independently inverted to solve for subsurface models expressed in terms of the electrical resistivity and the seismic velocity, respectively. In case of the ERT, the  $\rho_a$  values are gathered in the data vector  $\mathbf{d}_{ERT} = (\rho_{a,1}, \rho_{a,2}, \dots, \rho_{a,M})^T$  and the model vector  $\mathbf{m}_{ERT} = (\rho_1, \rho_2, \dots, \rho_C)^T$  holds the electrical resistivity  $\rho$  values (after Ronczka et al., 2017):

$$\mathbf{J}_{ERT} \Delta \mathbf{m}_{ERT} = \mathbf{d}_{ERT} - \mathcal{F}_{ERT}(\mathbf{m}_{ERT}) . \quad (2.43)$$

In Equation 2.43, the Jacobian matrix  $\mathbf{J}_{ERT}$  holds changes in the apparent resistivity values with respect to the changes in the resistivity values:

$$J_{ERT,i,j}(\mathbf{m}_{ERT,k}) = \frac{\partial \rho_{a,i}}{\partial m_j} . \quad (2.44)$$

Similarly, for the SRT the data vector  $\mathbf{d}_{SRT} = (t_1, t_2, \dots, t_M)^T$  and the model vector  $\mathbf{m}_{SRT} = (v_1, v_2, \dots, v_C)^T$  hold the measured traveltimes and the seismic velocity  $v_p$  values, respectively:

$$\mathbf{J}_{SRT} \Delta \mathbf{m}_{SRT} = \mathbf{d}_{SRT} - \mathcal{F}_{SRT}(\mathbf{m}_{SRT}) . \quad (2.45)$$

In case of the SRT, the elements of the Jacobian matrix  $\mathbf{J}_{SRT}$  refer to the changes in the traveltimes with respect to the changes in the seismic velocity values:

$$J_{SRT,i,j}(\mathbf{m}_{SRT,k}) = \frac{\partial t_i}{\partial m_j} . \quad (2.46)$$

The resolved subsurface models given in terms of  $\rho$  and  $v_p$  are subsequently joined for a qualitative interpretation, which commonly refers to a graphical correlation based on the superposition of the independently obtained results (e.g., Marzan et al., 2021). However, such qualitative joint interpretation might be affected by diverging resolutions and dimensions of the resolved models as well as the different uncertainties of the solutions due to the errors associated with the different geophysical data sets (Pérez-Díaz et al., 2020).

### 2.3.3 Joint inversion of multiple geophysical data sets

To overcome the limitations of joint interpretation approaches, joint inversion schemes have been developed to jointly invert different geophysical data sets aiming at an enhanced consistency and reliability in the resolved models and their interpretation compared to approaches based on independent inversions (Linde and Doetsch, 2016). Existing joint inversion schemes can be grouped into approaches that leverage upon the sensitivity of different geophysical methods to common structural features (e.g., Haber and Oldenburg, 1997; Gallardo and Meju, 2003; Gallardo and Meju, 2004; Jordi et al., 2020), and approaches that are built upon empirically and/or theoretically based petrophysical relationships between the input data and target parameters (e.g., Gao et al., 2012; Rücker et al., 2017; Wagner et al., 2019).

Structurally coupled joint inversion approaches have proven to be applicable for the investigation of landslides (Garofalo et al., 2015), slope stability (Hellman et al., 2017) and the detection of a fracture zone (Ronczka et al., 2017), as well as for the characterization of an aquifer (Doetsch et al., 2010) and the investigation of embankments based on time-lapse data (Rittgers et al., 2016). However, in particular for ERT and SRT, a similar structural sensitivity is not always guaranteed. For instance, landfills are an illustrative example where the ERT might not be sensitive to the geometry of the landfill in the same way as the SR method. Such divergent sensitivity is due to the leakage of leachate associated with an increased electrical conductivity, which masks the contrast between the waste unit and the natural soils in the conductive properties of the subsurface materials (e.g., Flores Orozco et al., 2020). Hence, structurally coupled joint inversion schemes for SR and ER data might not always be applicable and joint inversion approaches built upon a petrophysical relationship linking the SR and ER data might be a more suitable technique allowing to overcome such limitations. In particular, the possibility to formulate the inverse problem in terms of the parameters of interest is a substantial advantage of petrophysically coupled joint inversion schemes (Linde and Doetsch, 2016). Accordingly, successful applications of PJI schemes have been reported, e.g., for the exploration of natural resources (target parameters density and susceptibility; Kamm et al., 2015), in permafrost studies (target parameter ice content; Wagner et al., 2019) and related to geotechnical investigations (target parameter porosity; Carrier et al., 2022). However, a possible drawback of PJI schemes refers to the fact that the resolved models are a function of an *a priori* imposed petrophysical relationship, which might not be known and applicable over an entire study area or at different sites (e.g., Binley et al., 2015).

In general, the coupling of different geophysical data sets requires a formal link to

## 2 Basic principles of the employed methods

a common target parameter  $p$  (e.g., Rücker et al., 2017), i.e., the physical properties  $\xi$  assessed through the geophysical methods are expressed as functions of  $p$ :

$$\begin{aligned}\xi_1 &= f(p) \\ \xi_2 &= f(p) \\ &\vdots \\ \xi_D &= f(p) ,\end{aligned}\tag{2.47}$$

where  $D$  is the number of considered data sets and the set of Equations 2.47 is referred to as the petrophysical model. Commonly, the different physical properties are functions of more than one petrophysical parameter; yet, all  $\xi$  share a common target parameter to constrain the inversion (Binley et al., 2015), e.g.,

$$\begin{aligned}\xi_1 &= f_1(p_1, p_2) \\ \xi_2 &= f_2(p_1, p_2, p_3) \\ &\vdots \\ \xi_D &= f_D(p_1, p_3) .\end{aligned}\tag{2.48}$$

The different measured data sets  $ds$  are concatenated in a single data vector

$$\mathbf{d} = (\mathbf{d}_{s_1}, \mathbf{d}_{s_2}, \dots, \mathbf{d}_{s_D})^T ,\tag{2.49}$$

and the parameter vector  $\mathbf{p}$  holds the petrophysical target parameters for each mesh cell:

$$\mathbf{p} = (\mathbf{p}_1, \mathbf{p}_2, \dots, \mathbf{p}_U)^T ,\tag{2.50}$$

where  $U$  denotes the number of different target parameters. As suggested by Rücker et al. (2017) the target parameters can be restricted to vary between specific limits to ensure physically plausible solutions (Wagner et al., 2019). A popular choice is the usage of logarithmic barriers (Kim and Kim, 2011) where the elements of the transformed model vector  $\mathbf{m}$  are obtained as

$$m_c^u = \log(p_c^u) - \log(1 - p_c^u) .\tag{2.51}$$

In Equation 2.51, the indices  $c$  and  $u$  denote the cells of the finite-element mesh and the petrophysical target parameters, respectively.

The petrophysical joint inversion of multiple geophysical data sets refers to the

minimization of an objective function of the general form (following Wagner et al., 2019):

$$\Psi_{PJI} = \| \mathbf{W}_d (\mathbf{d} - \mathcal{F}(\mathbf{m})) \|_2^2 + \lambda \| \mathbf{W}_m \mathbf{m} \|_2^2 \quad (2.52)$$

$$+ \gamma \| \mathbf{W}_p (\mathbf{p} - \mathbf{p}_0) \|_2^2 . \quad (2.53)$$

In Equation 2.53, the first term quantifies the data misfit between the observed data and the model response  $\mathcal{F}(\mathbf{m})$ , which depends on the formulations provided by the petrophysical model (Equation 2.48); whereas the second term describes the smoothness regularization applied to the transformed model vector  $\mathbf{m}$ . Considering that the inverse problem is formulated in terms of the petrophysical target parameters the third term in Equation 2.53 allows for the incorporation of *a priori* information through the reference parameter vector  $\mathbf{p}_0$  (Wagner et al., 2019); whereas  $\mathbf{W}_p$  refers to a square matrix holding ones or zeros in its diagonal depending on which target parameter should be kept close to a reference value. The scaling parameter  $\gamma$  is set equal to zero if no prior knowledge should be considered, whereas  $\gamma > 0$  is used to promote solutions closed to the prescribed *a priori* parameter values. Note, that additional terms can be included in this objective functions, e.g., to account for an interparameter regularization (e.g., Wagner et al., 2019).

Similar to the independent inversion, minimizing Equation 2.53 yields the model update  $\Delta \mathbf{m}_k$  at the  $k^{th}$  iteration by solving (after Wagner et al., 2019)

$$\begin{bmatrix} \mathbf{W}_d \hat{\mathbf{J}} \\ \lambda \mathbf{W}_m \\ \gamma \hat{\mathbf{W}}_p \end{bmatrix} \Delta \mathbf{m} = \begin{bmatrix} \mathbf{W}_d (\mathbf{d} - \mathcal{F}(\mathbf{m})) \\ -\lambda \mathbf{W}_m \mathbf{m} \\ \gamma (\mathbf{p}_0 - \hat{\mathbf{W}}_p \mathbf{m}) \end{bmatrix} \quad (2.54)$$

in a least-squares sense. The Jacobian matrix in Equation 2.54 holds the changes in the physical properties with respect to the changes in the petrophysical target parameters:

$$J_{d,u} = \frac{\partial ds_d}{\partial p_u} . \quad (2.55)$$

Due to the non-linearity between  $\mathbf{m}$  and  $\mathbf{p}$  a respective scaling of the model weighting matrix  $\mathbf{W}_p$  and the Jacobian matrix  $\mathbf{J}$  is necessary at each iteration step. In particular, the matrices are scaled with the reciprocals of the partial derivatives of  $\mathbf{m}$  with respect to  $\mathbf{p}$  prior to the multiplication with  $\Delta \mathbf{m}$ , i.e.,  $\hat{\mathbf{W}}_p = \mathbf{W}_p \text{diag}(\partial \mathbf{m} / \partial \mathbf{p})^{-1}$  and  $\hat{\mathbf{J}} = \mathbf{J} \text{diag}(\partial \mathbf{m} / \partial \mathbf{p})^{-1}$ , respectively (Wagner et al., 2019).



# 3 | formikoj: A flexible library for data management and processing in geophysics - Application for seismic refraction data<sup>1</sup>

## 3.1 Introduction

The acquisition of spatially quasi-continuous data in a non-invasive manner renders geophysical methods suitable for the acquisition of information about the subsurface conditions with high spatio-temporal resolution in engineering and environmental investigations (e.g., Parsekian et al., 2015; Nguyen et al., 2018; Romero-Ruiz et al., 2018). However, the processing of geophysical data often relies on commercial software solutions with the associated licensing costs rendering their use prohibitively expensive, which might in particular be the case for academic projects or institutions. The most popular packages are Res2DInv<sup>2</sup> for electrical methods, Halliburton Landmark SeisSpace ProMAX<sup>3</sup> or ParkSeis<sup>4</sup> for seismic methods, or ReflexW<sup>5</sup> for ground-penetrating radar and seismic methods. A common limitation of the aforementioned software solutions refers to their specific platform requirements mainly related to the type and version of the operating system; moreover, the possibility to adapt the code are limited if possible at all. Considering the substantial changes regarding the market shares of operating systems within the last two decades, platform-specific software packages are becoming particularly obstructive for academic research and teaching. In particular, the increasing popularity of the Python programming language led to the development of various cross-platform open-source software packages for processing, modeling and inverting geophysical data. Available packages can focus on specific geophysical methods, for instance, ResIPy (Blanchy et al., 2020) for electrical data, GPRPy (Plattner, 2020) for ground-penetrating radar data, or ObsPy (Beyreuther et al., 2010) and Pyrocko (Heimann et al., 2017) for seismological data. In contrast,

---

<sup>1</sup>This chapter is based on: M. Steiner and A. Flores Orozco. "A flexible library for data management and processing in geophysics - Application for seismic refraction data". Submitted to: *Computers & Geosciences*. URL: <https://git.geo.tuwien.ac.at/msteine1/formikoj.git>

<sup>2</sup><https://www.geometrics.com/software/res2dinv/>, last accessed on December 2, 2022

<sup>3</sup><https://www.landmark.solutions/SeisSpace-ProMAX>, last accessed on December 2, 2022

<sup>4</sup><https://www.parkseismic.com/parkseis/>, last accessed on December 2, 2022

<sup>5</sup><https://www.sandmeier-geo.de/reflexw.html>, last accessed on December 2, 2022

### 3 The formikoj library

other packages provide frameworks for the inversion and permit the inclusion of forward models for different geophysical methods, e.g., SimPEG (Cockett et al., 2015), Fatiando a Terra (Uieda et al., 2013) or pyGIMLi (Rücker et al., 2017).

The seismic refraction tomography (SRT) is a standard technique in environmental and engineering studies. Often applied together with other geophysical methods, the SRT is routinely used, e.g., in permafrost studies (e.g., Draebing, 2016; Steiner et al., 2021), for the investigation of landfills (e.g., Nguyen et al., 2018; Steiner et al., 2022), or for hydrogeological characterizations (e.g., Bücken et al., 2021). The market for seismic processing software has long been dominated by software packages designed for the processing of large data sets, e.g., associated with oil or gas exploration. Accordingly, these seismic processing solutions may not be suited for small-scale projects, or for teaching activities. ReflexW overcomes such limitations by providing processing tools specifically designed for near-surface investigations at substantially lower costs. In terms of licensing costs, Stockwell (1999) went a step further by making the Seismic Unix framework available entirely free of charge; whereas Guedes et al. (2022) recently presented RefraPy, a python processing tool for seismic refraction data. Implemented in python, RefraPy is potentially suitable for cross-platform usage, yet it was developed and tested solely for Windows operating systems (Guedes et al., 2022). Moreover, RefraPy does not offer the possibility to generate synthetic seismic waveform data, as required for survey design, as well as for teaching and interpretation purposes.

The formikoj library presented here is an open-source framework for creating synthetic data sets, as well as for managing and processing numerical and field data independently from the operating system and without licensing costs; thus, overcoming limitations associated with existing solutions. The design of the library follows the multi-method concept of pyGIMLi and SimPEG, which allows the implementation of custom designed tools for different geophysical methods. The usage of transparent file formats, e.g., the unified data format (udf<sup>6</sup>), and data management concepts (SQLite database) within the formikoj framework facilitates a simple data exchange between partners in research projects and academia, which is required to guarantee the repeatability of results and good research practices. Considering the diverse applications of the SR method we demonstrate the applicability of the proposed library based on tools for the modeling and processing seismic waveform data implemented within the formikoj framework. In particular, we present here a series of illustrative use cases based on the formikoj library referring to (i) the modeling of synthetic seismic refraction (SR) waveform data, (ii) the processing of a 2D SR field data set collected with a roll-along survey geometry, and (iii) the processing of a 3D SR field data set.

<sup>6</sup>[http://resistivity.net/bert/data\\_format.html](http://resistivity.net/bert/data_format.html), last accessed on December 2, 2022

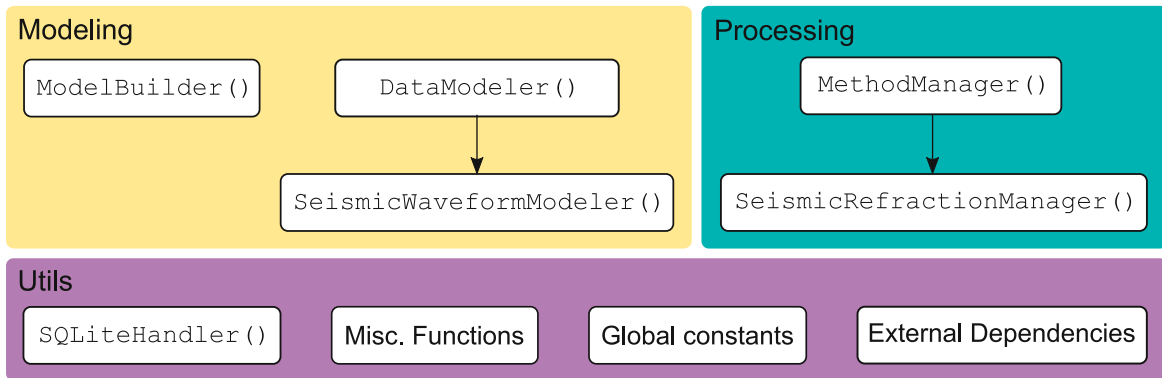


**Figure 3.1:** General architecture of the *formikoj* library comprising a utility, modeling and processing module. The base classes `DataModeler` and `MethodManager` can be used to build tools for specific geophysical methods, e.g., seismic refraction.

## 3.2 Design and structure of the *formikoj* library

As illustrated in Figure 3.1, the *formikoj* library comprises a modeling and a processing module, which both rely on a common utilities module. The `DataModeler` and the `MethodManager` class provide the basis to add modeling or processing functionalities for specific geophysical methods. In particular, we present here two classes implemented within the *formikoj* framework, namely the `SeismicWaveformModeler` and the `SeismicRefractionManager`, which aim at facilitating the creating and processing of seismic waveform data, respectively. Similar to *RefraPy*, these classes are built upon the functionalities of existing packages such as *ObsPy* for the processing of seismological data (Beyreuther et al., 2010) and *pyGIMLi* for the modeling and inversion of different geophysical data (Rücker et al., 2017). Other important third party dependencies refer to *NumPy* (Harris et al., 2020) and *Pandas* (McKinney, 2010) for general data handling, as well as *matplotlib* (Hunter, 2007) and *PyVista* (Sullivan and Kaszynski, 2019) for data visualization. In the current version, we implemented and tested *formikoj* primarily on Linux machines, yet the library has been successfully tested and used on all major operating systems, i.e., Linux, MacOS and Windows.

### 3.2.1 Generation of seismic waveform data for synthetic subsurface models: The `SeismicWaveformModeler`

The SR method exploits the ground motion recorded by sensors installed in the surface (e.g., geophones) to characterize the propagation of seismic waves generated at well known locations (i.e., shot stations). The visualization of the ground motion as function of time yields a so-called seismogram for each geophone position. Accordingly, the `SeismicWaveformModeler` class provides a flexible way to generate synthetic seis-

### 3 The formikoj library

mic waveform data either through a python script as well as interactively in a jupyter notebook or an ipython shell, respectively. To create an instance of the class the path to the working directory is provided as parameter to the constructor:

```
from useis import SeismicWaveformModeler
```

```
swm = SeismicWaveformModeler('.')
```

**INFO** : Created instance of SeismicWaveformModeller

The working directory needs to contain a subdirectory *in*, whereas the output directory *out* will be created automatically:

```
working_directory
├── in
└── out
```

The required input files are provided via the subdirectory *in* of the working directory. The key input file is the measurement scheme, which contains information regarding the distribution of the shot and geophone stations. If given in the unified data format the measurement scheme is imported directly with pyGIMLi into a so-called **DataContainer**. In case the measurement scheme is provided as a csv file the **SeismicWaveformModeler** reads the information and converts it to a pyGIMLi **DataContainer**. In the csv format the measurement scheme contains a single line for each station in the survey layout, where a station either hosts a geophone or a shot, or both (see Table 3.1). The values provided in each line need to be separated by a unique delimiter, and the file must not contain a header.

**Table 3.1:** Description of the information to be provided in the columns of a measurement scheme in csv format.

Column	Content	Data type	Description
1	x coordinate	float	Station x coordinate, e.g., given in (m)
2	y coordinate	float	Station y coordinate, e.g., given in (m)
3	z coordinate	float	Station z coordinate, e.g., given in (m)
4	Geophone	bool	1 in case of a receiver station, 0 otherwise
5	Shot	bool	1 in case of a shot station, 0 otherwise

For the modeling of the seismic waveform data, the parameters describing the base wavelet, the synthetic subsurface model and the resulting waveform data sets are provided (see Table 3.2) in a configuration file following the yaml format, e.g.:

```

wavelet:
  length: 1.024
  frequency: 100
  sampling_rate: 2000
  pretrigger: 0.02

dataset:
  number: 2
  names: [dataset1, dataset2]
  noise: 0
  noise_level: 1.e-4
  missing_shots: 0
  broken_geophones: 0
  wrong_polarity: 0

model:
  velmap: [[1, 750.], [2, 3000.]]
  layers: [[1, 3.], [2, 10.]]
  quality: 32
  area: 10
  smooth: [1, 10]
  sec_nodes: 3

traveltimes:
  noise_relative: 0.
  noise_absolute: 0.

```

In the exemplary configuration file shown above, the first block contains information regarding the wavelet controlling the modeling of the seismic waveform data as described in Table 3.2. In the second block, it is possible to define specific names for the data sets to be created, whereas the number of data sets is automatically determined. Alternatively, the number of data sets to be created can be defined and the data set names are automatically generated with the prefix *dataset\_*. Furthermore, this block contains various parameters controlling the random error (*noise*) and systematic errors in the modeled seismic waveform data (see Table 3.2 for a detailed description). The amount and position of shot or geophone stations affected by systematic errors are randomly chosen; yet, the maximum is defined as 5% of the total station count in order to avoid a disproportionately high number of invalid trace data. The third block contains information regarding the synthetic subsurface model. For each layer the corresponding velocity (*velmap*) and layer thickness (*layers*) need to be provided and all layers are considered to be parallel to the surface topography (geometrical information regarding the stations in the measurement scheme). The remaining parameters, namely *quality*, *area*, *smooth* and *sec\_nodes*, define the properties of the mesh to be generated (for further information and examples we refer to the respective

### 3 The formikoj library

pyGIMLi resources<sup>7</sup>). Alternatively, the user can provide a more complex mesh in the binary mesh format (i.e., a bms file) created with external tools (e.g., gmsh; Geuzaine and Remacle, 2009):

```
swm.load('mesh')
```

```
INFO      : Mesh loaded
```

The parameters in the final block control the error model used for the forward modeling of the corresponding seismic travel times (see Table 3.2 for further details). If stored in the input directory, such a configuration file can be imported through the load method:

```
swm.load('config')
```

```
INFO      : Configuration loaded
```

Once the parameterization of the `SeismicWaveformModeler` instance is completed the synthetic seismic waveform data can be created as follows:

```
swm.create('waveforms')
```

```
INFO      : Measurement scheme loaded
INFO      : Velocity model created
INFO      : Wavelet created
[+++++ 100% +++++] 2048 of 2048 complete
...
[+++++ 100% +++++] 2048 of 2048 complete
INFO      : Dataset 'clean' created
```

As can be seen from the text output, the `SeismicWaveformModeler` loads the measurement scheme and creates the velocity model used for the waveform modeling. Based on the wavelet properties a Ricker wavelet is generated through the pyGIMLi function `ricker`. Subsequently, mesh, velocity model and Ricker wavelet are used to solve the pressure wave equation for each shot station defined in the measurement scheme with the pyGIMLi function `solvePressureWave`. The resultant waveform data at the corresponding geophone stations are extracted and stored in an `ObsPy Stream` data structure.

---

<sup>7</sup>[https://www.pygimli.org/pygimliapi/\\_generated/pygimli.meshtools.html#pygimli.meshtools.createMesh](https://www.pygimli.org/pygimliapi/_generated/pygimli.meshtools.html#pygimli.meshtools.createMesh), last accessed December 2, 2022

**Table 3.2:** Description of the parameters, which can be defined in a configuration file used for modeling synthetic seismic waveform data.

Parameter	Unit/ Data type	Description
<b>wavelet</b>		
length	s	Length of the base wavelet, which also defines the length of the synthetic seismic waveform data
frequency	Hz	Frequency of the base wavelet
sampling_rate	Hz	Defines temporal resolution of the seismic waveform data
pretrigger	s	Add buffer to the seismic waveform data before the onset of the actual data
<b>data set</b>		
number	int	Number of data sets to be created
names	list (string)	Names of the data sets
noise	bool	1 in case noise should be added to the synthetic waveform data, 0 otherwise
noise_level	-	Level of the seismic background noise
missing_shots	bool	1 in case the data sets should be affected by missing shot files, 0 otherwise
broken_geophones	bool	1 in case the data sets should comprise broken geophones (i.e., no data in the corresponding seismograms), 0 otherwise
wrong_polarity	bool	1 in case the data sets should contain traces with inverse polarity, 0 otherwise
<b>model</b>		
velmap	list (float/int)	For each layer the first value defines the marker and the second one the seismic velocity within the layer
layers	list (float/int)	For each layer the first value defines the marker and the second one the thickness
<b>travel times</b>		
noise_relative	%/100	Relative noise to be added to the forward modeled seismic travel times
noise_absolute	s	Absolute noise to be added to the forward modeled seismic travel times

For each data set defined in the configuration file a directory will be created in the output directory (*out*) with the following structure and contents:

```

working_directory
├── in
├── out
│   └── data set1
│       ├── data
│       │   ├── protocol.txt
│       │   ├── station_coords.csv
│       │   ├── Shot_1001.syn
│       │   ├── ...
│       │   └── Shot_10nn.syn
│       ├── data set1_tt.pck
│       └── info.txt

```

### 3 The formikoj library

In the subdirectory *data*, the synthetic seismic waveform data forward modeled for each shot position are stored as a separate shot file in the miniseed format (Ahern et al., 2012; Ringler and Evans, 2015). The synthetic seismic shot files are saved with the file extension *syn* to allow for an straight-forward identification of files holding forward modeled trace data, e.g., *Shot\_1001.syn*. Additionally, the *data* directory contains the measurement protocol (protocol.txt) and the station coordinates provided as a csv file (station\_coords.csv). The header of the measurement protocol provides information regarding survey parameters relevant for the processing of the seismic waveform data, namely sampling rate, recording length, number of geophones and geophone spacing. Moreover, the protocol associates each shot file of the data set to a specific location within the survey geometry, i.e., with respect to the geophone positions:

```
#####  
Line: SYN_dataset_1  
Sampling rate: 2000 Hz  
Recording length: 1.024 s  
Number of geophones: 48  
Geophone spacing: 6 m  
#####  
  
File number | Station  
1001      | G001  
:         | :  
1048      | G048
```

The corresponding synthetic travel times (`sww.create('travel times')`) are stored in the data set directory as udf files, e.g., data set1\_tt.pck. The file extension *pck* is an abbreviation of the word 'pick' and refers to the first break travel times stored in the file.

The auxiliary file *info.txt* provided in the data set directory summarizes the parameters from the configuration file and information regarding the amount and index of stations affected by systematic errors in the synthetic seismic waveform data:

```
Number of geophones: 48  
Number of shots: 48  
Recording length (s): 1.024  
Sampling frequency (Hz): 2000  
Wavelet type: Ricker  
Frequency of the wavelet (Hz): 100  
  
Missing shot(s): 16  
Broken geophone(s): 6, 14  
Wrong polarity geophone(s): 35
```

### 3.2.2 Managing and processing of seismic refraction data sets: the `SeismicRefractionManager`

The SR method is based on measuring the travel times of seismic waves based on the first onset of the seismic energy in the seismograms recorded by geophones. In the SRT, the inversion of travel times gathered from tens to hundreds of seismograms permits the computation of variations in the seismic velocities in an imaging framework. Obtaining the travel times from seismograms – commonly referred to as first break picking – is either done manually or semi-automatically in an iterative process. The signal-to-noise ratio S/N in the recorded seismograms substantially influences the quality of the picked travel times; thus, enhancing the perceptibility of first onsets is critical for obtaining reliable SRT imaging results.

The `SeismicRefractionManager` class presented here provides functionalities for processing seismic waveform data by means of a seismic refraction analysis. These functionalities involve the reading of seismic waveform data, combining the data with information about the survey geometry, filtering of the waveform data as well as the picking of first break travel times. In particular, the `SeismicRefractionManager` is designed primarily for usage from within an ipython shell as the often challenging S/N in near-surface seismic waveform data renders the first break picking a highly interactive process.

#### 3.2.2.1 Compiling the survey information and creating a project

An instance of the `SeismicRefractionManager` can be created by providing the path of the working directory as parameter to the constructor. Based on the content of the working directory, the `SeismicRefractionManager` automatically decides whether (i) to start in the data preview mode, (ii) create a new project, or (iii) load an existing project from disk.

The data preview mode is primarily initiated if the provided directory contains seismic shot files:

```
from useis import SeismicRefractionManager
```

```
srm = SeismicRefractionManager('./01_data/raw')
```

```
INFO      : Starting in data preview mode
Progress <=====> 100.0% completed
INFO      : Read 48 files
```

In the data preview mode, the user can iterate through the shot files found in the directory; yet, beyond applying frequency filters on the trace data no further processing

### 3 The formikoj library

is possible.

For the actual processing of the seismic waveform data, a project has to be created or loaded. To this end, the provided working directory needs to contain specific subdirectories:

```
working_directory
├── 01_data
│   └── raw
├── 02_geom
└── 03_proc
```

In this directory structure, the seismic shot files are stored in *01\_data/raw* and the geometry file (*geometry.csv*) is provided in *02\_geom*. The geometry file is provided in the csv format without a header (line) and provides an abstract representation of the survey layout based on the parameters summarized in Table [reftab:geometry](#). The fundamental element for the description of the survey layout is the station, which refers either to a geophone position, a shot position or a position with co-located shot and geophone. For each station the required geometric and semantic information (see Table 3.3) are given column-wise, i.e., each line in the geometry file corresponds to a single station with a unique position within the survey layout.

**Table 3.3:** Description of the information to be provided in the columns of the geometry file.

Col	Content	Data type	Description
1	x coordinate	float	Station x coordinate
2	y coordinate	float	Station y coordinate
3	z coordinate	float	Station z coordinate
4	Geophone	bool	1 if a geophone was deployed at station, 0 otherwise
5	Shot	int	Numerical part of the file name if a shot was conducted at this station (e.g., 1001), -1 otherwise
6	First geophone	int	First active geophone in case of shot station, -1 otherwise
7	Number of geophones	int	Number of active geophones in case of shot station, -1 otherwise

If shot files as well as a geometry file are provided and a basic sanity check of the geometry file was successful, the `SeismicRefractionManager` creates a new project:

```
from useis import SeismicRefractionManager
```

```
srm = SeismicRefractionManager('.')
```

```
INFO      : Read geometry information from file
INFO      : Extracted shot geometry
INFO      : Extracted receiver geometry
INFO      : Applied geometry
INFO      : Standard pickset 'picks' created
INFO      : Pickset 'picks' loaded
INFO      : 'picks' set as active pickset
Progress <=====> 100.0% completed
INFO      : Read 48 files
```

In particular, the `SeismicRefractionManager` creates an SQLite database (`prj.db` in the working directory) that stores the geometry information with stations being numbered consecutively as illustrated in Figure 3.2. To allow for an efficient data selection through the user the `SeismicRefractionManager` links the station numbers to shot index numbers (SIN) and receiver index numbers (RIN) assigned to shot and receiver stations, respectively (see Figure 3.2). Based on this information, the geometry is applied, i.e., the database tables required for the processing of the seismic waveform data are created. The first break travel times for each SIN-RIN pair are stored in a dedicated database table *fbpicks* together with the name of the corresponding pickset, i.e., the a common label for an entire set of first break travel times. By default, each project contains the default pickset 'picks', which is loaded and activated on startup. Once the database is initialized, the waveform data are read from disk and the project is ready for processing.

If the `SeismicRefractionManager` discovers a database file in the provided working directory, the project information, the seismic waveform data as well as the default pickset 'picks' are automatically loaded from disk to allow resuming the data processing based on a previous session:

```
from useis import SeismicRefractionManager
```

```
srm = SeismicRefractionManager('.')
```

```
INFO      : Project information loaded
Progress <=====> 100.0% completed
INFO      : Read 48 files
INFO      : Pickset 'picks' loaded
INFO      : 'picks' set as active pickset
```

In contrast to the data preview mode that solely provides sequential access to the shot files, creating a project allows for trace data selection based on a common shot

(`sin`), a common receiver (`rin`) or a common absolute offset (`aoffset`) through the `select` method of the `SeismicRefractionManager`:

```
srm.select('sin 1')
```

**INFO** : 48 traces selected

```
srm.select('rin 10')
```

**INFO** : 48 traces selected

```
srm.select('aoffset 6')
```

**INFO** : 90 traces selected

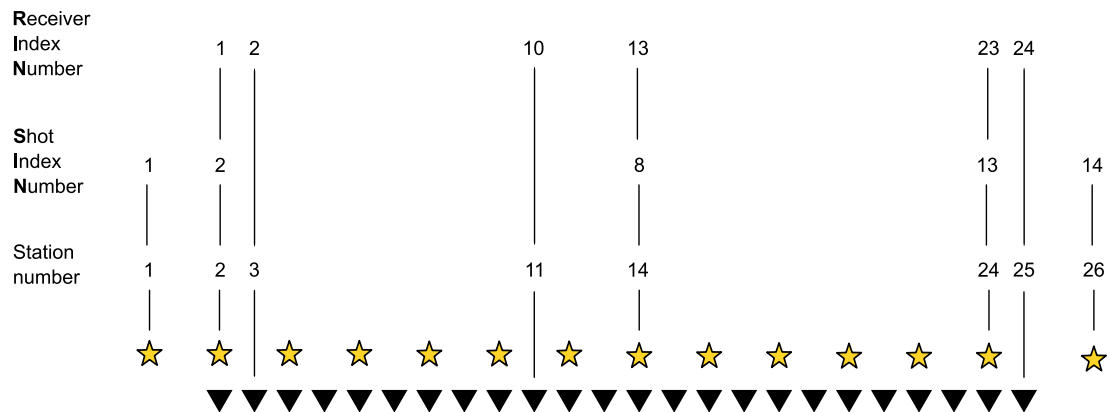


**Figure 3.2:** The `SeismicRefractionManager` addresses the stations through consecutive station numbers based on the sort order in the geometry file. The shot index numbers (SIN) and receiver index numbers (RIN) are assigned to the shot and receiver stations, respectively, to allow for an intuitive data handling by the user.

### 3.2.2.2 Visualization and filtering of the seismic waveform data

Executing the `plot` method without passing any parameter opens the so-called seimogram plot that visualizes the currently selected trace data:

```
srm.plot()
```

The default visualization refers to the combination of wiggle trace and variable area data representation, i.e., the trace data are shown as curves; whereas the area beneath the curves is colored red for negative and blue for positive amplitudes, respectively (not shown for brevity). Pressing the up or down arrow key on the keyboard toggles the visualization mode between the variable area and the variable density representa-

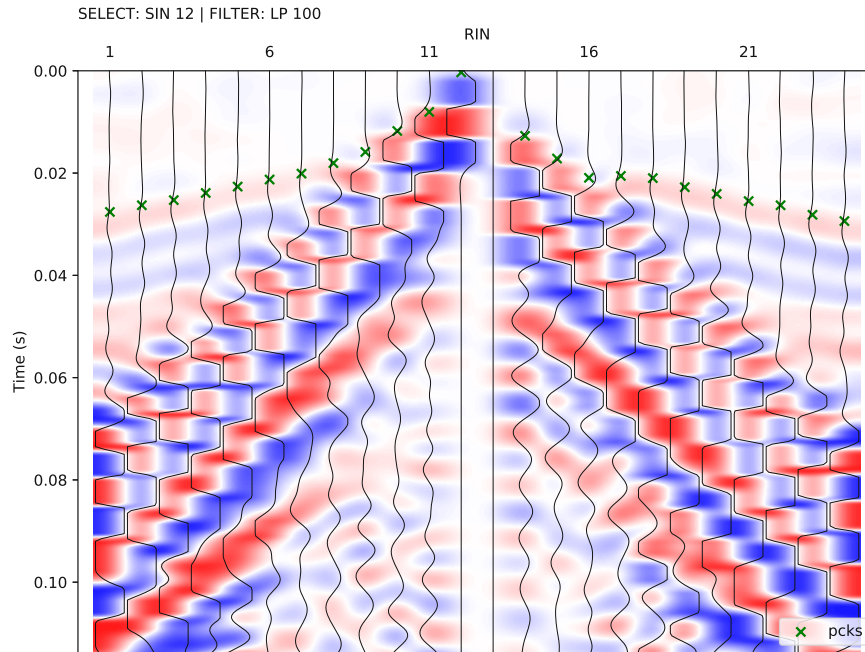


**Figure 3.3:** The seismogram plot presents the currently selected traces along the x-axis with the sort order being determined based on the geometry. The corresponding trace data are illustrated as a function of time along the y-axis (solid curves), with positive and negative amplitudes depicted in blue and red, respectively. The selection criterion and the applied filter are shown in the upper left corner of the plot. Green crosses refer to the picked travel times stored in the currently active pickset.

tion. In the variable density mode, the sign of the amplitude is also color-coded, yet the strength of the amplitudes is additionally reflected by the color saturation, i.e., high amplitudes refer to a stronger shade than low amplitudes (see Figure 3.3).

The active processing mode and data scaling modes are reported together with the travel time at the current cursor position in the status bar of the seismogram plot window (see Figure 3.4). The initial processing mode is 'Fb pick', i.e., first break picking is possible. The user can switch between different modes by pressing dedicated keys on the keyboard. Pressing the 'm' key activates the trace mute mode ('Trc mute'), which allows setting the amplitude of a trace to zero by a left mouse button click on the respective trace; clicking again on the same trace restores the amplitude information. The trace reverse mode ('Trc rev') is activated by pressing the 'r' key and enables the user to toggle the polarity of a specific trace by clicking with the left mouse button. The default data scaling mode is 'Zoom', which allows scaling the y-axis by turning the mouse wheel, i.e., the time range along the y-axis can be adjusted. In the amplitude scaling mode ('Amp scal') activated by pressing the 'a' key, turning the mouse wheel increases or decreases the amplitudes of the trace data shown in the seismogram plot, which might enhance the perceptibility of the first

onsets. Pressing the key corresponding to the currently active mode again sets the `SeismicRefractionManager` back in the default mode; whereas switching between the different modes is possible in any arbitrary order (as illustrated in Figure 3.4).



**Figure 3.4:** The status bar in the interactive seismogram plot window displays the active processing and data scaling modes as well as the time (in seconds) at the current cursor position. By pressing the keys 'a', 'm', 'r', 'v' on the keyboard the different modes can be activated.

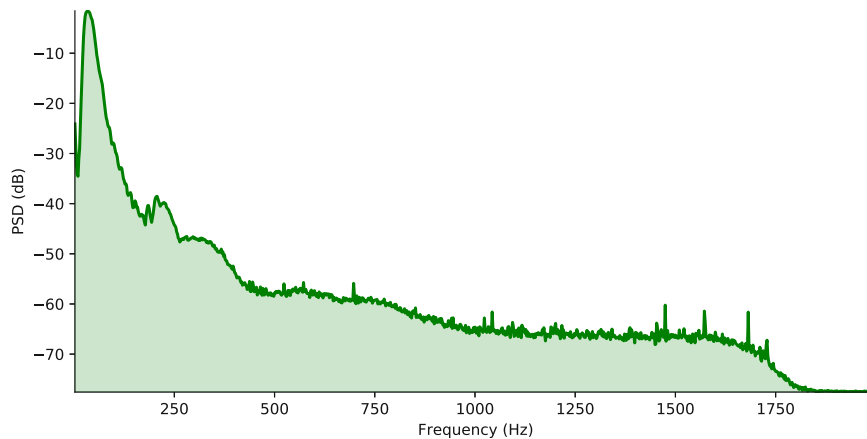


**Figure 3.5:** The frequency spectrum illustrates the frequency content of the currently selected traces, which allows for the identification of frequency ranges associated with noise, which can be omitted through the application of corresponding frequency filtering.

The processing options presented above allow for the elimination of systematic errors in the seismic waveform data and enable the user to adjust the representation of the amplitude information. A further enhancement of the seismograms refers to the selective removal of signal components associated with noise sources. To this end, the `plot` method can be used to visualize the frequency spectrum of the currently selected

trace data:

```
srm.plot('spectrum')
```

A frequency spectrum as shown in Figure 3.5 allows for the discrimination of dominating signal frequencies from those associated with the background noise. Such information is particularly useful for the definition of adequate filter settings in the frequency domain. To improve the signal-to-noise ratio of the seismograms filter parameters are passed to the `filter` method, which utilizes the frequency filters implemented in the ObsPy package (low-pass, highpass, bandpass and bandstop; Beyreuther et al., 2010), e.g.:

```
srm.filter('lp 120')
```

**INFO** : Applied 120.0 Hz lowpass filter

```
srm.filter('bp 10 120')
```

**INFO** : Applied bandpass filter (10.0 to 120.0 Hz)

```
srm.filter('hold on')
```

**INFO** : Set filter hold on

By default, filters are solely applied to the currently selected traces, yet setting the filter on hold (`srm.filter('hold on')`) automatically filters all subsequently selected traces with the same filter settings. The effect of the applied filter on the seismic waveform data is interactively visualized if the seismogram plot window is open.

### 3.2.2.3 Analysis of the seismic waveform data and first break travel time picking

The analysis of the waveform data in the seismogram plot window yields information about the subsurface conditions. A simple approach to approximate the seismic velocity values associated with subsurface structures, e.g., a refractor, is provided through the velocity estimation mode ('Vel est'; activated by pressing the 'v' key on the keyboard). In particular, the seismic velocity is estimated along a straight line drawn by the user by pressing the left mouse button and moving the cursor within the seismogram plot, e.g, to connect the first onsets stemming from a common refractor. Once the left mouse button is released the velocity is computed from the slope of the line by taking into account the geometry information retrieved from the project database. The line connecting start and end point is then labeled with the estimated velocity; whereas, such estimation can be removed from the seismogram plot by clicking on it

with the right mouse button.

In the first break picking mode ('Fb pick'), the picking of first break travel times is done individually by clicking with the left mouse button on the respective trace. Changing the travel time is achieved by clicking on the same trace again with the left mouse button; whereas clicking with the right mouse button deletes the picked travel time. Alternatively, first break picks can be set for multiple traces at once by pressing the left mouse button and moving the cursor, i.e., based on a straight line connecting the first onsets of adjacent traces. Once the left mouse button is released, first break picks are defined at the intersections between the line and the seismograms. In a similar way, multiple picks can be deleted by drawing a line across the respective traces with the right mouse button pressed. All first break travel times determined in a seismogram plot are automatically synchronized with the project database either by closing the window or loading another set of traces by pressing the 'left' or 'right' arrow key on the keyboard.

Often it is useful to visualize all first break travel times for an entire data set together in one digaram, e.g., prior to sharing or inverting the travel time data. This so-called travel time diagram can be created by passing the keyword `traveltimes` to the `plot` method:

```
srm.plot('traveltimes')
```

Figure 3.6 presents an exemplary travel time diagram, which is commonly use for assessing the quality of the first break picking. In particular, such presentation of the travel times allows for the identification of outliers or other erroneous first break picks, e.g., indicated by travel times substantially deviating from those observed at adjacent stations such as the first break pick for the SIN-RIN pair (23, 11). Outliers can be removed by clicking on the corresponding symbol ('x') in the travel time diagram, which is instantly synchronized with the project database. If the seismogram plot and the travel time diagram are used side-by-side, changes made to the first break picks in one window will interactively trigger an update of the other one and vice versa.

The `SeismicRefractionManager` organizes first break picks in so-called picksets, with 'picks' being the name of the default pickset, as mentioned above. The user can access and manage the picksets of a project through the `picksets` method based on various keywords and options. The subsequent exemplary workflow aims at illustrating some basic concepts associated with the handling of picksets within a `SeismicRefractionManager` project:

```
srm.picksets()
```

pickset	loaded	active
picks	Y	Y

```
srm.picksets('import picking_part1.pck pck_p1')
```

```
INFO : Created new pickset 'pck_p1'
INFO : Pickset 'pck_p1' loaded
INFO : 'pck_p1' set as active pickset
INFO : Imported 'picking_part1.pck' to pickset 'pck_p1'
```

```
srm.picksets('copy pck_p1 pck_all')
```

```
INFO : Created new pickset 'pck_all'
INFO : Pickset 'pck_all' loaded
INFO : 'pck_all' set as active pickset
INFO : Copied pickset 'pck_p1' to 'pck_all'
```

```
srm.picksets('unload pck_p1 picks')
```

```
INFO : Pickset 'pck_p1' removed from workflow
INFO : Pickset 'picks' removed from workflow
```

```
srm.picksets('delete pck_p1')
```

```
INFO : Pickset 'pck_p1' deleted
```

```
srm.picksets()
```

pickset	loaded	active
picks	N	N
pck_all	Y	Y

As can be seen from the text output, calling the `pickset` method without parameters provides information regarding the status of each pickset. This example shows that by default the pickset 'picks' is loaded from the database and activated. Activating a pickset means that any modifications of first break travel times are synchronized with this pickset in the database. A new empty pickset can be created by typing `srm.picksets('create picksnew')`, i.e., by using the keyword `create` followed by the name of the new pickset. As shown in the exemplary use case above, a new pickset is also created by importing first break picks from another source (provided as udf file in `03_proc/picks`). For the first break picking, it generally is sufficient to keep only one pickset in the workflow, i.e., not required picksets can be unloaded from the current workflow. Any pickset that is not loaded and no longer required can be permanently removed from the project, i.e., the corresponding travel times are deleted

### 3 The formikoj library

in the database.

The `picksets` method also allows loading a specific pickset from the database into the current workflow:

```
srm.picksets('load picks')
```

```
INFO      : Pickset 'picks' loaded
```

```
srm.picksets()
```

pickset	loaded	active
picks	Y	N
pck_all	Y	Y

```
srm.picksets('use picks')
```

```
INFO      : Pickset 'picks' loaded
```

```
INFO      : 'picks' set as active pickset
```

```
srm.picksets()
```

pickset	loaded	active
picks	Y	Y
pck_all	Y	N

As shown by the use case above, loading a pickset does not automatically make it the active pickset; an already loaded pickset can be activated by passing the keyword `activate` followed by the pickset name to the `picksets` method. The more convenient approach is, however, to use the keyword `use`, which combines loading and activating of the pickset.

Exporting the first break travel times of a pickset creates a pck file that is saved in `03_proc/picks`, whereas the file name being composed by the pickset and name and the current timestamp as suffix:

```
srm.picksets('export pck_all')
```

```
INFO      : pickset 'pck_all' saved to pck_all_20220428T145648.pck
```

Such pck files can be directly used for the inversion of the travel times with `pyGIMLi`. Moreover, pck file provide an easy way to exchange first break picks between different users processing the same data set considering the possibility to import pck files into an existing project, as demonstrated above.

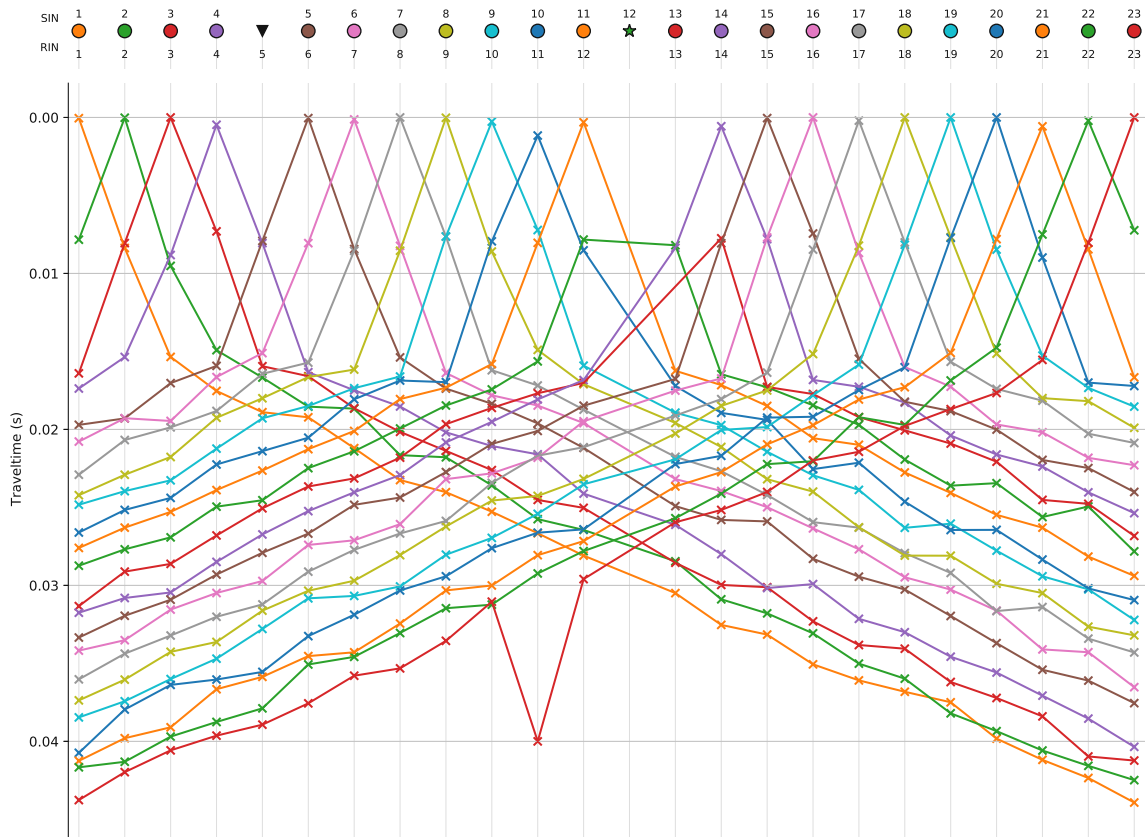


**Figure 3.6:** The travel time diagram shows the first break travel times stored in the currently active pickset along the y-axis (x symbols), where solid lines connect travel times corresponding to a common SIN. The sort order of the stations along the x-axis is controlled by the geometry. Filled circles indicate stations with co-located shot and geophone (receiver), whereas triangles and stars refer to receiver stations (no shot) and shot stations (no geophone), respectively.

### 3.3 Exemplary use cases

#### 3.3.1 Modeling and use of synthetic seismic waveform data

To demonstrate the applicability of the `SeismicWaveformModeler` class, we generate two synthetic seismic waveform data sets based on a model with two horizontal layers and no topography. Table 3.4 summarizes the parameterization used for the forward modeling of one data set without noise (`dataset_1`) and another data set contaminated with random noise and systematic errors (`dataset_2`). For the visualization of these synthetic data sets, we use the `SeismicRefractionManager` in order to have full control regarding data selection and processing capabilities.

The synthetic seismic waveform data for SIN 24 of `dataset_1` presented in Figure 3.7 reveal clear negative first onsets and allow for the identification of distinct crossover

**Table 3.4:** Measurement scheme and parameters provided in the yaml files used for creating synthetic seismic waveform data sets without added noise (`dataset_1`) as well as with added random noise and systematic errors (`dataset_2`).

<b>Measurement scheme</b>		
Number of stations	48	
Station spacing	2 m	
Number of geophones	48	
Number of shots	48	
<b>Model</b>	<i>Layer 1</i>	<i>Layer 2</i>
Thickness	3 m	10 m
Velocity	750 m <sup>-1</sup>	3000 m <sup>-1</sup>
<b>Data set</b>	<i>dataset_1</i>	<i>dataset_2</i>
Noise	False	True
Noise level	0	1 × 10 <sup>-5</sup>
Missing shots	False	True
Broken geophones	False	True
Wrong polarity	False	True
<b>Wavelet</b>		
Length	1.024 s	
Frequency	100 Hz	
Sampling rate	2000 Hz	

points, i.e., the inflexion points separating first arrivals associated with the first layer (RIN 17 to 30) and the first onsets stemming from the second layer (RIN 1 to 16 and RIN 31 to 48). Figure 3.8 presents synthetic seismic waveform data from `dataset_2` for the same shot position (SIN 24). In contrast to `dataset_1`, the signal-to-noise ratio of `dataset_2`s is a function of the offset between shot and geophone position, i.e., traces farther away from the shot contain a higher level of seismic background noise. Moreover, `dataset_2` also contains systematic errors with RIN 6 and 14 referring to broken geophones, and RIN 35 is an example for readings with wrong polarity. We believe that such synthetic data sets can be particularly useful for investigating the effect of complex survey geometries or topographies on the measured seismic data. Furthermore, the possibility to create synthetic seismic waveform data with specific noise characteristics might also aid in the development and evaluation of processing strategies.

The concept of the formikoj library aims at facilitating the implementation of supplementary functionalities. Such custom extensions should be implemented either as internal methods or as functions in the utilities module, and made available to the user through the `compute` method with a custom keyword. As an illustrative exam-

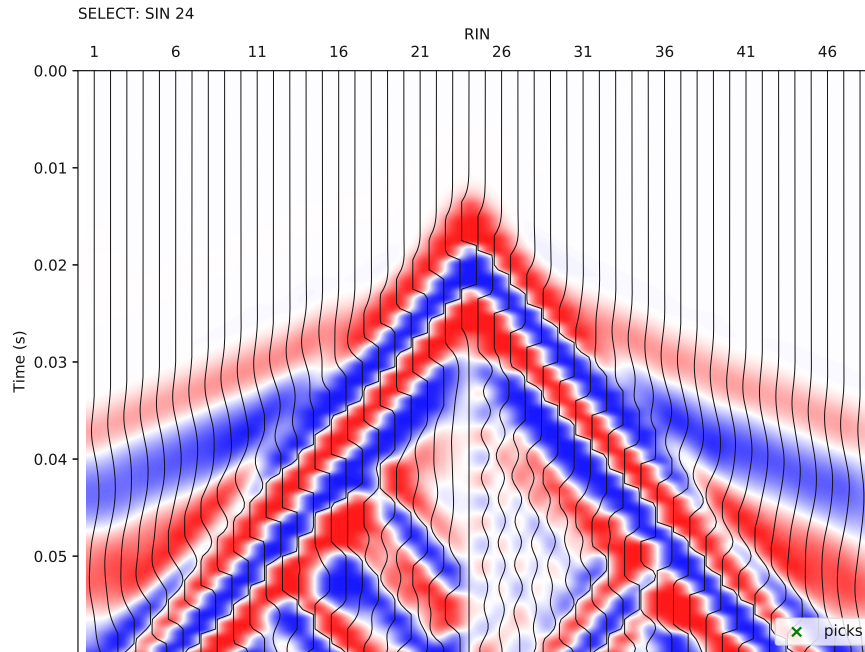


**Figure 3.7:** Synthetic seismic waveform data without random or systematic errors created with the `SeismicWaveformModeler()` class for a shot position in the center of the survey layout.

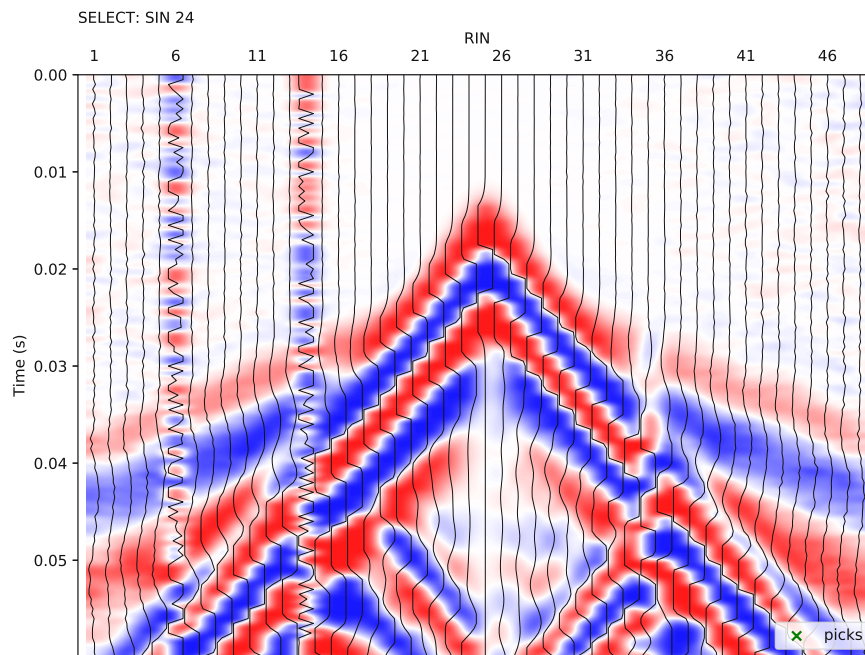


**Figure 3.8:** Synthetic seismic waveform data with added noise created with the `SeismicWaveformModeler()` class for a shot position in the center of the survey layout. The random noise refers to an offset dependent decrease of the signal-to-noise ratio, while the systematic broken geophones and wrong polarity are systematic errors.

ple, we implemented a simplified version of an automatic first break picking algorithm, which determines the travel times based on the energy ratio method (e.g., Earle and Shearer, 1994). The algorithm is added to the `SeismicRefractionManager` in form of two internal methods `_manage_autopicking` and `_compute_autopicks`, respectively. The autopicking process can be started by passing the new keyword `autopick` as the first parameter to the `compute` method:

```
srm.compute('autopick all autopicks')
```

```
INFO      : Created new pickset 'autopicks'
```

```
INFO      : Pickset 'autopicks' loaded
```

```
INFO      : 'autopicks' set as active pickset
```

```
Progress <=====> 100.0% completed
```

The second parameter defines whether travel times should be determined for the entire data set (`all`) or for the currently selected traces (`cur`). The third parameter provides the name of the corresponding pickset in the project database. In this way, the automatically picked travel times are available for visualization and processing with the existing functionalities presented above or further custom implementations.

#### 3.3.2 First break travel time picking for a 2D roll-along field data set: the Danube island example

The seismic data used in this example were collected at the Danube island (Vienna) in June 2021, using 48 geophones deployed with 2 m spacing between them and shot locations located between the geophone positions. As illustrated in Figure 3.9, the survey layout refers to a roll-along geometry, i.e., the geophone spread was moved along the profile with 50 % overlap yielding a total of five segments. The objective of the survey was to define the contact between different sediments within the tertiary and quaternary deposits used to build the man-made Danube island. Additionally, the survey aimed to identify lateral changes that might indicate the position of a fault, which has been inferred from sediments recovered from drillings.

In the field, each segment was measured separately, yet for the processing all measurements are combined to a single profile. To this end, a single geometry file is prepared, which joins all stations of the different roll-along segments as illustrated in Table 3.5. The key parameter for replicating the roll-along survey layout is '1st Geo', which provides information regarding the first active geophone for each shot file. For the first segment in a roll-along survey geometry, the first active geophone is always geophone 1. Based on the number of geophones used in each segment and the known overlap of 50 % the first geophone for segments two to five are found to be 25, 49, 73 and 97, respectively.

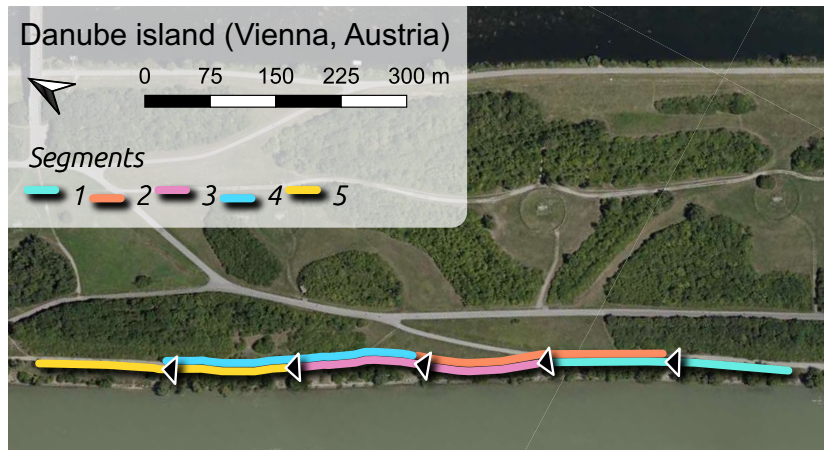


**Figure 3.9:** The Danube island field data set was collected along a single line with a roll-along survey layout; the filled triangles indicate the direction of the measurements. The five segments have an overlap of 50 % to ensure an adequate data coverage along the entire profile.

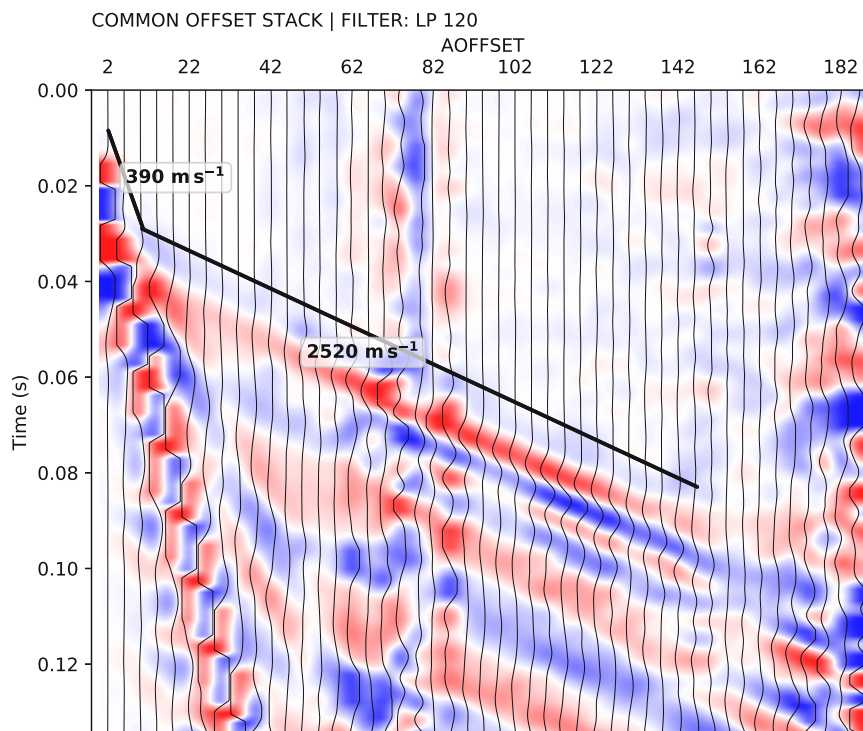


**Figure 3.10:** The common offset stack computed for the Danube island data set clearly showing a two-layered subsurface. The seismic velocities within the layer can be estimated from the gradient of the lines drawn along the corresponding first onsets of the seismic waves.

**Table 3.5:** Extract from the roll-along survey geometry file showing how the information regarding the first geophone assigns the traces in the shot files to the correct stations.

x (m)	y (m)	z (m)	Geo	Shot	1st Geo	# Geo
0.0	0.0	163.5	1	-1	-1	-1
2.0	0.0	163.5	0	1001	1	48
⋮	⋮	⋮	⋮	⋮	⋮	⋮
94.0	0	163.5	0	1024	1	48
96.0	0	163.5	1	-1	-1	-1
98.0	0.0	163.5	0	1037	25	48
⋮	⋮	⋮	⋮	⋮	⋮	⋮
194.0	0.0	163.5	0	1049	25	48
196.0	0.0	163.5	1	-1	-1	-1
198.0	0.0	163.5	0	1073	49	48
200.0	0.0	163.5	1	-1	-1	-1
202.0	0.0	163.5	0	1050	25	48
⋮	⋮	⋮	⋮	⋮	⋮	⋮
286.0	0.0	163.5	0	1084	49	48
288.0	0.0	163.5	1	-1	-1	-1
290.0	0.0	163.5	0	1097	73	48
⋮	⋮	⋮	⋮	⋮	⋮	⋮
386.0	0.0	163.5	0	1109	73	48
388.0	0.0	163.5	1	-1	-1	-1
390.0	0.0	163.5	0	2025	97	48
⋮	⋮	⋮	⋮	⋮	⋮	⋮
570.0	0.0	163.5	0	2048	97	48
572.0	0.0	163.5	1	-1	-1	-1

For the processing of the Danube island data set, a `SeismicRefractionManager` project can be created by saving the shot files and the geometry file in the required directory structure. Once the geometry is applied, i.e., the project is ready for processing, it is possible to obtain a first illustration of the subsurface conditions by computing the common offset stack (COS):

```
srm.compute('cos')
```

Progress <=====> 100.0% completed

**INFO** : Computed the common offset stack

A COS is obtained by stacking all traces recorded at the same absolute offset from a shot point, i.e., by computing the mean of the summed trace data. This procedure

reduces the influence of the incoherent noise, and thus yields stacked traces with an enhanced signal-to-noise ratio. The COS for the Danube island data set presented in Figure 3.10 shows first onsets for absolute offsets up to approximately 150 m; thus, indicating, in general, a good data quality. The first onsets visible in the COS suggest a two-layered subsurface structure, whereas the velocity estimation functionality of the `SeismicRefractionManager` can be used to approximate the corresponding seismic velocity values.

For the Danube island data set, the first break picking was performed manually by selecting subsets of the recorded seismograms and applying an adequate filter to enhance the S/N:

```
srm.select('sin 99')
```

```
INFO      : 48 traces selected
```

```
srm.filter('lp 120')
```

```
INFO      : Applied 120.0 Hz lowpass filter
```

```
srm.plot()
```

In this illustrative example, the trace data for SIN 99 are selected, which refers to a shot position located in segment four as indicated by RIN 73 for the first trace shown in Figure 3.11. Although the data are contaminated by a substantial seismic background noise at large offsets (particularly from RIN 73 to 90) the first onsets are easily perceptible.

Once first break travel times are determined for the entire data set, plotting a so-called pseudosection provides an illustration of the corresponding apparent seismic velocity values:

```
srm.plot('pseudosection')
```

In a pseudosection, as presented in Figure 3.12 for the Danube island data set, the apparent velocity values computed from the picked travel times and the absolute offsets are assigned to pseudolocations. The x- and z-coordinates of these pseudolocations are determined as the midpoint and as 1/3 of the absolute offset between the corresponding shot and geophone positions, respectively. In particular, a pseudosection allows for the identification of outliers in the data, e.g., stark velocity contrasts for adjacent points, or systematic errors, e.g., velocities erroneously influenced by a single shot or receiver. The main assumption here is that the pseudosection should reveal smooth transitions between lateral and vertical neighbors, considering that the data were collected with gradual changes in the position of the source and the receiver. The pseudosection will

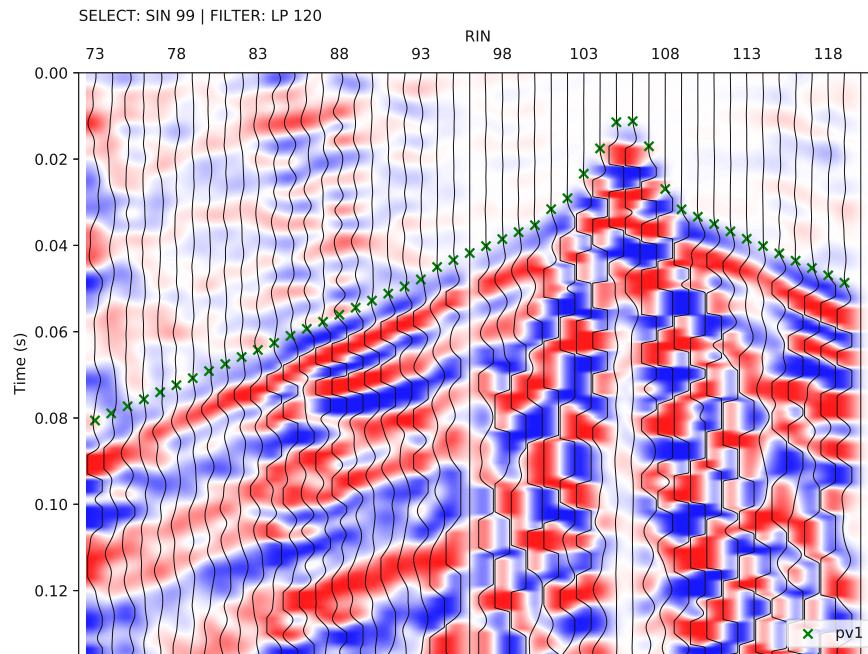


**Figure 3.11:** Exemplary seismic waveform data from the Danube island data set shown for shot index number (SIN) 99 with a 120 Hz low-pass filter applied to suppress high frequency noise. The receiver index numbers (RIN) start at 73 indicating that the data were collected in a roll-along survey layout.

reveal large variations in case of abrupt changes in the topography or the geometry of the array, yet this can be taken into account by the user. For the Danube island data set, the pseudosection suggests an increase in the seismic velocity along profile direction in deeper subsurface regions (i.e., larger pseudodepth). Such pattern could be related to a fault expected in this area of the Danube island; thus, indicating that the geophysical survey was sufficiently designed to detect such feature. Moreover, the pseudosection presented in Figure 3.12 shows a low number of data points in the first segment of the Danube island survey. This lack of data points at large pseudodepths is due to a low number of picked travel times at large offsets, and thus might indicate a low S/N in the trace data.

To review the data quality along the entire profile it is possible to visualize the picking percentage for each SIN, i.e., the ratio of actually picked travel times and total number of SIN-RIN pairs:

```
srm.plot('pickperc')
```

In general, a low picking percentage observed for several adjacent SIN can be related to a low signal-to-noise ratio in the affected traces; whereas anomalously low values might be due to systematic errors. Furthermore, a picking percentage plot can be

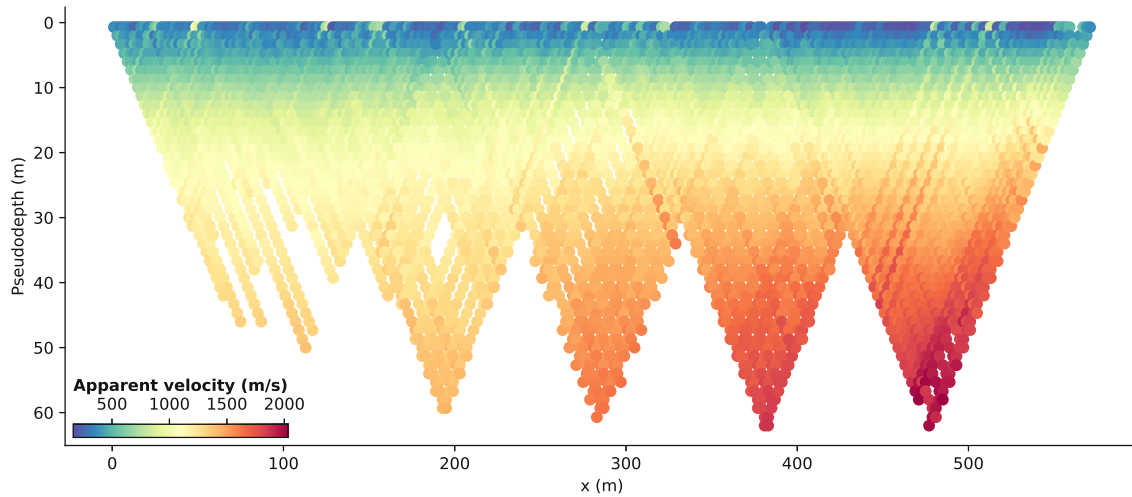


**Figure 3.12:** Pseudosection showing the apparent seismic velocities determined from the first break travel times obtained from the Danube island data set and the corresponding absolute offset between the shot and receiver stations. The apparent velocity for each shot-receiver pair is illustrated at the corresponding midpoint and pseudo-depth (1/3 of the absolute offset).

used for tracking the picking progress, e.g., to identify parts of the data set for which no first break picks have been determined. Hence, it is advisable to check the picking percentage plot before exporting the travel times for the inversion.

In case of the Danube island data set, the picking percentage plot presented in Figure 3.13 reports a low picking percentage in the first segment, which corresponds to the lack of data points observed in the pseudosection. Along the profile individual SIN are also characterized by a low picking percentage likely indicating systematic errors associated to the data acquisition process. Accordingly, the picking percentage plot allows for the identification of shots or receivers for which the first break picking might require a further review.

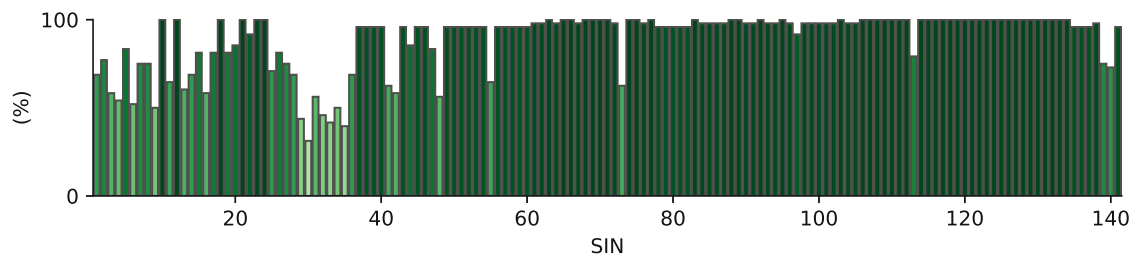


**Figure 3.13:** Picking percentage for the Danube island roll-along data set. Low values in the first third of the data set indicate a low signal-to-noise ratio in the seismograms hindering the picking of first break travel times for each shot-receiver pair.

### 3.3.3 Processing of a 3D seismic refraction data set: the soda lake example

The `SeismicRefractionManager` can also be used for the visualization and processing of data collected in a 3D survey layout. To illustrate the corresponding capabilities, we present here an application to a 3D data set collected in a desiccated soda lake located close to Vienna. The soda lake corresponds to quarternary sediments where capillary forces have developed a low permeable layer close to the surface (between 50 and 100 cm) with a high clay and salt content. The seismic survey aims to support the interpretation of the electrical and electromagnetic models obtained in a monitoring framework. Accordingly, the survey geometry shown in Figure 3.14 was specified by previously conducted electrical measurements with electrodes arranged along two perpendicular lines. In particular, the seismic data were collected with 48 geophones deployed along the North-East to South-West oriented line, and 48 geophones deployed along the North-West to South-East oriented line, with a spacing of 2 m between the geophones. Shots were generated with an 8 kg sledgehammer at the geophone positions as well as at positions along the diagonals.

By providing the 3D coordinates of the shot and receiver stations in the geometry file the `SeismicRefractionManager` detects the 3D survey layout and automatically configures the project for 3D processing. In this way, the specific requirements for the 3D data handling are ensured internally, while the user interacts with the `SeismicRefractionManager` through the same commands used for the processing of 2D data sets.

Figure 3.15 presents the seismic waveform data recorded for SIN 1, i.e., the shot position co-located with the first geophone (Station 01 in Figure 3.14). The data for RIN 1 to 48 appear familiar as the corresponding SIN-RIN geometry is the same as for conventional 2D profiles. In contrast, the seismic waveform data for RIN49 to 96 show an entirely different pattern. To understand this visualization, it is important to take into account that RIN49 to 96 are deployed perpendicular to the direction of propagation of the wavefront originating from SIN 1. Accordingly, the observed curvature in the first onsets is due to the varying offset of the different SIN-RIN pairs.

The travel times can be determined through the same approaches as for 2D data sets, i.e., individual, batch or automatic first break picking. For the trace data presented in Figure 3.15, the first onsets are easily perceptible; thus, allowing to set first break picks for almost all traces.

Due to the 3D survey geometry, a 2D pseudosection is not suitable for visualizing the apparent velocity values computed from the picked first break travel times. Accord-

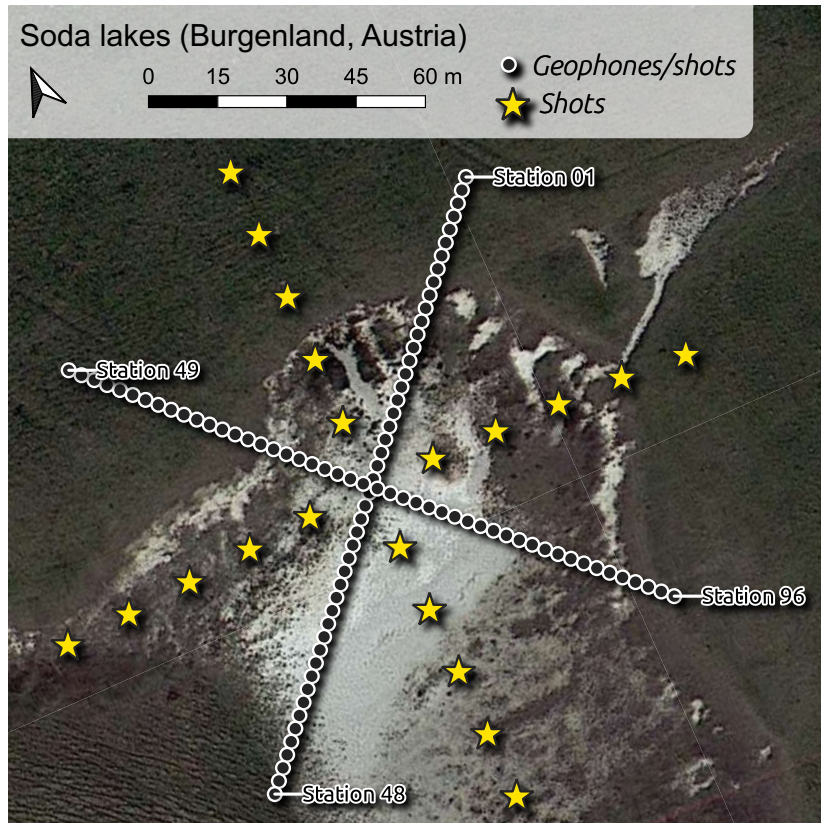


**Figure 3.14:** The soda lakes field data set was collected in a 3D survey layout with stations (co-located geophones and shots indicated by filled dots) deployed in form of a cross. Additional shots (yellow stars) were conducted in from of a cross rotated by  $45^\circ$  to increase the coverage of the data set.

ingly, the `SeismicRefractionManager` automatically switches to a 3D visualization technique, which plots the apparent velocity values in an interactive 3D pseudosection. The 3D pseudosection can be rotated and the image section can be zoomed and panned allowing the user to easily investigate the data quality for 3D geometries. Figure 3.16 shows a screenshot of the 3D pseudosection obtained for the salt lake data set; yet, such a screenshot cannot reveal the full capabilities implemented in the `SeismicRefractionManger` for the interactive analysis and visualization of 3D pseudosections.

Once the first break picking is finished, the corresponding pickset can be exported for the inversion of the obtained travel times. In contrast to 2D data sets, the pck file will contain the 3D coordinates of the survey stations. The inversion results and their interpretation are not the scope of this manuscript, yet Figures 3.15 and 3.16 reveal the capabilities provided by the proposed framework for the visualization and processing of seismic data collected in 3D survey geometries.

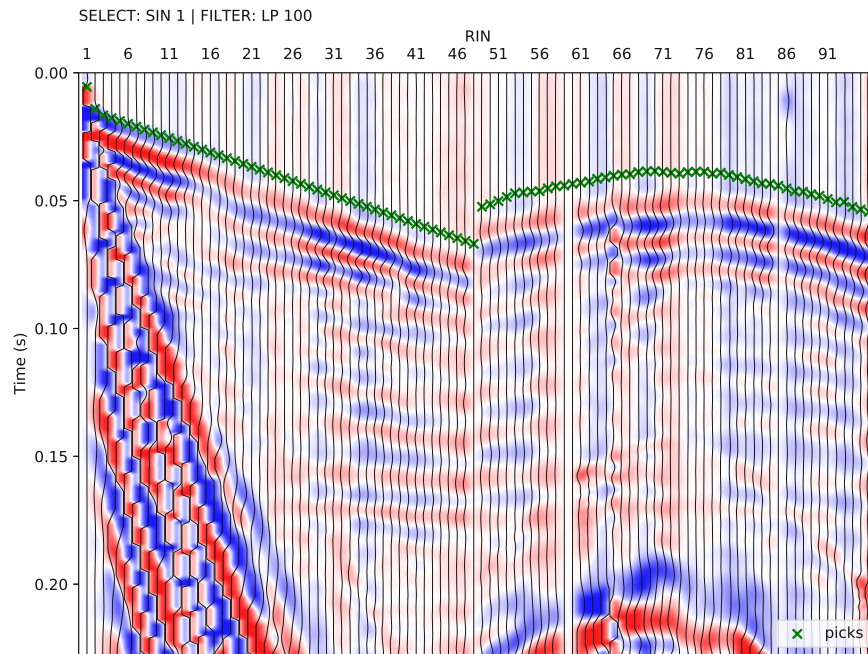


**Figure 3.15:** Exemplary seismic waveform data from the soda lakes data set shown for shot index number (SIN) 1 with a 100 Hz low-pass filter applied to suppress high frequency noise. The recorded seismic waveform data clearly reflect the geometry of the geophones with RIN 1 to 48 deployed along the direction of wave propagation, while RIN 49 to 96 are deployed perpendicular to the propagating wavefront.

### 3.4 Conclusions and Outlook

We have presented formikoj, a flexible open-source library facilitating the development of modeling and processing tools for geophysical data. Implemented in python and tested on all major operating systems (Linux/Unix, MacOS, Windows), formikoj is suitable for multi- and cross-platform applications; thus, allowing for the collaboration between users free from licensing costs and platform requirements.

We demonstrated the capabilities of the formikoj framework to develop versatile and easily scalable classes for the modeling and processing of waveform data in seismic refraction surveys. The required interaction with the user is reduced to a minimum as crucial processing steps are automatized within the `SeismicWaveformModeler` and `SeismicRefractionManager` classes. This is achieved through efficient data input strategies, for instance regarding the preparation and import of the geometry file or the keyboard-based interaction associated with the first break picking. In this regard, the user controls the formikoj library by providing text-based commands preferably through an ipython shell to exploit the full interactive potential of the modeling and processing tools. However, applications of the formikoj library can also be automatized by implementing workflows in python scripts or jupyter notebooks.

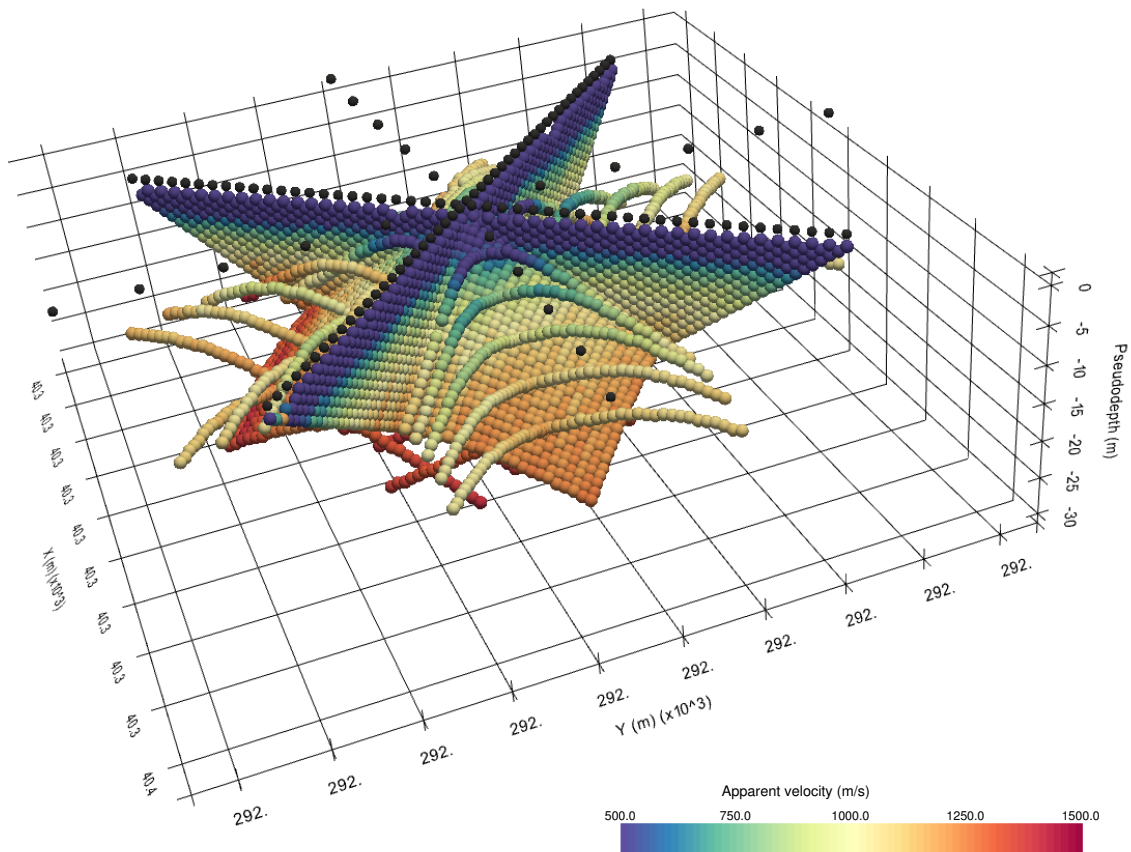


**Figure 3.16:** 3D pseudosection showing the apparent seismic velocities determined from the first break travel times obtained from the soda lakes data set and the corresponding absolute offset between the shot and receiver stations. The apparent velocity for each shot-receiver pair is illustrated at the corresponding 2D midpoint and pseudodepth (1/3 of the absolute offset), thus yielding a 3D representation.

Based on three exemplary use cases, we illustrated the applicability of both the `SeismicWaveformModeler` and the `SeismicRefractionManager` class. In the first use case, we showed the possibility to forward model seismic waveform data based on custom subsurface models and survey geometries with the `SeismicWaveformModeler`. Additionally, we subjected the resulting waveform to systematic and random noise sources to highlight the ability to emulate typical data quality and error behavior observed in field data. The capabilities of the `SeismicRefractionManager` were demonstrated through the processing of field data sets collected in complex survey layouts, namely a roll-along and a 3D geometry, respectively. Moreover, we showed how the different data visualization options can assist during the data processing to ensure consistency in the first break travel times. In particular, we implemented a visual-

### 3 *The formikoj library*

ization of the travel times by means of pseudosections illustrating the corresponding apparent seismic velocities. Such plots allow for a quick identification of systematic errors and outliers in both 2D and 3D data sets.

By making the source code of the formikoj library available under the MIT license we intend to spark the development of further modeling and processing tools for various geophysical models based on this framework. Future developments will focus on the implementation of tools for other wave-based geophysical methods used in frame of research activities within our group, such as the multi-channel analysis of (seismic) surface waves or transient electromagnetic surveys.

# 4 | Improved estimation of ice and water contents in alpine permafrost through constrained petrophysical joint inversion: The Hoher Sonnblick case study<sup>1</sup>

## 4.1 Introduction

Permafrost is an essential component of the alpine cryosphere (Gruber and Haeberli, 2009), and thus of the hydrosphere; its areal extent even exceeds that of the glacier-covered area in the Alps (Boeckli et al., 2012). Changes in the alpine permafrost have been linked to relevant consequences such as stability problems for infrastructure (e.g., roads and buildings) or increased natural hazard risk (e.g., rock falls; Duvillard et al., 2015). Alpine regions also represent an important catchment and storage area for groundwater (Schrott, 1998). As shown by a series of studies, climate change is particularly pronounced in mountainous regions such as the Alps (e.g., Pepin et al., 2015). If compared with the global changes, climate sensitivity for the temperature in the Greater Alpine Region has been about twice as large as at the global level in the past (Böhm et al., 2001), and it is also expected to be greater in the future (Gobiet et al., 2014).

Permafrost degradation in the Alps is correlated to this rise in air temperature (e.g., Harris et al., 2003; Noetzli and Gruber, 2009), although it should be noted that the response of permafrost to climate change is much more complex than a simple temperature signal effect, i.e., generally a response to the energy balance between the atmosphere and the soil (Sokratov and Barry, 2002). Permafrost is a thermally defined phenomenon referring to subsurface areas characterized by temperatures of less than 0 °C for at least two consecutive years (Harris et al., 1988). However, such a definition neither refers to the ice and water content in the subsurface nor to freezing and thawing processes. Moreover, as noted by (Mollaret et al., 2019), in fine-grained environments, a high content of unfrozen water can still be observed at negative temperatures. In

<sup>1</sup>This chapter is based on: Steiner, M., F. M. Wagner, T. Maierhofer, W. Schöner, and A. Flores Orozco (2021). “Improved estimation of ice and water contents in Alpine permafrost through constrained petrophysical joint inversion: The Hoher Sonnblick case study”. In: *Geophysics* 86.5, pp. 1–84. DOI: 10.1190/geo2020-0592.1

this regard, there is a growing interest in the development of accurate techniques to quantify the ice and water content values in alpine environments and their evolution accompanying the increase in temperatures (Rogger et al., 2017; Beniston et al., 2018; Jones et al., 2019). Such investigations permit the assessment of variations in the ice-water interchange between the atmosphere and the cryosphere and the associated seasonal and annual variations. Boreholes facilitate the in situ measurement of parameters of interest, such as temperature (e.g., the global terrestrial network for permafrost; Biskaborn et al., 2015), soil moisture (e.g., Pellet et al., 2016), and ice content (through borehole nuclear magnetic resonance logs; see, e.g., Parsekian et al., 2013; Kass et al., 2017). Due to the logistic challenges associated with the drilling of boreholes in mountainous environments and the related installation costs, the number and spatial distribution of boreholes is limited in the Alps. Moreover, investigations solely based on borehole data typically require interpolation, which might bias the spatial resolution of the results and their interpretation. Geophysical methods provide means for permafrost investigations with high spatial resolution in a non-invasive manner (for an overview, see Hauck and Kneisel, 2008).

Based on the contrasting electrical properties of water and ice, and the linear correlation between electrical resistivity and temperature, electrical resistivity tomography (ERT) is one of the most widely used geophysical methods to delineate frozen materials in the subsurface and to differentiate between unfrozen and frozen water content (e.g., Hauck and Vonder Mühl, 2003; Hilbich et al., 2008; Krautblatter et al., 2010; Kneisel et al., 2014; Dafflon et al., 2016; Emmert and Kneisel, 2017; Oldenborger and LeBlanc, 2018; Mollaret et al., 2019; Farzamian et al., 2020). However, the ERT measurements might be affected by the poor signal-to-noise ratio (S/N) due to limited current densities injected in compacted frozen rocks and snow-covered surfaces (e.g., Supper et al., 2014b; Mollaret et al., 2019). As an alternative approach, the seismic refraction tomography (SRT) is a geophysical method based on the propagation of elastic waves, which is used in permafrost research due to its sensitivity to changes in the mechanical properties in the subsurface due to freeze and thaw processes (Hilbich, 2010; Schöner et al., 2012a; Krautblatter and Draebing, 2014; Pogliotti et al., 2015; Draebing, 2016; Rogger et al., 2017). Yet, the SRT method cannot be easily automated for monitoring purposes. Moreover, SRT data might also be affected by a low S/N for measurements collected in areas with difficult terrain (e.g., a debris-covered slope) where the geophones are poorly coupled to the ground, and the hammer blows might result in seismic waves with low amplitudes. Contactless instruments have also been explored in permafrost studies; among them, the ground-penetrating radar (GPR) method has become a well-established technique (Hinkel et al., 2001; Hauck

and Kneisel, 2008; Hubbard et al., 2013; Rogger et al., 2017). The GPR method relies on the propagation of electromagnetic waves, and is used in permafrost investigations to delineate lithologic units and the contact to frozen materials in the subsurface based on their dielectrical properties (Hausmann et al., 2007; Schöner et al., 2012a; Monnier and Kinnard, 2013; Merz et al., 2016). However, rough topography might impair the quality of GPR data, for instance, due to the variable separation between the antenna and the surface. Moreover, during the melt season, an increase in electrical conductivity causes a rapid attenuation of the electromagnetic waves, and thus a reduced depth of investigation (Annan, 2005).

Considering the challenging conditions in alpine permafrost investigations, the combination of different geophysical methods aims at reducing the limitations of single techniques, thereby gaining a better site characterization. Moreover, such a multi-method approach reduces the ambiguity in the interpretation of results obtained with a single geophysical method and benefits from the partially complementary sensitivities of the different methods to the physical subsurface properties (e.g., ERT, SRT, and GPR). The processing of multi-method geophysical data sets can follow different strategies, such as (1) conventional independent inversion (CI) followed by joint interpretation, (2) constrained inversion, and (3) joint inversion. Independently, the inversion of geophysical data is an ill-posed problem (e.g., Zhdanov, 2002; Lesparre et al., 2017), which means that it is affected by non-uniqueness and instability. Non-uniqueness refers to the fact that the same data set can be sufficiently described by different models, whereas instability refers to the fact that small changes in the data lead to large changes in the obtained inversion results.

In joint interpretation approaches, the different data sets are processed independently and subsequently joined for a qualitative interpretation (e.g., Hausmann et al., 2007; Hubbard et al., 2013; Pogliotti et al., 2015; Rogger et al., 2017; Kunz and Kneisel, 2020). For permafrost investigations, Hauck et al. (2011) propose the so-called four-phase model (4PM), in which ERT and SRT results obtained through independent inversions are transformed to estimates of the subsurface water, ice, and air content (e.g., Schneider et al., 2013; Pellet et al., 2016; Hauck et al., 2017; Mewes et al., 2017). However, quantitative interpretations based on the 4PM might result in the estimation of physically implausible parameters, i.e., negative values that cannot occur in nature (e.g., Hauck et al., 2011; Mewes et al., 2017; Wagner et al., 2019; Mollaret et al., 2020). Constrained inversion approaches enhance the consistency of results obtained through different geophysical methods by including complementary data, e.g., structural information, toward an improved estimation of physical parameters (Karaoulis et al., 2011; Doetsch et al., 2012; Robinson et al., 2013; Chou et

al., 2016). Nonetheless, the quantitative interpretation of the obtained results still requires the subsequent application of a petrophysical model such as the 4PM to retrieve parameters of interest such as the ice or water content.

Joint inversion approaches simultaneously invert different geophysical data sets to improve consistency in the resolved models. Structural joint inversion approaches exploit the common sensitivity of different geophysical methods for structural features (e.g., Haber and Oldenburg, 1997; Gallardo and Meju, 2003; Gallardo and Meju, 2004; Doetsch et al., 2010; Garofalo et al., 2015; Linde and Doetsch, 2016; Hellman et al., 2017; Ronczka et al., 2017), whereas petrophysical joint inversion (PJI) approaches rely on a model describing the relationship between different geophysical methods through one or more common petrophysical parameters (e.g., Gao et al., 2012; Zhang and Revil, 2015; Sun and Li, 2016; Rücker et al., 2017; Wagner et al., 2019). With regard to permafrost research, the PJI framework developed by Wagner et al. (2019) permits the estimation of water, ice, air, and rock contents from apparent electrical resistivity and seismic travel time data simultaneously, by leveraging upon Archie's law and the time-averaging Timur equation applied by the 4PM. Wagner et al. (2019) and Mollaret et al. (2020) demonstrate the benefits of the PJI, namely, (1) the physical plausibility of the obtained results, i.e., no negative values in the fractional contents, (2) the possibility to incorporate non-geophysical measurements (e.g., temperature or soil moisture), and (3) the possibility to estimate a porosity model, due to the fact that the underlying petrophysical equations are honored during the parameter estimation. Despite these advantages, both studies emphasize that the results obtained through PJI still suffer from non-uniqueness, in particular with regard to the ice and rock contents because both components are characterized by relatively high acoustic velocities and act as electrical insulators (provided that the surface conductivity is negligible, which might not be the case; see, e.g., Duvillard et al., 2018). This means that depending on the *a priori* input and inversion settings (e.g., the lower and upper limits of a particular phase), the algorithm can produce a multitude of ice and rock matrix distributions, which equally well explain a single set of ERT and SRT data sets.

Our study aims at investigating the subsurface conditions at the summit of Hoher Sonnblick (Austria), at 3106 m above sea level (Schöner et al., 2012b). The study area is particularly relevant for several reasons, e.g., it hosts the Sonnblick Observatory, where climate change has been observed since 1886 and because permafrost degradation also affects the stability of the observatory buildings. However, only a few studies have addressed the investigation of subsurface conditions, in particular, the monitoring of permafrost degradation. So far, Schöner et al. (2012a) conduct the most detailed

study at Hoher Sonnblick by combining the geophysical and direct investigations, but only for a single time in 2012. In our study, we collected ERT and SRT data sets at two different times, which correspond approximately to the beginning and end of the melt season. Moreover, GPR is used to obtain structural information in the near surface and to support the interpretation of the seismic and electric inversion results. In particular, we extend the approach from Schöner et al. (2012a) by considering not only seismic but also electric data sets to estimate the water and ice content based on the 4PM. Taking into account the known limitation of this conventional approach, e.g., the physical implausibility of the resolved values, we aim to improve these estimates through PJI of the seismic and electric data sets. Moreover, we explore the possibility to further improve the quantitative estimates for the water and ice content by considering structural and porosity constraints in the PJI. In a first step, we investigate the incorporation of structural information derived through joint interpretation of the SRT, ERT, and GPR results and complementary data. Such constraints aim at an improved delineation of lithologic boundaries by combining the benefits of constrained and petrophysically coupled joint inversion. In a second step, we define a porosity distribution based on the analysis of time-lapse imaging results and use this information as a petrophysical constraint in PJI. We hypothesize that porosity information from multiple time steps is essential for improved estimates of the ice and water content. For an evaluation of our approach, we also present here a numerical study that permits a quantitative comparison of the deviations from the real model in terms of the water, air, ice, and rock content resolved by different inversion strategies.

## 4.2 Materials and Methods

### 4.2.1 PJI solving for water, ice, air, and rock content

To image the changes in the ice and water content at Hoher Sonnblick, we use the open-source PJI framework developed by Wagner et al. (2019), built on the modeling and inversion functionality provided by pyGIMLi (Rücker et al., 2017). Implementing the equations of the 4PM developed by Hauck et al. (2011), Wagner et al. (2019) describe the petrophysical relation between the electrical resistivity ( $\rho$ ) and the seismic velocity ( $v$ , commonly expressed by its reciprocal the seismic slowness  $s$ ). According to Hauck et al. (2011), permafrost systems are composed of the volumetric fractions of four phases, namely, the solid rock matrix  $f_r$ , and water  $f_w$ , ice  $f_i$ , and air  $f_a$  filling the pore space, related by the volume conservation constraint

$$f_w + f_a + f_i + f_r = 1 \quad (4.1)$$

To describe the seismic slowness, the 4PM uses a modification of the Timur (1968) equation, a time-averaging equation summing up the individual seismic velocities of the four phases weighted by their corresponding volumetric fraction (Hauck et al., 2011)

$$s = \frac{1}{v} = \frac{f_w}{v_w} + \frac{f_a}{v_a} + \frac{f_i}{v_i} + \frac{f_r}{v_r} \quad (4.2)$$

Assuming that electrolytic conduction dominates, the bulk electrical resistivity can be linked to the pore water content ( $f_w$ ) by Archie's second law (Archie, 1942):

$$\rho = \rho_w (1 - f_r)^{-m} \left( \frac{f_w}{1 - f_r} \right)^{-n}, \quad (4.3)$$

where the Archie parameters  $m$  and  $n$  denote the cementation exponent and the saturation exponent, respectively, and  $\rho_w$  corresponds to the pore water resistivity.

The volumetric fractions of the four phases for each model cell are elements of the parameter vector  $\mathbf{p} = [f_w, f_a, f_i, f_r]^T$  which permits the estimation of physically plausible values, i.e., positive values, for each phase and enables the flexible incorporation of prior information. During parameter estimation, elements in the transformed model vector are computed as  $m_j^k = \log(\rho_j^k) - \log(1 - \rho_j^k)$ , where the use of logarithmic barriers ensures that the petrophysical target parameters  $\mathbf{p}$  vary between zero and one. The data vector  $\mathbf{d}$  is composed of the observed seismic travel times and logarithmic apparent resistivities, i.e.,  $\mathbf{d} = [\mathbf{t}, \log(\boldsymbol{\rho}_a)]^T$ . The inversion scheme minimizes the objective function (following the notation in Zhdanov and Lin, 2017):

$$\begin{aligned} \Psi(\mathbf{m}) = & \| \mathbf{W}_d (\mathbf{d} - \mathcal{F}(\mathbf{m})) \|_2^2 + \alpha^2 \| \mathbf{W}_m \mathbf{m} \|_2^2 \\ & + \beta^2 \| \mathbf{W}_p^{sum} \mathbf{p} - \mathbf{1} \|_2^2 \\ & + \gamma^2 \| \mathbf{W}_p (\mathbf{p} - \mathbf{p}_0) \|_2^2 \rightarrow \min \end{aligned} \quad (4.4)$$

The first term of the objective function presented in Equation 4.4 specifies the misfit between the observed data  $\mathbf{d}$  and the model response  $\mathcal{F}(\mathbf{m})$  considering the reciprocals of the data errors on the diagonal of the data weighting matrix  $\mathbf{W}_d$ . The second term describes a smoothness regularization applied to the model vector  $\mathbf{m}$ , where  $\alpha$  denotes the dimensionless smoothness regularization parameter chosen to fit the data within their respective error bounds. The spatial regularization matrix  $\mathbf{W}_m$  controls the smoothness in the distribution of each component of the four-phase system. The third term is another regularization term required to ensure the adherence to the volume conservation constraint (Equation 4.1), where  $\beta$  denotes the correspond-

ing dimensionless regularization parameter, which, when chosen accordingly, restrains non-physical solutions. The matrix  $\mathbf{W}_p^{sum}$  consists of four adjacent identity matrices and acts on the parameter vector  $\mathbf{p}$  to promote solutions for which the sum of the four volumetric fractions is close to unity. The fourth term in the objective function is optional and permits the incorporation of *a priori* knowledge regarding the petro-physical target parameters (Wagner et al., 2019). Prior information on one or more target parameters are concatenated in the reference and starting model vector  $\mathbf{p}_0$ . The square matrix  $\mathbf{W}_p$  contains ones along its diagonal for target parameters to be kept close to the corresponding reference model and zeros otherwise. This term is scaled by using  $\gamma = \beta$  to penalize solutions for which the resolved models deviate from the reference models or omitted by using  $\gamma = 0$  for cases in which no prior information should be considered during the parameter estimation.

The incorporation of structural constraints in the CI of geophysical data is a widely used practice to enhance contrasts in models resolved through a CI (e.g., Günther et al., 2011; Doetsch et al., 2012; Bergmann et al., 2014; Wagner et al., 2015). Günther et al. (2011) implement structural constraints by adding structural information to the spatial regularization matrix used during the inversion. The spatial regularization matrix  $\mathbf{W}_m$  in Equation 4.4 is a block matrix and holds four first-order finite-difference roughness operators ( $\mathbf{C}$ ) on its diagonal to promote smoothness in each individual volumetric fraction:

$$\mathbf{W}_m = \begin{bmatrix} \mathbf{C} & \mathbf{0} & \mathbf{0} & \mathbf{0} \\ \mathbf{0} & \mathbf{C} & \mathbf{0} & \mathbf{0} \\ \mathbf{0} & \mathbf{0} & \mathbf{C} & \mathbf{0} \\ \mathbf{0} & \mathbf{0} & \mathbf{0} & \mathbf{C} \end{bmatrix} \quad (4.5)$$

The matrix  $\mathbf{C}$  has as many rows as cell boundaries exist in the mesh (lines separating adjacent triangles in 2D and triangles/quadrangles separating tetrahedral/hexahedra when moving to 3D) and as many columns as model cells. Based on the structural joint interpretation of complementary geophysical data, we set rows in  $\mathbf{C}$  corresponding to expected lithologic discontinuities to zero. This effectively allows, but does not enforce, the inversion to develop sharp parameter contrasts, which would not be possible in conventional smoothness-constrained inversions.

An important data fit measure is the error-weighted chi-square fit  $\chi^2 = \Psi_d/N$ , where  $\Psi_d$  is the first summand in Equation 4.4 and  $N$  is the number of measurements. A value of  $\chi^2 = 1$  means that the data are described by the model within their respective error bounds (Günther et al., 2006; Günther and Rücker, 2015). All of the inversion

results presented in this study have  $\chi^2$  values close to one for synthetic data and 0.8 - 1.2 for field data.

#### 4.2.2 The study area at Hoher Sonnblick (Austria)

The Hoher Sonnblick located at the border between the federal states of Salzburg and Carinthia (Austria) is a mountain of the Goldberggruppe in the Austrian Central Alps (Figure 4.1a). The Goldberggruppe is characterized by a northwest-striking gneiss zone ("Sonnblick-Gneisskern"; Exner, 1964) mainly consisting of granite gneiss with a predominant portion of potash feldspar (Exner, 1962). The summit of Hoher Sonnblick (Figure 4.1b) is formed by three steep rock walls facing toward east, north, and northeast (indicated in Figure 4.1a). Our study area is located on the southwest-facing slope (Figure 4.1c) covered by debris predominantly consisting of small to large blocks (Figure 4.1d). Subsurface conditions within the study area correspond to a three-layer case with the debris cover on top followed by a layer of fractured rocks and the bedrock (e.g., Schöner et al., 2012a). Direct information regarding the thickness of the fractured rock layer can be inferred from drill logs and the length of rock bolts, yet such information is solely available for the rock walls (Figure 4.2a). In Figure 4.2b, we present average air temperatures for Hoher Sonnblick indicating that the melt season approximately extends from May to October. Rock temperatures measured in boreholes provide information about the active layer thickness (ALT) as shown for borehole A in Figure 4.2c. Nonetheless, subsurface investigations within the study area are rare (e.g., Schöner et al., 2012a), and no permanent geophysical monitoring of permafrost is available.

#### 4.2.3 Acquisition and processing of geophysical data sets

To assess changes in the subsurface properties associated with freezing and thawing processes, we collected geophysical data along a profile located on the southwest-facing slope of the Hoher Sonnblick summit (indicated in Figure 4.1a). As illustrated by the thermal states in the atmosphere (Figure 4.2b) and the subsurface (Figure 4.2c), the first data set was collected on 27 June 2019 approximately at the beginning of the melt season, whereas the second data set was acquired on 18 October 2019 at the end of the melt season.

Measurements were conducted with 32 electrodes (ERT) and geophones (SRT), deployed with a separation of 2 m and hammer blows for the collection of the SRT data conducted at each geophone position. In June 2019, the study area was covered by a snow layer with the thickness ranging between approximately 0.5 and 2.0 m;

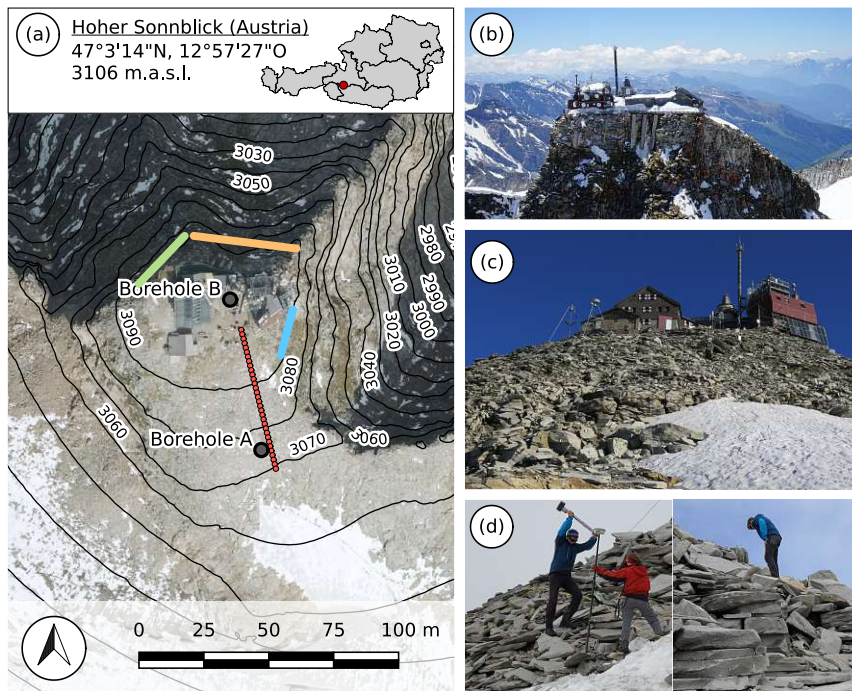


**Figure 4.1:** The summit of Hoher Sonnblick (Austria): (a) map of the summit area showing the locations of geophones, shots and electrodes (the red symbols), and the positions of the boreholes (the gray circles). Steep walls form the boundaries of the summit pyramid to the northwest (green), north (orange), and east (blue). Orthophoto published by the Government of Carinthia (flights between 2013 and 2015). (b) Aerial photo showing the exposed location of the observatory situated on top of the summit pyramid (provided by E. Ludewig). (c) The study area located on the southeast facing slope as seen from the foot of the summit pyramid. (d) Pictures taken during data acquisition illustrating the composition of the debris cover.

thus, to ensure galvanic contact between the ground and the electrodes and a firm coupling between the ground and the geophones, we dug 32 holes in the snow cover to place the geophones and the electrodes. We surveyed the positions of these holes with differential global navigation satellite system (dGNSS) to enable redeployment of the sensors at the same locations in October 2019.

### SRT data collection and processing

For the seismic refraction surveys at Hoher Sonnblick, we used the DMT Summit data acquisition system and vertical geophones with a corner frequency of 30 Hz deployed at the surface. To ensure a firm coupling between the geophones and the ground, we drilled holes in larger boulders of the debris cover to take up the spikes of the geophones. At the shot positions, we generated elastic waves with a 7.5 kg sledgehammer striking a 3 cm thick plastic plate and stacked four hammer blows to improve the S/N.

#### 4 Ice content quantification at the Hoher Sonnblick

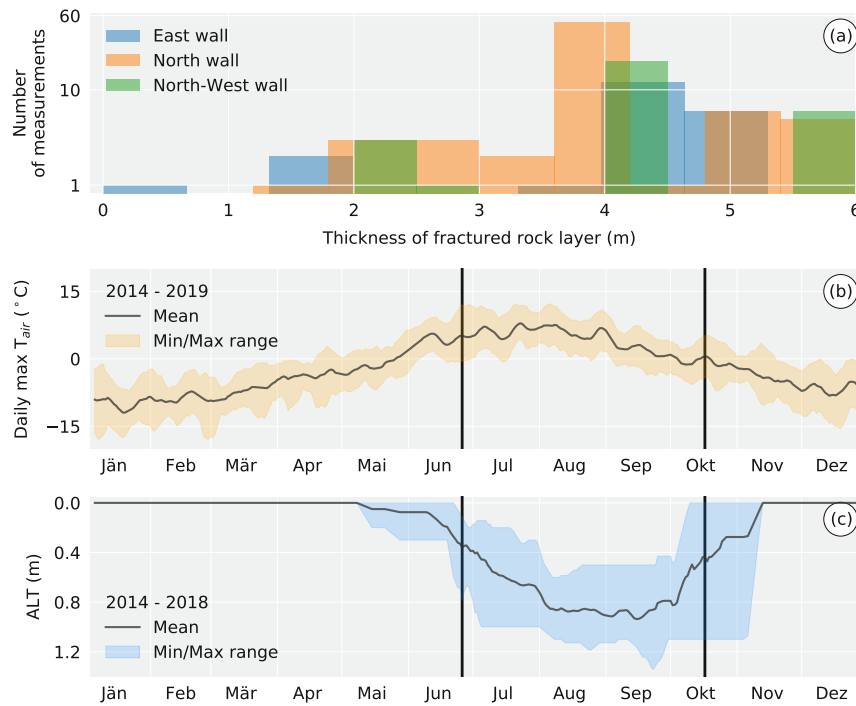


**Figure 4.2:** Complementary information available for the study area at Hoher Sonnblick. (a) Thickness of the fractured rock layer as obtained from drill logs and the length of rock bolts installed in the three major rock walls. (b) The average air temperature observed between 2014 and 2019. (c) The average ALT as derived from rock temperatures collected in borehole A between 2014 and 2018. The vertical black lines in (b and c) illustrate the times of the ERT and SRT field campaigns.

Picking of first-break travel times was done with a Python script based on the ObsPy toolbox (Beyreuther et al., 2010), which provides the means for reading and processing of seismic waveform data. We applied a 120 Hz low-pass filter on the seismic traces to attenuate signals associated with high-frequency noise. Yet, the S/N remained low – especially at larger offsets – requiring manual correction of automatically picked first onsets. Based on different gathers, i.e., common shot, receiver, and offset, we managed to determine 992 and 991 travel times for the June and October data set, respectively.

#### ERT data collection and processing

ERT data were acquired using the eight-channel Multi-Phase Technologies DAS-1 Electrical Impedance Tomography System. To facilitate sufficiently low contact resistances, we (1) coupled two stainless steel electrodes with a copper wire, (2) deployed such electrode couples in predrilled holes, (3) filled the remaining voids in the holes with quartz sand, and (4) saturated the sand with salt water. The method used by the DAS-1 to estimate contact resistances is limited to approximately 300 k $\Omega$ , whereas

readings of greater than 200 k are considered to be an open circuit. For both campaigns conducted at the Hoher Sonnblick, contact resistances were well below 100 k for most electrodes. Similar values were reported by Mollaret et al. (2019) for different permafrost sites in the Swiss Alps. In October 2019, we observed values up to 140 k for some electrodes and one electrode had to be excluded due to contact resistances higher than 200 k. For the data collection, we prepared a measurement protocol combining multiple gradient and dipole-dipole configurations, varying in the size of the voltage dipole in the range between 1.0 and 4.0 times the electrode spacing (i.e., skip 0–3, such as, for example, described by Flores Orozco et al. (2018b) leading to a higher S/N than other configurations. Measurements were collected using a square waveform with a pulse length of 0.125 s and a 50 % duty cycle. We collected normal and reciprocal readings, where reciprocal refers to recollecting data for each quadrupole with interchanged current and potential dipoles (Binley et al., 1995). After removing erroneous measurements related to negative apparent resistivity readings or zero current injection, followed by the removal of readings with poor reciprocity (e.g., Flores Orozco et al., 2012b; Flores Orozco et al., 2018b), out of 276 normal readings initially acquired 110 readings remained for both campaigns.

### Inversion of SRT and ERT data sets

For the CI of the observed travel times and collected apparent resistivity values for each individual time step, we used the corresponding modules of pyGIMLi (Rücker et al., 2017), whereas the PJI framework (Wagner et al., 2019) was used for the joint inversion of the data sets. We considered estimated absolute SRT data errors of 2.5 and 2.0 ms for inversion of the seismic data in June and October, respectively. Relative errors of 7.5 and 3.0 % were used for inversion of the ERT measurements in June and October, respectively, corresponding to the standard deviation of the misfit between the normal and reciprocal readings. All of the inversions, i.e., conventional and PJI, were conducted at 4:1 preferential smoothing in the horizontal direction, i.e., a four times larger horizontal smoothing.

### GPR data collection and processing

The GPR survey was aimed at delimiting the thickness of the debris cover along the seismic and electric profile. Information about lithologic contacts is needed in our study to structurally constrain the PJI under investigation. GPR measurements were conducted in June 2019, when conditions permitted dragging the antennas on top of the snow for improved data quality. We used a shielded antenna with a center

frequency of 200 MHz connected to a GSSI SIR-3000 system operated in time-based collection mode (120 scans per second). The SIR-3000 system was configured to apply 32 stacks for each trace to improve the S/N and to store the raw radargram with 512 samples per trace with a time range of 250 ns. With the commercial software ReflexW (Sandmeier, 2020), we processed the raw radargram by applying (1) a time-zero correction, (2) a dewow filter, (3) a 100 to 400 MHz band-pass Butterworth filter, and (4) gain correction. We applied an elevation correction based on the dGNSS data measured along the profile. For the time-depth conversion, we considered a velocity of 0.13 m/ns as obtained from the optimal stack power of the observed diffraction hyperbolas.

The processed radargram showed a first strong reflection associated with the interface between the snow and the debris cover, high reflection amplitudes within the debris layer, and lower amplitudes for the frozen bedrock. To verify such interpretation, we performed numerical modeling of electromagnetic wave propagation by means of the finite-difference scheme implemented in the ReflexW modeling module (Sandmeier, 2020) following an approach similar to Hausmann et al. (2007). To validate our interpretation, we computed synthetic radargrams with varying values of the dielectric permittivity ( $\epsilon$ ) and electrical conductivity ( $\sigma$ ) and considering different geometries of the subsurface interfaces. Moreover, we included near-surface heterogeneities, i.e., water- and air-filled voids, to model the internal structure of the debris. Assessing the agreement between the synthetic and measured radargrams enabled refinement of the parameters in the numerical model, and thus validation of the interpretation of the signatures observed in the GPR data.

### 4.3 Results

#### 4.3.1 Assessing the reconstruction capabilities of different inversion approaches

In a first step, we conduct a synthetic study to quantify deviations in the water, air, ice, and rock contents resolved through different inversion approaches, taking into account that it is practically impossible to obtain continuous spatial information about the true physical and thermal properties of the subsurface at real field conditions. For our numerical investigations, we build a model in 2D without topography consisting of three horizontal layers and we parameterize the layers according to values expected for Hoher Sonnblick. Based on this model, we compute the synthetic seismic and electric data sets considering geophones, shots, and electrodes to be co-located at 32

**Table 4.1:** Petrophysical parameters used for the application of the 4PM and in the PJI as obtained from permafrost literature (e.g., Hauck and Kneisel, 2008)

Archie parameters			Constituent velocities		
Parameter	Value	Unit	Parameter	Value	Unit
$\rho_w$	220	$\Omega\text{m}$	$v_w$	1500	$\text{ms}^{-1}$
$n$	2.4	-	$v_i$	3750	$\text{ms}^{-1}$
$m$	1.4	-	$v_a$	330	$\text{ms}^{-1}$
			$v_r$	5000	$\text{ms}^{-1}$

stations with a separation of 2 m. The computed travel times are subjected to additive Gaussian white noise with a standard deviation of 0.5 ms. For the simulation of apparent resistivity measurements, we use the same configuration as in the field and apply a normally distributed relative error of 5 %. From these synthetic data sets, we estimate the water, air, ice, and rock content through (1) the independent inversion of data sets and subsequent application of the 4PM, (2) PJI (as applied by Wagner et al. (2019) and Mollaret et al. (2020)), (3) structurally constrained PJI, and (4) PJI with structural and porosity constraints. The parameterization of the petrophysical model used in the conventional and PJI approaches is based on the values summarized in Table 4.1. The synthetic study permits the evaluation of how inaccurate prior information used as constraints in the PJI affects the resolved water, air, ice, and rock content. Hence, we defined five different scenarios (summarized in Table 4.2) referring to correct and erroneous prior information regarding the depth of the interface between the top and intermediate layer (shallow interface), the depth of the interface between the intermediate and bottom layer (deep interface), and the porosity model. To facilitate a clear comparison of the true model with the models resolved through the different inversion approaches, in Figure 4.3 we present the results of our synthetic study as 1D curves extracted from the center of the inverted models. The values of the true model for each component are indicated in Figure 4.3 for a direct evaluation of the results. Assuming a homogeneous porosity of 30 %, the independent inversion of the data sets and subsequent application of the 4PM resolves the main structural characteristics, i.e., the layering of the true model, and the estimated values approximate the true water and air content. Yet, in terms of the ice content, the results obtained through this conventional approach suffer from negative values in the near surface. Moreover, the ice content in the intermediate layer is underestimated, whereas at depth the resolved values are too high. The unconstrained PJI yields results for the water and air content similar to the conventional approach, provides an estimate of the true rock content, and solves for a non-negative ice content. Although

**Table 4.2:** Prior information considered for the assessment of the benefits and limitations of the constrained PJI approaches.

Scenario	Shallow interface	Deep interface	Porosity model
1	True depth	True depth	True
2	+ 2 m depth	True depth	Approximated (kNN smoothing and random noise)
3	True depth	+ 2 m depth	Approximated (kNN smoothing and random noise)
4	True depth	True depth	Approximated and values decreased by 15 %
5	True depth	True depth	Approximated and values increased by 15 %

the ice content resolved within the top layer is a good estimate for the true values, at larger depths the estimated ice content fails to resemble the true model. To overcome such limitations, we include prior knowledge in the PJI to reduce the degrees of freedom, and thus provide improved estimates for the different fractional values. In scenario 1, we incorporate the true interface depths as structural constraints in the PJI and invert the synthetic data sets based on a homogeneous porosity distribution. The results presented in Figure 4.3a illustrate that, for the water content and to a lesser extent for the air content, the structural characteristics of the true model are accurately resolved and also the obtained values are a good approximation of the true values. With regard to the ice and rock content, the incorporation of structural information does not yield the true values. As illustrated in Figure 4.3b, prescribing the true porosity distribution ensures that the values of the true models are accurately resolved. Results obtained through the structurally constrained PJI based on (partially) erroneous prior knowledge, defined by scenarios 2 to 5 (Figure 4.3a), illustrate that the estimated water content and air content do not significantly deviate from the true values. However, the resolved ice and rock content models do not reflect the true structures and values. For the PJI with porosity constraints, we approximate the PJI with porosity constraints, we approximate the true porosity distribution by k-nearest neighbors (kNNs) smoothing of the true values (where  $k = 100$  model cells) and subsequent adding of normally distributed noise. In scenarios 4 and 5, we additionally distort the approximated porosity distribution by  $\pm 15\%$  to simulate gross errors in the *a priori* porosity information. As illustrated in Figure 4.3b, the estimates for the water and air content still solve for the true values. In the case of the ice and rock content, we observe large variations in the resolved values dependent of the prescribed

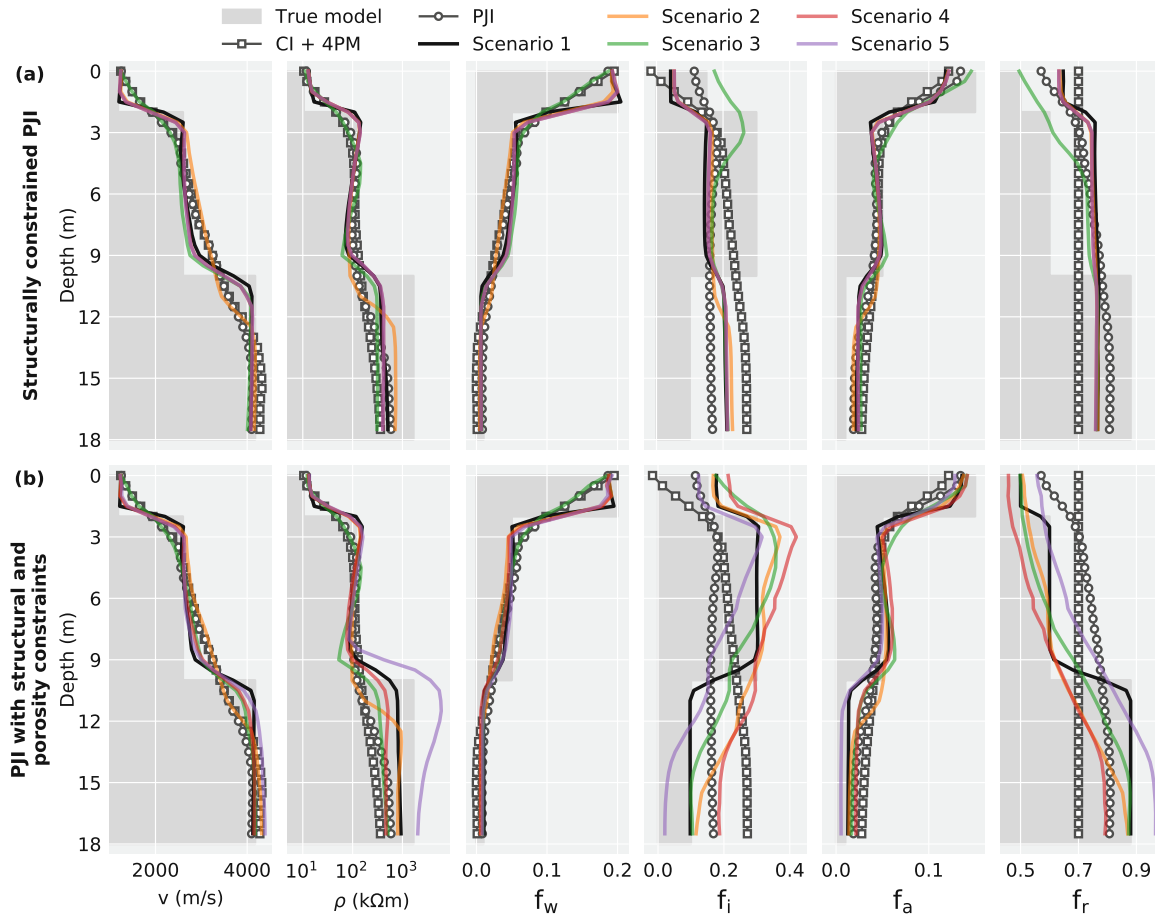


**Figure 4.3:** Synthetic study comparing different inversion strategies against the true model. The ability of (a) structurally constrained PJI and (b) PJI with structural and porosity constraints to resolve the water, ice, air, and rock content of the synthetic model is evaluated based on five scenarios referring to different assumptions regarding the *a priori* knowledge of interface depths and porosity distribution, i.e., the effect of incorrect *a priori* information on the inversion results is investigated.

porosity model. Still, the estimates clearly resemble the general characteristics of the true model and approximate the true fractional values. Hence, our synthetic study demonstrates that the results obtained through the PJI are significantly improved by incorporating a petrophysical constraint that at least roughly resembles the true subsurface porosity distribution. We also note here that this sensitivity of the 4PM, underlying the PJI framework, was already described by Hauck et al. (2011).

### 4.3.2 Subsurface structures resolved at Hoher Sonnblick through joint interpretation

Figure 4.4 presents the processed radargram and the imaging results obtained through independent inversion of the seismic and electrical datasets collected at different ac-

quisition times in June and October 2019. The SRT solves for similar structures for June (Figure 4.4a) and October 2019 (Figure 4.4b). Nonetheless, we observed substantial variations in the resolved seismic velocities in the near surface, whereas seismic velocities are consistently resolved with values higher than  $4000 \text{ m s}^{-1}$  for June and October 2019 at depths greater than approximately 8 m. Likewise, we delineate similar structures in the ERT imaging results for June (Figure 4.4c) and October 2019 (Figure 4.4d). Yet, the resolved resistivity values show a general decrease of approximately 60% from June to October 2019, which can be explained by the inverse correlation between the resistivity and the temperature (e.g., Krautblatter et al., 2010; Zisser et al., 2010; Bairlein et al., 2016). Still, the structural consistency of the ERT results for both times clearly indicates that the electrical images are related to lithologic contacts, whereas the amplitude of the values is controlled by variations in the water content (Mollaret et al., 2019). The interpretation of the independently processed and inverted datasets (i.e., joint interpretation) enables derivation of a subsurface model that delineates the principal lithologic units at the summit of Hoher Sonnblick. We consider the chaotic relationship between the reflections observed in the shallow areas of the radargram presented in Figure 4.4e to be associated with the debris cover. Based on this interpretation, the geometry of the debris layer can be delineated in the first half of the profile. Although not easily observable from the radargram, SRT and ERT consistently resolve an increase in the thickness of the debris layer in the lower part of the profile. Similar to Schöner et al. (2012a), we identify the possible interface between the fractured and consolidated rocks at the contact to acoustic velocities higher than  $4000 \text{ m s}^{-1}$ . To approximate the geometry of the bedrock interface along the geophysical section, we fitted a cubic spline to the  $4000 \text{ m s}^{-1}$  isolines computed from SRT results obtained for both times (see Figure 4.4a and 4.4b). The agreement in the geometry of the seismic interface obtained from the two SRT data sets supports our interpretation that such an interface corresponds to the contact between fractured and consolidated rocks, which is likely not affected by seasonal variations. Combining the different structural information yields the lithologic model presented in Figure 4.4f. The interpretation of SRT and GPR data previously collected at Hoher Sonnblick (Schöner et al., 2012a) supports the proposed lithologic model. Moreover, the consistency in the main features observed across GPR, SRT, and ERT in the near surface might demonstrate that these are controlled by the contact between the debris and the weathered gneiss. The increased thickness of the debris layer inferred from the SRT and ERT images corresponds with weak reflections in the radargram suggesting the deposition of saturated fine-grained debris below the blocky material. However, the contact between the weathered gneiss and the bedrock is solely resolved from the

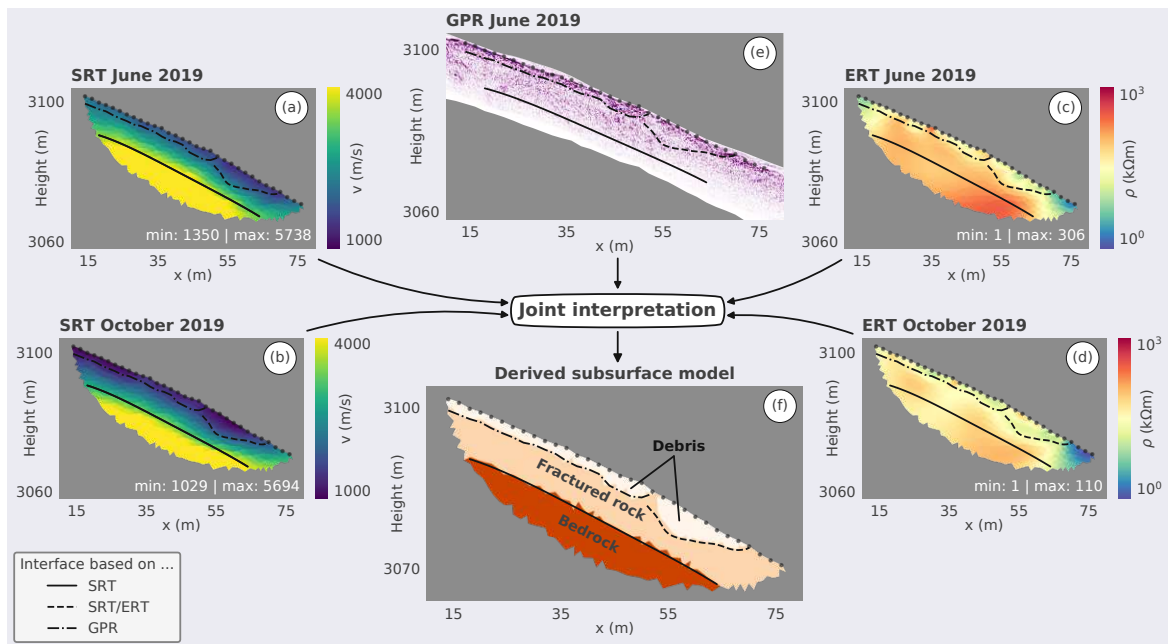


**Figure 4.4:** Joint interpretation of results obtained from different geophysical data sets collected at Hoher Sonnblick in 2019. The black circles in (a-f) indicate the sensor/shot positions. SRT results for data collected in (a) June 2019 and (b) October 2019. ERT results for data collected in (a) June 2019 and (b) October 2019. (e) The radargram collected during the June 2019 GPR campaign. (f) The resolved subsurface model refers to a three layer case.

SRT imaging results obtained through smoothness-constraint inversions. Hence, this interface requires further verification to be considered as a legible source for structural constraints.

In absence of direct information regarding the depth to the layer of consolidated rocks, we need to refer to the results of previous studies providing the corresponding information. Schöner et al. (2012a) infer the contact between fractured and compacted rocks through modeling of the thermal diffusivity based on rock temperatures observed in borehole B. Their model indicated a distinctive change in the thermal diffusivity from  $2.3 \times 10^{-6}$  to  $0.5 \times 10^{-6} \text{ m}^2 \text{ s}^{-1}$  in a depth of approximately 8.8 m. They attributed the strong heat transfer from the surface down to a depth of 8.8 m to fractured rocks and interpreted the decreased heat transfer at larger depths to be associated with the compacted bedrock. Comparing the bedrock depth inferred from the thermal diffusivity model with a 1D representation of the resolved seismic velocities allowed for a verification of the SRT imaging results (Schöner et al., 2012a). This approach is not directly applicable for our study because our SRT profile does not cover the location of borehole B (see Figure 4.1a). Hence, in Figure 4.5, we provide a comparison of the rock temperatures observed in borehole A and seismic velocities in the vicinity

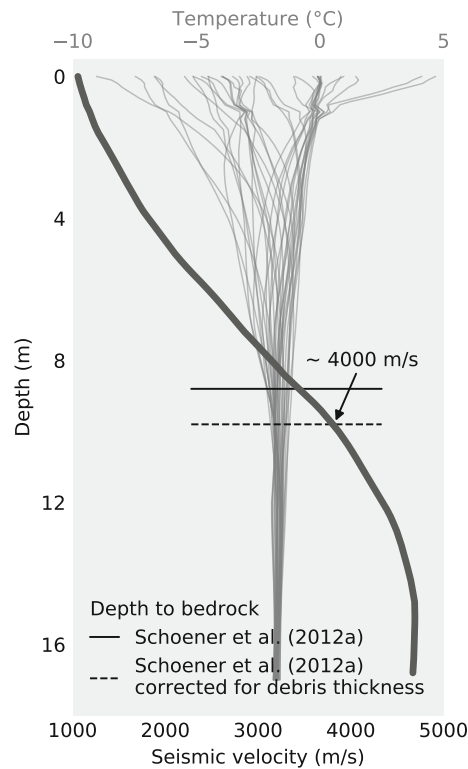


**Figure 4.5:** Monthly median borehole temperatures observed in borehole A between 2014 and 2018 (gray lines) and seismic velocities resolved through the smooth-constrained inversion in the vicinity of the borehole (bold black line). The horizontal solid black line illustrates the bedrock depth obtained by Schöner et al. (2012a) through modeling of the thermal diffusivity based on rock temperatures observed in borehole B. The horizontal dashed black line corresponds to the modeled bedrock depth corrected considering the larger debris cover thickness in the vicinity of borehole A (derived from GPR data).

of borehole A ( $\pm 2$  m) with the bedrock depth reported by Schöner et al. (2012a). Note that the modeled bedrock depth needs to be corrected for the larger debris cover thickness observed at borehole A, for instance, in the GPR results presented in Figure 4.4e. Figure 4.5 illustrates that the reported bedrock depth coincides well with a distinct decrease in the variability of the rock temperatures, which we attribute to the reduced heat transfer in the bedrock. From the 1D seismic velocity curve, we can infer a velocity of approximately  $4000 \text{ m s}^{-1}$  for the compacted rocks at depth. In this regard, we consider our SRT imaging results to be verified by an approach based on direct borehole information and, thus, consider the geometry of the  $4000 \text{ m s}^{-1}$  isoline to be representative for the contact between fractured and consolidated rocks along the entire geophysical profile.

### 4.3.3 Quantifying the subsurface ice-water content at Hoher Sonnblick

Although the joint interpretation approach is commonly applied in multi-method investigations, the obtained results remain qualitative because they do not provide estimates of relevant parameters such as the porosity or the ice and water content. Nonetheless, SRT and ERT images can be transformed to quantitative results through a petrophysical model such as the 4PM. For the parameters of the 4PM, i.e., the variables in Equations 4.2 and 4.3, we use the values summarized in Table 4.1, which are common in permafrost literature (e.g., Hauck and Kneisel, 2008). We note here that literature values might represent a good approximation to highly heterogeneous materials such as debris and weathered rock. Considering the imaging results presented in Figure 4.4 and results from previous investigations (Schöner et al., 2012a), we prescribe a porosity model characterized by a gradual decrease in the porosity with depth, where high values in the near surface correspond to the debris layer and a low porosity at depth refers to the less weathered gneiss and bedrock. Based on the 4PM, the independent SRT and ERT imaging results can be transformed to the water, air, and ice contents. The fractional values obtained for the data sets collected in June and October 2019 are presented in Figure 4.6a. The blanked regions illustrate that this approach yields non-physical values, i.e., negative values, in the estimated ice and air contents. Based on the same petrophysical parameters and governing equations, the PJI framework solves for physically plausible values for each phase, i.e., water, ice, air, and rock content for data collected in June and October 2019 (Figure 4.6b). Furthermore, in Figure 4.6c, we present images resolved through the structurally constrained PJI, which incorporates structural information from the lithologic model obtained through joint interpretation.

Results illustrated in Figure 4.6 reveal consistent water contents resolved through different inversion approaches. The highest water content (approximately 20 %) is resolved in the near surface within the debris cover and within a deep-seated anomaly located at the lower end of the profile, whereas a lower water content (< 10 %) is found below the debris cover. Large variations can be observed in the estimated ice content following the different inversion approaches. In particular, the ice content values estimated based on structural constraints show substantially lower values (< 10 % in June 2019 and < 5 % in October 2019) than those obtained through the conventional approach and the unconstrained PJI (> 10 % for June 2019 and up to 20 % for October 2019). In the case of the air content, similar values are resolved through the conventional approach and the PJI. A high air content is resolved for the debris layer, with values up to 10 % in June and 30 % for measurements collected in October 2019.

#### 4 Ice content quantification at the Hoher Sonnblick

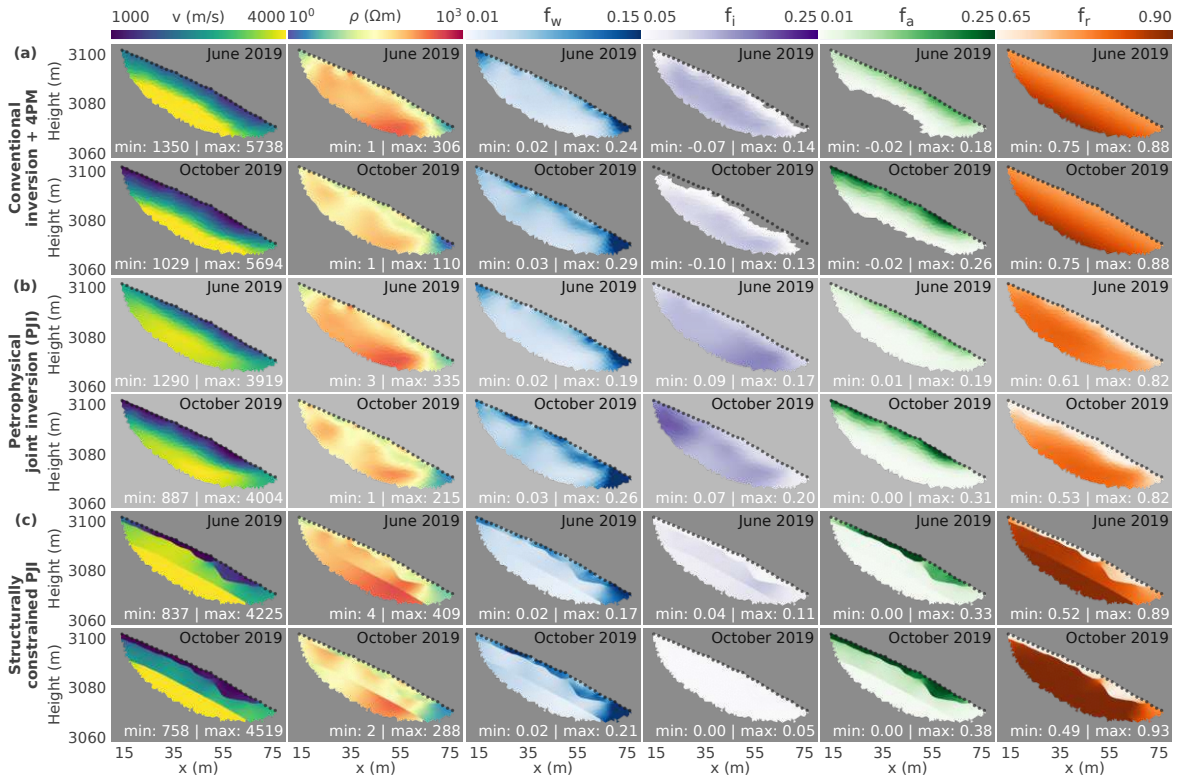


**Figure 4.6:** Imaging results for the seismic and electric data sets collected at Hoher Sonnblick in June 2019 and October 2019 resolved through (a) CI and subsequent transformation by means of a petrophysical model, (b) unconstrained PJI, and (c) structurally constrained PJI. Black circles indicate the sensor/shot positions.

For June 2019, the structurally constrained PJI solves for higher air content values within the debris layer than the other approaches (approximately 10 % points higher). As expected, both PJI approaches solved for the lowest rock content (approximately 50 to 60 %) in the near surface corresponding to the debris cover, whereas the rock content increases with depth and reaches maximum values in the bottom layer (up to 90 %), yet the range of values differs significantly.

To investigate the consistency in the results obtained through different inversion approaches, we present in Figure 4.7 the computed time-lapse differences in the inverted parameters ( $\Delta f_x = f_{x(Oct)} - f_{x(Jun)}$  with  $x = w, a, i, r$  for the water, air, ice, and rock content, respectively). The temporal changes in the water content are comparable for all three approaches showing similar patterns and a consistent range of values. In the case of ice and rock content, the resolved temporal changes differ significantly for the different inversion approaches. The CI and subsequent application of the 4PM results in non-physical values for the ice content close to the near surface, yet a general decrease in the ice content is observed from June to October, as expected, due to the higher temperatures in summer (Figure 4.2b). The unconstrained PJI yields an in-

crease in the ice content in the upper part of the profile during the melt season, which is physically implausible, especially when compared to the increase in the ALT (see Figure 4.2c). For the air content, the conventional approach and the unconstrained PJI resolve similar temporal changes, yet in the conventional results the coverage at depth is limited due to non-physical values. The temporal changes resolved through the structurally constrained PJI yield plausible values in the entire imaging plane, with an overall decrease in the ice content, which agrees with the expected increase in the subsurface temperatures during the melt season. Moreover, the structurally constrained PJI solves for a more detailed image of spatial variations in the air content within the debris cover than resolved through the other approaches. However, both PJI approaches resolve for temporal changes in the rock content implicating alterations in the rock-air matrix over the course of four months.

## 4.4 Discussion

### 4.4.1 Benefits and limitations of different PJI approaches

The results of our synthetic study (see Figure 4.3) illustrate that the PJI framework provides the means to overcome the estimation of non-physical values as obtained through the conventional approach, which becomes evident in the case of the near-surface ice content. Comparing the resolved values with the values of the true model demonstrates that the PJI also provides an improved estimation of the true ice and rock content by allowing variations in porosity during parameter estimation and honoring the volume conservation constraint (Equation 4.1). Yet, the estimates for the ice and rock content provide only a rough approximation of the true model. As demonstrated by synthetic scenario 1 (see Figure 4.3), through the incorporation of prior knowledge, i.e., interface depths and porosity distribution, the constrained PJI, accurately solves for the characteristics of the true model. The assumption of extensive and accurate existing information may be challenging for field investigations in which information might be scarce (e.g., at Hoher Sonnblick), or complementary data might be affected by uncertainties. Results obtained for scenarios 2 to 5 illustrate that the true water and air content can still be quantitatively estimated in the case of inaccurate prior information and thus demonstrate that the constrained PJI significantly improves the stability of the inversion. Considering that the estimates for the ice and rock content show a substantial sensitivity to changes in the structural and porosity constraints, the constraints need to be carefully defined. Still, the models obtained through constrained PJI approaches provide a sufficiently accurate approximation of the true model. The

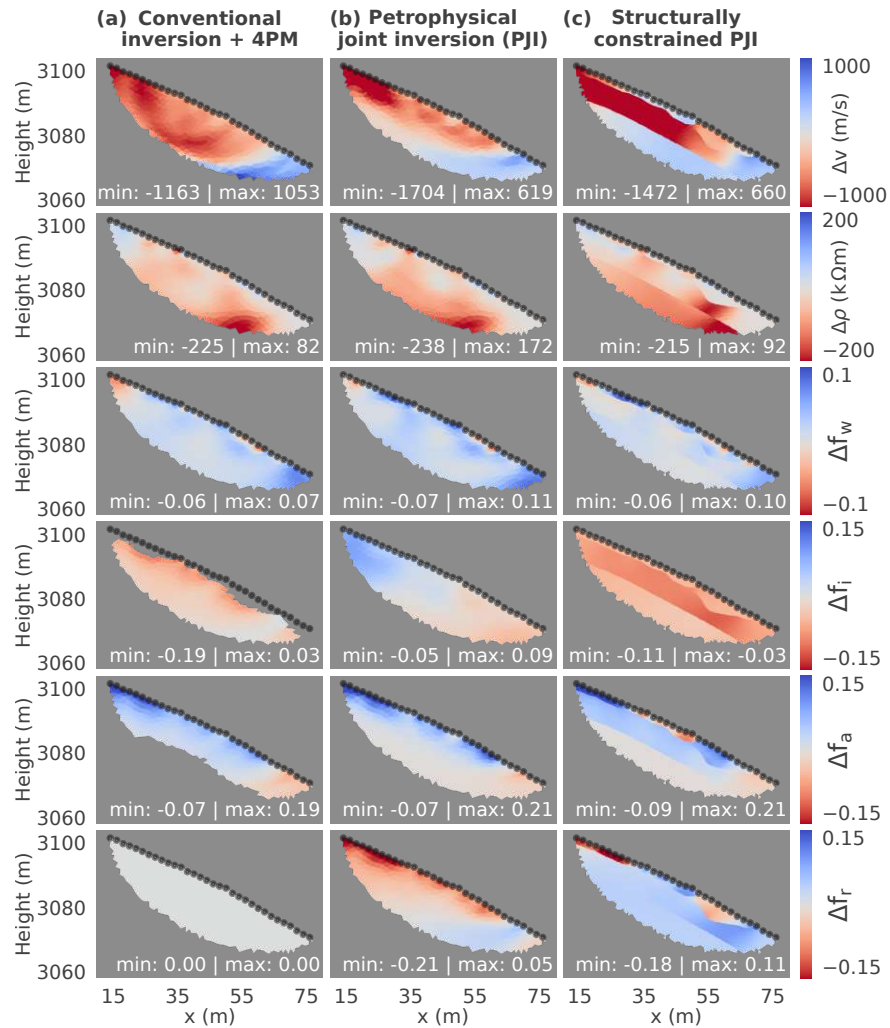


**Figure 4.7:** Temporal changes (i.e., absolute differences) between June 2019 and October 2019 in the imaging results resolved through (a) CI and subsequent transformation by means of a petrophysical model, (b) unconstrained PJI, and (c) structurally constrained joint inversion. The black circles indicate the sensor/shot positions.

comparison with results obtained through the conventional approach and through the PJI demonstrate that even inaccurate prior knowledge can improve the estimates for the ice and rock content. In this regard, we consider constrained PJI approaches to yield improved estimates compared with other inversion approaches.

#### 4.4.2 Improving the estimates for ice and water content at Hoher Sonnblick

Similar to our synthetic study, the unconstrained PJI prevents the estimation of negative values in the ice content also for the field data collected at Hoher Sonnblick. However, considering other permafrost studies (e.g., Hauck, 2002; Hilbich et al., 2008),

the resolved increase in the ice content during the summer months is physically implausible (Figure 4.7b). Aiming at an improved estimation for the fractional contents of each phase, we incorporate structural constraints into the PJI to enhance the consistency in the results obtained for both times (see Figure 4.6c). The corresponding temporal changes presented in Figure 4.7c illustrate that the structurally constrained PJI resolves a decrease in the ice content within the debris cover along the entire profile, as expected due to the higher air temperatures in summer (June to October; see Figure 4.2b and 4.2c) compared with the winter months. However, Figure 4.7b and 4.7c still reports substantial changes in the rock content, which we consider physically implausible because the rock matrix should remain constant over the course of our investigation (approximately four months). Although the PJI framework demonstrably provides better estimates for the fractional contents in the different phases, Figure 4.7 demonstrates that this approach can still be limited due to the inherently similar physical properties of rock and ice; i.e., both materials are characterized by a high seismic velocity and a high electrical resistivity. In particular, porosity estimates will be largely biased because the 4PM underlying the PJI requires sufficiently high contrasts in the seismic velocities of rock and ice to distinguish between these two solid phases, a problem already highlighted by Hauck et al. (2011). Accordingly, temporal variations in the seismic velocities might result in implausible estimations of the ice and rock content, as observed in Figure 4.7b and 4.7c. Prescribing the *a priori* information regarding the porosity distribution would be a step toward the estimation of physically plausible values (e.g., Hauck et al., 2011), which refers to the incorporation of a petrophysical constraint in the PJI. Laboratory estimations of porosity values in rock samples, however, might not be representative for the bulk porosity of the different subsurface layers, i.e., the debris cover or the weathered gneiss observed at Hoher Sonnblick (see Figure 4.1). Borehole information is not available at the site, which is not equipped for subsurface investigations on the same level as other study areas (Mollaret et al., 2019). Moreover, such information might be valid only at the borehole position, thus limiting its application in an imaging framework. To overcome the lack of ground truth, we propose to use the porosity distribution resolved through the unconstrained PJI for one time step as a petrophysical constraint in the PJI of data collected at another time step to solve for improved estimates of the ice and water content. We consider this approach to be more concise and easier to apply at different sites than the approach used in, e.g., the study by Pellet et al. (2016), in which the authors estimated the porosity distribution based on a modified petrophysical model, which was solely applicable in an unfrozen part of the study area. Assuming a minimum subsurface ice content at the end of the melt season, we suggest that the October

2019 rock content distribution resolved through the unconstrained PJI provides the best possible estimation of the subsurface porosity distribution  $\Phi_{(Oct)} = 1 - f_{r(Oct)}$  at Hoher Sonnblick.

Following the argumentation from Hauck et al. (2011), we prescribe the porosity model  $\Phi_{(Oct)}$  as fixed in the PJI; i.e., we implement it as a petrophysical constraint. Moreover, by prescribing  $\Phi_{(Oct)}$  for June and October 2019, we couple the PJI of datasets collected at different times by means of a common parameter, which is kept constant in the inversion of two different time lapses. In this regard, the proposed incorporation of the porosity distribution in the PJI can be seen as a time-lapse constraint. Prescribing a fixed porosity decreases the degree of freedom in the PJI by penalizing variations in the rock content during the inversion. Following such an approach, we are able to increase the physical consistency between time steps, as required to solve for reliable changes in the parameters at different times, and improve the quantification of the ice and water dynamics.

Figure 4.8a and 4.8b presents the results resolved through the structurally and time-lapse-constrained PJI for June and October 2019, respectively. To assess seasonal variations in the different phases, we compute the absolute differences illustrated in Figure 4.8c. For the water content, variations are largely confined to the debris layer showing lateral variations along the profile. The highest increase in the water content (approximately 10 % points) is resolved at the lower end of the profile, likely associated with meltwater discharge, which can be observed in summer within this area of the Hoher Sonnblick summit. The temporal changes in the ice content indicate the largest ice loss (approximately  $-15$  % points) within the debris layer in the upper part of the profile, i.e., close to the observatory building. Moreover, the area around the depression in the debris layer in the lower half of the profile (i.e., between 50 and 70 m along the profile direction) is characterized by a considerable decrease in the ice content (approximately  $-10$  % points), potentially related to the infiltration of warm meltwater and rainwater. The air content mainly varies within the debris layer, when melting ice is replaced by air (approximately 20 % points) indicated by the corresponding changes in these fractional contents. The reduced near-surface air content can be related to an increase in the water content. We interpret the resolved variations in the different phases to be a result of the increased available atmospheric energy input during the melt season, which results in meltwater infiltration within the debris layer caused by the melting snow (e.g., in June) and near-surface ice.

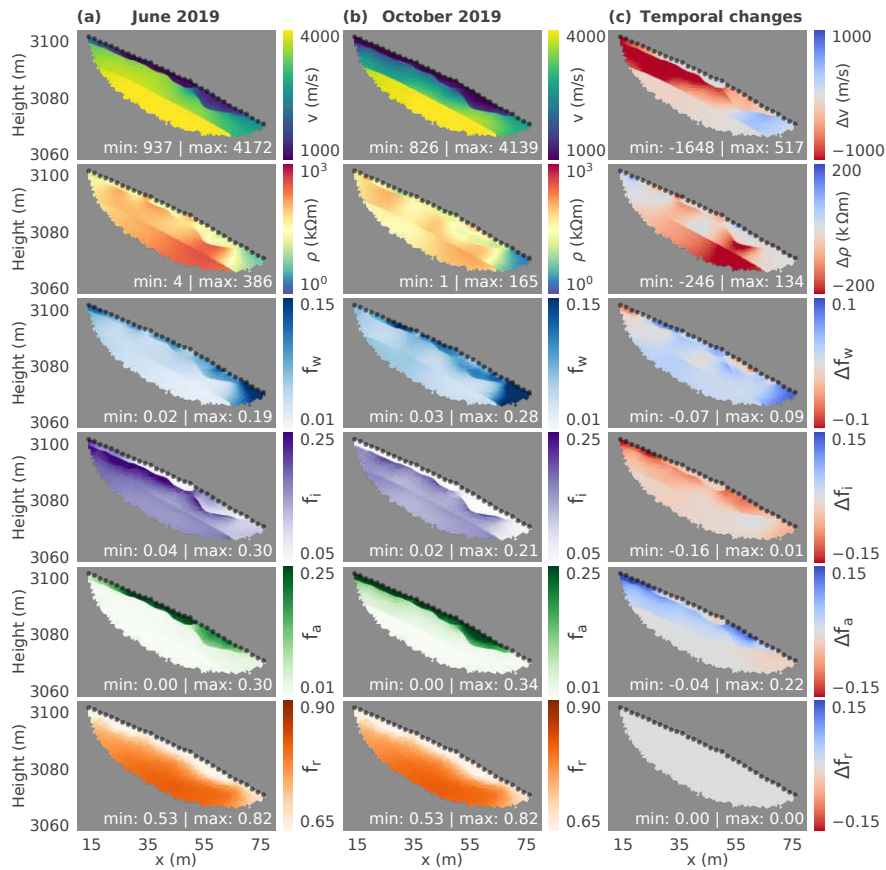


**Figure 4.8:** Subsurface models resolved through the structurally constrained PJI for the electric and seismic data sets collected in (a) June 2019 and (b) October 2019 and (c) the corresponding temporal changes. In the inversions, we prescribed the porosity model resolved for the October 2019 data set obtained through the unconstrained PJI. Black circles indicate the sensor/shot positions.

#### 4.4.3 Outlook

Further developments with regard to the PJI could address the incorporation of additional geophysical methods and monitoring data, both of which could potentially be added to the PJI framework in the form of a time-lapse joint inversion. In addition, it might be worth it to explore the possibility of imposing time-lapse petrophysical constraints on selected phases, e.g., temperature-dependent constraints on the ice content while the other phases remain unconstrained. Considering the expected system dynamics, the use of individual spatial and temporal regularization strategies for the different phases should be investigated. Such an approach would allow the PJI, e.g., to solve for large contrasts in one parameter and use a smoothness constraint for another one and, thus, might permit enhancement of the estimates for the constituents of the four-phase system in space and time.

Regarding long-term permafrost monitoring at Hoher Sonnblick, we propose to es-

establish a geophysical monitoring system collecting seismic and electric data on an annual basis. This would allow assessment of variations in the water and ice content, which in turn might provide a better understanding of the groundwater system in the summit area. To obtain information regarding the water, air, ice, and rock content for the entire summit area, we suggest conducting SRT, ERT, and GPR investigations along multiple profiles. Depending on the SRT measurement profiles. Depending on the SRT measurement scheme, such a data set would permit a quasi-3D or even real 3D PJI of ERT and SRT data in an alpine permafrost site.

### 4.5 Conclusion

In our study, we presented the application of a PJI scheme to solve for variations in subsurface water and ice contents and investigated the possibility of improving the quantitative reconstruction capabilities based on the incorporation of prior knowledge in the form of structural and porosity constraints.

The results of the synthetic study highlighted that the PJI might not solve for the true rock and ice content due to the similar physical properties of rock and ice. Instead, the stability of the PJI can be improved by incorporating structural or petrophysical constraints or a combination of both. Despite the substantial sensitivity of the estimates for the ice and rock content to inaccurate constraints, the values resolved through a constrained PJI still sufficiently approximate the true values and might even provide improved estimates compared to the independent inversion and to the unconstrained PJI.

For our study at the summit of Hoher Sonnblick, we demonstrated that the collection of time-lapse data sets allows for the evaluation and improvement of the consistency in the water, air, ice, and rock content models resolved through the PJI. In agreement with our numerical study, the prescription of a common porosity model in the PJI for the different time steps permitted overcoming the estimation of implausible ice and rock content in the case of a weak contrast in the physical properties of these two phases. Based on our results, we conclude that the joint inversion of collocated seismic and electrical data sets permitted us to extend our understanding about the subsurface conditions at the summit of Hoher Sonnblick and the accompanying seasonal changes.

# 5 | Quantitative water content estimation in landfills through joint inversion of seismic refraction and electrical resistivity data considering surface conduction<sup>1</sup>

## 5.1 Introduction

The disposal of municipal solid waste (MSW) in landfills refers to the prevalent method of waste management at the global scale (Laner et al., 2012). However, MSW landfills pose a threat to the environment as they are related to the release of pollutants for groundwater and soil citep[e.g.,][fellner2009, porowska2015, han2016, rezapour2018, stefania2019, and are responsible for approximately 5 % of the anthropogenic greenhouse gas emissions (Lou and Nair, 2009). Moreover, landfills located in populated areas pose a threat to human health considering the migration of landfill gases (LFG) into adjacent buildings as well as the risk for fires and explosions (e.g., Kjeldsen and Fischer, 1995; Frid et al., 2010).

The moisture content within MSW landfills is an important factor triggering methanogenic fermentation, and thus the production of methane (CH<sub>4</sub>, e.g., Barlaz et al., 1990; Gurijala and Suffita, 1993; Sanphoti et al., 2006). Therefore, the assessment and monitoring of the moisture or water content are crucial for an adequate MSW management, for instance to reduce LFG production. The combination of direct investigations, e.g., laboratory analysis of waste, gas and water samples, with indirect geophysical methods has proven to be a suitable approach for the characterization of landfills (e.g., De Carlo et al., 2013; Maurya et al., 2017; Soupios and Ntarlagiannis, 2017; Flores Orozco et al., 2020). In this regard, the geophysical investigations overcome the spatial limitations of direct methods as they provide information about the subsurface properties with high spatio-temporal resolution in a non-invasive manner (for a review see Nguyen et al., 2018). In particular, the electrical resistivity tomography (ERT) and the seismic refraction tomography (SRT) are routinely applied for landfill investigations and

<sup>1</sup>This chapter is based on: Steiner, M., T. Katona, J. Fellner, and A. Flores Orozco (2022). “Quantitative water content estimation in landfills through joint inversion of seismic refraction and electrical resistivity data considering surface conduction”. In: *Waste Management* 149, pp. 21–32. ISSN: 0956-053X. DOI: 10.1016/j.wasman.2022.05.020

provide complementary results as they map different physical properties (e.g., Nguyen et al., 2018; Kondracka et al., 2021).

The ERT is sensitive to spatial and temporal variations in the salinity, temperature and water content (Nguyen et al., 2018). Investigating the distribution of the electrical resistivity, or its inverse the electrical conductivity, is particularly useful to assess the production, migration and leakage of leachate due to the associated increase in salinity and fluid conductivity (e.g., Ogilvy et al., 2002; Clément et al., 2010; De Carlo et al., 2013; Bichet et al., 2016; Maurya et al., 2017). The MSW moisture content has been quantitatively assessed from electrical resistivity images through time-lapse investigations (e.g., Guérin et al., 2004) or petrophysical models (e.g., Grellier et al., 2007; Dumont et al., 2016; Feng et al., 2017; Hu et al., 2019; Aranda et al., 2021). Furthermore, the induced polarization (IP) method, an extension of the ERT, has emerged as a suitable technique to characterize the disposed waste and to delineate the landfill geometry (e.g., Leroux et al., 2007; Dahlin et al., 2010; Gazoty et al., 2012a; Gazoty et al., 2012b; Frid et al., 2017), and recently has been used to map biogeochemical active zones (Flores Orozco et al., 2020).

Seismic techniques have also been proposed for the investigation of the landfill geometry (e.g., Lanz et al., 1998; Dumont et al., 2017; Barone et al., 2021) and assessing the distribution of water or leachate (e.g., Soupios et al., 2007; Konstantaki et al., 2016). In particular, the seismic refraction tomography (SRT) can assess changes in the mechanical properties of the subsurface allowing for a refined characterization of the landfill geometry and the waste composition (Lanz et al., 1998; De Iaco et al., 2003; Kondracka et al., 2021). The contrast in the mechanical properties between the waste and the host materials is, however, weaker than in the electrical resistivity (Nguyen et al., 2018).

The joint application of geophysical methods sensitive to different physical properties, where the data sets are processed independently and then compared, has revealed an improved interpretation of the landfill characteristics (Soupios et al., 2007; Konstantaki et al., 2015; Dumont et al., 2017; Frid et al., 2017; Di Maio et al., 2018; Barone et al., 2021; Kondracka et al., 2021). However, the combination of results might be limited due to inconsistent models obtained through the independent inversions. Joint inversion schemes provide the means to overcome such limitation by simultaneously inverting multiple geophysical data sets (Linde and Doetsch, 2016), which are sensitive for common structural features (e.g., Haber and Oldenburg, 1997; Gallardo and Meju, 2003; Gallardo and Meju, 2004; Jordi et al., 2020) or a common petrophysical parameter, for instance porosity (e.g., Gao et al., 2012; Rucker et al., 2017). Structurally coupled joint inversion approaches have been used, for instance,

in landslide and slope stability investigations (Garofalo et al., 2015; Hellman et al., 2017), for aquifer characterization (Doetsch et al., 2010) and fracture zone detection (Ronczka et al., 2017) as well as time lapse investigations of embankments (Rittgers et al., 2016). Successful applications of petrophysical joint inversion approaches have been reported, e.g., for the exploration of natural resources (Kamm et al., 2015), in permafrost studies (Wagner et al., 2019) and related to geotechnical investigations (Carrier et al., 2022).

Petrophysical models linking water content and electrical resistivity often assume that the current conduction through the pore fluid dominates the observed response (e.g., Grellier et al., 2007; Hauck et al., 2011; Dumont et al., 2016; Feng et al., 2017; Hu et al., 2019; Aranda et al., 2021). This assumption is not valid for MSW landfills due to the high surface area and charge of the organic waste and the presence of clays (e.g., Castaldi et al., 2005; Flores Orozco et al., 2020). Numerous models have been developed to consider the effect of the surface conductivity on the electrical response (e.g., Slater and Lesmes, 2002a; Titov et al., 2002; Binley et al., 2005; Brovelli and Cassiani, 2011; Weller et al., 2013; Revil et al., 2015b; Revil et al., 2017c; Bucker et al., 2019a). However, to our knowledge the influence of the surface conductivity on the estimation of the water content in MSW landfills has not been addressed by previous studies.

Hence, we propose here the simultaneous inversion of seismic and electrical data to solve quantitatively for hydrogeological parameters relevant for the characterization of MSW landfills (see Figure 5.1). To achieve this, we use the joint inversion framework developed by Wagner et al. (2019), yet we modify the underlying petrophysical model to consider the effect of the surface conductivity during parameter estimation based on the formulations of the dynamic Stern layer model (DSL<sub>M</sub>) proposed by Revil et al. (2017c).

In the second section, we provide a description of our study area, review the principles of the seismic and electrical method and describe the acquisition and processing of the geophysical data. This is followed by a detailed presentation of the extended petrophysical joint inversion framework and its application to our field data. In the third section, we present our joint inversion imaging results and discuss the quantification of the water content as well as the delineation of the landfill geometry and the discrimination of different waste types. We provide an evaluation of the obtained results based on ground-truth information and imaging results resolved through independent investigations, followed by our conclusions.

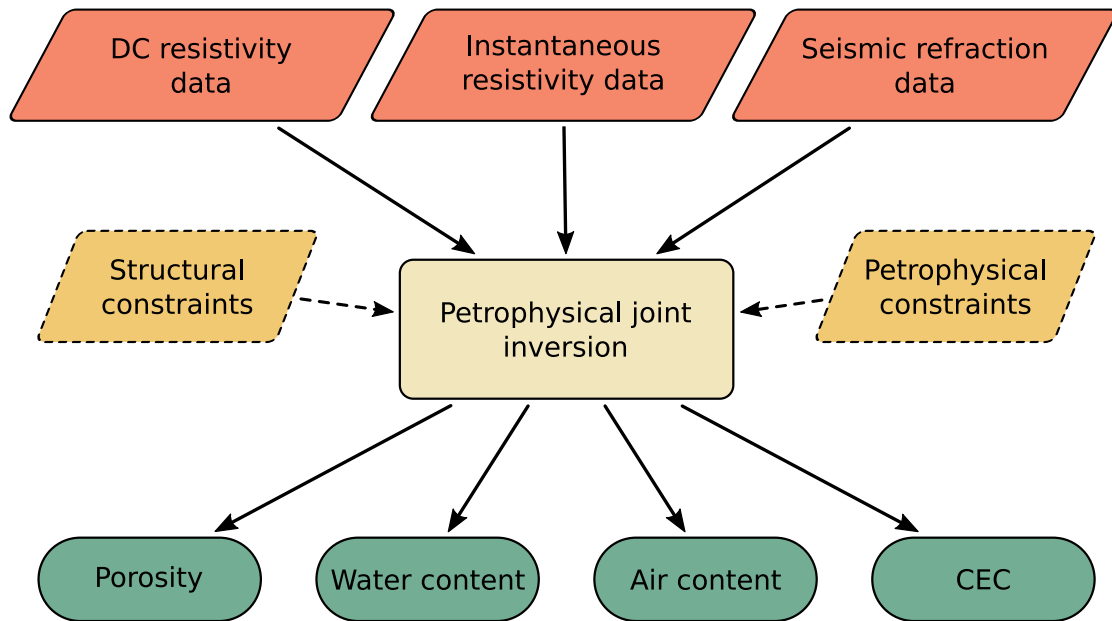


**Figure 5.1:** Schematic illustration of the estimation of hydrogeological parameters through the petrophysical joint inversion based on the dynamic Stern layer model using seismic refraction data, as well as low frequency (DC) and high frequency (instantaneous) resistivity data to take into account surface conductivity.

## 5.2 Materials and methods

### 5.2.1 Study area: The Heferlbach landfill (Vienna, Austria)

The Heferlbach landfill is located southwest of Vienna (Austria) and is formed by a cutoff meander of the Danube river that was backfilled with 219000 m<sup>3</sup> of waste between 1965 and 1973. This old deposit is about 950 m long, its width varies between 50 and 150 m and its bottom is found between 3.0 and 4.5 m depth. From a geological point of view, the landfill is located in the border area of the Danube lowlands and the Mannswörther Terrasse. The subsurface is characterized by a layer of quarternary gravels that form a potent aquifer atop of tertiary sands, referring to an aquiclude (Austrian Environmental Agency, 2005). The groundwater table is found much below the waste unit at approximately 10 m depth (Austrian Environmental Agency, 2005; Brandstätter et al. (2020)). The largest share of the disposed waste volume refers to municipal solid waste (MSW, 660 kg t<sup>-1</sup> moist mass) followed by excavated soil (180 kg t<sup>-1</sup> moist mass), and construction and demolition waste (CDW, 160 kg t<sup>-1</sup> moist mass).

The Heferlbach landfill lacks a bottom liner and leachate is not collected, yet in 2012 a low-pressure horizontal aeration system was installed, which allows for different



**Figure 5.2:** The study area at the Heferlbach landfill (Vienna, Austria). The landfill border is delineated by dashed lines, while dotted lines indicate the borders between the different landfill sections (1 to 8). The solid lines show the position and orientation of the geophysical profiles, with the direction of the measurements indicated by the filled triangles. The imposed circles indicate the position of waste samples collected for laboratory analysis, with the size of the symbols reflecting the variations in the total organic carbon (TOC).

aeration rates in eight landfill sections (see Figure 5.2) to accelerate the biodegradation of organic matter and to avoid landfill gas production (Fellner et al., 2015; Brandstätter et al., 2020). Laboratory analyses of solid waste samples collected at excavation points A7 to A13 provide information regarding relevant parameters such as water content or total organic carbon (TOC), which indicates changes in the biogeochemical activity (Figure 5.2). The variations in the methane production reported by Brandstätter et al. (2020) reveal heterogeneities within the landfill regarding water flow and storage, and can be associated with areas of increased methanogenesis (Flores Orozco et al., 2020). Further information can be found, e.g., in Brandstätter et al. (2013), Brandstätter et al. (2020) and Fellner et al. (2015).

### 5.2.2 Geophysical survey - Basic principles, experimental setup and data processing

The seismic refraction (SR) method uses elastic waves propagating through the subsurface to quantify changes in its seismic velocities, which can be interpreted in terms of lithology. Seismic waves are generated at well-defined shot points, commonly by an impulse source (e.g., hammer blows, weight drop, explosives), and the associated ground motion is registered by geophones deployed some distance away. In the recorded seismograms, the travel time  $t$  of the seismic wave is determined by the first onset of the seismic energy. Recording simultaneously with several geophones deployed at different offsets from the shot points allows for the computation of interface depths and layer velocities. In case of heterogeneous subsurface conditions or weaker contrasts in the mechanical properties of adjacent layers, the SRT is a more suitable method. Based on hundreds to thousands of shot-geophone pairs the SRT inverts the observed travel times  $\mathbf{t}$  to solve for a velocity model in an imaging framework.

The ERT relies on measurements with a four-electrode array, where current is injected through one electrode pair (current dipole) and the resulting voltages are measured with the second electrode pair (potential dipole). As an extension of the ERT, the frequency domain IP (FDIP) measures the impedance phase shift  $\varphi_{Z_e}$  between the injected alternating current ( $I^*$ ; given in A) and the observed voltage ( $U^*$ ; given in V), i.e., the complex electrical impedance  $Z_e^* = U^*/I^*$  (given in  $\Omega$ ). Conducting FDIP measurements at various frequencies (typically  $< 1$  kHz) is commonly referred to as spectral induced polarization (SIP). At such low frequencies the complex conductivity (CC) can be expressed as

$$\sigma^*(\omega) = \sigma'(\omega) + i\sigma''(\omega), \quad (5.1)$$

where  $i = \sqrt{-1}$  is the imaginary unit and  $\omega$  denotes the angular frequency. The real ( $\sigma'$ ) and the imaginary ( $\sigma''$ ) component of the CC refer to the conductive and capacitive (i.e., polarization) properties, respectively. Alternatively, we can express the CC in terms of its magnitude ( $|\sigma|$ ) and phase ( $\varphi$ )

$$\sigma^* = |\sigma| e^{i\varphi}. \quad (5.2)$$

$|\sigma|$  is also obtained through the ERT and for sufficiently small phase shifts ( $< 100$  mrad) we can assume that  $\sigma' = |\sigma|$ .

The CC is, in general, controlled by three main conduction mechanisms (Ward, 1988): (1) the matrix conduction ( $\sigma_m$ ) through the grains and minerals in the sub-

surface that can be neglected in case of a negligible amount of metals and electronic conductors; (2) electrolytic conduction ( $\sigma_f$ ) due to charge migration through the fluid-filled pores; (3) surface conduction ( $\sigma_s$ ) due to the accumulation (and polarization) of ions within the electrical double layer (EDL) formed at the interface between the grains and the pore fluid. The surface conduction dominates the electrical response in areas characterized by fine grains (e.g., clay or organic matter) due to their large surface area and high surface charge (Waxman and Smits, 1968; Revil and Glover, 1998; Slater and Lesmes, 2002b). Assuming a negligible amount of metallic minerals we can describe the CC after Lesmes and Frye (2001) as

$$\sigma^*(\omega) = [\sigma_f + \sigma'_s(\omega)] + i\sigma''_s(\omega) . \quad (5.3)$$

The real part of the CC is related to the conductive properties of the soil, and thus affects  $|\sigma|$  obtained from single-frequency ERT measurements. Hence, collecting  $|\sigma|$  at different frequencies provides information about the frequency dependence of the electrical properties. The imaginary part is due to the capacitive properties of the soil, i.e., the so-called induced polarization effect, that can be assessed through IP measurements.

In frame of this study, we conducted geophysical measurements along three profiles located in sections 2 and 3 of the Heferlbach landfill (see Figure 5.2). The vegetation on top of the landfill, as well as adjacent buildings and property boundaries influenced location, orientation and length of the profiles.

We collected seismic refraction data with the DMT Summit data acquisition system together with 24 vertical geophones (corner frequency 4.5 Hz) mounted on a land streamer. The separation between the geophones was 2 m and shots were conducted between the geophone positions. Along P1 and P2, we acquired the data through roll-along measurements with an overlap of 12 geophones, whereas along P3 a single layout was sufficient. We generated elastic waves by striking a plastic plate (3 cm thick) with a 7.5 kg sledgehammer. The measurements revealed distortions due to ground vibrations caused by people moving within the study area as well as ground-based and airborne traffic (motorway, railroad, airport). Hence, we stacked four hammer blows at each shot point to increase the signal-to-noise ratio. For the first break picking, we applied an 80 Hz low-pass filter on the recorded seismograms to attenuate the influence of high-frequency noise, and thus improve the visibility of the first onsets. We determined the first break travel times in an iterative process based on different gathers, i.e., common shot, receiver and offset.

We used the DAS-1 Electrical Impedance Tomography System from Multi-Phase

Technologies to collect electrical data at different frequencies. Our measurements were conducted using 64 stainless steel electrodes deployed with 1 m separation between them. Measurements along P1 and P3 refer to single layouts, whereas along P2 we conducted roll-along measurements with an overlap of 16 electrodes. We acquired data sets with two stacks for 14 frequencies ranging from 0.5 to 225 Hz by using dipole–dipole (DD) configurations, namely DD skip-0 (dipole length given by the electrode spacing) and DD skip-3 (dipole length defined as four times the electrode spacing). For DD skip-3, data were collected as normal and reciprocal readings, where reciprocal refers to the recollection of data with current and potential dipoles interchanged for each quadrupole (Binley et al., 1995). Our measurement sequence performed voltage readings always ahead of the current dipole to avoid measurements with electrodes previously used for current injections, thus ensuring that the data are not contaminated due to the polarization of the electrodes themselves (Flores Orozco et al., 2020).

The high electrical conductivity in the clay-rich top layer of the Heferlbach landfill reduces the amount of current effectively delivered to deeper areas. Since the landfill has a maximum thickness of 6 m (e.g., Flores Orozco et al., 2020; Barone et al., 2021) our measurements aimed at a maximum depth of investigation of approximately 8 m, which is possible using the measurement configuration described above. Anthropogenic structures such as buried metallic infrastructure affect the electrical measurements (see Flores Orozco et al., 2019); yet, the electrical data collected in frame of this study does not reveal such distortions. Each data set was filtered by removing erroneous readings associated with negative impedance magnitudes or zero current injection, as well as poor reciprocity (Flores Orozco et al., 2012b; Flores Orozco et al., 2018b). For data sets collected at frequencies above 25 Hz we encountered a poor reciprocity in the data likely due to inductive coupling or cross-talking within the multi-core cables used for the data collection (Flores Orozco et al., 2021). Accordingly, we consider electrical data sets collected at 0.5 and 25.0 Hz as the DC and instantaneous data, respectively, and use them as input data in the joint inversion.

### 5.2.3 Quantitative estimation of subsurface properties through petrophysical joint inversion

The proposed petrophysical model assumes the soil respectively the landfill material to be composed of three phases (e.g., Powrie, 2018): a solid (e.g., soil grains, rock, waste), a fluid (e.g., the pore water), and a gas (e.g., the pore air). Accordingly, we describe the relationship between these three phases as

$$f_r + f_w + f_a = 1, \tag{5.4}$$

with the volumetric rock content  $f_r$ , the volumetric water content  $f_w$  and the volumetric air content  $f_a$ . We describe the seismic slowness  $s$  of this three-phase soil system through a modification of the time-averaging Timur (1968) equation that sums up the seismic velocities of the three phases weighted by the respective volumetric fraction (after Hauck et al., 2011)

$$s = \frac{1}{v} = \frac{f_w}{v_w} + \frac{f_a}{v_a} + \frac{f_r}{v_r}. \quad (5.5)$$

Waxman and Smits (1968) proposed a mixing law to describe the electrical conductivity as (after Glover, 2010)

$$\sigma = a\sigma_w (1 - f_r)^m \left( \frac{f_w}{1 - f_r} \right)^n + \sigma_s. \quad (5.6)$$

The first term in Equation 5.6 corresponds to Archie's second law (Archie, 1942), with  $a$ ,  $m$  and  $n$  referring to the tortuosity, the cementation and the saturation exponent, respectively; whereas,  $\sigma_w$  (in  $\text{S m}^{-1}$ ) corresponds to the conductivity of the fluid filling the pore space. The second term,  $\sigma_s$  (in  $\text{S m}^{-1}$ ), denotes the surface conductivity that controls the observed electrical conductivity in presence of grains with a high surface area and charge.

Considering the frequency dependence of  $\sigma_s$  (e.g., Lesmes and Frye, 2001), we can assess the effect of the surface conductivity based on data sets collected at a low and a high frequency (e.g., Marshall and Madden, 1959; Zonge et al., 1972; Lesmes and Frye, 2001). To include this approach in our petrophysical model, we consider the system of equations defined by the DSLM (Revil, 2013a; Revil, 2013b; Revil et al., 2017c). The DSLM provides formulations for the instantaneous conductivity  $\sigma_\infty$  (in  $\text{S m}^{-1}$ , high frequency) and the DC conductivity  $\sigma_0$  (in  $\text{S m}^{-1}$ , low frequency). We can write these equations as (e.g., Tartrat et al., 2019):

$$\sigma_\infty = \left( \frac{f_w}{1 - f_r} \right)^n (1 - f_r)^m \sigma_w + \left( \frac{f_w}{1 - f_r} \right)^{n-1} (1 - f_r)^{m-1} \delta_g B C E C \quad (5.7)$$

$$\sigma_0 = \left( \frac{f_w}{1 - f_r} \right)^n (1 - f_r)^m \sigma_w + \left( \frac{f_w}{1 - f_r} \right)^{n-1} (1 - f_r)^{m-1} \delta_g (B - \Lambda) C E C \quad (5.8)$$

## 5 Water content quantification considering surface conduction

In Equations 5.7 and 5.8, the first term refers to the fluid conductivity, whereas the second term corresponds to the surface conductivity. In the second term,  $\delta_g$  denotes the grain density (in  $\text{kg m}^{-3}$ ),  $B$  the apparent mobility of the counterions for the surface conduction (in  $\text{m}^{-2} \text{s}^{-1} \text{V}^{-1}$ ),  $\Lambda$  the apparent mobility of the counterions for the polarization (in  $\text{m}^{-2} \text{s}^{-1} \text{V}^{-1}$ ), and  $CEC$  the cation exchange capacity (in  $\text{C kg s}^{-1}$ ), as mentioned in Revil et al. (2020). The  $CEC$  is a function of surface area and surface charge, and thus is related to the textural properties of the soil, the chemical composition of the materials and the pore water. Due to the large surface area of negatively charged fine grains, the  $CEC$  is an important parameter in the DSLM related to the effect of the surface conductivity. The  $CEC$  is proportional to the normalized chargeability  $M_n$ , which describes the polarization of subsurface materials (e.g., Vinegar and Waxman, 1984; Slater and Lesmes, 2002b; Mao et al., 2016) and is defined by Revil et al. (2015a) as:

$$M_n \equiv \sigma_\infty - \sigma_0. \quad (5.9)$$

By substituting Equations 5.7 and 5.8 in Equation 5.9 we obtain

$$M_n = (1 - f_r)^{m-n} f_w^{n-1} \delta_g \Lambda CEC, \quad (5.10)$$

which can be rearranged to solve for the  $CEC$ :

$$CEC = (1 - f_r)^{n-m} \frac{M_n}{f_w^{n-1} \delta_g \Lambda}. \quad (5.11)$$

Following Revil et al. (2020) we combine Equations 5.7 and 5.10 to solve for the volumetric water content  $f_w$  as

$$f_w = \left[ \frac{1}{\sigma_w} (1 - f_r)^{n-m} \left( \sigma_\infty - \frac{M_n}{R} \right) \right]^{1/n} \quad (5.12)$$

where  $R$  refers to a dimensionless number reported as  $R = \Lambda/B \approx 0.10 \pm 0.02$  (Revil et al., 2017b; Revil et al., 2017a; Revil et al., 2017c). In a similar way, we solve for the subsurface air content as

$$f_a = v_a \left[ \frac{1}{v} - \frac{f_r}{v_r} - \frac{f_w(\sigma_0, \sigma_\infty)}{v_w} \right], \quad (5.13)$$

and obtain the rock content by rearranging Equation 5.4 as

$$f_r = 1 - f_w - f_a. \quad (5.14)$$

Eventually, we can compute the porosity as

$$\Phi = 1 - f_r = 1 - (f_w + f_a). \quad (5.15)$$

For the implementation of the petrophysical model described above (Equations 5.4 to 5.15), we extend the joint inversion framework developed by Wagner et al. (2019), which is built on the forward modeling capabilities provided by pyGIMLi (Rücker et al., 2017). As illustrated in Figure 5.1, the proposed joint inversion scheme uses seismic refraction as well as DC and instantaneous electrical resistivity data to quantify porosity, water content, air content and *CEC*. In this way, we solve for a model that simultaneously explains three different data sets, and thus reduce the uncertainty associated with the inversion of geophysical data. Moreover, we can compute the polarization response in terms of the normalized chargeability  $M_n$  based on the resolved DC and instantaneous resistivity models (see Equation 5.9). The incorporation of structural or petrophysical constraints (Steiner et al., 2021) is not considered in this study. For further information regarding the petrophysical joint inversion, we refer to the supplementary material.

The application of the proposed joint inversion scheme requires the proper parameterization of the underlying petrophysical model. For the fitting parameters  $a$ ,  $m$  and  $n$  presented in Table 5.1 we chose values from available literature (e.g., Glover, 2015). Liu et al. (2020) found that the pore space in MSW becomes disconnected in case of microbial activity as observed at the Heferlbach landfill by Flores Orozco et al. (2020). Accordingly, we selected the cementation exponent  $m = 2$  similar to, e.g., Grellier et al. (2006). The fluid conductivity  $\sigma_w$  was selected according to available information for the Heferlbach landfill. Regarding the parameters related to the surface conductivity ( $B$ ,  $\Lambda$ ,  $\delta_g$ ), we use the values reported in Revil et al. (2020). The seismic velocity for rock ( $v_r$ ), water ( $v_w$ ) and air ( $v_a$ ) can be taken from literature (e.g., Kearey et al., 2002), yet  $v_r$  needs to be chosen with respect to the local geology.

In Table 5.1, we also present values for the regularization and smoothing parameters ( $\alpha$ ,  $\beta$ ,  $z_{Weight}$ ) and data error models, as well as the corresponding convergence values ( $\chi^2$ ) for the three profiles discussed here. We determined the values for the regularization parameters  $\alpha$  and  $\beta$  by investigating different parameter settings aiming at a  $\chi^2$  close to 1.0; thus indicating that the joint inversion converges, i.e, the resolved models can explain the collected data. The parameter  $z_{Weight}$  describes the ratio between vertical and horizontal smoothing, where  $z_{Weight} = 1$  refers to anisotropic smoothing. We chose a ten times stronger horizontal smoothing ( $z_{Weight} = 0.1$ ) to favor the delineation of the horizontal layering in the subsurface reported by previous studies (Brandstätter

**Table 5.1:** Petrophysical parameters, data error models and inversion parameters used for the joint inversion of seismic and electrical data sets collected along profiles P1, P2 and P3. The corresponding fit between the measured and modeled seismic and electrical data is expressed in terms of the error-weighted  $\chi^2$ .

Petrophysical parameters			Inversion parameters					
<b>Electrolytic conductivity</b>	$a$	1	<b>P1</b>	<b>Error model</b>	<b>Regularization</b>	<b>Data fit</b>		
	$m$	2.5		$\rho_0$	4%	$\alpha$	500	$\chi^2$ 1.40
	$n$	1.5		$\rho_\infty$	8%	$\beta$	$1 \times 10^4$	
	$\sigma_w$	$0.2 \text{ S m}^{-1}$		$t$	4.0 ms	$z_{Weight}$	0.01	
<b>Surface conductivity</b>	B	$3.1 \times 10^{-9} \text{ m}^{-2} \text{ s}^{-1} \text{ V}^{-1}$	<b>P2</b>	$\rho_0$	6%	$\alpha$	500	$\chi^2$ 1.79
	$\Lambda$	$3.0 \times 10^{-10} \text{ m}^{-2} \text{ s}^{-1} \text{ V}^{-1}$		$\rho_\infty$	6%	$\beta$	$1 \times 10^4$	
	$\delta_g$	$1500 \text{ kg m}^{-3}$		$t$	4.5 ms	$z_{Weight}$	0.01	
<b>Seismic velocity</b>	$v_w$	$1450 \text{ m s}^{-1}$	<b>P3</b>	$\rho_0$	5%	$\alpha$	500	$\chi^2$ 1.71
	$v_a$	$330 \text{ m s}^{-1}$		$\rho_\infty$	8%	$\beta$	$1 \times 10^4$	
	$v_r$	$2000 \text{ m s}^{-1}$		$t$	5.0 ms	$z_{Weight}$	0.01	

et al., 2013; Flores Orozco et al., 2020).

To facilitate the interpretability of the obtained models we present the resolved air content in terms of the air saturation  $S_a = f_a/\Phi$ . The water content reported for the waste samples was computed as

$$WC_{samp} = \frac{m_w}{m_s + m_w}, \quad (5.16)$$

where  $m_w$  and  $m_r$  denote the mass of the water and the solids, respectively. Accordingly, we compute the water content from the resolved hydrogeological models as

$$WC = \frac{f_w \delta_w}{f_r \delta_s + f_w \delta_s}, \quad (5.17)$$

with  $\delta_w = 997 \text{ kg m}^{-3}$  for the density of the water and  $\delta_s = 1200 \text{ kg m}^{-3}$  for the density of the solids.

To validate the  $M_n$  models resolved through our joint inversion approach, we conduct independent inversions of the IP data collected during our survey. In particular, we invert the electrical impedance data (magnitude and phase) with CRTomo (Kemna et al., 2000), a complex-valued inversion algorithm that simultaneously solves for the magnitude and phase of the CC. As demonstrated by Flores Orozco et al. (2020), the imaginary component ( $\sigma''$ ) of the resolved CC is a reliable measure for the polarization effect associated with MSW.

## 5.3 Geophysical and hydrogeological characterization of the Heferlbach landfill

### 5.3.1 Longitudinal section through the landfill

Figure 5.3 summarizes the joint inversion imaging results for data collected along P2 extending from landfill section 2 to 3. The seismic image resolves a layer characterized by low seismic velocities to a depth of approximately 4 to 5 m corresponding to the landfill body. Within this layer, we observe lateral changes, with seismic velocities around  $500 \text{ m s}^{-1}$  found in the first 50 m along profile direction, whereas the seismic velocities increase to approximately  $750 \text{ m s}^{-1}$  in the eastern part of the profile. At the expected contact to the natural soils (gravel and sands, with a varying content of clay), the seismic image delineates a relatively sharp contrast to higher seismic velocities ( $v_p > 1000 \text{ m s}^{-1}$ ).

In the electrical images ( $\rho_0$ ,  $\rho_\infty$ ) we can delineate, in general, three main layers. A shallow layer characterized by a moderate to high electrical resistivity ( $\rho > 50 \text{ m}$ ) corresponding to the top soil and waste unit with a thickness varying between 0.5 and 1.5 m. The intermediate layer shows the lowest electrical resistivity ( $\rho < 20 \text{ m}$ ) related to the MSW found at depths between 1.5 and 5.0 m. Below this unit, we find high electrical resistivity values ( $\rho > 100 \text{ m}$ ) corresponding to the geological media. Similarly, we can delineate three subsurface layers based on the polarization effect expressed in terms of the normalized chargeability  $M_n$ . The shallowest layer, characterized by low to moderate  $M_n$  values ( $1 \times 10^{-3} \leq M_n < 2 \text{ mS m}^{-1}$ ), corresponds to the top soil (unsaturated sand and silty soils) on top of a shallow waste unit formed by excavated soils. We interpret the considerable variations in the thickness of this layer (approximately 0.5 to 1.0 m) as changes in the excavated soil unit and the silt content. The highest  $M_n$  values ( $M_n > 5 \text{ mS m}^{-1}$ ) are observed in the intermediate layer corresponding to the MSW deposited at varying depth with an average thickness of 2 m (consistent to Flores Orozco et al., 2020). Beneath the MSW unit, the  $M_n$  image resolves a sharp contrast to substantially lower values ( $M_n \approx 1 \times 10^{-3} \text{ mS m}^{-1}$ ) at depths between 4 and 5 m, corresponding to the landfill base as confirmed by observations during the excavations at sampling points A9, A10 and A11 (indicated in Figure 5.3).

The different sensitivity of  $\rho$  and  $M_n$  to the contact between the MSW and the geological host formation is in agreement with previous studies, which report a more accurate delineation of the landfill geometry based on IP images (Leroux et al., 2007; Dahlin et al., 2010; Gazoty et al., 2012b; Flores Orozco et al., 2020). The low resistivity

values resolved below the MSW unit indicate an increased fluid conductivity due to the leakage of leachates since substantially higher values would be expected in presence of gravels and coarse sands (see Clément et al., 2010; Flores Orozco et al., 2020).

Our joint inversion scheme solves for a gradual increase in porosity with depth, where high values ( $40\% \leq \Phi < 60\%$ ) are found within the landfill body and low values ( $\Phi < 40\%$ ) correspond to the natural soils beneath the landfill. However, the porosity model lacks a sharp contrast at the expected contact between the MSW and the host materials. In contrast, the air saturation model shows a substantial contrast between the MSW ( $S_a \approx 50\%$ ) and the natural soils beneath the landfill ( $S_a < 30\%$ ). The resolved interface is in agreement with the depth of the landfill base as observed at the excavation points.

Along P2, the water content shows substantial variations within the landfill body. Particularly low values ( $WC < 10\%$ ) correspond to unsaturated top soils, whereas a  $WC$  of approximately 25% was found for the MSW. A further increase in the water content ( $WC > 30\%$ ) is observed at the bottom of the landfill and the host rock below it likely related to the lack of a bottom liner, which favors leachate migration due to gravitational forces. From the resolved  $CEC$  model we can identify three main units with the highest values ( $CEC > 100 \text{ meq}/100 \text{ g}$ ) observed in the second layer corresponding to the MSW. Low  $CEC$  values ( $< 5 \text{ meq}/100 \text{ g}$ ) are found in the top soil layer, as well as in the host rocks beneath the landfill. The low  $CEC$  values in the gravels and sands forming the natural soil are consistent with literature values for such materials (e.g., Carroll, 1959).

### 5.3.2 Cross section through a MSW unit

In Figure 5.4, we present the imaging results obtained for data collected along P3 located within landfill section 3.

The seismic image resolves a layer with varying thickness (approximately 3 to 5 m) characterized by low seismic velocities ( $v_p < 750 \text{ m s}^{-1}$ ). Beneath this layer, the sharp increase to seismic velocities higher than  $1000 \text{ m s}^{-1}$  corresponds to the expected contact to the natural soils. The electrical resistivity images are dominated by a low resistivity anomaly ( $\rho < 10 \text{ m}$ ) extending from 1 to 5 m depth and 10 to 25 m along profile direction. In the same area we observe a strong polarization response ( $M_n > 10 \text{ mS m}^{-1}$ ), which would be expected due to electrode polarization mechanisms in the presence of metals (e.g., Pelton et al., 1978; Wong, 1979; Revil et al., 2015b; Bucker et al., 2018). However, a negligible iron content was found in the excavated solid waste samples, and thus the high  $M_n$  suggests that the surface conductivity

### 5.3 Geophysical and hydrogeological characterization of the Heferlbach landfill

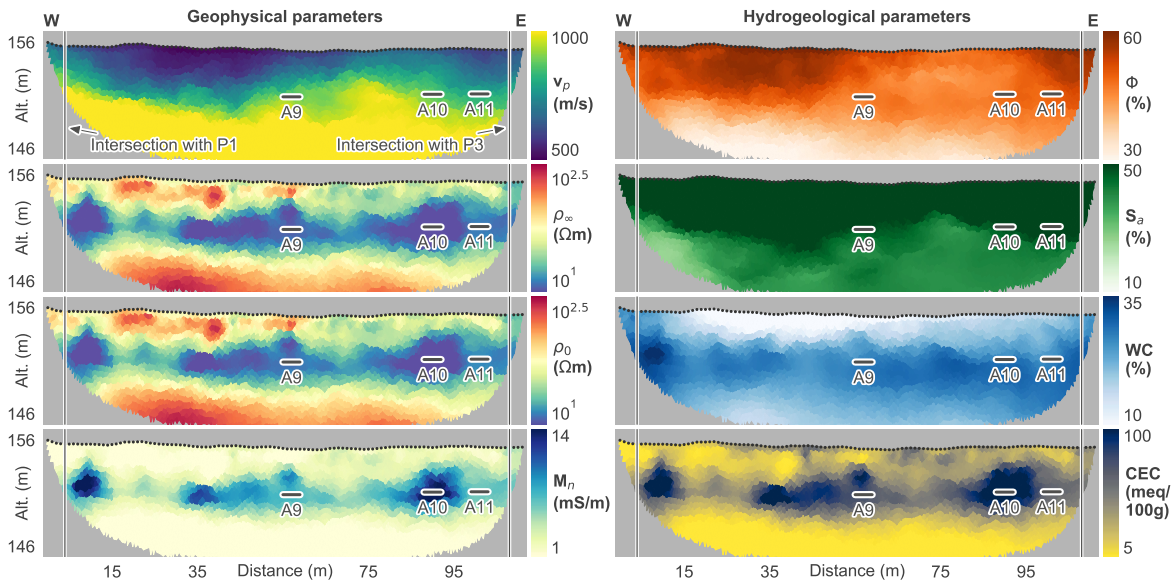


**Figure 5.3:** Joint inversion imaging results for data collected along P2 expressed in terms of seismic velocity ( $v_p$ ), electrical resistivity ( $\rho_0$ ,  $\rho_\infty$ ) and normalized chargeability ( $M_n$ ), as well as porosity ( $\Phi$ ), air saturation ( $S_a$ ), water content ( $WC$ ) and cation exchange capacity ( $CEC$ ). The black dots along the surface of each model represent the sensor/shot positions. Horizontal lines at the position of sampling points A9, A10 and A11 indicate the bottom of the landfill as observed during excavations for the collection of waste samples.

dominates the observed electrical response by controlling both the conductivity ( $\sigma'$ ) and the polarization ( $\sigma''$ ). Accordingly, we relate this strong polarization response to organic waste, grains with a high surface charge and interactions between these grains and the organic matter (Ponziani et al., 2012; Schwartz and Furman, 2014; Katona et al., 2021). Such interpretation is sustained by the high  $CEC$  (more than 100 meq/100 g) resolved in this part of the landfill.

Along P2, the porosity model shows high values ( $40\% \leq \Phi < 60\%$ ) within the MSW and  $\Phi < 40\%$  for the natural soils. Additionally, we observe a low porosity anomaly ( $\Phi \ll 30\%$ ) in the near-surface, which extends along the last 15 m of P3. In the geophysical images, the anomaly is characterized by high seismic velocity ( $v_p \gg 1000 \text{ m s}^{-1}$ ) and electrical resistivity ( $\rho > 300 \text{ m}$ ) values. The location of this anomaly corresponds to the intersection of P3 with the flood dam, which forms the northern boundary of the landfill, and thus we relate it to the compacted materials of the dam. The joint inversion scheme solves for a high air saturation ( $S_a \approx 50\%$ ) within the waste body, whereas the air saturation of the natural soils beneath the landfill is substantially lower ( $S_a < 20\%$ ). The resolved contrast in the air saturation between these two units corresponds to the base of landfill as observed at excavation points A11 to A13.

## 5 Water content quantification considering surface conduction

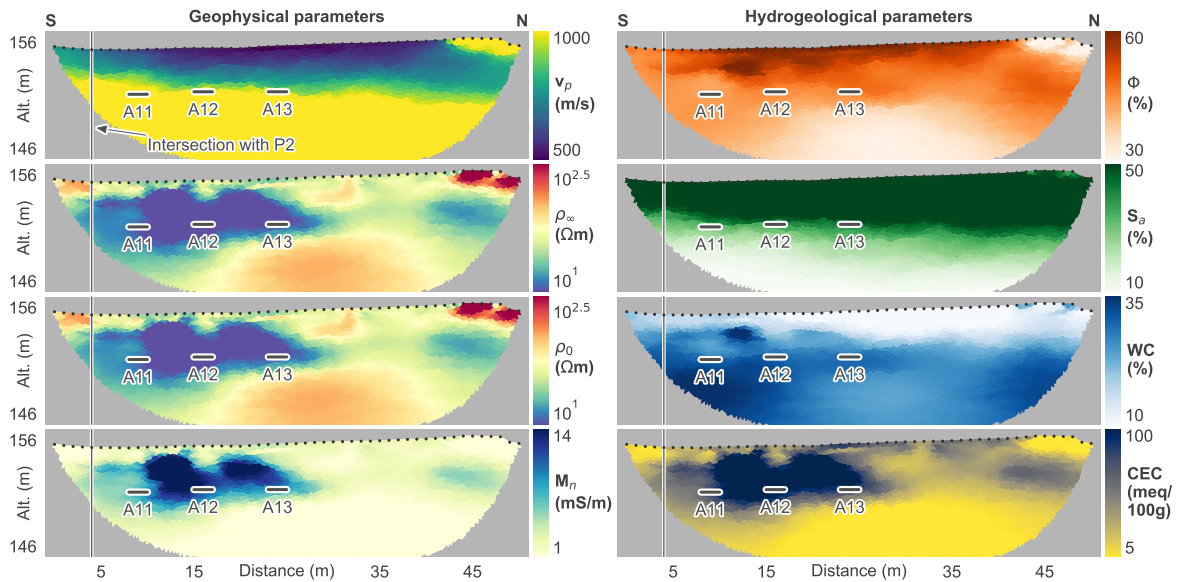


**Figure 5.4:** Joint inversion imaging results for data collected along P3 expressed in terms of seismic velocity ( $v_p$ ), electrical resistivity ( $\rho_0$ ,  $\rho_\infty$ ) and normalized chargeability ( $M_n$ ), as well as porosity ( $\Phi$ ), air saturation ( $S_a$ ), water content ( $WC$ ) and cation exchange capacity ( $CEC$ ). The black dots along the surface of each model represent the sensor/shot positions. Horizontal lines at the position of sampling points A11, A12 and A13 indicate the bottom of the landfill as observed during excavations for the collection of waste samples.

Within the landfill body, the images resolve substantial variations in the water content. In the first 30 m along profile direction, the WC is approximately 25 % with an anomaly located between excavation points A11 and A12 that is characterized by an increased water content of more than 35 %. At this location we also observe a high polarization response ( $M_n > 10 \text{ mS m}^{-1}$ ), suggesting an increased microbial activity (Flores Orozco et al., 2020), which has been argued to be related to the methanogenic fermentation of waste facilitated by an increased water content (e.g., Barlaz et al., 1990). This interpretation is sustained by the methane production and the high TOC content observed in this landfill section (c.f. Figure 5.2 and Brandstätter et al., 2020). The reduced water content in the northern part of the profile ( $WC \approx 10\%$ ) indicates the presence of unsaturated top soils or CDW; thus, also related to negligible methanogenesis.

### 5.3.3 Cross section through a CDW unit

In Figure 5.5, we present imaging results obtained for data collected along P1 located within landfill section 2 where solely CDW was found.

The seismic model shows low seismic velocities ( $v_p < 750 \text{ m s}^{-1}$ ) down to depths of

approximately 4 m corresponding to the landfill body. Within this unit, the lateral variations in the seismic velocity are less pronounced than along P2 and P3. Beneath the landfill body, an increase in the seismic velocity ( $v_p > 1000 \text{ m s}^{-1}$ ) indicates the transition to the natural soils. The electrical resistivity images show a high resistivity anomaly ( $\rho > 300 \text{ m}$ ) extending between ca. 0.5 and 4.0 m depth from 15 to 45 m along profile direction, which we relate to the disposed CDW (consistent to the response observed by Flores Orozco et al., 2020). The polarization effect of the CDW ( $M_n < 1 \text{ mS m}^{-1}$ ) is substantially lower than for the MSW found along P2 and P3 ( $M_n > 5 \text{ mS m}^{-1}$ ).

In the porosity model, the CDW is characterized by low values ( $30 \% \leq \Phi < 40 \%$ ), whereas the surrounding materials have a higher porosity ( $40 \% \leq \Phi < 50 \%$ ). Similar to P2 and P3, the joint inversion scheme solves for a high air saturation within the landfill ( $S_a > 50 \%$ ) and considerably lower values beneath it ( $S_a < 20 \%$ ). The interface between the landfill and the natural soils is in agreement with direct observations during excavations at sampling points A7 and A8. The low water content ( $WC < 20 \%$ ) and the low *CEC* (below 5 meq/100 g) resolved for the CDW unit suggest a negligible microbial activity (i.e., methanogenesis), as evidenced by the low TOC observed in the leachate of the solid waste samples ( $\text{TOC} < 950 \text{ mg kg}^{-1}$ ).

#### 5.3.4 Independent verification based on the observed polarization response

Our results demonstrate that the models obtained through the proposed joint inversion scheme are consistent for data collected along different profiles and in agreement with previous studies. While our joint inversion scheme primarily aims at the quantitative estimation of the water content it also solves for the polarization ( $M_n$ ) in the subsurface, which is a suitable parameter for the characterization of landfill geometry (e.g., Leroux et al., 2007; Ustra et al., 2012; Gazoty et al., 2012a) and microbial activity (Flores Orozco et al., 2020). In Figure 5.6, we compare the  $M_n$  with the imaginary component  $\sigma''$  of the CC resolved with CRTomo to allow for the evaluation of our joint inversion approach.

We observe a relatively high  $M_n$  in areas characterized by MSW ( $M_n > 5 \text{ mS m}^{-1}$ ), whereas the  $M_n$  is negligible for CDW ( $M_n < 1 \text{ mS m}^{-1}$ ). Strong contrasts in the  $M_n$  images are resolved at the contact between the waste unit and the natural soils. Hence, our results demonstrate that the  $M_n$  obtained through the proposed joint inversion approach is sensitive to landfill geometry and waste composition similar to IP surveys reported in previous studies (Leroux et al., 2007; Dahlin et al., 2010;

## 5 Water content quantification considering surface conduction

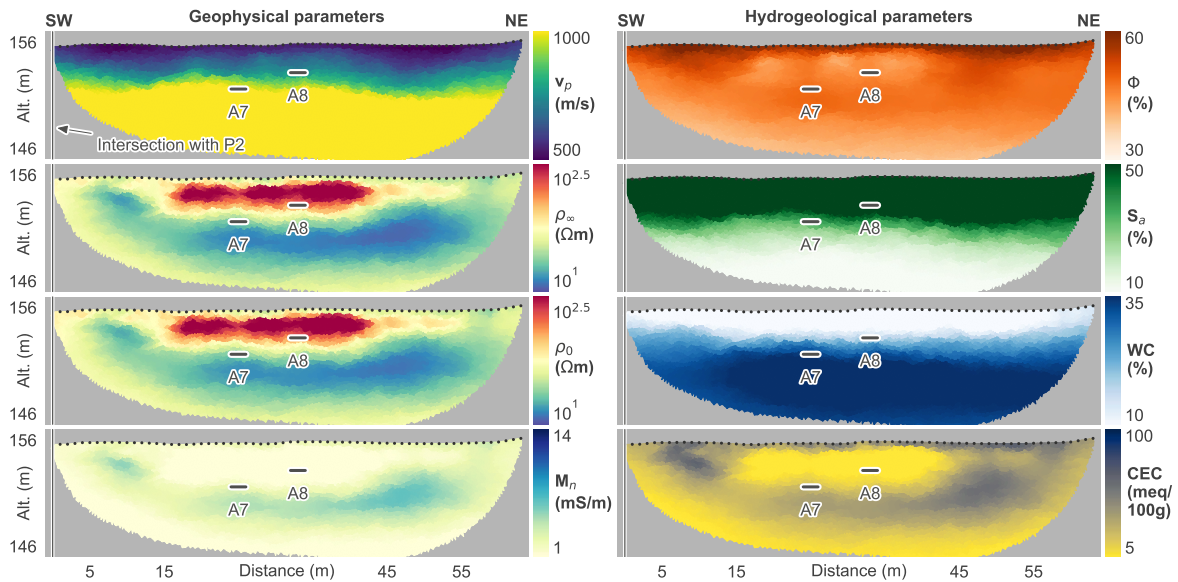


**Figure 5.5:** Joint inversion imaging results for data collected along P1 expressed in terms of seismic velocity ( $v_p$ ), electrical resistivity ( $\rho_0$ ,  $\rho_\infty$ ) and normalized chargeability ( $M_n$ ), as well as porosity ( $\Phi$ ), air saturation ( $S_a$ ), water content ( $WC$ ) and cation exchange capacity ( $CEC$ ). The black dots along the surface of each model represent the sensor/shot positions. Horizontal lines at the position of sampling points A7 and A8 indicate the bottom of the landfill as observed during excavations for the collection of waste samples.

Gazoty et al., 2012a; Gazoty et al., 2012b; Ustra et al., 2012; Flores Orozco et al., 2020). Moreover, the polarization images ( $M_n$  and  $\sigma''$ ) presented in Figure 5.6 reveal that our joint inversion scheme and the CCI qualitatively solve for similar polarization images. The observed quantitative differences in  $M_n$  and  $\sigma''$  are due to the different inversion approaches.

CRTomo independently inverts the impedance magnitude and phase data sets collected at 0.5 and 25.0 Hz to solve directly for the CC. In contrast, the joint inversion inverts only the impedance magnitude data (i.e., resistance readings), yet simultaneously for a low and a high frequency together with the seismic travel times. In case of the proposed joint inversion approach the polarization response is computed from the resolved DC and instantaneous electrical resistivity images ( $\rho_0$ ,  $\rho_\infty$ ). Accordingly, the IP provides imaging results for data collected at two separated frequencies and the Mn approach is rather an equivalent to the frequency effect, i.e., the change in the electrical responses observed at a low and a high frequency (e.g., Marshall and Madden, 1959; Zonge et al., 1972; Lesmes and Frye, 2001). Considering the possibility to easily adopt the joint inversion framework, the estimation of the polarization response could be further improved by including different mechanistic (Bücker et al., 2018; Bücker et al., 2019b; Bücker et al., 2019a) or experimental polarization models

(Binley et al., 2005; Weller et al., 2013).

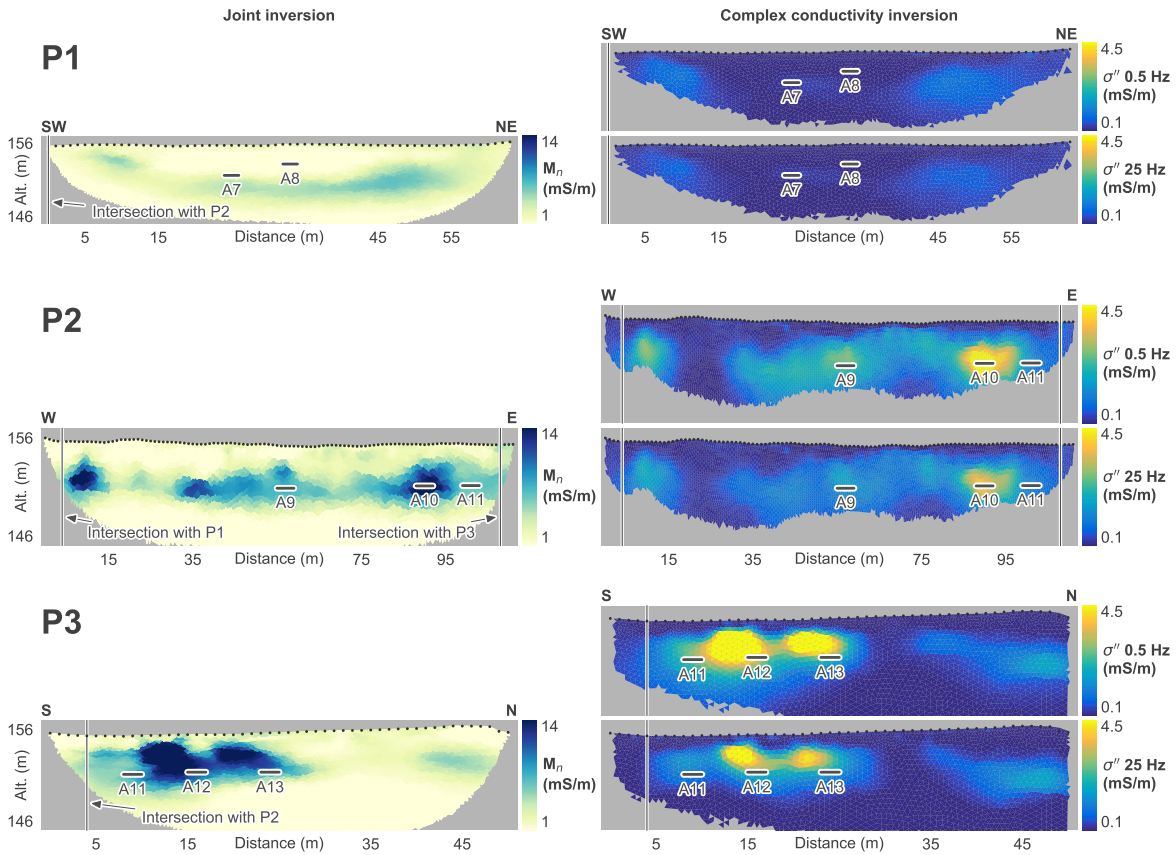


**Figure 5.6:** Capacitive properties of the subsurface expressed by the normalized chargeability  $M_n$  and the imaginary part of the complex conductivity  $\sigma''$  resolved from electrical data collected at 0.5 and 25.0 Hz through the proposed joint inversion approach and a complex conductivity inversion, respectively. The black dots along the surface of each model represent the sensor/shot positions. Horizontal lines at the position of sampling points A7 to A13 indicate the bottom of the landfill as observed during excavations for the collection of waste samples.

Nonetheless, our approach provides comparable results to IP surveys allowing for the mapping of polarizable areas in the subsurface, which can be used to delineate the landfill geometry as well as biogeochemically active zones. While a high polarization response has been linked to high concentrations of organic carbon (i.e., TOC) and materials with high surface charge (e.g., Ponziani et al., 2012; Flores Orozco et al., 2020; Katona et al., 2021), the models obtained through our joint inversion approach show that the high polarization anomalies correspond to areas characterized by a high water content (see Figures 5.3 to 5.5). Accordingly, we argue that the presence of carbon sources, water and anoxic conditions enhance the methanogenic fermentation of MSW, as evidenced by the methane generation observed at the Heferlbach landfill.

### 5.3.5 Evaluation of the resolved water content

The imaging results presented in Figures 5.3 to 5.5 illustrate the applicability of the proposed joint inversion scheme to solve quantitatively for hydrogeological parameters relevant in landfill investigations. For the Heferlbach landfill,  $WC$  models are of particular interest as they permit the identification of potential areas for methane production. To allow for a quantitative evaluation, Figure 5.7 shows the  $WC$  measured in the solid waste samples taken at sampling points A7 to A13 versus the  $WC$  estimated through the proposed joint inversion approach (a tabular overview of the data can be found in the supplementary material of this manuscript). We can see that the joint inversion performs well as it is able to resolve the  $WC$  in the same order and only a few estimates are flagged as outliers. However, the corresponding median percentage error suggest only limited reconstruction capabilities of our approach regarding the  $WC$ . As shown in Figure 5.2, most sampling points are situated some distance away from the geophysical profiles, with only A8 and A12 being located directly along a profile (largest symbols in Figure 5.7). Hence, we can relate larger deviations between measured and estimated  $WC$  in the near-surface ( $< 2$  m) to the heterogeneous composition of the corresponding materials (Flores Orozco et al., 2020), which might differ substantially between the sampling points and the corresponding points along the profiles. Accordingly, we argue that the overall median percentage error is biased due to location and distribution of the sampling points and should be interpreted carefully.

Existing approaches for the quantification of the water content in landfills assume that the observed electrical response depends only on saturation, porosity and salinity (e.g., Grellier et al., 2007); however, surface conductivity cannot be neglected even in saline solutions (e.g., Lesmes and Frye, 2001; Lesmes and Morgan, 2001). Commonly, the lack of knowledge regarding the surface conductivity is counterbalanced by incorporating direct information about physical and chemical properties of the MSW (Grellier et al., 2006). In this way, the resolved electrical resistivity can be transformed to quantitative estimates of the water content (Grellier et al., 2007); yet, the limited spatial resolution of the direct information and the post inversion transformation might bias the obtained water content. In contrast, our approach uses electrical data collected at two different frequencies to account explicitly for the effect of the surface conductivity during parameter estimation. Moreover, by jointly inverting seismic and electrical data sets we reduce the inherent uncertainty associated with the inversion of geophysical data and solve directly for the water content, i.e., a transformation after the inversion process is not required. Accordingly, the resolved subsurface model simultaneously explains three different geophysical data sets, and thus provides reliable

estimates for the water content within the landfill as demonstrated in Figure 5.7.

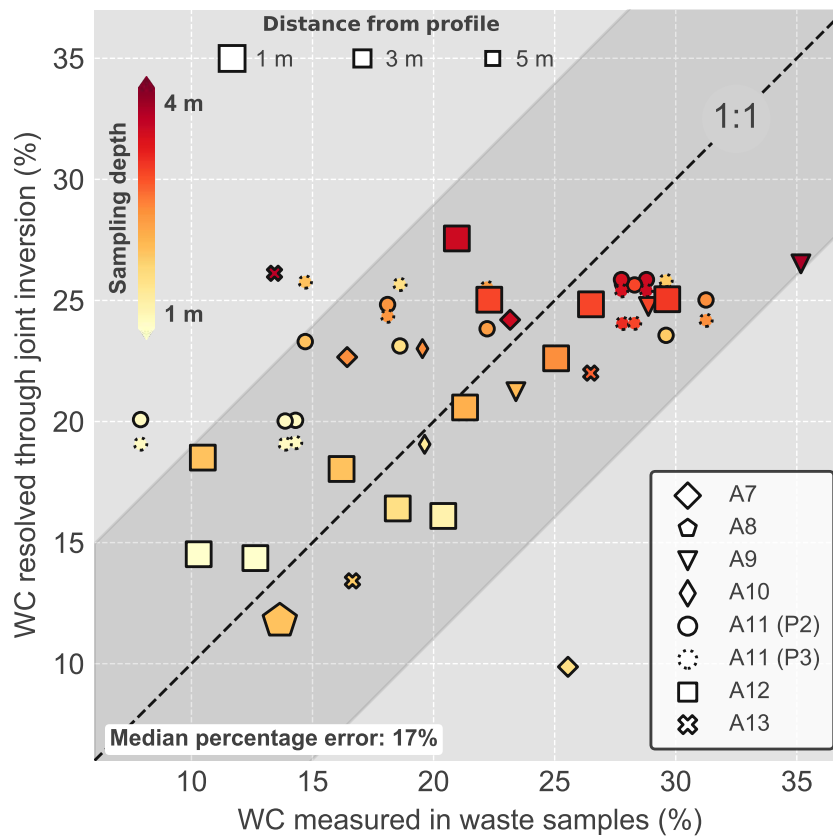


**Figure 5.7:** Measured versus estimated water content ( $WC$ ) as obtained at sampling points A7 to A13 in different depths. The shaded area refers to the triple median deviation from the perfect correlation (dashed line) to allow for the identification of outliers.

## 5.4 Conclusion

We presented a petrophysical joint inversion approach that uses seismic refraction and electrical resistivity data to quantitatively solve for the porosity, air saturation, water content and the cation exchange capacity. To ensure a valid quantification of the water content, the proposed approach is based on a petrophysical model, which considers the surface conductivity during the parameter estimation by leveraging upon electrical resistivity data collected at a high and a low frequency. Accordingly, we also resolve a model for the polarization response in terms of the normalized chargeability.

Imaging results obtained for data collected at the Heferbach landfill (Vienna, Austria) illustrated the applicability of this approach regarding the quantitative estimation of the subsurface water content, the delineation of the landfill geometry, and the dis-

crimination of waste types (i.e., MSW and CDW). A high water content ( $WC > 20\%$ ) was found for areas characterized by a strong polarization response, which indicates an increased level of biogeochemical activity, as evidenced by the correspondingly increased landfill gas production. We evaluated the resolved models based on information from direct investigations and the results obtained through independent methods, which demonstrated the validity of our approach.

Further studies should investigate the incorporation of different petrophysical models, for instance to include the effect of biogeochemical activity or aiming at the exploration of metallic materials disposed in landfills. In this regard, using the entire electrical impedance data (magnitude and phase) in the joint inversion is expected to improve the quantitative estimation of the parameters of interest. Moreover, the proposed joint inversion approach should be applied to data collected at different landfills to evaluate its applicability, e.g., in case of different waste compositions or deeper waste deposits.

# 6 | Application of induced polarization imaging across different scales to understand surface and groundwater flow at the Hofermuehle landslide<sup>1</sup>

## 6.1 Introduction

Landslide processes are of high interest due to their impact on infrastructure, human life and property as well as their role in landscape development. Clay-rich materials are especially prone to shallow and deep sliding processes (Lacroix et al., 2020; Sidle and Ochiai, 2006). In Austria, such mass mobilizations are typical for clay-rich materials corresponding to the Flysch and Klippen zone at the northern fringe of the Eastern Alps (e.g., Bell et al., 2013; Damm and Terhorst, 2010; Petschko et al., 2013; Promper and Glade, 2016; Lima et al., 2017; Steger et al., 2016; Stumvoll et al., 2020; Gallistl et al., 2018). Landslides in clay-rich areas are mainly triggered by changes in groundwater level (see Lacroix et al., 2020, for a review), and are thus controlled by recharge (i.e., following precipitation and snowmelt) and by the hydraulic properties of the subsurface. The Hofermuehle landslide, located in the Flysch Zone of Lower Austria, is exemplary for landslide processes in the region. Both slow earth (sliding) movements coupled with fast earth flow processes can occur, characterizing it as complex landslide (see Stumvoll et al., 2021; Stumvoll et al., 2022, and references therein). Landslide processes at the site are complex also in terms of their behavior, with non-linear processes varying in space and time regarding location, volume of mobilized material, duration and velocity (Stumvoll et al., 2022).

The study area has been thoroughly investigated by means of direct methods, such as terrestrial and airborne laser scanning (TLS and ALS), dynamic probing, analysis of soil samples recovered from core drilling and the monitoring of a piezometer network (for details see Stumvoll et al., 2021; Stumvoll et al., 2022). On the one hand, such studies have gained detailed information about the rates of surface deformation at different positions of the catchments, evidencing that there is probably more than

---

<sup>1</sup>This chapter is based on: Flores Orozco, A., M. Steiner, T. Katona, N. Roser, C. Moser, M. J. Stumvoll, and T. Glade (2022). "Application of induced polarization imaging across different scales to understand surface and groundwater flow at the Hofermuehle landslide". In: *CATENA* 219, p. 106612. ISSN: 0341-8162. DOI: 10.1016/j.catena.2022.106612

one sliding plane, with shallow planes (at a depth between 2 and 3 m) being likely interconnected. On the other hand, these investigations have also revealed large variations in the depth to the water level at different locations within the study area, as well as a different response to precipitation events. Therefore, the interpolation of such data is likely to provide a skewed picture of the subsurface conditions, especially regarding the groundwater flow.

Textural properties of the soils (e.g., clay content, grain size and interconnection of the pore space) play an important role in the hydraulic conductivity of the subsurface materials, and thus in the ability of the soils to permit infiltration and groundwater flow. An increase in the clay content commonly reduces the effective porosity, and thus the hydraulic conductivity ( $K$ ). Although analysis of sediments provides a direct measure of the textural properties, it fails to recover the spatial variability of the subsurface properties away from the drilling point and may provide little evidence regarding pore-space geometry. Geophysical methods have demonstrated the ability to gain information on subsurface properties with high spatial and temporal resolution in a non-invasive manner. In particular, electrical and electromagnetic methods sensing variations in the electrical conductivity of soils and rocks have been developed to evaluate changes in hydraulic properties (e.g., Danielsen et al., 2003; Linde et al., 2006; Slater, 2007; Binley and Kemna, 2005; Binley et al., 2015; Binley et al., 2016). The link between electrical and hydraulic conductivity has also been previously addressed in landslide investigations through electrical resistivity monitoring (Supper et al., 2014a; Travelletti et al., 2012; Perrone et al., 2014; Gance et al., 2016), yet excluding the contribution of surface conductivity to the bulk conductivity. Weller et al. (2015) recently proposed a model linking the hydraulic conductivity and the polarization effect resolved for measurements collected at 1 Hz over a broad range of samples in the laboratory, considering both consolidated and unconsolidated rocks. Binley et al. (2016) revealed the applicability of such model to interpret time-domain induced polarization (TDIP) data collected at the field-scale.

At the laboratory-scale, induced polarization (IP) measurements collected at different frequencies, the so-called spectral IP (SIP) method, have evidenced that textural properties controlling water flow also control the frequency-dependence of the complex conductivity. Accordingly, petrophysical models have been proposed to link the SIP response and the hydraulic conductivity (e.g., Slater, 2007; Revil and Florsch, 2010; Revil, 2013a; Revil et al., 2020; Binley et al., 2015; Abdulsamad et al., 2019, and references therein). However, for landslide investigations, geophysical methods have been mainly used to map the geometry of the sliding plane (Bichler et al., 2004; Chambers et al., 2011; Lapenna et al., 2005; Lapenna et al., 2003) and monitor the landslide

activity (see for example Whiteley et al., 2019, for a review). To the best of our knowledge, few studies have applied the IP method for understanding landslides (e.g., Flores Orozco et al., 2018b; Gallistl et al., 2018; Marescot et al., 2008). Gallistl et al. (2018) demonstrated that IP images permit a better mapping of structures favoring water flow or water storage in a shallow clay-rich landslide. Likewise, Flores Orozco et al. (2018b) revealed that IP images permit an improved delineation of the sliding plane geometry compared to investigations using solely resistivity results for the La Valette landslide. Moreover, the authors revealed that active areas of the landslide were in agreement with polarizable anomalies and a significant frequency-dependence; thus, suggesting a link between the pore-space geometries and the activity of the landslide. Nonetheless, Gallistl et al. (2018) as well as Flores Orozco et al. (2018b) evidenced the challenges to collect good quality IP data above 1 Hz due to electromagnetic coupling (EM-coupling). Recently, Flores Orozco et al. (2021) and Maierhofer et al. (2022) have demonstrated the possibility to minimize EM-coupling and improve the quality in IP readings up to 75 Hz through the use of coaxial cables.

Revil et al. (2020) proposed an approach to estimate the hydraulic conductivity and water content in an imaging framework through TDIP measurements. To properly account for the petrophysical model linking IP and hydraulic properties (see Revil, 2013a), the authors invert for the Cole-Cole parameters directly from the voltage reading during current injection and after the current is switched off through the modeling of the primary and secondary current. While Abdulsamad et al. (2019) already demonstrated the applicability of TDIP for the hydraulic investigations of embankments, Revil et al. (2020) reveal the potential of the IP methods for landslide investigations beyond the delineation of the geometry of the sliding plane, and the quantitative interpretation of geophysical measurements at the field-scale.

Revil et al. (2020) argue that the normalized chargeability, as obtained from the inversion of field-scale TDIP measurements, is consistent to the one obtained from the analysis of the frequency-dependence of IP measurements collected in the frequency-domain (FDIP). Hence, the authors obtain hydraulic conductivity and volumetric water content from TDIP, with their results supported through laboratory measurements. Accordingly, hydrogeological investigations can be conducted through TDIP measurements without the necessity to repeat data collection at different frequencies or by recording the full-waveform. However, the influence of the pulse length used to collect the decay-curve in the polarization data is not addressed by Revil et al. (2020), and only a qualitative analysis of the data-error is presented, although those two issues are critical for the application of the IP method for landslide investigations. On the one hand, short pulse lengths reduce the total acquisition time, but may not be able

to capture the slow polarization responses. On the other hand, not all instruments permit to capture the entire decay curve, especially at the early times; thus, limiting the content of the IP data collected with short pulse lengths. Hence, the selection of an adequate pulse plays a critical role in the quantitative estimation of IP parameters. Additionally, low polarization signatures, may result in readings distorted by noise due to poor signal-to-noise ratios (S/N), which in turn reduce the accuracy of the inversion results (e.g., Flores Orozco et al., 2018a; Flores Orozco et al., 2018b; Flores Orozco et al., 2012b, and references therein).

In this study, we present TDIP and FDIP data collected at the Hofermuehle catchment in an area that is recently stable, but was active in the past and may reactivate in the future. Based on our measurements, we address in detail the advantages and drawbacks of both TDIP and FDIP techniques, in particular regarding the estimation of hydraulic properties. In particular, we aim at investigating the potential of IP data (single and multi-frequency) to identify clay rich areas with a poor drainage, and thus susceptible to sliding. To evaluate the frequency-dependence of the IP field data and subsurface electrical properties, we present the intrinsic response as measured in the laboratory for different samples retrieved from the site. We also compare field-scale  $K$ -estimations based on TDIP measurements, data collected at a single frequency (with FDIP) and the analysis of multi-frequency IP data (i.e., SIP).

Additionally, we present independent estimations of the hydraulic conductivity based on a novel approach by Steiner et al. (2022) that permits the joint inversion of electrical resistivity tomography (ERT) and seismic refraction tomography (SRT) data sets taking into account the contribution of surface conductivity. Such inversion approach permits to solve for the spatial variations of the porosity in the imaging plane, which can then be used to independently solve for  $K$ . Accordingly, we can evaluate our hydraulic conductivity estimations from IP data through those obtained by means of the joint inversion.

Our results demonstrate that IP imaging results can map areas with poor drainage prone to land sliding. We also show that TDIP and single frequency FDIP provide very consistent results, yet a better understanding of the hydrogeological units may be resolved only by the analysis of the frequency-dependence through SIP measurements.

## 6.2 Material and methods

### 6.2.1 The complex conductivity as an expression of the electrical conductivity and polarization properties of the subsurface

The IP method is a geophysical electrical technique based on four-electrode measurements, where one electrode pair is used to measure the electrical impedance (i.e., complex-valued voltages) resulting from the injection of current in a second electrode pair. Imaging measurements consist of hundreds to thousands of four-electrode readings collected with tens to hundreds of electrodes placed along profiles (2D) or planes (3D). The inversion of such imaging data sets permits solving for the variations of the complex resistivity (CR) – or its inverse the complex conductivity (CC). Hence, this method is also known as CR or CC imaging or electrical impedance tomography (EIT). The complex-valued electrical conductivity ( $\sigma^*$ ), expressed in terms of its real ( $\sigma'$ ) and imaginary ( $\sigma''$ ) components, permits the representation of both the electrical conductive and capacitive properties of the materials. Alternatively, the CC can also be expressed in terms of its magnitude ( $|\sigma|$ ) and phase angle ( $\varphi$ ), such as:

$$\sigma^* = \sigma' + i\sigma'' = |\sigma| e^{i\varphi} \quad (6.1)$$

Considering that the polarization response of natural media without electrical conductors is commonly low ( $< 100$  mrad), it can be assumed that  $\sigma' = |\sigma|$  and that the phase angle is given by the ratio of polarization to conduction ( $\varphi \approx \sigma''/\sigma'$ ).

The electrical conductivity represents the ability of materials to permit the migration of ions, which in case of natural media with a negligible amount of electronic conductors (i.e., metals), takes place along two paths: through the electrolyte and within the electrical double layer (EDL) formed at the contact between grain and the electrolyte. On the one hand, the electrolytic conduction ( $\sigma_f$ ) is defined by the water saturation ( $S_w$ ), the porosity ( $\Phi$ ) and the fluid conductivity ( $\sigma_w$ ) (e.g., the electrical conductivity of the groundwater). On the other hand, grains with a high surface charge, such as clays, attract charges from the electrolyte forming an EDL, which also permits the conduction of current by surface conductivity ( $\sigma'_s$ ). Additionally, the charges accumulated at the EDL polarize in the direction of the injected current, which contributes to the imaginary component of the complex conductivity ( $\sigma''_s$ ). The strength of such polarization is primarily controlled by the surface charge and surface area of the grain (for further details we recommend Lesmes and Friedman, 2005; Slater and Glaser, 2003; Binley and Slater, 2020). Thus, at low frequencies ( $< 1$  kHz), the

complex conductivity of the subsurface can be written:

$$\sigma^*(\omega) = \sigma'(\omega) + i\sigma''(\omega) = \sigma_{el} + i\sigma_s^*(\omega) = [S_w^n \Phi^m \sigma_f + \sigma'_s(\omega)] + i\sigma''_s(\omega) \quad (6.2)$$

In Equation 6.2,  $\sigma_s^*$  represents the complex-valued surface conductivity,  $i = \sqrt{-1}$  the imaginary unit,  $\omega$  the angular frequency related to the frequency  $f$  ( $\omega = 2\pi f$ ) of the alternating current injected to the ground and  $n$  is the so-called saturation exponent associated with changes in the electrical conductivity from partially to fully saturated rocks (see Glover, 2017, and the references therein). The cementation exponent  $m$  is related to the connectivity of the pores permitting groundwater flow (Archie, 1942; Sen et al., 1981). Accordingly, the formation factor  $F$  (dimensionless) linking the amount of pore volume (i.e., porosity) and the way such pores are arranged (for a review we refer to Glover, 2009), can be written as:

$$F = \Phi^{-m} \quad (6.3)$$

As observed in Equation 6.2, the electrical conductivity is controlled by both  $\sigma_f$  and the frequency-dependent  $\sigma'_s$ , while the capacitive properties, or polarization, are only controlled by the surface conductivity ( $\sigma''_s$ ). Measurements collected at different frequencies (below approximately 1 kHz) can be used to gain information about the frequency-dependence of the complex conductivity in the so-called spectral IP (SIP) or multi-frequency IP. Plenty of studies have demonstrated a link between the SIP response and textural and hydraulic properties of soils (e.g., Binley et al., 2005; Revil, 2013a; Zisser et al., 2010, and references therein). The Cole-Cole model has been widely adopted to describe the frequency-dependence of the complex conductivity, which can be written in terms of the electrical conductivity (e.g., see Tarasov and Titov, 2013) as:

$$\sigma^*(\omega) = \sigma_\infty \left( 1 - \frac{M}{1 + (i\omega\tau)^c} \right) \quad (6.4)$$

In Equation 6.4,  $M$  is the chargeability, which is defined in terms of the conductivity at high and low frequencies ( $\sigma_\infty$  and  $\sigma_0$  respectively) as  $M = (\sigma_\infty - \sigma_0) / \sigma_\infty$ , while  $\tau$  is the relaxation time (in s), inversely proportional to the critical frequency ( $f_c$ , with  $f_c = 1/2\pi\tau$ ), which refers to the frequency at which the highest polarization response is observed (for further details see Tarasov and Titov, 2013). The exponent  $c$  (dimensionless) describes the broadness of the frequency-dependence. The strength of the polarization (e.g., Lesmes and Frye, 2001) is quantified by the normalized chargeabil-

ity (in  $\text{S m}^{-1}$ ), defined by:

$$M_n = M\sigma_\infty = \sigma_\infty - \sigma_0 \quad (6.5)$$

### 6.2.2 Hydraulic conductivity ( $K$ ) estimations based on IP measurements

In the last decade several approaches have been proposed to estimate the hydraulic conductivity  $K$  (or expressed in terms of the hydraulic permeability,  $k$ ) from IP measurements (e.g., Hördt et al., 2007; Slater, 2007; Revil and Florsch, 2010; Kemna et al., 2012; Weller et al., 2015). Börner et al. (1996) proposed an inverse correlation between hydraulic conductivity and the induced polarization (e.g.,  $K \approx (F\sigma'')^{-1}$ ) assuming that  $\sigma''$  is a direct measure of the surface area per unit pore volume ( $S_{por}$ ), the inverse of the hydraulic radius (see Slater, 2007, and references therein). Kemna et al. (2004) modified the model proposed by Börner et al. (1996) to obtain  $k$  estimations from cross-borehole TDIP imaging data. Slater and Lesmes (2002a) extended the Börner et al. (1996) model to fit a wide range of samples from unconsolidated sediments. However, in their study the authors only investigated samples with a limited range in porosities (Slater, 2007). More recently, Weller et al. (2015) demonstrated the possibility to predict the hydraulic permeability by means of IP measurements collected at 1 Hz over a large number of samples considering both unconsolidated sediments and sandstones. In terms of hydraulic conductivity such model can be written as:

$$K = \frac{g\delta}{\eta} \frac{3.47 \times 10^{-16} \sigma_0^{1.11}}{\sigma''^{2.41}} \quad (6.6)$$

Moreover, Weller et al. (2015) demonstrated that a slightly better prediction can be obtained when using the normalized chargeability, with such model written in terms of the hydraulic conductivity as:

$$K = \frac{g\delta}{\eta} \frac{4.03 \times 10^{-9}}{F^{3.68} M_n^{2.41}} \quad (6.7)$$

In our study, we use reference values for the groundwater dynamic viscosity ( $\eta = 1.0016 \times 10^1 \text{ kg m}^{-1} \text{ s}^{-1}$ ) and the density ( $\delta = 1000 \text{ kg m}^{-3}$ ), as well as for the gravitational acceleration ( $g$ ), which we assumed to be  $9.81 \text{ m s}^{-2}$ .

Alternatively, Revil et al. (2020) apply a different set of equations to derive the volumetric water content ( $\theta$ ) and the hydraulic conductivity from TDIP data sets. Such petrophysical model is based on the dynamic Stern layer model (after Revil et al., 2017c). Written in terms of the volumetric water content ( $\theta$ ), the cation exchange

capacity ( $CEC$ ) and the density of the grains ( $\delta_g$ ), the dynamic Stern layer model can be written (Revil, 2013a; Revil et al., 2020) as:

$$\sigma_0 = \theta^m \sigma_f + \theta^{m-1} \delta_g B CEC \quad (6.8)$$

$$\sigma_\infty = \theta^m \sigma_f + \theta^{m-1} \delta_g (B - \Lambda) CEC \quad (6.9)$$

$$M_n = \theta^{m-1} \delta_g \Lambda CEC \quad (6.10)$$

In Equations 6.8 to 6.10,  $B$  denotes the apparent mobility of counterions for surface conduction and  $\Lambda$  the apparent mobility of the counterions for the polarization associated with the quadrature conductivity (Revil et al., 2017c). Abdulsamad et al. (2019) argue that Equations 6.8 to 6.10 can be applied for the quantitative interpretation of TDIP in terms of the hydraulic permeability, considering that  $M_n$  and  $\sigma_0$  are obtained through the inversion of the data. Written in terms of the hydraulic conductivity, the model proposed by Abdulsamad et al. (2019) is given by:

$$K \approx \frac{g\delta}{\mu} \frac{k_0 \theta^6}{(\delta_g CEC)^2} \quad (6.11)$$

In Equation 6.11,  $k_0 = 10^{4.3}$  (dimensionless) and the variables  $CEC$  and  $\theta$  can be derived from combinations of Equations 6.8 and 6.10. In particular, as presented in Revil et al. (2020) the volumetric water content is obtained by:

$$\theta = \left[ \frac{1}{\sigma_w} \left( \sigma_\infty - \frac{M_n}{R} \right) \right]^{\frac{1}{m}} \quad (6.12)$$

with  $R = \Lambda/B \approx 0.1 \pm 0.02$  after Revil et al. (2020).

### 6.2.3 Time-domain and frequency-domain IP measurements at the Hofermuehle site

Investigations presented here were conducted in pasture lands located to the East of the most active area of the Hofermuehle site, which has been stable over the last 10 years and is defined as a dormant landslide. Figure 6.1 shows the area under investigation as well as existing ground truth information at the study site. Measurements

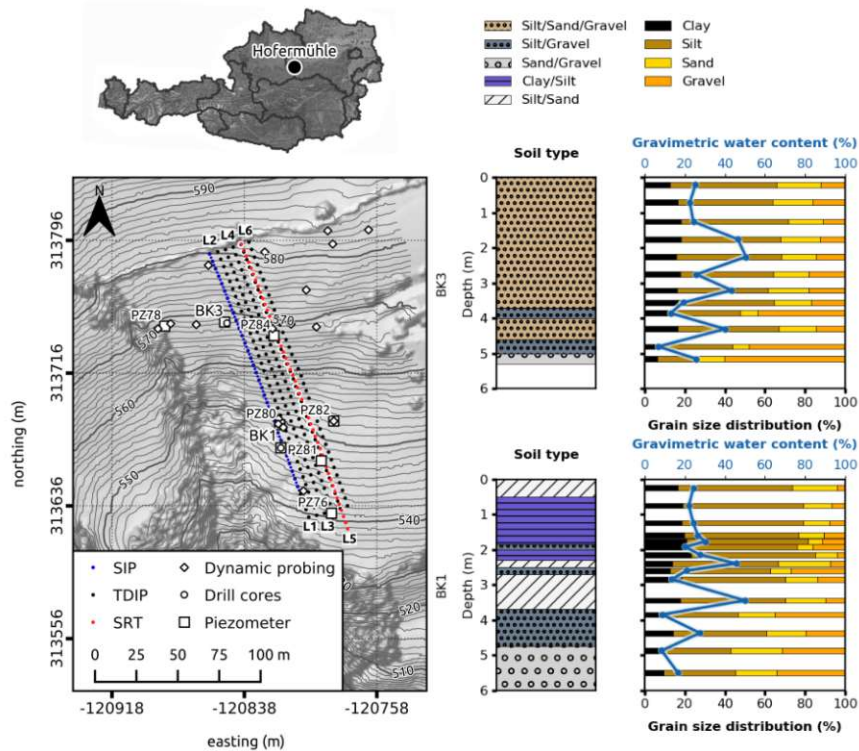


**Figure 6.1:** Location and existing ground truth information at the Hofermühle landslide located in Austria. The map presents the elevation of the study area and the position of the available ground truth data as well as the location of the geophysical lines. The analysis of samples collected from the cores BK1 and BK3 are used to construct the plots illustrating the lithological logs (using the DIN 18 196 classification), grain size analysis and variations in gravimetric water content. The position of the electrodes for the collection of time- and frequency-domain induced polarization (TDIP and FDIP) is indicated with the black and blue symbols respectively, whereas the position of the geophones for the seismic refraction tomography (SRT) is indicated with the red ones.

in time-domain (TDIP) were collected in November 2017 using a Syscal pro 72 switch unit (from IRIS instruments), which permits connecting 72 electrodes and collecting ten voltage readings simultaneously for a given current injection using ten measuring channels. In TDIP, the voltage is measured during the current injection to compute the transfer resistance. Subsequent voltage readings are collected once the current is switched off to calculate the integral chargeability ( $M_{int}$ ), which is a measure of the polarization effect. TDIP measurements presented here were conducted along six parallel lines roughly oriented North-South with 36 electrodes (in each line) with a separation of 5 m between electrodes and profiles as presented in Figure 6.1. Measurements along line L1 were conducted with different pulse lengths, namely 0.25, 0.5, 1, 2 and 4 seconds (s) to investigate their influence in the  $M_{int}$  readings, with

**Table 6.1:** Acquisition settings for time-domain induced polarization (TDIP) collected along lines 1 to 6. For completeness we provide the acquisition frequencies for the frequency-domain induced polarization (FDIP) data collected along line 1. The IP gates refer to the number of sampling points used to collect the integral chargeability within the sampling time after switching the current off (plus the delay). The DD-skip refers to the dipole length used for the data collection, with the acquisition times refer to the total time needed to collect the entire imaging data set.

Data	Line	Pulse length (ms)	Delay (ms)	IP gates	Sampling time (ms)	DD-skip	Acquisition time (minutes)	Electrodes	Spacing (m)	
TDIP	1	250	20	7	140	0, 1, 2, 3, 4	10	7	36	
TDIP	1	500	20	20	400	0, 1, 2, 3, 4	10	11	36	
TDIP	1	1000	40	20	880	0, 1, 2, 3, 4	10	19	36	
TDIP	1	2000	40	20	1800	0, 1, 2, 3, 4	10	35	36	
TDIP	1	4000	160	20	3520	0, 1, 2, 3, 4	10	66	36	
TDIP	2	500	20	20	400	0, 1, 2, 3, 4	10	11	36	
TDIP	3	500	20	20	400	0, 1, 2, 3, 4	10	11	36	
TDIP	4	500	20	20	400	0, 1, 2, 3, 4	10	11	36	
TDIP	5	500	20	20	400	0, 1, 2, 3, 4	10	11	36	
TDIP	6	500	20	20	400	0, 1, 2, 3, 4	10	11	36	
FDIP	1	0.5, 1, 3, 6, 8, 10, 15, 25, 37.5, 60, 75, 92, 120, 130, 171, 240 Hz				1 and 3	16	194	64	2.5

samplings of the decay curve favoring slow polarization effects for long pulse lengths. We collected lines L2 to L6 with a pulse length of 500 ms, which revealed the best compromise between short acquisition time and high S/N, as well as the possibility to sample the decay curve with the maximum of 20 windows available in the Syscal pro unit. We used a dipole-dipole (DD) skip-3 configuration, which means that current injection and voltage measurements are conducted with electrode pairs skipping three electrodes within them. Three electrodes were the minimum separation between the current and potential dipole in this configuration; whereas the maximum separation was 26 electrodes to use the 10 measuring channels. To increase the resolution in the near surface, we also include DD skip-0, skip-1 and skip-2 readings, always considering a maximum spread defined by the 10 measuring channels and a minimum separation between current and potential dipoles defined by the skip. Reciprocals are available only for readings along line L1 collected with 500 ms pulse length, with reciprocal readings referring to those collected after interchanging the electrodes used for current and potential dipoles (e.g., Flores Orozco et al., 2018b). Table 6.1 summarizes the settings for collecting the different TDIP data.

Frequency-domain (FDIP) measurements were collected in October 2021 along line L1 using a Data Acquisition System Multisource (DASM, from MPT-IRIS Inc.), deploying 64 electrodes with a separation of 2.5 m between them. Such instrument allows to physically separate the transmitter (i.e., current injections) and the receiver (used for voltage readings); thus, minimizing the contamination of the data due to parasitic electromagnetic (EM) fields arising from cross talking within the device (see Flores

Orozco et al., 2018a; Flores Orozco et al., 2020). As the transmitter and receiver are separated, in a first step we collected measurements connecting the transmitter to odd number electrodes, while electrodes with even numbers were connected to the receiver. In a second step, we interchanged the position of the transmitter and receiver to permit the collection of all possible combinations. In case of FDIP, the device records the electrical impedance given by the voltage to current ratio (impedance magnitude or transfer resistances) and the phase-shift between the sinusoidal current and voltage. Measurements were recollected for each quadrupole across 16 frequencies distributed in the range between 0.25 and 240 Hz to gain information about the frequency-dependence of the IP data (i.e., the complex conductivity). Measurements with the DASM were conducted using a DD skip-3 to permit comparison with the TDIP readings with a maximum separation of 16 electrodes between current and potential dipoles. We also collected a DD skip-1 configuration with all possible combinations, including the maximum separation between current and potential dipoles (i.e., 60 electrodes). The use of separated cables, as deployed here, does not permit to collect DD data with an even number of skipped electrodes. All FDIP data sets presented here were collected as normal-reciprocal pairs.

Both time-domain and frequency-domain measurements were conducted with multi-core cables, although Flores Orozco et al. (2021) revealed that such cables cause distortions in the measurements of the impedance phase-shift due to cross talking between the cables. Nonetheless, the same study demonstrated that such EM fields minimally distort TDIP readings, as the  $M_{int}$  is only measured after the current injection is switched off. In case of FDIP measurements, the separation of transmitter and receiver as well as cables connected to current and voltage electrodes also minimizes cross talking (i.e., Flores Orozco et al., 2021; Dahlin and Leroux, 2012). Inductive EM coupling with the subsurface materials is known to be proportional to the conductivity of the subsurface, the acquisition frequency and the square of the length of the cables (Hallof, 1974). Therefore, EM coupling in the FDIP is expected for high frequencies and in our data we only observed a linear increase in the IP data with increasing the frequencies above 70 Hz, evidencing possible EM-coupling at such frequencies. Such data contamination may not be observed in TDIP considering the 10 Hz analogous filter in the Syscal unit (see Martin et al., 2020).

#### 6.2.4 Analysis in soil samples: grain size analysis and SIP measurements

We conducted multi-frequency FDIP measurements (i.e., SIP) in soil samples recovered from two wells to evaluate the frequency-dependence of the IP data observed at

the field-scale. The SIP measurements in the lab were conducted in 19 samples, 11 taken from BK1 (extracted from depths between 0 and 5.5 m), and 8 samples from BK3 (extracted in depths between 0 and 6 m). The grain size distribution in the soil samples investigated here is illustrated in Figure 6.1, together with the lithological logs constructed using the soil classification DIN 18 196. Complementary information here corresponds to four dynamic probing heavy (DPH) and groundwater levels measured in piezometers as shown in Figure 6.1. Details on the grain size analysis and DPH can be found in Stumvoll et al. (2022).

For the collection of SIP data in the soil samples, we used the PSIP (portable spectral induced polarization) unit (from Ontash & Ermac Inc.), which is an instrument with high accuracy commonly used for laboratory investigations (e.g., Mellage et al., 2018). The sample holder is a cylindrical probe made of PVC with an internal diameter of 40 mm and a length of 150 mm. Current electrodes are located at each end of the probe and consist of a mesh of stainless steel covering the entire cross-sectional area of the holder. For the voltage measurements, the electrodes are placed with a separation of 50 mm between each other and to the current electrodes. Considering the 4 measuring channels available in the PSIP unit, the sample holder is designed to collect simultaneously three voltage readings, with each pair of electrodes placed around the column with a distance of 41.9 mm among them. Accordingly, one measurement represents the average of three electrical impedance measurements (one for each voltage pair) in the frequency range between 0.01 Hz and 10 kHz, consisting of 61 frequencies, with ten frequencies in each logarithm decade linearly distributed. The potential electrodes are made of stainless steel and drilled 1 to 2 mm deep into the sample through the cylindrical barrel yet these are not in direct contact with the soil within the sample holder, following a similar setup as presented by Cassiani et al. (2009). We used demineralized water to saturate the samples and a wet packing, where the column was filled by adding soil samples and water simultaneously to avoid the formation of bubbles, which decrease the quality of the readings. Measurements were collected 1 and 24 hours after the packing to investigate changes in the signal due to lack of equilibrium (e.g., Ustra et al., 2012). As we observed minimal changes we only present the data collected 24 hours after the packing. The geometric factor was estimated using the approach presented in López-Sánchez, Mansilla-Plaza, et al. (2017) and experimentally. For the latter case, we filled the column with tap water, with the geometric factor obtained as the ratio of the fluid conductivity of the tap water divided by the resistance measured. We observed negligible variations in the geometric factor obtained for our three voltage dipoles, as well as impedance phase values close to zero mrad (as expected) with fluctuations of  $\pm 0.15$  mrad in the range

between 1 mHz and 100 Hz. For the sample holder only filled with water, we observed an increase in the phase readings with increasing the frequency due to EM coupling, yet values still below 5 mrad at 1 kHz, demonstrating the good quality of our data and the experimental set-up.

Similar to previous studies (e.g., Revil, 2012; Weller et al., 2015; Revil et al., 2017c), we conducted SIP measurements in four soil samples, with measurements repeated in each sample after varying the salinity to estimate the formation factor  $F$ . The preparation and packing of the sample into the column followed the recommendations by Bairlein et al. (2014). Before the measurements at each salinity, the soil samples are first dried, then mixed with a brine at a given salinity and packed into the sample holder to collect the SIP data. Such steps are repeated for brines at different salinity. For the estimation of  $F$  and  $m$ , it is assumed that  $\sigma'_s$  is salinity-independent and a linear relationship between  $\sigma'$  and  $\sigma_w$  exists, such as:

$$\sigma' = \frac{1}{F}\sigma_w + \sigma'_s \quad (6.13)$$

These measurements were conducted in a similar probe as the one described by Bairlein et al. (2014), with a cell diameter of 2.5 cm and a total length of 16.6 cm. The soil samples were saturated with three to four different sodium chloride brines (with  $\sigma_w$  ranging from 0.5 to 140 mS m<sup>-1</sup>) as well as demineralized water as reference. The porosity of the samples was estimated based on the volume of the sample holder and the difference between the saturated and dry sample mass. Combination of Equations 6.3 and 6.13 were used to determine the cementation exponent.

### 6.2.5 Complementary data: field-scale seismic refraction tomography (SRT)

We also conducted a seismic survey to (1) validate the interpretation of the IP imaging results regarding the geometry of layers of potential instability, i.e., the potential shear surface, and (2) solve directly for the porosity ( $\Phi$ ), saturation ( $S_w$ ) through the joint inversion of electrical resistivity and seismic refraction data as presented recently by Steiner et al. (2022). The TDIP readings revealed minimal lateral variations in the electrical response, hence we maintained a distance of several meters between the SRT and FDIP profiles to allow for the simultaneous collection of these data sets and avoid a possible contamination between the readings. The seismic refraction data were measured using a Summit data acquisition system (DMT) with a recording length of 1024 ms, a sampling rate of 0.25 ms, and a pre-trigger of 20 mss. We deployed 48 geophones (corner frequency 30 Hzs) at the ground surface with 4 m spacing between

them. At each geophone position, we generated seismic waves by striking a plastic plate (3.5 cm thick) with a 7.5 kg sledgehammer and stacked four hammer blows to ensure an adequate S/N.

### 6.2.6 Processing and inversion of TDIP, FDIP, SRT data

For FDIP measurements, we filtered all readings whose normal-reciprocal misfit (NRM) was larger than the standard deviations of the NRM of the entire data set. This was done for data sets collected at each frequency (see Flores Orozco et al., 2012b; Flores Orozco et al., 2018a). In a second step, we compared the data sets collected at the 16 frequencies and kept only those quadrupoles found in all data sets. The TDIP data sets were processed using the decay-curve analysis proposed by Flores Orozco et al. (2018a). Integral chargeability readings from TDIP were linearly converted to impedance phase values to permit the inversion in terms of complex resistivity. Such approach has been demonstrated to permit a quantitative comparison of the data (Flores Orozco et al., 2012b), although it assumes a constant phase value, i.e., neglects the frequency-dependence in the data. Such assumption is valid considering the relatively short time range used to sample the decay curve. Accordingly, the conversion factor needs to be recalculated for data collected with different pulse lengths.

We used CRTomo (Kemna et al., 2000), a smoothness-constrained algorithm based on a complex calculus, to invert electrical impedances collected at a given frequency and solve for the distribution of the complex resistivity as a 2D section. The algorithm allows fitting the data to a level of confidence as defined by a data-error parameter to minimize the risk of creating artifacts within the inversion (Flores Orozco et al., 2012a); further details about the inversion algorithm can be found in Kemna et al. (2000). Error parameters were defined as 1% and 0.1 m for the inversion, yet a robust inversion scheme was deployed. All inversion results presented here converged to an error-weighted root mean square (RMS) error of ca. 1.0, which indicates that the forward response of the inverted complex conductivity models accurately resolved for the data accounting for the data-error. For the 3D inversion of IP data we used ResIPy (Blanchy et al., 2020), which is also based on complex calculus and the fitting of the data to a defined error-model (see Binley and Kemna, 2005).

To gain information about the frequency-dependence of the  $\sigma^*$ , we fitted a Cole-Cole model (Equation 6.4) pixel-wise to the complex conductivity imaging results obtained after the inversion of the FDIP data sets. We used the algorithm by Weigand and Kemna (2016) to fit the Cole-Cole models, with the root mean square error (RSME) computed as the misfit between the data and the fitted model. Initial analysis of the

results demonstrated a first peak below 60 Hz and the increase in the phase values for higher frequencies. Accordingly, in this study we only present the Cole-Cole parameters obtained for fitting the imaging results obtained between 1 and 60 Hz, to avoid the interpretation of possible EM-coupling (Pelton et al., 1978; Flores Orozco et al., 2013; Flores Orozco et al., 2018b; Flores Orozco et al., 2021) or Maxwell-Wagner polarization (e.g., Revil, 2013a).

From the seismic waveform data, we manually determined the P-wave travel time for each shot-geophone pair in an iterative process based on different data gathered, i.e., common shot, common receiver and common offset. We applied a 100 Hz low-pass filter on the data to enhance the perceptibility of the P-wave arrivals. Such filter mitigates the influence of high frequency noise, which is particularly relevant for larger offsets, i.e., larger distances between shot and geophone. For the joint inversion of SRT and resistivity tomography data, we used the petrophysical joint inversion framework implemented by Wagner et al. (2019) built upon the forward modelling and inversion capabilities provided by the open-source library pyGIMLi (Rücker et al., 2017). In particular, this joint inversion scheme solves for the volumetric water, air, ice and rock content, yet the underlying petrophysical model does not account for the surface conduction. Recent investigations (Mollaret et al., 2020; Steiner et al., 2021) have demonstrated the applicability of this petrophysical joint inversion scheme for field data collected at different alpine sites. Exploiting the frequency-dependence of  $\sigma_s$ , Steiner et al. (2022) proposed an extension to the petrophysical joint inversion algorithm that simultaneously inverts seismic travel times as well as electrical resistivity measurements collected at two frequencies (i.e., at low and high frequency) to quantify the surface conductivity during the parameter estimation. Built upon the formulations of the mechanistic polarization model by Revil (2013a), as presented in Equations 6.8 to 6.10 above, the modified joint inversion scheme solves for the volumetric water, air and rock content, while the surface conductivity is quantified by means of the *CEC*. For more details about the joint inversion schema including surface conduction we refer to Steiner et al. (2022).

In this study, we used the transfer resistances recorded during FDIP measurements collected at 1 and 60 Hz to be consistent with the above mentioned Cole-Cole analysis. In the petrophysical model underlying the joint inversion framework we set the parameters  $m$  and  $n$  (see Equation 6.2) as 2 and 1.5, respectively; whereas the conductivity of the groundwater  $0.075 \text{ mS m}^{-1}$  as measured at the site. With regard to the mechanical properties, we set seismic P-wave velocities ( $v_p$ ) of water, air and rock as  $1500 \text{ m s}^{-1}$ ,  $330 \text{ m s}^{-1}$  and  $3500 \text{ m s}^{-1}$ , and the density of the silty loam in the Hofermuehle site is assumed to be  $1300 \text{ kg m}^{-3}$ . For the inversion we used an initial homogeneous porosity

model of 40% to honor the porosity measured in the soil samples. No changes were observed if the initial porosity model was defined as a gradient with increasing values at depth. Joint inversion results presented here converged to an error-weighted root mean square (RMS) error close to 4.0, which indicates that the resolved subsurface model sufficiently explains the measured data within their respective error bounds.

### 6.3 Results

#### 6.3.1 Time-domain IP surveys: the effect of the pulse length and a first map of the study area

In Figure 6.2, we present the visualization of the TDIP data collected along line L1 with different pulse lengths. The data are presented in terms of the apparent resistivity ( $\rho_{app}$ ) and integral chargeability ( $M_{int}$ ). The  $\rho_{app}$  refers to the multiplication of the measured transfer resistances by the geometric factor, which in this case was modelled using CRTomo to account for the topography; whereas the  $M_{int}$  is directly obtained from the measurements without further conversions. The position of the pixel values representing the different measurements is based on the separation between the mid-point of the current and potential dipoles, allowing for the investigation of the variability in the measured data at different pulse lengths. The  $\rho_{app}$  plots reveal negligible changes between acquisitions using different pulse lengths, whereas large changes are observed in the  $M_{int}$ . In particular, for measurements along line L1,  $M_{int}$  readings with short pulse lengths are at least two times higher than those collected at 1000, 2000 and 4000 ms. We also observe that the pseudosections of  $M_{int}$  are smoother for short pulse lengths, while pulse lengths  $> 1000$  ms show more abrupt changes between adjacent measurements, especially for deeper readings, as they are related to lower voltage readings (e.g., Flores Orozco et al., 2018b) and, thus, lower S/N.

Figure 6.3 presents the imaging results for the TDIP data collected along lines L1 to L6 expressed in terms of the real and imaginary components of the complex conductivity. We resolved consistent images for all profiles, which suggest minimal lateral variations in East-West direction and significant changes can be observed in North-South direction. The DPH information available along the IP lines is indicated in the imaging results in Figure 6.3 as vertical lines that extend to the depth of refusal interpreted as the contact with bedrock (see Stumvoll et al., 2022). As exhibited in Figure 6.3, the bedrock resolved by means of the DPH is in agreement with the contact to the highest conductive ( $\sigma' > 40 \text{ mS m}^{-1}$ ) and polarizable ( $\sigma'' > 0.2 \text{ mS m}^{-1}$ )

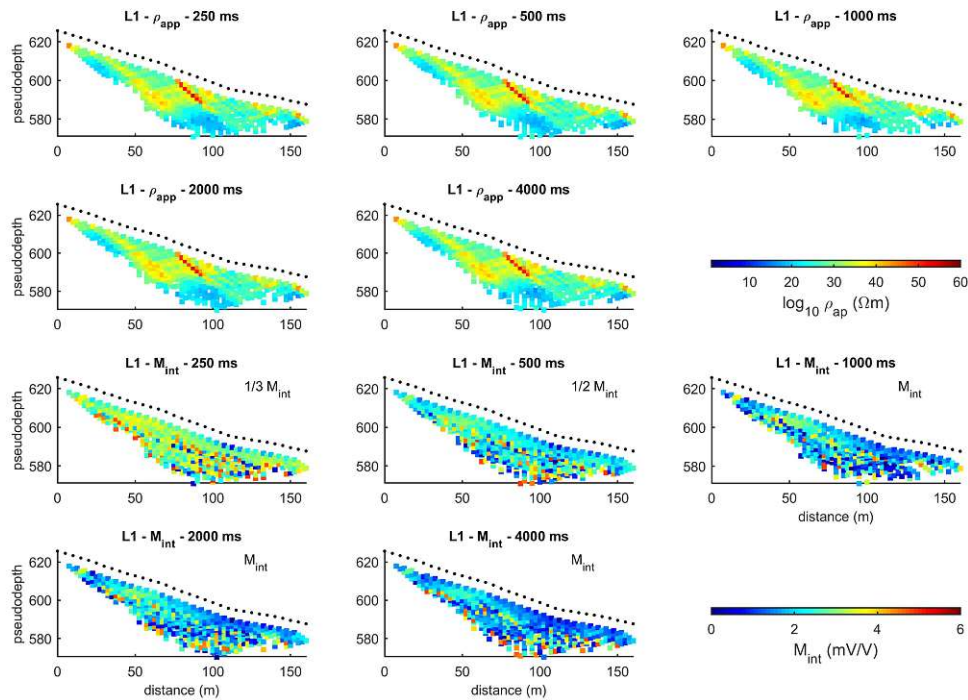


**Figure 6.2:** Visualization of the TDIP raw data collected along line L1 with five different pulse lengths. The raw data are expressed in terms of the apparent resistivity ( $\rho_{app}$ ) and the integral chargeability ( $M_{int}$ ). The  $M_{int}$  readings collected at pulse lengths of 250 and 500 ms are scaled ( $1/3$  and  $1/2$ , respectively) to permit using the same color scale. The black dots represent the position of the electrodes at the surface.

materials resolved with the inversion of TDIP data. The DPH resolved a shallower contact to the bedrock at ca. 100 m (along profile distance), which is also consistent with a lateral change in the shape of the highest conductivity and polarization values. Groundwater levels are expected at ca. 1 m bgs along the TDIP lines with the only exception of the piezometer PZ-78 located at the end of the Line 1, which revealed a depth of ca 3 m (see Table 6.2). Both  $\sigma_f$  and  $\sigma_s^*$  are dependent on saturation; thus, unsaturated soils explain the low conductivity and polarization response in the top soils (within 1 to 3 m depth) and lateral changes indicating variations in the textural properties. Below the top soil layer, between ca. 3 and 10 m depth, the moderate  $\sigma'$  and  $\sigma''$  values are related to weathered materials; whereas the high polarization and conductivity values in the bedrock correspond to materials of the Flysch formation. However, between 60 and 90 m along the profile there is a clear anomaly characterized by lowest  $\sigma'$  and  $\sigma''$  values, suggesting a lower content of clay minerals than to both ends of the profile. Increasing  $\sigma^*$  values are related to increasing clay contents and the contribution of both electrolytic and surface conduction. The polarization of clay is

**Table 6.2:** Depth to the water table observed in 2021. The values represent the mean depth (below ground surface) from observations in 2021 for the piezometers in the experimental plot at the Hofermuehle landslide. We provide also the computed variance.

Piezometer	Water level (m bgs)	Variance (m)
BK1	0.72	0.01
BK3	0.67	0.068
PZ-76	1.27	0.016
PZ-78	3.07	0.008
PZ-80	1.06	0.048
PZ-81	1.09	0.053
PZ-82	0.69	0.052
PZ-84	3.03	0.058

expected to increase with frequency, with a maximum around 100 Hz (e.g., Leroy and Revil, 2009). However, the instrument deployed has a built-in analogue low pass filter, limiting the content of the data below the cut-off frequency of 10 Hz (Martin et al., 2020). The lack of information in  $M_{int}$  in the early times (i.e., above 10 Hz) explains the relatively low polarization values observed in Figure 6.3. Such interpretation cannot be validated as the steep slope forbids the collection of soil samples or the conduction of DPH on top of the low polarization anomaly. Due to the low  $\sigma'$  and  $\sigma''$  values these anomalies indicate areas characterized by coarse grain sizes (e.g., sands), thus facilitating infiltration (in the top soils) as well as groundwater drainage at depth.

TDIP anomalies characterized by high conductivity ( $> 40 \text{ mS m}^{-1}$ ) also correspond with the highest polarization values ( $> 0.2 \text{ mS m}^{-1}$ ); thus, likely indicate high clay content, i.e., grains characterized by high surface area and charge where both surface and electrolytic conduction contribute to the observed bulk conductivity. Increasing the clay content commonly reduces the hydraulic conductivity, and likely such polarizable structures hinder groundwater flow. Hence, the combined analysis of conductivity and polarization results may improve the interpretation of the electrical images and the delineation of subsurface structures controlling water flow. Nonetheless, the TDIP inversion results provide no information on the actual frequency-dependence of the complex conductivity and taking into account the limited bandwidth in the frequency content recorded by the Syscal pro unit (Martin et al., 2020), we opted to present the  $\sigma^*$  images obtained from TDIP linearly converted at a frequency of 1 Hz.

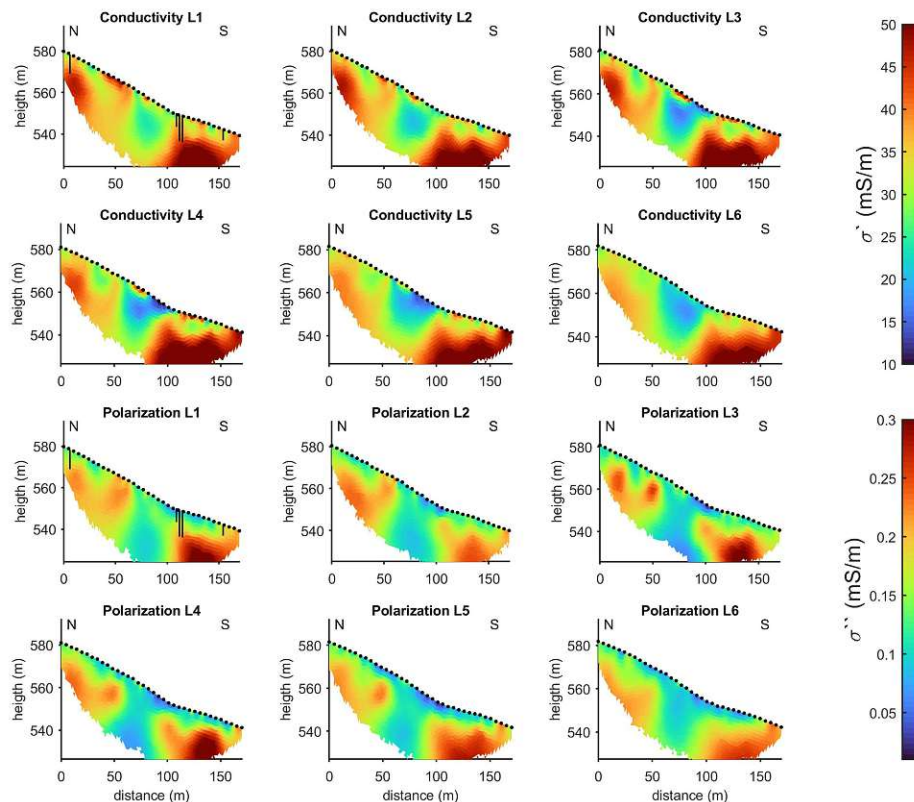


**Figure 6.3:** Visualization of the TDIP raw data collected along line L1 with five different pulse lengths. The raw data are expressed in terms of the apparent resistivity ( $\rho_{app}$ ) and the integral chargeability ( $M_{int}$ ). The  $M_{int}$  readings collected at pulse lengths of 250 and 500 ms are scaled (1/3 and 1/2, respectively) to permit using the same color scale. The black dots represent the position of the electrodes at the surface.

### 6.3.2 Frequency-domain imaging results for data collected at line L1

The inversion of FDIP data resolved in general for negligible changes in the conductivity ( $\sigma'$ ) at different frequencies. In contrast, the polarization images reveal a considerable frequency-dependence, with the  $\sigma''$  increasing over two orders of magnitude with increasing the frequency from 1 to 240 Hz. Hence, in Figure 6.4 we present the conductivity imaging results for data collected at 1 Hz as well as the polarization images ( $\sigma''$ ) resolved at different frequencies. Inversion results obtained at 1 Hz are of particular interest, as this is the frequency used in the petrophysical model proposed by Weller et al. (2015) to predict  $K$  from FDIP measurements. Due to the large differences in the range of values, we use different color scales to present FDIP and TDIP imaging results. Plots in Figure 6.4 reveal that FDIP imaging results are not deep enough to capture the response from the bedrock, with the sensitivity of the data sets only recovering the response from the weathered materials. This is due to the combination of a shorter electrode spacing and profile length, as well as the EM

## 6 Understanding surface and groundwater flow in landslides

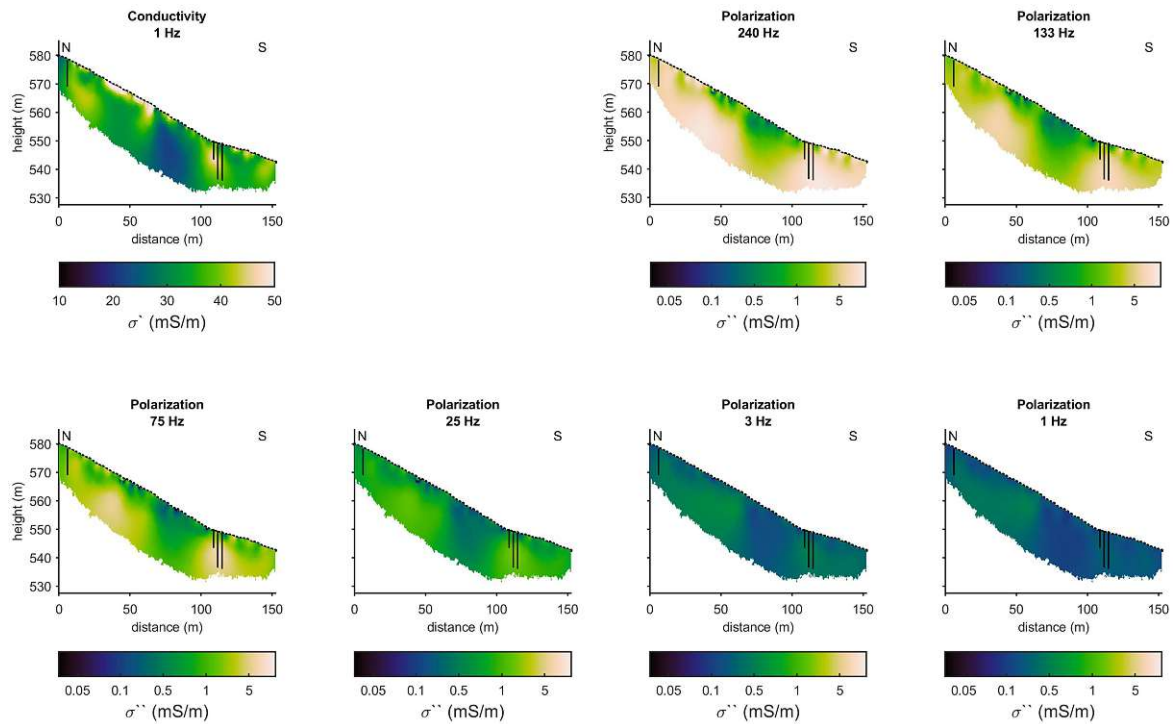


**Figure 6.4:** Inversion results for FDIP data collected along line L1 expressed in terms of the real ( $\sigma'$ ) and imaginary ( $\sigma''$ ) components of the complex conductivity. The conductivity results are consistent across all frequencies in the measured range (0.25 to 240 Hz) and we present only the conductivity image for data collected at 1 Hz; whereas polarization images are presented for data collected at different frequencies. We use a different color map to present the FDIP imaging results considering the larger dynamic in the polarization values than resolved in TDIP. The black points in each image represent the electrodes at the surface. The vertical lines imposed in plots of L1 indicate the position and maximum depth reached with the DPH. The plots have a vertical exaggeration 2:1 to better identify subsurface changes at depth.

coupling affecting the readings with a low S/N, i.e., those deep measurements with large separation between current and potential dipoles.

As described above, the groundwater table is expected at a depth of 1 m bgs; thus, explaining the low polarization and conductivity observed in the unsaturated soils at the top soil layer also in agreement with TDIP images presented before. The anomalous region between 60 and 90 m distance shows low polarization values across all frequencies under investigation; thus, supporting our interpretation of a low clay content, as proposed for the interpretation of TDIP results. Within the weathered materials, the main variations are observed at depths below ca. 5 m, where the polarization increases, especially for high frequencies. Fine grains are related to shorter times to fully establish the polarization of the charges coating the EDL than coarser grains, where the charges need to move across larger distances (i.e., Revil and Florsch,

2010). Measurements in sands have revealed a stronger polarization response around 1 Hz (e.g., Koch et al., 2011); while the increase in the polarization with increasing the frequency has also been reported from laboratory measurements in clayey materials (e.g., Leroy and Revil, 2009), supporting our interpretation regarding the increase in the  $\sigma''$  values. A potential plane of instability has been identified at a depth fluctuating around 10 m bgs based on the DPH data (see Stumvoll et al., 2022). In their study, the geometry of such plane was only interpolated between three DPH soundings. In contrast, the FDIP images provide quasi-continuous information about the depth to such plane across the entire slope. In particular, the variations in the depth of the potential plane of instability can be easily observed in the polarization image at 240 Hz corresponding to the contact to the high polarization values ( $\sigma'' > 5 \text{ mS m}^{-1}$ ). Such plane of instability is close to the surface at both ends of the profile, while a depth of ca. 12 m can be resolved to the center of the profile, between 60 and 90 m approximately. Although it is associated with larger acquisition times (see Table 6.1), SIP results presented in Figure 6.4 clearly resolve the frequency-dependence of the polarization, with a clear increase in the values at high frequencies. The low polarizable anomaly resolved through TDIP, FDIP and SIP, is presumably dominated by coarse grains as indicated by its low conductivity and polarization. Accordingly, it may permit the accumulation of water, either due to infiltration from the surface or groundwater flow from northern areas along the top soil layer. Such water cannot easily flow downhill (i.e., towards south), due to the increase in clay materials in the polarizable anomaly. Thus, this polarizable anomaly may be a relevant subsurface feature controlling surface deformation, considering that the accumulation of groundwater in such area may, in turn, result in the increase in pore pressure.

### 6.3.3 The frequency dependence of the SIP measurements

Grain size distributions obtained through laboratory analysis of soil samples retrieved at the Hofermuehle site report a high silt (varying between 20 and 50 %) and clay (varying between 6 and 25 %) content (Stumvoll et al., 2022). Such analysis also revealed that the fine grains (silt and clays) comprise 70 % of the materials above 4 m bgs and about 40 % between 4 and 6 m depth (c.f. Figure 6.1). In Figure 6.5, we present the measured spectra for all samples extracted from wells BK1 and BK3 located at 44 and 125 m, respectively, along the FDIP profile (see Figure 6.1). In general, the spectra reveal a similar trend with low polarization values in the range between 1 and 10 Hz, and higher values with increasing the frequency. The resolved peaks observed at in the range between ca. 200 and 600 Hz suggest that the measurements are not dominated

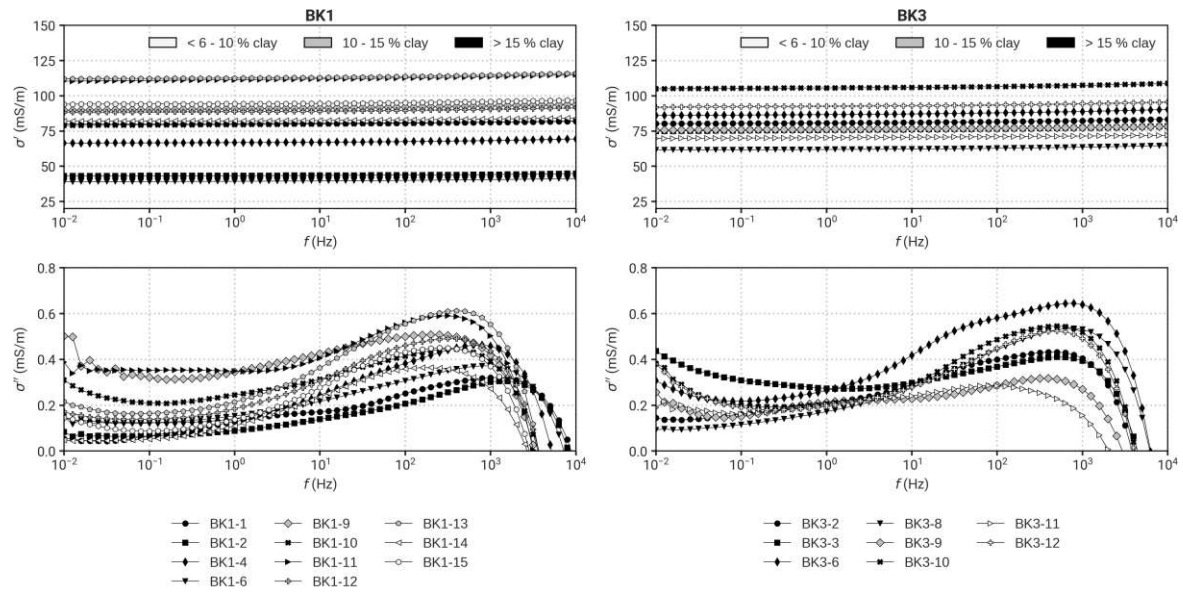


**Figure 6.5:** Frequency-dependence of the complex resistivity for SIP data collected in the soil samples. The data are presented in terms of the real ( $\sigma'$  - top row) and imaginary ( $\sigma''$  - bottom row) components of the complex conductivity. The measured data are represented with the solid symbols. We use different symbols to aid in the identification of spectra resolved for samples taken at different depths. The color-coded spectra aim at identifying samples with variable clay content.

by EM coupling, which is commonly related to a linear increase with increasing the frequency (Hallov, 1974; Pelton et al., 1978). Moreover, in Figure 6.5, it is possible to observe a peak (i.e., critical frequency) in the polarization around 1000 Hz for samples with the highest clay content (> 15 %); while the peak is observed around 200 Hz for lower clay contents. We also observe that high clay contents (> 10 %) are also related to higher polarization values; although no clear trend is observed for the conductivity values. Nevertheless, sediments in BK1 (downhill) reveal also the lowest  $\sigma''$  values for the samples with high clay content, clearly evidencing the high heterogeneity of the study area and stressing the relevance of field-scale investigations. The Cole-Cole parameters fitted to the measured spectra revealed only a weak correlation with the dominating grain size and are not discussed in this study. Thus, we believe that not only the grain size controls the frequency-dependence, but other textural parameters are critical, such as the pore size (e.g., Binley et al., 2005).

The analysis of multiple-salinity measurements and application of Equation 6.13 results in estimations of formation factor ( $F$ ) varying between 4.24 and 10.83, while the values for the cementation exponent ( $m$ ) were found to be between 1.68 and 3.26, as presented in Table 6.3. Consistent to other laboratory observations (see Weller et al., 2015, and references therein), we can see that  $F$  increases in samples taken from the

**Table 6.3:** Laboratory SIP analysis of fully-saturated soil samples after varying the fluid conductivity to obtain the formation factor ( $F$ ), the cementation exponent ( $m$ ) and the real component of the surface conductivity ( $\sigma'_s$ ).

Sample	$F$ (-)	$\sigma'_s$ (mS m <sup>-1</sup> )	$\Phi$ (%)	$m$ (-)	Description
BK1-2	4.24	43.67	47	1.9	Clay/Silt
BK1-10	4.94	146.43	39	1.68	Silt/Sand
BK1-12	10.83	144.22	48	3.26	Silt/Gravel
BK1-13	7.23	117.68	-	-	Silt/Gravel

deeper areas, where soil samples reveal an increasing content of gravels. However,  $m$  and  $F$  values need to be taken with caution, as we may have unintentionally changed the geometry of the pore space during the preparation of the SIP columns in the laboratory. As mentioned above, we dried the sample before mixing it with the brine to fill the column, with such steps repeated for the different salinity levels. While we took extra care to maintain the porosity constant along our measurements, we cannot neglect changes in the packing of the samples, i.e., in the connectivity between pores, which is the key factor controlling  $m$ . Accordingly, as the  $\sigma'_s$ ,  $m$  and  $F$  obtained from Equation 6.13 may be influenced due to changes in the interconnected porosity while filling the column, they may not reflect the field conditions.

The comparison with the imaging results shows that the laboratory analysis presented in Figure 6.5 confirms the polarization response increase with the clay content. Moreover, the presented spectra evidence a  $f_c$  above 100 Hz, consistent to the increase in  $\sigma''$  observed in our field results. Figure 6.5 also confirms the low polarization values ( $\sigma'' < 0.5$  mS m<sup>-1</sup>) in the frequency range between 0.25 and 5 Hz, which was also resolved in both the FDIP and the TDIP data. The observed increase in the polarization response at frequencies below 0.1 Hz in our laboratory measurements is also similar to the one reported by Leroy and Revil (2009), which was explained by the membrane polarization. Such low frequencies require several hours to be collected, especially for imaging configurations; thus, they are not suited for field-scale measurements and we will not discuss them further.

To better quantify the frequency-dependence of the  $\sigma^*$  of the field SIP data, we present in Figure 6.6 the Cole-Cole parameters (Equation 6.4) describing the frequency-dependence observed in SIP imaging results. The Cole-Cole model was fitted pixel-wise to the inversion obtained for data collected between 1 and 60 Hz, considering that higher frequencies may be related to possible Maxwell-Wagner polarization (e.g., Revil and Florsch, 2010) and EM-coupling (e.g., Flores Orozco et al., 2013; Flores Orozco et al., 2018b; Flores Orozco et al., 2021). Figure 6.6 reveals patterns in the images of

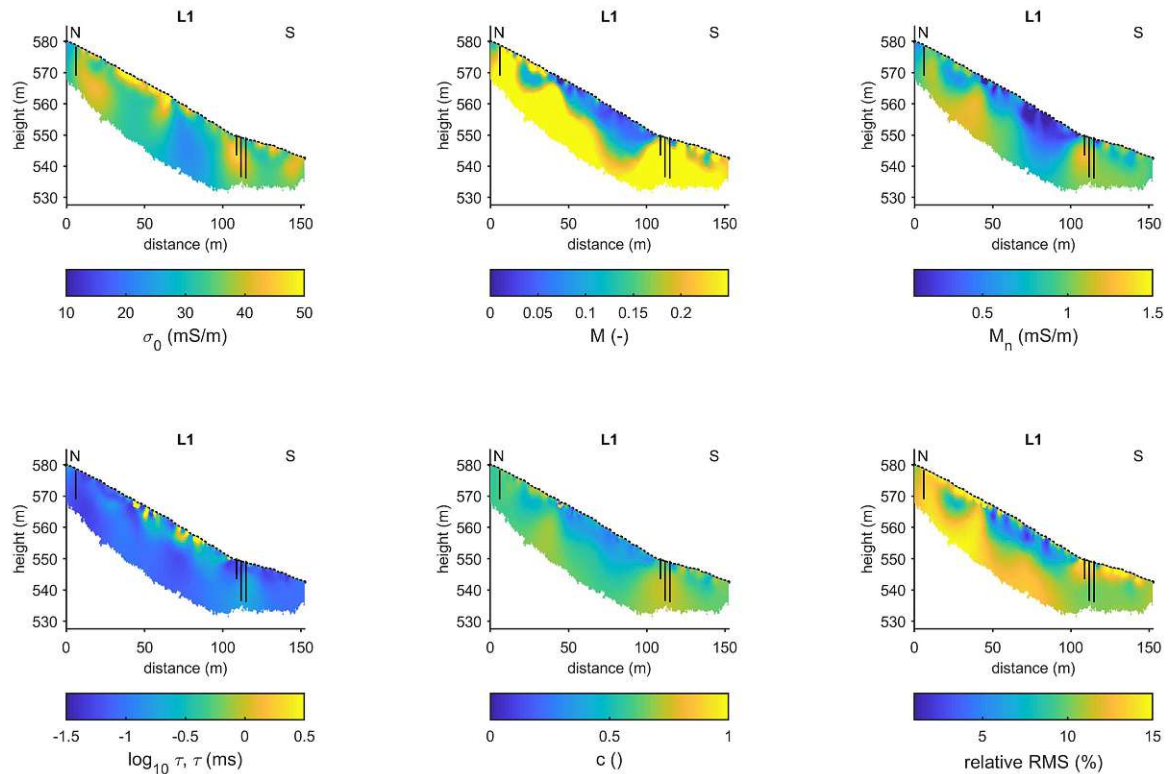


**Figure 6.6:** Plots of the Cole-Cole parameter fitted to the imaging results obtained for the inversion of SIP data collected along L1. The vertical lines imposed in the plots indicate the position and maximum depth reached with the DPH. The plots have a vertical exaggeration 2:1 to better identify subsurface changes at depth.

Cole-Cole parameters that are consistent with those also described before for TDIP and FDIP. Hereafter we will only discuss the DC-conductivity ( $\sigma_0$ ) and the normalized chargeability ( $M_n$ ) considering that both parameters are required for the estimation of hydraulic conductivity (see Equations 6.6 and 6.7). The  $\sigma_0$  presented in Figure 6.6 is equivalent to the conductivity obtained through traditional ERT surveys, and obviously shows similar patterns and values as the inverted  $\sigma'$  from TDIP and FDIP data (Figures 6.3 and 6.4). Likewise, the normalized chargeability illustrated in Figure 6.6 quantifies the polarization response obtained from multi-frequency SIP data and shows features consistent to the  $\sigma''$ . Such observation demonstrates the good quality of all data sets presented and the possibility to obtain similar results from TDIP, FDIP and SIP data. Quantitatively, we can see that the normalized chargeability resolved through SIP has values ranging between 1 and 1.5 mS m<sup>-1</sup>; while the values in the  $\sigma''$  reach a maximum of 5 mS m<sup>-1</sup> for inversion of FDIP data collected at 240 Hz, and below 0.5 mS m<sup>-1</sup> for both FDIP data collected at 1 Hz and TDIP images.

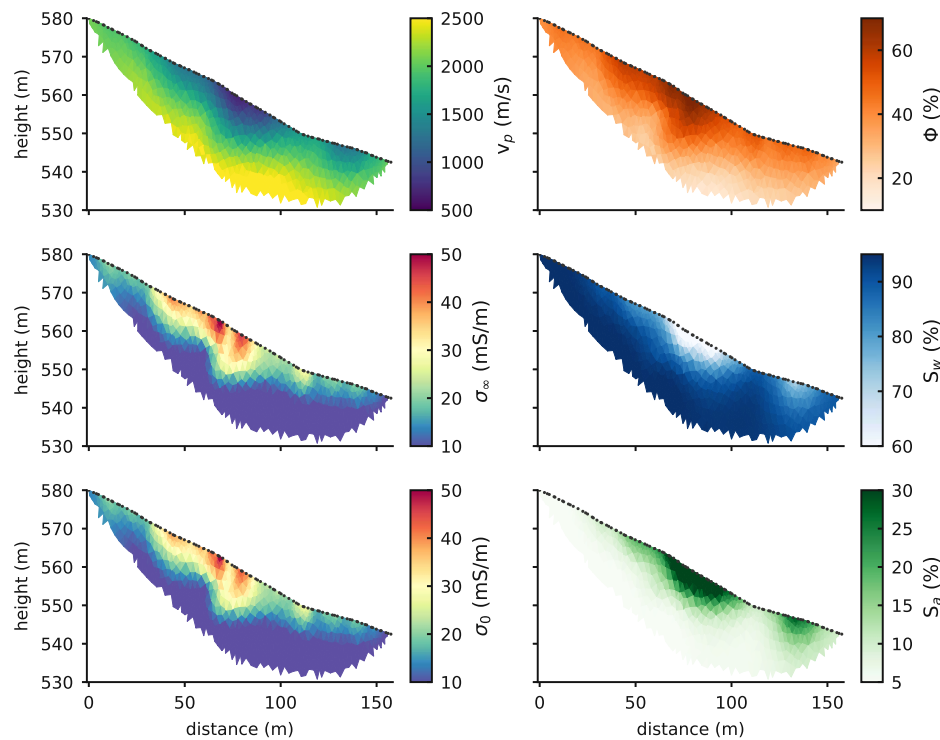


**Figure 6.7:** Imaging results obtained from the joint inversion of electrical resistivity and seismic refraction tomography expressed in terms of the geophysical parameters, i.e., the seismic velocity of the P-waves ( $v_p$ ) and the electrical conductivity at low and high frequency ( $\sigma_0$  and  $\sigma_\infty$ ). The joint inversion directly resolves for relevant hydrogeological parameters: here expressed in terms of the water saturation ( $S_w$ ), air saturation ( $S_a$ ) and porosity ( $\theta$ ). The black dots on the top of the plots represent the position of the electrodes as well as the geophones and shot points. All plots are oriented North–South.

### 6.3.4 Joint inversion of electrical resistivity and seismic refraction tomography

We have proposed an interpretation of the complex conductivity results and their frequency dependence. However, the use of other geophysical methods could help to shed light on the lateral variation observed within the  $\sigma^*$  interpreted as variations in the clay content. Seismic methods are primarily sensitive to variations in the density, and thus offer the opportunity to map variations within the weathered materials as well as the contact to the bedrock. Moreover, seismic images can also help to delineate possible changes within the Flysch that may point to possible fractures as an alternative interpretation of the  $\sigma^*$  images. To avoid the interpretation of independently resolved electrical and seismic models, we present in Figure 6.7 the results obtained through the joint inversion of the two data sets, namely P-wave travel times and resistivity data.

Figure 6.7 reveals, as expected, negligible changes in the images resolved for  $\sigma_0$  and  $\sigma_\infty$ , and both models are consistent with the  $\sigma'$  inverted from TDIP, FDIP data (also with  $\sigma_0$  from SIP) as well as in the same range of values from laboratory measurements. The  $v_p$  clearly resolves two layers: (1) the unconsolidated materials related to low values ( $v_p < 1000 \text{ m s}^{-1}$ ) on top, with a thickness varying between 5 and 10 m; and (2) the weathered rocks characterized by higher velocity values ( $v_p > 2000 \text{ m s}^{-1}$ ) on the bottom. A third layer may be suggested at larger depth associated with velocities above  $2200 \text{ m s}^{-1}$ , which may reflect a contrast to less weathered materials. The joint inversion results do not extend to the same depth as the TDIP imaging results and cannot resolve the contact to the bedrock. This is due to the limited extension of the seismic survey as well as the filtering of deep measurements in the resistivity data caused by poor reciprocity in the phase readings.

Due to the lack of deep resistivity readings, the subsurface model resolved through the joint inversion scheme reflects the layering sensed by the seismic method, which is less sensitive to variations in the textural properties of the materials than the IP measurements. Accordingly, the  $v_p$  model reveals only the two layers corresponding to the unconsolidated materials and the weathered materials, with the interface between both likely resolved by the  $2200 \text{ m s}^{-1}$  isoline. Hence, spatial variations in this isoline are related to the geometry of the plane of instability. Moreover, the conductivity images presented in Figure 6.7 also resolve the lateral variations within the top layer, with low seismic velocity values (approximately  $1000 \text{ m s}^{-1}$ ) between 60 and 90 m, in agreement with the conductivity and polarization anomalies observed in TDIP and FDIP images. However, the  $v_p$  model does not reveal any lateral variation within the bottom layer that may indicate possible fractures, supporting the interpretation that low polarizable anomalies in TDIP, FDIP and SIP images are likely related to changes in the textural properties.

The joint inversion solves directly for water saturation ( $S_w$ ) and porosity ( $\Phi$ ), two relevant parameters for landslide characterization. Figure 6.7 shows a high water saturation ( $> 60\%$ ) across the entire image plane, with the lowest areas close to the surface, in agreement with the shallow groundwater level (ca. 1 m) as presented in Table 6.3. The lowest water saturation ( $\leq 60\%$ ) is resolved within the anomalous region, between 60 and 90 m profile distance and close to the surface, where the highest air saturation ( $> 25\%$ ) is resolved. The highest porosity (ca. 60%) is observed in the top layer corresponding to the unconsolidated sediments, with the maximum values observed between 60 and 90 m distance. The weathered rocks unit reveals porosity values ranging between 30 and 40%.

In case of the joint inversion results presented here, the impedance phase values

are disregarded and we only use the transfer resistances (at high and low frequencies) as model parameters. Although computed without involving the IP readings, the images of water content and porosity provide consistent structures and confirm the geometry of both the plane of instability and the anomaly between 60 and 90 m distance resolved through TDIP, FDIP and SIP images. Such anomaly corresponds to the lowest porosity and water content, supporting the interpretation of unsaturated materials with lower clay content described above for the IP images. Besides supporting the interpretation of the IP images, the resolved porosity model can be used to obtain the formation factor (Equation 6.3), which is critical for estimating the hydraulic conductivity (see Weller et al., 2015).

## 6.4 Discussion

### 6.4.1 Quantification of the hydraulic conductivity based on different IP methods

In this study, subsurface information at different scales has been gained through TDIP, FDIP and SIP investigations, permitting the interpretation of a plane of instability between the unconsolidated materials and the weathered Flysch, with a depth varying between 1 and 5 m across the slope. The contact to the bedrock is resolved through TDIP images at depths below 12 m, with some lateral variations (especially to the south). Such contacts are in agreement with results of previous investigations at the site based on DPH (Stumvoll et al., 2022) as well as with variations in the  $v_p$  values obtained from the joint inversion results. Moreover, to the center of the images, we can observe an anomaly of low polarization which we interpret as an area of low clay content within both the unsaturated materials and the weathered Flysch. The imaging results presented earlier reveal the complexity of the study area where the thickness and textural properties of the units might suddenly change in a few meters.

So far, the interpretation of the TDIP, FDIP and joint inversion results have pointed to variations in the clay content and, thus, we have inferred lateral variations in the hydraulic properties of the subsurface at the Hofermuehle site. However, no hydrogeological information is available at the site. To overcome this and provide a quantitative interpretation of the IP results, we decided to apply the petrophysical models proposed by Weller et al. (2015) linking IP parameters and the hydraulic conductivity. Figure 6.8a and 6.8b present the estimations after applying the  $K-\sigma''$  relationship presented in Equation 6.6. For  $\sigma''$  we use inversion results resolved at 1 Hz obtained from both the linearly converted TDIP (Figure 6.8a) and the FDIP (Figure 6.8b)

## 6 Understanding surface and groundwater flow in landslides

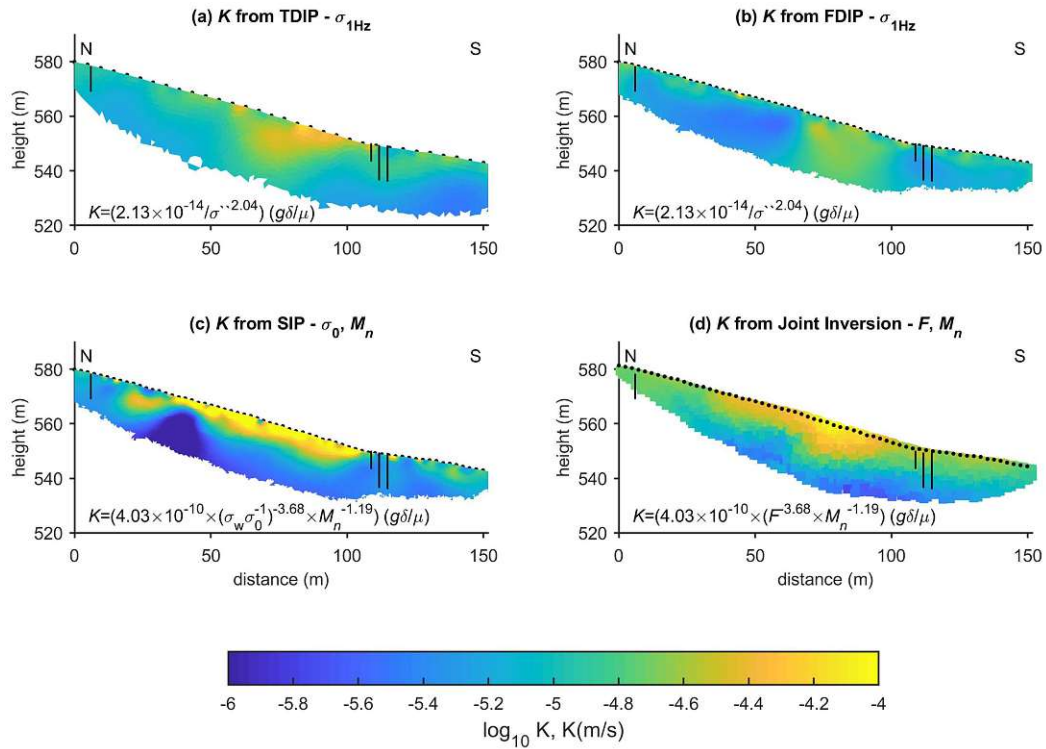


**Figure 6.8:** Estimated values of hydraulic conductivity ( $K$ ) from the inverted TDIP, FDIP and SIP data collected along line L1. The first row presents estimations using the link between  $K$  and the  $\sigma''$  at 1 Hz obtained from (a) TDIP, and (b) FDIP imaging results. The second row presents the results using the relationship between  $K$  and the normalized chargeability ( $M_n$ ), as obtained from: (c) fitting the Cole-Cole model to SIP data, and (d) the joint inversion results. For the formation factor ( $F$ ), we used  $\sigma_0$  as a first approximation for SIP data, while porosity models are used to compute  $F$  for the joint inversion results. To allow a better visual comparison, the TDIP image was only plotted to a distance of 150 m that is the maximum length of the FDIP profile. All plots are presented in a 1:1 aspect ratio.

measurements collected at profile L1.

As discussed during the interpretation of the imaging results above, the top unit represents the unconsolidated materials related to high  $K$  values ( $> 1 \times 10^{-5} \text{ m s}^{-1}$ ), as expected due to their poor compaction. The unit below corresponds to weathered Flysch, with  $K$  values  $\approx 1 \times 10^{-5} \text{ m s}^{-1}$  estimated from TDIP, and slightly lower values from FDIP data ( $K \approx 1 \times 10^{-5.5} \text{ m s}^{-1}$ ). Considering the smaller electrode spacing (see Table 6.1), and thus, higher resolution, we believe that the FDIP provides a better estimate of  $K$  for the unconsolidated and the weathered materials than the TDIP images. The bedrock is resolved only in the TDIP images revealing much lower hydraulic conductivity ( $< 1 \times 10^{-5.5} \text{ m s}^{-1}$ ), as expected for consolidated materials (in this case from the Flysch formation). The highest  $K$  values can be observed in the before men-

tioned anomaly between 60 and 90 m profile distance, supporting our interpretation of low clay content. The agreement in the values and structures demonstrates that both measuring techniques (TDIP and FDIP) provide quantitatively similar results.

Although promising, the  $K$ - $\sigma''$  model presented in Equation 6.6 disregards the frequency-dependence observed in the electrical properties for both fields (Figure 6.4) and laboratory (Figure 6.5) data. Alternatively, we can use the obtained Cole-Cole parameters (i.e.,  $M_n$  and  $\sigma_0$ ) in the Equation 6.7 to obtain the hydraulic conductivity image presented in Figure 6.8c. The  $K$ - $M_n$  estimations are consistent with those resolved through a single frequency (i.e.,  $\sigma''_{1\text{Hz}}$ ), with high values ( $1 \times 10^{-4.5} \text{ m s}^{-1}$ ) close to the surface at both ends of the profile corresponding to the unsaturated, unconsolidated materials. Figure 6.8c reveals the highest  $K$  values ( $\leq 1 \times 10^{-4} \text{ m s}^{-1}$ ) close to the surface, between 40 and 110 m along the imaging plane. Although such anomaly is also observed in the  $K$ - $\sigma''$  images (i.e., Figure 6.8a and 6.8b), the hydraulic conductivity values are higher in Figure 6.8c and extended over a broader area. This discrepancy highlights the advantage of SIP surveys, which is sensitive to subsurface variations captured in a broad frequency range. Thus, the information gained through SIP measurements provides insight into subsurface heterogeneities that might not be resolved entirely through single frequency IP data.

We note here, that in order to solve for the same range of hydraulic conductivity values through single- and multi-frequency IP data, we had to modify the first experimental parameter in Equation 6.7 from  $4.03 \times 10^{-9}$  to  $4.03 \times 10^{-10}$ . This slight change is likely related to the lack of accurate measurements of the formation factor available for SIP measurements. In case of Figure 6.8c, we used an approximation (i.e.,  $F = \sigma_f/\sigma_0$ ), which neglects the contribution of  $\sigma'_s$  to the formation factor. In this regard, the Equation 6.6 linking  $K$ - $\sigma''_{1\text{Hz}}$  offer the advantage that does not require any information about  $F$ . Nonetheless, the consistency observed between Figures 6.8a, 6.8b and 6.8c demonstrates the applicability to our data of the experimental models proposed by Weller et al. (2015).

#### 6.4.2 Independent quantification of the hydraulic conductivity through a joint inversion scheme

Both resistivity and seismic refraction tomography are commonly used methods in landslide investigations (Jongmans and Garambois, 2007; Hibert et al., 2012; Pazzi et al., 2019; Whiteley et al., 2019; Uhlemann et al., 2016). Thus, in this study we decided to investigate the joint inversion of data coming from both techniques. Employing the joint inversion we can obtain the electrical conductivity, porosity, and

thus the formation factor in an imaging framework. The latter is linked to the effective porosity and, as mentioned by Weller et al. (2015), is a critical parameter for estimating the hydraulic conductivity from electrical data sets. Figure 6.8d presents the estimations using Equation 6.7, yet based on the  $M_n$  and  $F$  obtained from the joint inversion. We can observe that in general the hydraulic conductivity patterns are consistent with those resolved through SIP measurements (Figure 6.8c). We argue that such consistency demonstrates the ability to obtain a good approximation on the hydraulic conductivity at the field-scale either through TDIP, FDIP and SIP imaging as well as through the proposed ERT–SRT joint inversion approach deployed here. We believe such evaluation is fair considering that  $K$ -estimations presented in Figure 6.8 are computed using completely different data and inversion approaches (SIP data vs. ERT–SRT).

In general, the analysis of only conductivity data at low and high frequencies lacks the resolution required to assess variations in the polarization response that can only be retrieved through TDIP, FDIP or SIP measurements. Consequently, the IP has emerged as an important method in hydrogeological investigations (Revil and Florsch, 2010; Binley et al., 2015; Revil et al., 2020). However, the incorporation of a different source of data in the joint inversion scheme, such as the variations in the seismic velocities provides subsurface information that cannot be resolved through conductivity images. In particular, joint inversion results resolve for minimal changes for both  $\sigma_0$  and  $\sigma_\infty$  images in the weathered materials; thus, a low  $M_n$  value (see Equation 6.5), which is inconsistent with those resolved through SIP. However, the improved estimation of  $F$  through the joint inversion accounting for the increase in the  $v_p$  (and the decrease in the porosity) balances the lack of information regarding variations in  $M_n$ , thus, permitting to resolve for consistent  $K$  values in comparison with those obtained through SIP.

We have argued that hydraulic conductivity estimations based on the SIP imaging method as presented in Figure 6.8c can be evaluated through the  $K$  estimations obtained by means of the joint inversion results presented in Figure 6.8d. The lack of direct measurements of  $K$  at the study area limits a more rigorous evaluation. However, samples recovered from BK1 and BK3 were analyzed in the lab to quantify the gravimetric water content (c.f., Figure 6.1), which can be used to evaluate the estimations resolved through the joint inversion. The volumetric water content ( $\theta$ ) measured in soil samples fluctuates around 0.4, which is in agreement with the values obtained through the joint inversion. Hence, we believe that Figure 6.1 demonstrates that quantities estimated through our joint inversion fairly reproduce the subsurface properties, thus supporting the hydraulic conductivity estimation presented in Figure 6.8.

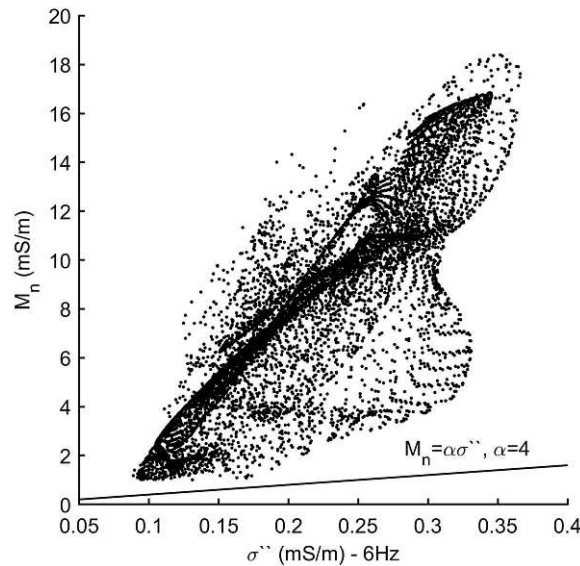


**Figure 6.9:** Plots of the normalized chargeability ( $M_n$ ) fitted to SIP imaging results and the imaginary conductivity ( $\sigma''$ ) after the inversion of the data collected at 6 Hz. Such frequency represents the closest one to the geometric mean between the minimum (1 Hz) and maximum (60 Hz) frequencies fitted with the Cole-Cole model for the hydraulic conductivity estimations. The solid line indicates the linear model proposed by Revil et al. (2020) to link both quantities.

As observed in plots presented in Figure 6.1, the soil samples reveal large variations in samples collected between 2 and 4 m depth for both grain size and (especially) the gravimetric water content. Such variations cannot be solved through the smooth-constrained algorithm used in this study (i.e., for either IP or the joint inversion). For instance,  $\theta$  obtained from gravimetric water content (assuming a constant density of  $1300 \text{ kg m}^3$ ) vary between 0.1 and 0.6; whereas our inversions resolve only for changes between 0.3 and 0.5. The changes observed in the laboratory data might be related to the characteristics of the samples (e.g., volume) and only provide information at the sampling location. Additionally, the discrepancies can be also explained considering that the calculation of water volumetric constant assumes a constant soil density although variations in the materials at depth are clear (see Figure 6.1). Accordingly, the lack of spatial resolution hinders the assessment of changes across the slope; thus, highlighting the advantage of the geophysical imaging techniques presented, namely SIP or the joint inversion.

To extend our analysis, we also investigated the applicability of the relationship proposed by Revil et al. (2020) linking  $K$  with  $\sigma_\infty$  and  $M_n$  presented in Equation 6.11. We used the parameters obtained after fitting the Cole-Cole model to the SIP data (see Figure 6.6); however, estimations resulted in negative  $K$  values. It means that

$\sigma_\infty < M_n/R$  in Equation 6.11, for  $R=0.1$  (as provided by Revil et al., 2020). In our case,  $M_n$  is fitted independently to the SIP inversion results and no constraint is imposed; thus, resulting in values that render Equation 6.11 inappropriate for our data. The inversion of the Cole-Cole ( $M$  and  $\sigma_\infty$ ) parameters directly from the primary and secondary voltages measured in the TDIP data as proposed by Soueid Ahmed and Revil (2018) warrants the computation of parameters that fulfill the petrophysical model underlying in Equations 6.11 and 6.12.

Instead of fitting a Cole-Cole model, Revil et al. (2021) estimate the normalized chargeability from the imaginary conductivity, using a linear approximation (i.e.,  $\sigma'' \propto M_n$ ). In Figure 6.9, we present plots of the  $M_n$  as a function of the  $\sigma''$ , with the latter obtained from the inversion of the data collected at 6 Hz, which is the data set closest to the geometric mean of the frequency range used to fit the Cole-Cole parameters (between 1 and 60 Hz). As observed in Figure 6.9,  $\sigma''$  increases with increasing  $M_n$ ; however, the values are spread over a wider range and it is not possible to obtain a linear correlation between both parameters. In Figure 6.9, we also impose the linear correlation using the equation proposed by Revil et al. (2020), demonstrating that such relationship is not applicable to our data. Nevertheless, Figure 6.7 demonstrates that positive water content can be solved through the joint inversion, which incorporates the dynamic Stern layer model (Equations 6.8 to 6.10), and the petrophysical model in Equation 6.12 linking  $\theta$  to  $\sigma_\infty$  and  $M_n$ . This is achieved due to the volume conservation constraint honored during parameter estimation to ensure that the volumetric fractions of soil, water and air equal unity (e.g., Wagner et al., 2019).

The joint-inversion algorithm used here is based on the Timur equation linking porosity and P-wave velocities (see Wagner et al., 2019, for further details). However, such approximation may be limited in unsaturated materials, where  $v_p$  is not only controlled by changes in density, but also due to interparticle stress and in-pore pressure (e.g., Shen et al., 2016). The Timur equation does not consider such effects and may mislead the inverted porosity values, and thus the  $K$  estimations, especially for low velocities (e.g.,  $v_p < 800 \text{ m s}^{-1}$ ) in the unsaturated clayey materials (see Hibert et al., 2012; Uhlemann et al., 2016). The incorporation of resistivity data may help to correct the porosity estimations in the joint inversion, yet future research requires evaluating the use of a different petrophysical model, for instance the Hertz-Mindlin theory (see Shen et al., 2016)(see Shen et al., 2016). Moreover, further research should also consider the extension of the joint-inversion to directly solve for the elastic properties by including S-wave or surface waves data (see Hibert et al., 2012; Uhlemann et al., 2016, and references therein). Including such measurements, may permit for an improved estimation of the moisture content and thus, the hydraulic conductivity.

### 6.4.3 3D subsurface model of study area

To fully exploit the TDIP data collected at the Hofermuehle site, we present in Figure 6.10 a visualization of the hydraulic conductivity as obtained from the 3D inversion of the six TDIP lines. Accordingly, we do not present an interpolation of the 2D images, but an actual subsurface 3D model that simultaneously fits data collected in all lines in terms of the complex conductivity, which is then transformed to  $K$  using Equation 6.6. The advantage of collecting mapping (i.e., 3D) data is that it allows to investigate spatial variations in the electrical and hydraulic properties of the landslides. The 3D inversion is recommended to improve the consistency between the obtained results for the data collected in each line. As expected from the Figure 6.3, the 3D model resolves minimal changes in the West-East direction, but is mainly dominated by the North-South variations in the central part of the investigated area. In particular, Figure 6.10 reveals the potential of a 3D model to accurately delineate the geometry of the poor drainage area identified in the Southern part of the landslide.

The lateral variations in subsurface properties resolved through the geophysical models, and the estimated variations in porosity and  $K$ , demonstrate a poor hydraulic connectivity between the North and South sections of our profile and may be a first step to explain the large changes in the water level recorded within the piezometers (between 1 and 3 m bgs) on the Northern and Southern part of the investigation area (see Table 6.2). We need to consider that the model proposed by Weller et al. (2015) was developed for fully saturated samples, limiting its applicability in the top layer at the Hofermuehle site, consisting of not fully saturated sediments (see Table 6.2). Accordingly, the extension of the experimental parameters in Equations 6.6 and 6.7 for estimating  $K$  in not fully saturated materials requires further investigation. Further investigations also need to consider 3D SIP measurements, where we can resolve the frequency-dependence as well as the spatial variations of the electrical properties of the subsurface.

## 6.5 Conclusion

We used geophysical methods to investigate the Hofermuehle landslide in two steps. First, we conducted a mapping with TDIP to cover extensive areas in short acquisition times. Second, we carried out measurements with SRT and multi-frequency FDIP. Inversion results for TDIP and FDIP data generally reveal low conductivity and polarization values in areas close to the surface, corresponding to the unconsolidated materials, while higher values are resolved below corresponding to clay-rich

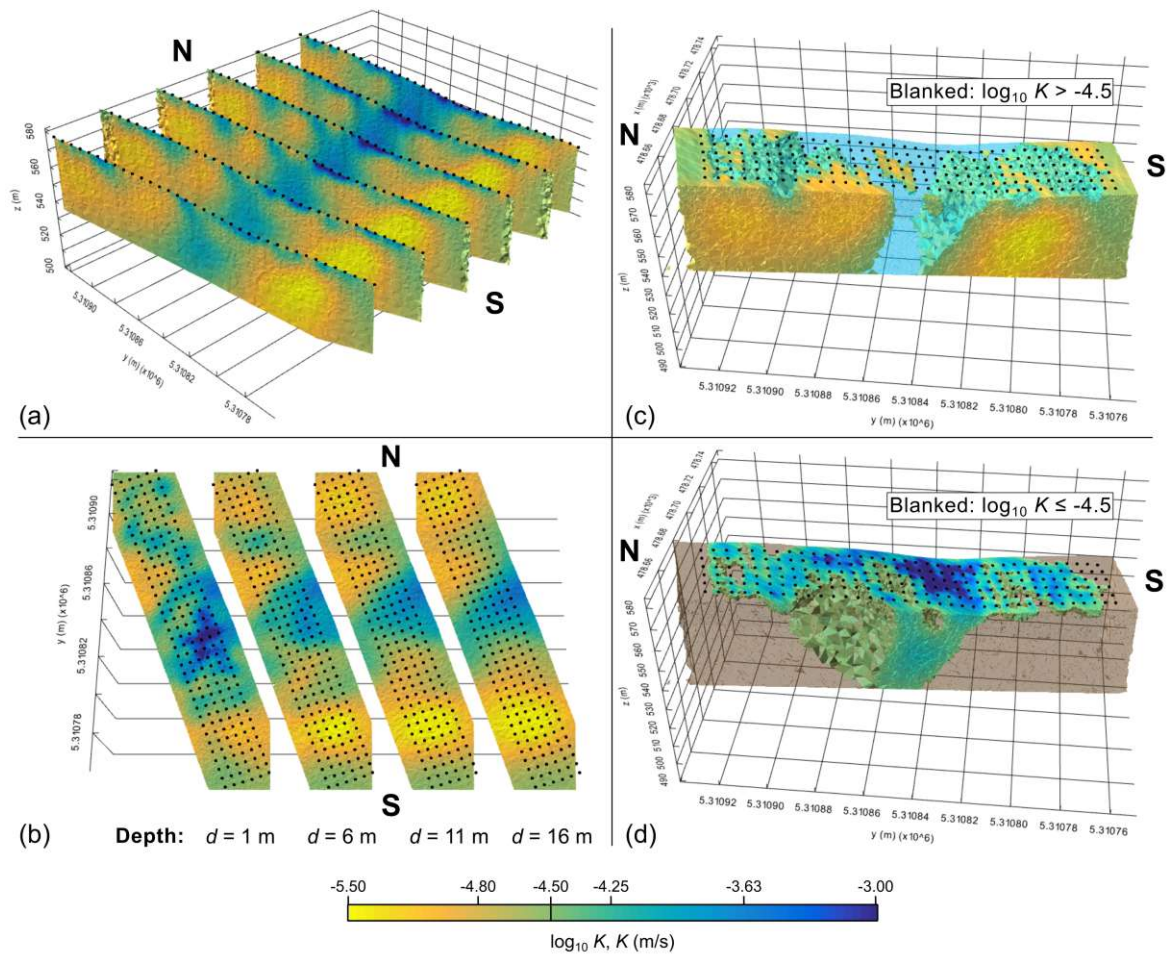


**Figure 6.10:** Inversion results for the 3D inversion of TDIP data expressed in terms of the hydraulic conductivity ( $K$ ). The dots on top of the plots indicate the position of the electrodes. All plots are oriented North-South.

materials from the Flysch formation. In FDIP data we resolve a layer with a thickness of ca. 8 m corresponding to weathered material with a polarization response that increases with increasing the frequency. The bedrock reveals the higher polarization response; however, this is only resolved in TDIP data, due to the longer electrode spacing and profile length used for the data collection. Thus, we have no information about the frequency-dependence of the Flysch materials in the bedrock. There is a clear discontinuity in the center of our geophysical profiles characterized by low values of  $\sigma'$  and  $\sigma''$  which we interpret as materials with lower clay content than those on the North and South sections of our profile.

The use of a petrophysical model, derived from laboratory investigations, permitted the estimation of the hydraulic conductivity in an imaging framework from TDIP and FDIP data. The hydraulic conductivity images permitted to delineate a preferential flow path corresponding to high  $K$  values in the central part of the IP profiles, where

the lowest polarization values were observed. Lower hydraulic values ( $< 1 \times 10^{-5} \text{ m s}^{-1}$ ) are resolved downhill to the South, indicating a possible area where groundwater may accumulate. SIP images are consistent to those obtained through TDIP and FDIP data, but reveal a significant frequency dependence, with the higher  $\sigma''$  values observed at high frequencies ( $> 60 \text{ Hz}$ ). Such frequency-dependence is also observed in laboratory measurements of soil samples. Although the  $K$  images are consistent between SIP and TDIP (and FDIP at 1 Hz), the former reveal a higher contrast in the resolved values and a slight variation in the geometry of the unit. Hence, hydraulic conductivity estimations based on a single frequency may not fully reveal subsurface heterogeneities, which can only be resolved through the collection of SIP data.

The seismic refraction data permitted the delineation of the contact between unconsolidated material and the weathered Flysch, corresponding to contrasting values in the velocity of the P-waves ( $v_p$ ) in agreement with the vertical variations in IP images. The application of an algorithm inverting resistivity and seismic data permitted the consistent estimation of  $K$  with those obtained by means of the SIP method. We argue that both approaches are independent and can be applied to evaluate the results presented. The joint inversion algorithm neglects the IP response and it is only controlled by variations in  $\sigma'$  and  $v_p$ ; thus permitting an improved estimation of the  $F$  and  $K$ . On the opposite, estimations based on  $M_n$  in our study are mainly controlled by the frequency of the IP response, which is then used to fit Cole-Cole parameters compute the hydraulic conductivity. Our results demonstrate that IP imaging permits delineating areas of poor-drainage (i.e., low  $K$ ) in the subsurface where groundwater may accumulate, which is commonly a precondition for land sliding.



# 7 | Geophysical imaging of the spatial variability in the pore space connectivity: A field-scale application in undisturbed natural soils

## 7.1 Introduction

Chapters 4 and 5 presented the application of the PJI scheme for the quantification of the subsurface water or ice content from geophysical data collected at specific times. In contrast, investigations conducted at the Hofermuehle landslide presented in chapter 6 aimed at the characterization of spatial variations in the hydraulic properties of the subsurface materials to delineate preferential water flow paths. To this end, the application of an empirical petrophysical model (Weller et al., 2015) permitted the estimation of the hydraulic conductivity  $K$  from IP data in an imaging framework; whereas PJI imaging results allowed for an independent evaluation of the resolved  $K$  estimates.

In case of the PJI, the  $K$  model was obtained through the petrophysical relationship proposed by Weller et al. (2015) based on the normalized chargeability  $M_n$  and the formation factor  $F = \Phi^{-m}$ . While the PJI scheme can solve for the spatial variability in the porosity  $\Phi$  and  $M_n$ , the cementation exponent  $m$  is considered constant within the model space. Hence, for the computation of  $F$ , a homogeneous model for  $m$  was considered, which is only a rough approximation of the true connectivity of the pore space. Moreover, the PJI neglects the IP response but instead is solely controlled by variations in the conductive and mechanical properties of the subsurface. Irrespective of such simplifying assumptions, the  $K$  model obtained through the PJI-based approach is consistent with  $K$  models obtained through approaches relying on IP measurements.

The results presented in chapter 6 indicate that in case of the Hofermuehle landslide the  $K$  estimation is likely more dependent on the formation factor than on the polarization response (e.g., Weller et al., 2015). Hence, by solving for the spatial variability in  $\Phi$  the PJI compensates for its inherent lack of information regarding the capacitive properties of the subsurface materials. Yet, for an enhanced estimation of the subsurface hydraulic properties, the connectivity of the pore space – expressed in terms of

$m$  – might be even more important as it controls water flow in the subsurface.

Direct methods for the quantification of  $m$  refer to the laboratory analysis of rock or soil samples, which allow for the formulation of petrophysical models relating hydrogeological and geophysical parameters (e.g., Slater and Lesmes, 2002a; Revil, 2012; Weller et al., 2013; Weller et al., 2015). Following Glover (2015), mean values of  $m$  correspond to the negative gradient in a  $\log(F)$ - $\log(\Phi)$  plot, whereas for individual samples  $m$  can be assessed as

$$m = -\frac{\log(F)}{\log(\Phi)} \quad (7.1)$$

Although soil samples provide direct information, the obtained data might not be able to resolve the variability in  $m$  across the study area due to their inherently limited spatial resolution. Moreover, measurements and results of laboratory investigations might be affected by the experiment design and sample preparation (e.g., Bairlein et al., 2014). Considering the importance of  $F$  for the estimation of hydraulic properties (e.g., Weller et al., 2015), quantifying the spatial variability in  $m$  with an adequate spatial resolution over the entire model space could lead to enhanced reliable  $K$ -estimates.

This part of the thesis investigates the possibility to estimate the spatial variability in  $m$  in an imaging framework by further expanding the PJI scheme. Such an approach would not only aid in the investigation of water drainage and water flow in landslides, but would also allow for an improved assessment and monitoring of contaminant movement (e.g., landfill leachate), and might also allow for the delineation of areas where water and ice can accumulate at (alpine) permafrost sites.

## 7.2 Materials and Methods

### 7.2.1 Quantitative estimation of the cementation exponent $m$

The PJI scheme developed and used in chapters 5 and 6 can be further modified to solve for the spatial variability in  $m$  through the joint inversion of seismic refraction and electrical resistivity data (see Figure 7.1). To this end, inversion framework is adapted, whereas the underlying petrophysical model remains unchanged, i.e., the set of equations is the same as in chapters 5 and 6.

In particular, the proposed modification of the PJI scheme expands the parameter vector  $\mathbf{p}$  holding the three fractional soil constituents, namely water ( $f_w$ ), air ( $f_a$ ) and

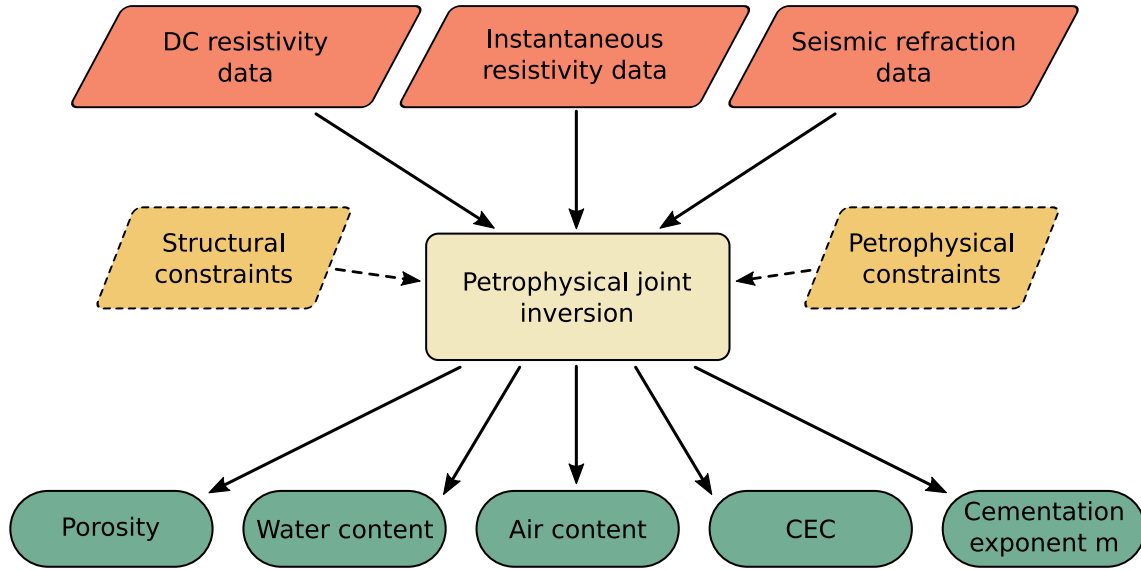


**Figure 7.1:** Schematic illustration of the proposed PJI scheme allowing for the estimation of the cementation exponent  $m$  in an imaging framework by jointly inverting seismic refraction data, as well as low frequency (DC) and high frequency (instantaneous) resistivity data.

rock ( $f_r$ ), by adding  $m$  as a new target parameter:

$$\mathbf{p} = [f_w, f_a, f_r, \mathbf{m}] \quad (7.2)$$

Similar to previous applications, the inversion scheme minimizes the following objective function:

$$\begin{aligned} \Psi(\mathbf{m}) = & \| \mathbf{W}_d(\mathbf{d} - \mathcal{F}(\mathbf{m})) \|_2^2 + \alpha^2 \| \mathbf{W}_m \mathbf{m} \|_2^2 \\ & + \beta^2 \| \mathbf{W}_p^{sum} \mathbf{p} - \mathbf{1} \|_2^2 \\ & + \gamma^2 \| \mathbf{W}_p(\mathbf{p} - \mathbf{p}_0) \|_2^2 \rightarrow \min \end{aligned} \quad (7.3)$$

The third term in Equation 7.3 constrains the inversion through an interparameter relationship, namely the volume conservation constraint (VCC)  $f_w + f_a + f_r = 1$ . For previous applications,  $\mathbf{W}_p^{sum}$  referred to a block matrix holding adjacent identity matrices acting on  $\mathbf{p}$  to penalize solutions for which the sum of the three fractional soil constituents deviates from unity. Due to the proposed modification  $m$  becomes part of the parameter vector yet is not affected by the VCC. Accordingly, the matrix  $\mathbf{W}_p^{sum}$  needs to be defined as  $\mathbf{W}_p^{sum} = [\mathbf{I}, \mathbf{I}, \mathbf{I}, \mathbf{0}]$ .

The expansion of the parameter vector requires an adaption of the Jacobian matrix  $\mathbf{J}$ , which needs to consider variations in the seismic travel times and the apparent

electrical resistivity at a low and a high frequency with respect to  $m$ :

$$\mathbf{J} = \begin{bmatrix} \frac{\partial t}{\partial f_w} & \frac{\partial t}{\partial f_a} & \frac{\partial t}{\partial f_r} & \frac{\partial t}{\partial m} \\ \frac{\partial \log(\rho_{a,\infty})}{\partial f_w} & \frac{\partial \log(\rho_{a,\infty})}{\partial f_a} & \frac{\partial \log(\rho_{a,\infty})}{\partial f_r} & \frac{\partial \log(\rho_{a,\infty})}{\partial m} \\ \frac{\partial \log(\rho_{a,0})}{\partial f_w} & \frac{\partial \log(\rho_{a,0})}{\partial f_a} & \frac{\partial \log(\rho_{a,0})}{\partial f_r} & \frac{\partial \log(\rho_{a,0})}{\partial m} \end{bmatrix} \quad (7.4)$$

By minimizing the misfit between the observed and the modeled data (first term in Equation 7.3) the model for  $m$  is updated at each iteration together with the fractional soil constituents. Accordingly, the spatial variations in  $m$  are resolved through the joint inversion of seismic refraction and electrical resistivity data collected at a high and a low frequency.

### 7.2.2 Application of the modified PJI scheme to field data

To investigate the applicability of this modified version of the PJI scheme an exemplary data set was collected in the Hydrological Open Air Laboratory (HOAL) in July 2022. The HOAL is located in Petzenkirchen (Austria) and refers to a 66 ha large catchment where the long-term scientific activities aim at an enhanced understanding of surface-groundwater interactions (for further details the reader is referred to Blöschl et al., 2016). In particular, the possibility to perform hydrological investigations, e.g., infiltration or pumping tests, renders the HOAL a suitable study area that facilitates the further development and testing of the PJI scheme.

For the data set considered here seismic refraction (SR) and SIP data were collected along a single profile (see Figure 7.2). Geological descriptions and the grain size distribution (GSD) obtained from the drill cores extracted from the borehole located in the center of the profile allow for a first evaluation of the obtained imaging results (see Table 7.1).

The SR survey was conducted using a DMT Summit data acquisition system together with 24 vertical geophones (corner frequency 30 Hz) deployed with 4 m spacing between them. Shots were conducted at the geophone positions as well as between geophones. Elastic waves were generated by hitting a plastic plate with a 9 kg sledgehammer; whereas two hammer blows per shot point sufficed to obtain a high signal-to-noise ratio due to the low ambient seismic noise in the study area. For the collection of the electrical data the Data Acquisition System Multisource (DASM, from MPT-IRIS Inc.) was used, which allows the physical separation of transmitter and receiver; thus, mitigating the effect of cross-talking within the device on the data (further details can be found in chapter 6). The measurements were conducted based on 64 electrodes deployed with a spacing of 1.5 m between them. The data were collected

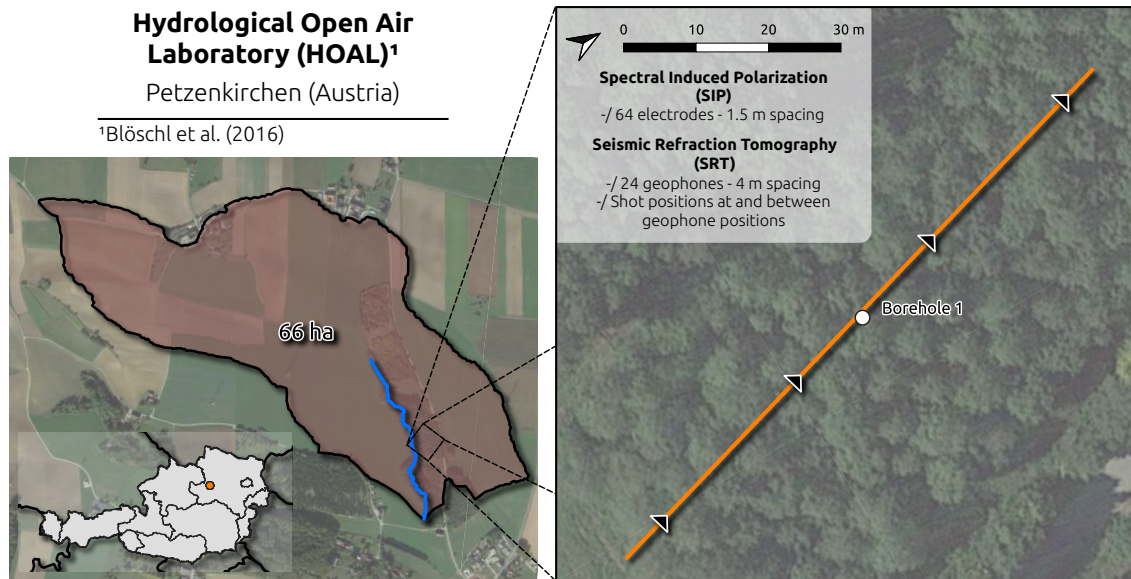


**Figure 7.2:** Map showing the extent of the Hydrological Open Air Laboratory (HOAL; Petzenkirchen, Lower Austria). The study area considered here is located close to the natural surface water outlet of the HOAL catchment. The solid line shows the position and orientation of the geophysical profile, with the direction of the measurements indicated by the filled triangles. The imposed circle in the center of the profile indicates the position of a borehole.

for 16 frequencies ranging from 0.1 to 240 Hz by using DD skip-0 and DD skip-3 configurations.

For the application of the modified PJI scheme, the SR and SIP data were processed following the procedures described in chapter 6. Due to the influence of coupling effects at frequencies above 80 Hz the  $|\sigma|$  collected at 1 Hz and 75 Hz are used as the DC and instantaneous conductivity. In the petrophysical model underlying the PJI the saturation exponent was defined as  $n = 2$  and for the conductivity of the groundwater a value of  $0.1 \text{ mS m}^{-1}$  was used as obtained from direct measurements. The seismic velocities ( $v_p$ ) of water, air and rock were chosen as  $1500 \text{ m s}^{-1}$ ,  $330 \text{ m s}^{-1}$  and  $3500 \text{ m s}^{-1}$ , respectively; whereas the grain density was assumed to be  $2650 \text{ kg m}^{-3}$ . The values for parameters  $B$  and  $\Lambda$  associated with the dynamic Stern layer model were taken from Revil et al. (2020). To reduce the degrees of freedom in the inversion and ensure physically plausible solutions, the upper and lower limits for the estimated  $m$  values were set to 1.5 and 4.5, respectively (e.g., after Glover, 2015). Based on homogeneous initial models for porosity  $\Phi$  and  $m$  referring to 40 % and 2, respectively, the PJI results presented here are associated with a  $\chi^2$  of approximately 3.0; thus, indicating that the resolved subsurface model can sufficiently explain the measured

**Table 7.1:** Direct information regarding geological and geochemical properties of the subsurface materials obtained from the borehole located in the center the investigated profile.

Sampling depth		Grain size distribution			pH	CaCO <sub>3</sub> (%mass)
From (m)	To (m)	Sand (%)	Silt (%)	Clay (%)		
2.2	2.4	63.4	23.5	13.1	7.63	80.6
2.8	3.0	15.2	64.8	20.0	7.62	12.0
3.4	3.6	12.4	67.8	19.8	7.71	11.4
3.6	3.8	7.0	72.9	20.2	7.49	21.2
4.0	4.2	12.7	69.1	18.2	7.53	28.8
4.6	4.8	9.1	68.1	22.8	7.42	15.7
5.2	5.4	10.5	70.2	19.3	7.56	27.9
5.4	5.6	12.9	69.2	17.9	7.59	30.8
7.2	7.4	5.0	58.6	36.4	7.60	19.0

data within their respective error bounds.

## 7.3 Results and Discussion

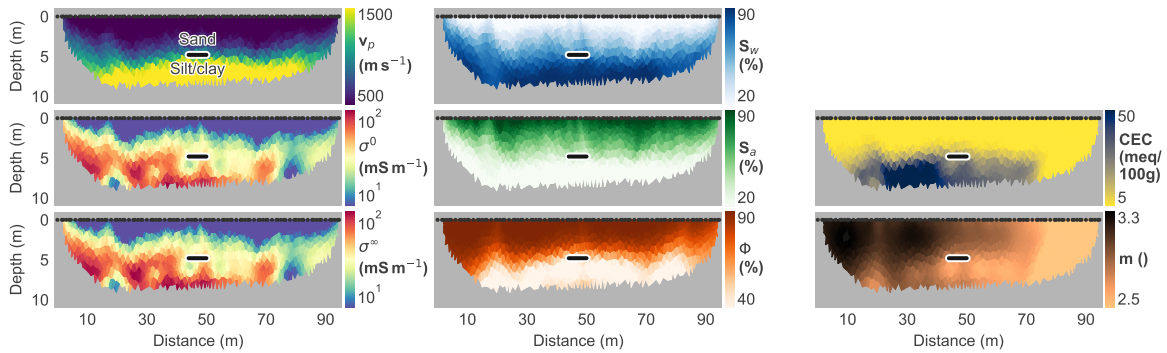
### 7.3.1 Interpretation of the resolved subsurface models

Figure 7.3 presents the imaging results obtained through the modified PJI scheme in terms of geophysical and hydrogeological parameters.

The seismic image solves, in general, for two layers in the subsurface. The top layer extending from the ground surface down to a depth of approximately 5 m is characterized by seismic velocity values below approximately  $750 \text{ m s}^{-1}$  indicating moderately consolidated materials. At 5 m depth the seismic image resolves a sharp increase of the  $v_p$  to values larger than  $1500 \text{ m s}^{-1}$  in the bottom layer. The resolved contrast coincides with the transition from sandy soil to a higher fraction of silts and clays observed in the drill cores recovered at the location of the borehole (see Table 7.1).

Similarly, the electrical images ( $\sigma_\infty$ ,  $\sigma_0$ ) solves for a two-layered subsurface model; yet, the resolved thickness of the layers is different than in the seismic image. For both frequencies, conductivity values below  $10 \text{ mS m}^{-1}$  are observed in the top layer suggest moderately saturated unconsolidated materials with a varying thickness of 0 to 3 m. Beneath this layer the electrical images resolve a sudden increase to conductivity values larger than  $25 \text{ mS m}^{-1}$ ; yet, the contact between the sandy soil in the near-surface and the silts and clays at depth cannot be resolved.

The model for the water saturation  $S_w$  confirms the interpretation of moderately saturated materials in the top layer ( $f_w < 20 \%$ ). At depths larger than approximately



**Figure 7.3:** Joint inversion imaging results for data collected along a single profile expressed in terms of the geophysical parameters seismic velocity ( $v_p$ ) and electrical conductivity ( $\sigma_0$ ,  $\sigma_\infty$ ), the fractional soil constituents porosity ( $\Phi$ ), air saturation ( $S_a$ ), water content ( $WC$ ), as well as the soil properties cation exchange capacity ( $CEC$ ) and cementation exponent  $m$ . The black dots along the surface of each model represent the sensor/shot positions. A horizontal line indicates the transition from the sandy top layer to the bottom layer characterized by silts and clays as observed in the drill core extracted from the borehole.

3 m  $S_w$  increases to an average value of ca. 40%. The transition to the silty/loamy layer coincides with a further increase in  $S_w$  to values of  $> 70\%$ .

For the air saturation  $S_a$ , values larger than 20% are resolved in the near-surface (depths between 0 to 5 m) corresponding to the sandy soil. Beneath this layer the  $S_a$  drops dramatically to values below 20% delineating the contact to the bottom layer characterized by an increase silt and clay content.

Similar to the  $S_w$  and  $S_a$  models, the transition from sands to silts and clays is delineated also in the porosity model  $\Phi$  indicated by contrasting values of  $\Phi > 50\%$  and  $\Phi < 40\%$  for the top and bottom layer, respectively. However, the resolved porosity values in the upper layer appear to be overestimated considering that the analysis of soil samples reported an average porosity of approximately 40% in this part of the HOAL catchment.

Along the investigated profile the PJI solves for low  $CEC$  values ( $< 5$  meq/100g) down to depths of approximately 5 m corresponding to the sandy top layer. Below 5 m depth the  $CEC$  models resolves a substantial increase to values above 30 meq/100g likely related to changes in the grain size with depth as reported from direct observations.

In terms of the cementation exponent  $m$ , the modified PJI scheme solves for a moderate spatial variability with values varying between 2.3 and 3.3. In general, the  $m$  model shows both horizontal and vertical variations, with the highest values (around  $m = 3.0$ ) found in the first 20 m along profile direction, and the lowest values

( $m < 2.5$ ) resolved between 70 m and 90 m along profile direction. The relatively high values resolved in the sandy top layer ( $m \approx 3$ ) indicate a low connectivity in the pore space, which is counterintuitive considering that such values would indicate moderately compacted carbonate rocks (e.g., Glover, 2015). The contact to the layer characterized by an increased silt and clay content coincides with a decrease to marginally lower values of  $m \approx 2.5$ ; yet, the contrast is weaker than in the other resolved subsurface models.

### 7.3.2 Deriving further soil properties from the PJI imaging results

The polarization of the subsurface materials expressed in terms of the normalized chargeability  $M_n$  can be obtained as the difference between the high and low frequency conductivity models (see Figure 7.4). Similar to the imaging results presented in Figure 7.3, the  $M_n$  model delineates two layers in the subsurface. The top layer with a varying thickness of 0 to 3 m is characterized by values lower than  $0.5 \text{ mS m}^{-1}$  indicating dry unconsolidated sediments. Beneath this layer, the polarization increases reaching values of more than approximately  $10 \text{ mS m}^{-1}$ . The sharpest increase is resolved at 5 m depth corresponding to the transition from the sandy top soils to the layer characterized by a higher silt and clay content.

The formation factor  $F = \Phi^{-m}$  is resolved from the  $\Phi$  and  $m$  models estimated through the modified PJI scheme (see Figure 7.4). The obtained  $F$  model resolves exceptionally low values ( $< 4$ ) for the sandy soil in the top layer (depths between 0 m and 5 m), whereas the silty/clayey bottom is characterized by values larger than 8. In contrast to previous applications (see chapter 6), the quantification of  $F$  considers the spatial variability in  $m$  instead of a homogeneous distribution, and thus refers to a methodically enhanced estimation of  $F$ .

The spatial variability in the hydraulic conductivity  $K$  can be computed from the  $M_n$  and  $F$  models as (Weller et al., 2015):

$$K = \frac{g\delta}{\eta} \frac{4.03 \times 10^{-10}}{F^{3.68} M_n^{2.41}}, \quad (7.5)$$

with  $g$ ,  $\delta$  and  $\eta$  denoting the gravitational acceleration, the bulk density and the fluid viscosity, respectively. The interpretation of the resolved subsurface models presented in Figures 7.3 and 7.5 indicates that the materials in the near-surface (0 to 3 m) refer to unsaturated sediments, which is sustained by the correspondingly high  $K$  values ( $> 1 \times 10^{-4} \text{ m s}^{-1}$ ). At depth between 3 m and 5 m a decrease of  $K$  to approximately  $1 \times 10^{-5} \text{ m s}^{-1}$  is resolved. The lowest  $K$  values ( $< 1 \times 10^{-6} \text{ m s}^{-1}$ ) are resolved in

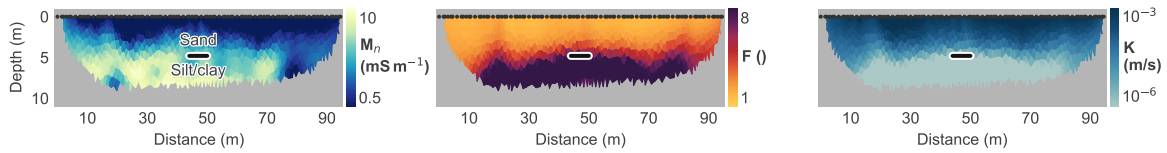


**Figure 7.4:** Subsurface models computed from the PJI imaging results: the normalized chargeability  $M_n$  as the difference between the high and low frequency conductivity model; the formation factor obtained from  $\Phi$  and  $m$ ; and the hydraulic conductivity  $K$  computed after Weller et al. (2015) based on  $M_n$  and  $F$ . The black dots along the surface of each model represent the sensor/shot positions. A horizontal line indicates the transition from the sandy top layer to the bottom layer characterized by silts and clays as observed in the drill core extracted from the borehole.

the bottom layer characterized by a low sand content. However, the exceptionally low  $F$  values resolved for depths between 0 m and 3 m might bias the quantification of  $K$  in the near-surface. A possible explanation for such low  $F$  values might be the extremely high porosity resolved in this layer, which in turn could be related to an insufficient modeling of the observed seismic travel times. In particular, the petrophysical model underlying the PJI uses a time-averaging approach based on the equation proposed by Wyllie et al. (1956) to describe the seismic velocity. However, the Wyllie equation is known to be associated with certain limitations especially in presence of sediments, where it tends to overpredict the porosity (Mavko et al., 2009). Similarly, the estimation of  $m$  might also be affected by shortcomings of the Wyllie equation yielding biased values for the pore space connectivity in presence of sediments.

### 7.3.3 Evaluation of the modified PJI scheme through independent geophysical methods and direct information

For an independent evaluation of obtained imaging results, Figure 7.5 compares  $M_n$  to the imaginary component of the CC ( $\sigma''$ ) resolved with CRTomo (Kemna et al., 2000) for the electrical data collected at 1 Hz and 75 Hz. The different ranges of values observed in  $M_n$  and  $\sigma''$  are due to the different input data and inversion approaches, as discussed in chapter 5; yet,  $M_n$  and  $\sigma''$  solve for similar structures in the subsurface. The largest polarization response is correspondingly resolved in the bottom layer characterized by a high fraction of silts and clays; whereas, the  $\sigma''$  model shows a sharper contrast at the contact between top and bottom layer than the  $M_n$  image. Accordingly, the consistency in the polarization images obtained through different inversion approaches evidences the general validity of the proposed modification of the PJI scheme.

Considering the sensitivity of the  $CEC$  to variations in the GSD the resolved  $CEC$

## 7 Field-scale imaging of the pore space connectivity

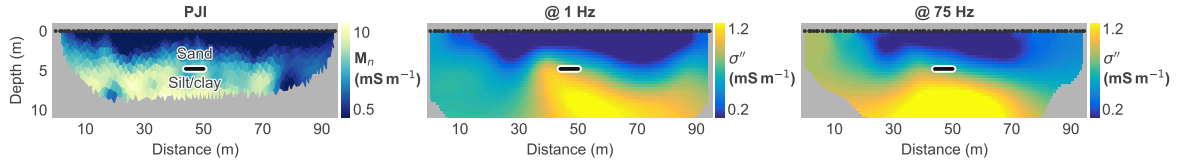


**Figure 7.5:** Capacitive properties of the subsurface expressed by the normalized chargeability  $M_n$  and the imaginary part of the complex conductivity  $\sigma''$  resolved from electrical data collected at 1 Hz and 75 Hz through PJI and a complex conductivity inversion, respectively. The black dots along the surface of each model represent the sensor/shot positions. A horizontal line indicates the transition from the sandy top layer to the bottom layer characterized by silts and clays as observed in the drill core extracted from the borehole.

model provides the means for a further independent evaluation of the PJI imaging results. To facilitate the comparison between the CEC and the GSD, Figure 7.6 presents the GSD at different depths observed in drill cores together with a 1D curve extracted from the resolved *CEC* at the position of the borehole.

Due to the lack of information regarding the GSD between 0 m and 2 m a direct comparison with the *CEC* in the top layer is not possible. Nonetheless, the high sand content (around 60 %) observed at ca. 2 m depth corresponds to the low *CEC* values resolved in the top layer. At depths larger than 2.5 m the *CEC* increases continuously; thus, suggesting an increase in the amount of fine grains in the soil. Such observation is confirmed by the sharp decrease in the sand content (< 20 %) reported at 3 m depth. As can be seen in Figure 7.6, the reduced sand content is largely compensated by an increase in the silt content, whereas the clay content stagnates at around 20 % down to approximately 5.5 m depth and doubling to ca. 40 % below 7 m depth. This relatively low and moderately increasing clay content suggest that the substantial increase in the *CEC* with depth cannot be explained by the amount of fine grains at depths larger than 3 m. Accordingly, the increase in the *CEC* is either associated with a different process in the subsurface or due to insufficiencies in the petrophysical model underlying the PJI scheme. In the proposed PJI scheme the *CEC* is estimated from the resolved polarization response as

$$CEC = (1 - f_r)^{m-n} \frac{M_n}{f_w^{n-1} \delta_g \Lambda}. \quad (7.6)$$

Equation 7.6 shows that the *CEC* is controlled by the resolved polarization response. However, the relatively low clay content observed in the drill cores cannot explain the high  $M_n$  values resolved at depths larger than 5 m. Accordingly, providing an explanation for the increase in the *CEC* requires the investigation of subsurface conditions

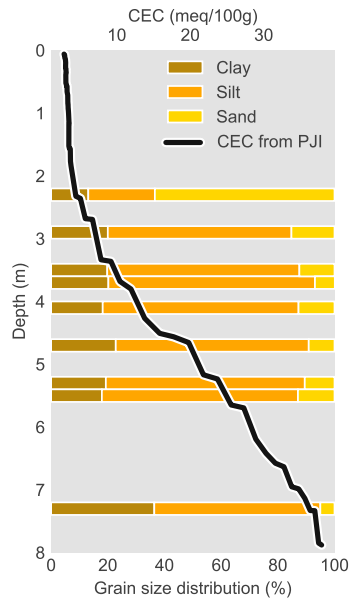


**Figure 7.6:** Comparison of the grain size distribution information obtained from the drill core extracted from the borehole located in the center of the profile. The solid curve represents the vertical distribution of the *CEC* extracted from the PJI-resolved *CEC* model at the location of the borehole.

or processes causing the strong polarization response.

Besides the GSD the analysis of the drill core also provides information regarding the pH value of the soil and the amount of calcium carbonate ( $\text{CaCO}_3$ ) in the subsurface (see Table 7.1). In natural environments, the precipitation of  $\text{CaCO}_3$  is a slow process occurring at geological time scales (Dhami et al., 2013). In frame of remediation or geotechnical engineering activities, the production of larger amounts of  $\text{CaCO}_3$  in a shorter amount of time is achieved through the microbially induced calcium carbonate precipitation (MICCP; Dhami et al., 2013) which is favored by increases in pH and alkalinity (Wu et al., 2010). Although no MICCP treatment has been reported in this area of the HOAL catchment, the increased pH values observed in the drill core could be an explanation for the high amount of  $\text{CaCO}_3$  in the soil (see Table 7.1).

The precipitation of  $\text{CaCO}_3$  is associated with the production of different polymorphs of carbonate crystals, with calcite and vaterite being the most common ones in case of MICCP (Dhami et al., 2013). In particular, the ability of the SIP method to monitor the precipitation of calcite in a non-invasive manner has been investigated by different studies (e.g., Wu et al., 2010; Saneiyani et al., 2018). Based on calcite precipitation induced in columns filled with glass beads Wu et al. (2010) were able to observe the associated polarization under controlled laboratory conditions. The observed quantitative correlation between the polarization response and the MICCP

demonstrated a linear increase in the polarization with the cumulative  $\text{CaCO}_3$  concentrations. From their observations Wu et al. (2010) concluded that the observed polarization response is due to electrochemical polarization in the EDL forming at the interface between the non-conductive calcite grains and the pore fluid. In a more recent study, Saneiyan et al. (2018) conducted a similar experiment, yet the authors used a sand-clay mixture instead of glass beads to allow for a more realistic approximation of field conditions. The experiment showed that SIP measurements provide information about different stages of the precipitation process, whereas surface area changes due to the  $\text{CaCO}_3$  precipitation is the key factor controlling the polarization.

The results of these studies can be considered as evidence for the increased  $M_n$  values observed at depths larger than 5 m; yet, the drill core analysis reports  $\text{CaCO}_3$  from approximately 2 to 7 m depth. Wu et al. (2010) associated the observed polarization to the EDL surrounding the calcite crystals, i.e., at the field-scale such effect has to be expected for (partially) saturated conditions. As presented in Figure 7.3, the water saturation  $S_w$  is low within the first 5 m below the ground surface and shows a sharp increase at larger depths. Accordingly, the increased  $S_w$  at depths larger than 5 m facilitates the formation of the EDL at the interface of the calcite grains, and thus the strong polarization response resolved with both the PJI scheme and the IP measurements. Although such argumentation provides an explanation for the observed polarization signatures, the implications for the estimation of the soil  $CEC$  requires further investigations at both laboratory- and field-scale.

Considering that the MICCP is used for soil stabilization measures, the investigations conducted by Saneiyan et al. (2018) also included measurements of the shear-wave velocity. In particular, the observed shear-wave velocity values increase with the ongoing  $\text{CaCO}_3$  precipitation, which indicates an increase in the soil stiffness (Saneiyan et al., 2018). Moreover, investigation of the samples columns at the end of the MICCP experiment revealed the stabilization of the sand-clay mixture demonstrating the role of calcite as a cementation agent (Saneiyan et al., 2018). Accordingly, the substantial amounts of  $\text{CaCO}_3$  found in the drill core might also provide an explanation for the relatively high  $m$  values resolved through the proposed PJI scheme.

However, as mentioned above, modeling the seismic velocity based on the Wyllie equation might be insufficient with regard to the quantification of the pore space connectivity. Several studies argue that for unconsolidated near-surface materials, modeling of the seismic velocity based on the Hertz-Mindlin and Biot-Gassmann theories is superior to approaches based on the Wyllie model (Bachrach et al., 1998; Shen et al., 2016). In particular, the recent model proposed by Shen et al. (2016) demonstrates that taking into account interparticle stress and variations in the pore

pressure enhances the prediction of seismic velocities in partially saturated unconsolidated sediments. Such improved estimation is due to the modified calculation of the total effective stress, which is particularly relevant in presence of clays.

In case of the HOAL imaging results presented here, the considerable amount of  $\text{CaCO}_3$  (increased soil stability) and the low clay content in the subsurface might counterbalance the shortcomings of the Wyllie equation. Moreover, the joint inversion of seismic and electrical data enhances the consistency in the resolved models; thus, potentially mitigating the effect of insufficiently modeled seismic velocity values on the estimated  $m$  model. Nonetheless, due to the lack of extensive ground truth information regarding the mechanical properties of the soil the resolved subsurface models have to be considered biased due to shortcomings in the approximation of seismic velocities. Such assumption is sustained by the particularly low porosity values resolved in the near-surface (0 to 3 m) indicating the need for further investigations.

## 7.4 Conclusions

This study proposed a modification of the PJI scheme developed and applied in chapters 5 and 6 to allow for the estimation of the cementation exponent  $m$  in an imaging framework. In particular, the presented implementation aims at the quantification of the spatial variability in  $m$  to obtain enhanced models for the formation factor  $F$ , and thus the hydraulic properties of the subsurface materials.

The application of the modified PJI scheme to seismic and electrical data collected in the HOAL (Petzenkirchen, Austria) demonstrated the practical applicability of the approach. In general, a good agreement between the resolved subsurface models and independently obtained imaging results as well as direct information was observed. Unexpectedly high values for  $m$  and a strong polarization response at depth could be associated with the presence of  $\text{CaCO}_3$  observed in drill cores. In particular, calcite increases soil stiffness, while the EDL forming at the interface between calcite grains and the pore fluid polarizes in presence of an external electrical field. Such agreement between the geophysical and direct observations at the field-scale with laboratory investigations were considered an independent evaluation of the proposed PJI scheme. However, further research is required to gain a deeper understanding of the subsurface properties and processes on the observed geophysical signatures and the effect on the hydrogeological parameters estimated through the PJI scheme proposed here.

Considering the evident shortcomings of the model used for the approximation of seismic velocities in near-surface unconsolidated materials the resolved PJI imaging results might be biased. Accordingly, future developments of the PJI scheme should

## 7 *Field-scale imaging of the pore space connectivity*

address the modification of the underlying petrophysical model to allow for an enhanced seismic velocity modeling taking into account the total effective stress during the parameter estimation.

## 8 | Conclusions and perspectives

This thesis provides transparent and scalable solutions for the processing and inversion of geophysical data collected in environmental and engineering investigations. In particular, the presented studies demonstrate the applicability of geophysical methods for the quantitative estimation of hydrogeological parameters related to both causes and consequences of climate change in Earth's near-surface regions. This final chapter summarizes the main advances of the self-contained studies presented in this thesis and also discusses the associated limitations and drawbacks aiming at the identification of potential topics for future research activities.

### 8.1 Modeling and processing of geophysical data sets

The `formikoj` library presented in chapter 3 provides a framework for the modeling and processing of geophysical data sets based on available open-source python libraries. Distributed under the MIT license and free of licensing costs `formikoj` enables users in academia to process their geophysical data in accordance with good research practices and following the FAIR data principle due to the usage of open file formats for data input and output.

In this thesis, the `formikoj` library was primarily used to develop a light-weight tool – the `SeismicRefractionManager` class – focused on the picking of first break traveltimes from seismic waveform data collected in 2D and 3D survey geometries. In particular, the `SeismicRefractionManager` provides innovative solutions and approaches for efficient data management, visualization and processing routines; thus, facilitating the development of transparent and reproducible seismic refraction processing workflows. Moreover, the `SeismicRefractionManager` is frequently used by students participating in geophysical data processing courses offered by the Research Unit of Geophysics at the TU Wien.

The development of the `SeismicWaveformModeler` class demonstrated the possibility to incorporate forward modeling functionalities of other libraries (here `pyGIMLi`; Rücker et al., 2017) into the `formikoj` framework to create synthetic seismic waveform data. Such modeling capabilities aim at supporting the design of seismic refraction survey layouts and the interpretation of signatures observed in field data. Moreover,

the `SeismicWaveformModeler` is routinely used to generate synthetic seismic waveform data with specifically defined random and systematic noise characteristics for teaching activities.

The concept of the `formikoj` library aims to facilitate the implementation of modeling and processing solutions for various geophysical methods. Present solutions focus on the processing of seismic waveform data collected with vertically oriented geophones, i.e., determining P-wave travel times. Although not presented in this work, the `SeismicRefractionManager` is also applicable for the processing of waveform data recorded with horizontal geophones, i.e., for the picking of S-wave travel times.

Another popular seismic method applied in environmental and engineering investigation is the multi-channel analysis of surface waves (MASW; Park et al., 1999), which leverages upon the frequency dependence of Rayleigh-type surface waves to solve for the shear-wave velocity. Commonly used MASW processing software packages are `ParkSeis`<sup>1</sup> or `SurfSeis`<sup>2</sup> as they provide functionalities for the visualization, picking and inversion of 1D dispersion curves. However, both software packages are exclusively developed for Windows operating systems and associated with licensing costs; thus, potentially limiting the usage in academia, as discussed in chapter 3. A recent open-source MASW solution is the `BEL1D` package developed by Michel et al. (2020) for the stochastic inversion of arbitrary 1D geophysical data. In particular, this package contains a module specifically designed for the inversion of MASW dispersion curves<sup>3</sup>. Accordingly, developing a light-weight MASW processing tool within the `formikoj` framework for the picking of dispersion curves and their subsequent inversion based on the `BEL1D` framework has the potential to overcome the limitations associated with existing commercial MASW software solutions.

Beyond seismic methods the `formikoj` library could be used for the development of processing tools for other geophysical methods applied in environmental and engineering studies, such as ERT, IP or electromagnetic methods. In particular, the processing of electrical (resistivity) data can be efficiently automatized in stand-alone python scripts; yet, the incorporation of these fundamental processing concepts in the `formikoj` library might facilitate the design of reproducible data processing workflows conducted within a freely available framework. Moreover, complementing automatized processing techniques through interactive visualization and processing capabilities could allow the user, e.g., to control the filtering of electrical data sets at the data point level through simple graphical user interfaces.

<sup>1</sup><http://masw.com/Software.html>, last accessed on December 2, 2022

<sup>2</sup><https://www.kgs.ku.edu/software/surfseis/index.html>, last accessed on December 2, 2022

<sup>3</sup>With the development of `pyBEL1D` the authors aim at providing the framework also as a python library (<https://github.com/hadrienmichel/pyBEL1D>)

## 8.2 PJI - advantages, limitations and the way forward

The studies presented in this thesis demonstrated that the petrophysical joint inversion is superior to the joint interpretation of seismic refraction and electrical resistivity data collected in near-surface environmental and engineering investigations. This is due to the fact that the PJI leverages upon the complementary sensitivities of the seismic and electrical methods to reduce the non-uniqueness associated with the geophysical inversion problem, and thus enhances the consistency in the resolved subsurface models. Furthermore, PJI schemes provide the means to directly solve for subsurface models in terms of the parameters of interest, e.g., soil constituents or hydrogeological properties of the subsurface materials; thus, reducing the uncertainty associated with the interpretation of the imaging results.

### 8.2.1 Quantitative estimation of hydrogeological parameters in different environments

#### *An alpine permafrost site*

Chapter 4 provided a detailed investigation of different inversion and interpretation approaches applied for data collected in alpine permafrost environments aiming at the quantification of the subsurface ice content. For the joint interpretation approach, independently resolved SRT and ERT images were transformed to the fractional soil constituents water, air, ice and rock content through the four-phase model (4PM) proposed by Hauck et al. (2011); whereas, the PJI scheme developed by Wagner et al. (2019) facilitated the joint inversion of the electrical resistivity and seismic refraction data sets solving directly for these parameters of interest.

A carefully designed synthetic study compared subsurface models resolved through the independent inversion and the PJI approach with special emphasis on the influence of structural and petrophysical constraints on the consistency in the obtained imaging results. This investigation showed that the rock and ice content are insufficiently estimated due to the similar properties of these media, i.e., both rock and ice are characterized by high seismic velocity and high electrical resistivity. In particular, the results highlighted that seasonal changes in the ice content tend to be resolved as changes in the rock content; thus, providing erroneous information about subsurface conditions. The incorporation of constraints has been demonstrated to reduce the degrees of freedom in the inversion, and thus improve the consistency in the obtained imaging results. Such observation was particularly evident for petrophysical constraints imposed on the joint inversion where a porosity model was prescribed to compensate for the lack of contrast in the physical properties of rock and ice.

The results of this synthetic study could be repeated for field data collected at the Hoher Sonnblick (Austria) at two different times (June and October 2019). The application of a constrained PJI strategy proved particularly efficient in enhancing both the spatial and temporal consistency in the imaging results at the field-scale. Due to the lack of comprehensive ground-truth data at the Hoher Sonnblick, the porosity model resolved from the October data set through the unconstrained PJI was considered as the best possible estimate for the porosity distribution assuming a low ice content at the end of the thaw period. By penalizing deviations from this porosity model in the PJI for both time lapses such petrophysical constraint acted as a time-lapse constraint that improved the temporal consistency in the resolved models. The obtained imaging results provided novel insights into the ice content distribution and the associated seasonal dynamics at the Hoher Sonnblick, which is critical for understanding the influence of the climate change related air temperature rise on subsurface conditions in Alpine regions; thus, highlighting the practical significance of the proposed solutions.

### **A MSW landfill**

An essential achievement of this thesis is the extension of the PJI scheme developed by Wagner et al. (2019) that allows its application to data collected at sites characterized by an increased amount of clay or organic matter. In particular, the study presented in chapter 5 modified the PJI framework to consider the spatial variability of the surface conductivity during the parameter estimation. This is achieved by expanding the underlying petrophysical model through the formulations of the dynamic Stern layer model (e.g., Revil et al., 2017c), thereby leveraging upon the frequency dependence of the surface conductivity observed in electrical resistivity data collected at a high and a low frequency.

The application of this modified PJI scheme to data collected at the Heferlbach landfill demonstrated the ability of the approach to resolve subsurface models in terms of hydrogeological parameters relevant for the characterization of MSW landfills. The obtained imaging results could be verified based on direct information regarding the landfill geometry, waste composition and water content within the waste unit. In particular, the correlation between the water content resolved through the PJI and the water content measured in waste samples evidenced the ability of the modified PJI scheme to provide reliable estimates for the subsurface water content. Although the modified PJI scheme does not consider the phase of the complex electrical impedance, the normalized chargeability  $M_n$  computed as the difference between the resolved high and low frequency electrical conductivity models provides a measure for the polarization in the subsurface. Comparing the  $M_n$  model to the imaginary component  $\sigma''$  of

the CC obtained through IP investigations demonstrated that both approaches solve for a similar polarization response; thus, further evidencing the validity of the proposed modification of the PJI scheme. In this regard, the work presented in this thesis is the first successful application of the 4PM-based PJI scheme (Wagner et al., 2019) beyond permafrost investigations, where surface conduction was not neglected and not assumed to be homogeneous over the entire model space, respectively (see, e.g., Carrier et al., 2022). Furthermore, previous geophysical investigations at the Heferlbach landfill revealed a positive correlation between the polarization response and the TOC content, with the latter being associated with microbial activity (Flores Orozco et al., 2020). The PJI imaging results revealed an increased water content in landfill areas characterized by a high TOC concentration and a high polarization response. Such observation showed that the observed increase in LFG concentration (Brandstätter et al., 2020) can be related to the methanogenic fermentation of the refuse due to microbial activity. Accordingly, the modified PJI scheme proposed in this thesis is the first stand-alone technique considering the spatial variability in the surface conductivity that provides quantitative estimates for the water content and the polarization; thus, allowing for the identification of biogeochemical hotspots in MSW landfills associated with the production of greenhouse gasses.

### *A recently active landslide*

The main objective of the investigations conducted at the Hofermuehle landslide presented in chapter 6 refers to the enhanced understanding of the hydraulic properties based on IP measurements. In particular, the application of a petrophysical model describing the relationship between the hydraulic permeability  $k$  and the IP response (Weller et al., 2015) permitted the quantification of the hydraulic conductivity  $K$ , and thus the delineation of preferential water flow paths, in an imaging framework.

The modified PJI scheme proposed in this thesis provided the means for an independent verification of the  $K$  estimates obtained from the TDIP and FDIP data. In particular, the PJI-based  $K$  model was computed from models for  $M_n$  and the formation factor  $F = \Phi^{-m}$  (assuming a uniform pore space connectivity) based on a petrophysical relationship proposed by Weller et al. (2015). The observed consistency in the  $K$  models obtained through the different geophysical approaches (i.e., TDIP, FDIP, SIP, PJI) demonstrated the possibility to quantify the hydraulic properties of the subsurface materials based on different input data and inversion techniques; thus, providing further evidence for the validity of the proposed extension of the petrophysical model underlying the PJI framework.

A more detailed evaluation of the resolved subsurface models was not possible due to

the lack of direct measurements of  $K$  at the Hofermuehle landslide. Nonetheless, this study presented the first successful application of the PJI scheme as an independent method within a multi-method site characterization. In particular, the obtained PJI imaging results highlight the relevance of the modified PJI scheme as a stand-alone tool for hydrological investigations in natural soils.

### ***The Hydrological Open Air Laboratory (HOAL)***

The feasibility study presented in chapter 7 was primarily motivated by the  $K$  models obtained for the Hofermuehle landslide resolved through the IP and the PJI approaches. In particular, the observed consistency in the resolved  $K$  models indicated that in case of the Hofermuehle landslide the polarization of the subsurface materials is likely less influential on the quantification of  $K$  than the formation factor. However, the  $F$  model obtained through the PJI was computed considering a homogeneous pore-space connectivity over the entire model space, which is only a rough approximation of the true subsurface conditions. Accordingly, chapter 7 proposed a further modification of the PJI scheme to allow solving for the spatial variability in  $m$  aiming at a refined model for  $F$ , and thus an enhanced quantification of  $K$  based on PJI imaging results.

Due to the possibility to access comprehensive ground truth data and the long-term perspective of conducting direct hydraulic investigations, the HOAL (Petzenkirchen, Austria) was considered a suitable study area. The investigation demonstrated the general applicability of the proposed PJI scheme to solve for  $m$  in an imaging framework, and refers to the first application of the PJI framework to data collected in undisturbed natural soils under unfrozen conditions (in contrast to chapters 6, chapter 5 and chapter 4, respectively).

The obtained subsurface models could be verified through information obtained from direct measurements conducted on drill cores extracted from a borehole located in the center of the investigated profile. Such evaluation showed that the spatial variability in the resolved hydrogeological soil parameters was in good agreement with lithological information and the grain size distribution. Moreover, the relatively high values resolved for  $m$  and  $M_n$  could be related to the  $\text{CaCO}_3$  found in the drill cores, which acts as a cementation agent enhancing soil stability and was related to an increased polarization response by different studies (e.g., Wu et al., 2010; Saneiyani et al., 2018). Nonetheless, the observed discrepancies between the resolved  $\Phi$  model and available direct information indicated the need for further research addressing the adequate modeling of the mechanical properties of subsurface materials, e.g., the approximation of the seismic velocity.

### 8.2.2 Perspectives for future research activities

As addressed above, the studies presented in chapters 4 through 7 demonstrated the practical applicability and significance of the PJI scheme with regard to various hydro-geological issues. At the same time, the obtained results also highlighted limitations associated with the proposed PJI scheme, concerning both the electrical and seismic part of the approach.

On the one hand, the PJI scheme omits the added value provided by IP data, but instead considers solely the conductivity magnitude measured at a high and a low frequency. Although this approach was deliberately chosen to allow for an independent verification of the PJI imaging results through IP methods, this section will outline potential benefits of taking into account IP data during the parameter estimation.

On the other hand, the petrophysical model underlying the PJI scheme approximates the seismic velocity based on the porosity following an approach proposed by Wyllie et al. (1956). The Wyllie equation provides a simple relationship to model  $v_p$ , yet its applicability is particularly limited in near-surface unconsolidated sediments (e.g., Mavko et al., 2009). The results presented in this thesis suggest that in case of the proposed PJI scheme the limitations of the Wyllie equation are compensated by the joint inversion of seismic and electrical data, as well as by favorable mechanical properties of the subsurface materials encountered in the different study areas. Nevertheless, this section addresses the main drawbacks of the Wyllie equation and suggest potential alternatives to be considered in the future.

#### 8.2.2.1 Taking into account IP data in the joint inversion scheme during parameter estimation

The modification of the PJI scheme developed by Wagner et al. (2019) proposed in chapter 5 takes into account the effect of the surface conductivity by leveraging upon its frequency-dependence (e.g. Lesmes and Frye, 2001):

$$\sigma_s^*(\omega) = \sigma_s'(\omega) + i\sigma_s''(\omega) \quad (8.1)$$

As the first term in Equation 8.1 refers to the conductivity magnitude  $|\sigma|$  provided by ERT measurements, the frequency-dependent effect of the surface conductivity can be assessed by conducting ERT measurements at a low and a high frequency (e.g., Marshall and Madden, 1959). The difference between the low and high frequency conductivity models provides the normalized chargeability  $M_n$  as a measure for the subsurface polarization; yet, such  $M_n$  model lacks the resolution to accurately estimate

variations in the polarization response. Accordingly, the IP has emerged as a suitable method in environmental and engineering studies such as investigations associated with landslides (e.g., Gallistl et al., 2018; Flores Orozco et al., 2018b), hydrogeological conditions (e.g., Slater, 2007; Binley et al., 2015), contaminated sites (e.g., Flores Orozco et al., 2013; Williams et al., 2009), biogeochemical processes (e.g., Flores Orozco et al., 2020; Kessouri et al., 2019; Williams et al., 2005) or peatlands (Katona et al., 2021; McAnallen et al., 2018), as well as the characterization of permafrost distribution (Maierhofer et al., 2022).

In particular, SIP investigations conducted by Maierhofer et al. (2022) at a permafrost site show that at low frequencies ( $\approx 10$  Hz) the surface conductivity dominates over the electrolytic conductivity even in ice-rich frozen conditions. The reported values for  $\sigma''$  are higher by an order of magnitude in frozen conditions indicating that the surface conductivity cannot be prescribed as a constant value across the imaging plane as suggested by Mollaret et al. (2020); thus, supporting the approach developed in this thesis. Maierhofer et al. (2022) argue that the discrimination between frozen and unfrozen bedrock might be biased if the quantitative interpretation uses petrophysical models based on Archie's law, i.e., surface conduction is not considered (e.g., Hauck et al., 2011; Wagner et al., 2019). Hence, the effect of the surface conductivity in frozen conditions might be another explanation for the lack of consistency in the imaging results resolved from the Hoher Sonnblick data sets through the unconstrained PJI scheme. From this point of view, the porosity constraint imposed on the PJI of the Hoher Sonnblick data sets facilitated not only the discrimination between the ice and rock phase but might have also compensated the lack of a surface conductivity term in the 4PM (Equation 4.3).

These observations highlight the importance of taking into account surface conduction during the parameter estimation not only in presence of fine-grained materials or organic matter, but also for investigations in alpine regions under frozen conditions. This is particularly relevant for PJI schemes since neglecting the effect of the surface conductivity overestimates the saturation (see Figure 2.2), and thus affects the resolved spatial variation in the other soil constituents or target parameters, respectively. Accordingly, future research activities should address the extension of the PJI scheme to allow for the incorporation of SIP data. Considering both conductivity magnitude and phase in the PJI scheme would account for the effect of the surface conduction and at the same time provide the resolution to solve for the spatial variations in the capacitive properties of the subsurface materials. Such an extension of the PJI scheme is expected to provide improved estimates for the target parameters in various environmental and engineering investigations, e.g., an enhanced quantifi-

cation of the subsurface ice content as demonstrated by Maierhofer et al. (2022) as well as refined hydraulic subsurface models relevant for exploring groundwater or contaminant flow. Furthermore, jointly inverting seismic traveltimes and the complex electrical impedance would also offer the possibility to solve for the content of metallic materials in the subsurface, which could allow for, e.g., assessing the potential of landfills or mining tails regarding the extraction of residual metals or metallic minerals, respectively.

### 8.2.2.2 Enhanced approximation of the seismic velocity

This thesis investigated shortcomings of the petrophysical relationship describing the observed electrical response with respect to the effect of the surface conduction. To overcome such limitations, a modified PJI scheme was proposed that allows the application for data collected in areas characterized by fine-grained materials or organic matter. However, up to this point, shortcomings in the approximation of the seismic velocity as well as the associated errors in the resolved models remained unaddressed.

The proposed PJI scheme uses the Timur equation to model the relationship between seismic velocity and porosity based on the time-averaging equation proposed by Wyllie et al. (1956), which provides a simple approach to obtain the measured bulk velocity assuming it to be equal to the sum of the seismic velocity of the different soil constituents weighted by the porosity. Investigations conducted by Raymer et al. (1980) revealed, however, that values resolved through the Wyllie equation are not consistent with laboratory data over the entire porosity range (i.e., 0% to 100%). According to Mavko et al. (2009), the Wyllie equation performs best for consolidated, isotropic and fluid-saturated rocks with intermediate porosity values ( $37\% < \Phi \leq 47\%$ ; Raymer et al., 1980) and negligible secondary porosity.

The studies presented in this thesis demonstrated that joint inversion of seismic and electrical data sets is able to compensate the inherent shortcomings of the Wyllie equation, considering the observed consistency between the PJI imaging results and direct information. In case of the ice content quantification at the Hoher Sonnblick, the PJI-resolved subsurface model was found to be in agreement with available information regarding the subsurface conditions (e.g., borehole temperature data; see chapter 4). The quantitative water content estimates obtained through the modified PJI scheme at the Heferlbach landfill could be verified based on the water content measured in extracted waste samples (see chapter 6). For the Hofermuehle landslide (see chapter 6) the resolved porosity model was in agreement with direct information obtained from DPH soundings as well as porosity estimates reported from the laboratory analysis of

soil samples extracted at the site. However, investigations conducted in the HOAL showed that the resolved porosity model (see Figure 7.3) might be affected by the limitations of the Wyllie equation in case of unconsolidated conditions (Mavko et al., 2009). In particular, the Wyllie equation tends to overpredict the porosity, which is likely the case for the HOAL data set; thus, illustrating the limitation discussed by Mavko et al. (2009) at the field-scale. Accordingly, future research should address the incorporation of more sophisticated relationships for the approximation of the seismic velocity either through modifications of the Wyllie equation or approaches based on the Biot-Gassmann/Hertz-Mindlin theory.

### ***Extended versions of the Wyllie equation***

A potential approach refers to the extension of the Wyllie equation, e.g., the set of equations proposed by Raymer et al. (1980)

$$v_{37} = (1 - \Phi)^2 v_r + \Phi v_f, \quad \Phi < 37\% \quad (8.2)$$

$$\frac{1}{\delta v_{47}^2} = \frac{\Phi}{\delta_f v_f^2} + \frac{1 - \Phi}{\delta_r v_r^2}, \quad \Phi > 47\% \quad (8.3)$$

which can be used to compute the seismic velocity for intermediate porosity values as

$$\frac{1}{v} = \frac{0.47 - \Phi}{0.10} \frac{1}{v_{37}} + \frac{\Phi - 0.37}{0.10} \frac{1}{v_{47}}, \quad 37\% < \Phi \leq 47\%. \quad (8.4)$$

As can be seen from Equations 8.2 - 8.4, Raymer et al. (1980) introduce the bulk density as well as the density for the solid and fluid phase densities ( $\delta_r$  and  $\delta_f$ , respectively) as parameters in the estimation of the seismic velocity at high porosity values ( $> 47\%$ ). While such extension provides a better correlation between measured and predicted seismic velocities in water-saturated sandstones, Mavko et al. (2009) show that similar to the Wyllie equation the Raymer-Hunt-Gardner relation cannot model the seismic response observed in unconsolidated uncemented rocks or sands.

Saleh and Castagna (2004) propose a generalized version of the Wyllie equation that permits the accurate quantification of the seismic velocity even in case of a complex pore geometry. The authors argue that the Wyllie equation is applicable only to rocks with interparticle or intercrystalline pores, yet it fails to describe the velocity-porosity relationship for combinations of intercrystalline and spherical pores. To address this problem, Saleh and Castagna (2004) consider a spherical porosity model to discriminate high-aspect-ratio pores enclosed in the host rock from the the matrix porosity.

The corresponding spherical porosity  $\Phi_s$  is defined as

$$\Phi_s = \frac{\Phi_b - \Phi}{1 - \Phi}, \quad (8.5)$$

where  $\Phi$  is the porosity as considered in the Wyllie equation and  $\Phi_b$  refers to the bulk porosity obtained from laboratory analysis, e.g., through the combination of density and neutron logs (Saleh and Castagna, 2004). To account for variations in the shape and distribution of the pores, Saleh and Castagna (2004) introduce the empirically determined pore shape factor  $S$

$$S = 1 + \frac{\Phi_s}{\frac{6.5}{v_r} - 3\Phi_s + 2\Phi_b\Phi_s}. \quad (8.6)$$

$S$  is then used as an exponent for  $v_r$  to obtain the modified version of the Wyllie equation as (after Saleh and Castagna, 2004):

$$\frac{1}{v} = \frac{1 - \Phi_b}{(v_r)^S} + \frac{\Phi_b}{v_f}. \quad (8.7)$$

This modification of the Wyllie equation does not provide a unique relationship between velocity and porosity but instead a velocity-porosity envelope with the lower limit ( $S = 1$ ) corresponding to the original Wyllie equation behavior (Saleh and Castagna, 2004). In particular, the parameter  $S$  is sensitive to pore-type variations similar to the cementation exponent  $m$  in Archie's law. The link between  $m$  and the ratio of spherical pores to bulk porosity is established as (after Saleh and Castagna, 2004):

$$m = \frac{2 \log \Phi}{\log \Phi_b} + \frac{\log \left[ \frac{2\Phi_s(1-\Phi^2) + 1 + 2\Phi^2}{1 + 2\Phi^2 - \Phi_s(1-\Phi^2)} \right]}{1 - \Phi_b} \quad (8.8)$$

Accordingly, estimating  $S$  through the petrophysically-coupled joint inversion of seismic and electrical data could complement the quantification of  $m$ , and thus enhance the quantification of the subsurface hydraulic properties.

### ***Approximate the seismic velocity based on elastic moduli***

Instead of relying on the empirical Wyllie model, the seismic P-wave ( $v_p$ ) and S-wave velocity ( $v_s$ ) can be modeled based on the effective moduli and the density of the subsurface materials (e.g., Mavko et al., 2009):

$$v_p = \left( \frac{K_e + \frac{4}{3}\mu_e}{\delta_b} \right)^{1/2} \quad (8.9)$$

$$v_s = \left( \frac{\mu_e}{\delta_b} \right)^{1/2} \quad (8.10)$$

In Equation 8.9,  $K_e$  is the effective bulk modulus and  $\delta_b$  refers to the bulk density. For an unconsolidated three-phase soil system,  $K_e$  can be calculated through the Biot-Gassmann theory (Biot, 1956; Gassmann, 1951) as

$$\frac{K_e}{K_0 - K_e} = \frac{K_r}{K_0 - K_r} + \frac{K_p}{\Phi(K_0 - K_p)}, \quad (8.11)$$

with  $K_0$ ,  $K_r$  and  $K_p$  denoting the bulk modulus of the minerals forming the rock, the bulk modulus of the rock matrix and the bulk modulus of the pore space, respectively (after Shen et al., 2016; Mavko et al., 2009). Assuming the pore space to be filled by a water-air mixture,  $K_p$  can be expressed as a function of the water saturation (Mavko et al., 2009)

$$\frac{1}{K_p} = \frac{S_w}{K_w} + \frac{1 - S_w}{K_a}, \quad (8.12)$$

where  $K_w$  and  $K_a$  refer to the bulk modulus of water and air, respectively (e.g., Shen et al., 2016). Due to the lack of shear resistance in water and air, the  $\mu_e$  equals the shear modulus of the rock matrix  $\mu_r$ , i.e., (after Mavko et al., 2009)

$$\mu_e = \mu_r, \quad (8.13)$$

which applies for a particular depth and  $S_w$  in unconsolidated sediments (Shen et al., 2016).

The Hertz-Mindlin theory (Hertz, 1882; Mindlin, 1949) describes the elastic moduli of the grain (or rock) matrix as (e.g., Mavko et al., 2009):

$$K_r = \left( \frac{n_{gc}^2 (1 - \Phi)^2 G_0^2}{18\pi^2 (1 - \nu)^2} P \right)^{1/3} \quad (8.14)$$

$$\mu_r = \frac{5 - 4\nu}{5(2 - \nu)} \left( \frac{3n^2 (1 - \Phi)^2 \mu_0^2}{2\pi^2 (1 - \nu)^2} P \right)^{1/3} \quad (8.15)$$

In Equations 8.14 and 8.15,  $n_{gc}$  is the grain coordination number quantifying the average number of contacts per grain,  $G_0$  is the shear modulus of the minerals forming

the rock,  $\nu$  is the Poisson's ratio and  $P$  is the total effective stress that approximates the rock matrix elasticity (Shen et al., 2016; Mavko et al., 2009). Shen et al. (2016) expand the Hertz-Mindlin model to consider both the net overburden stress as well as interparticle stresses due to soil suction and cohesive stress based on the formulation for  $P$  provided by Lu and Likos (2006). The soil suction stress is the result of interparticle physicochemical stresses associated with cementation, van der Waals attraction, EDL repulsion as well as capillary stress and can be approximated through soil-water characteristic curves (SWCC; e.g., Fredlund et al., 2011; van Genuchten, 1980). This extension allows for an enhanced approximation of variations in the seismic velocity due to changes in the saturation, which is particularly relevant for investigations in the near-surface.

The model proposed by Shen et al. (2016) provides the possibility to consider the Poisson's ratio as a target parameter in the PJI scheme, and thus resolve the spatial variability in this important soil parameter in an imaging framework. In particular,  $\nu$  is related to  $v_p$  and  $v_s$  as (e.g., Mavko et al., 2009):

$$\nu = \frac{v_p^2 - 2v_s^2}{2(v_p^2 - v_s^2)}. \quad (8.16)$$

Accordingly, such extension requires taking into account either S-wave travel time data or surface wave dispersion curves as additional input data sets in the PJI scheme, e.g., as demonstrated by Garofalo et al. (2015). Nonetheless, the approach to solve for  $\nu$  in an imaging framework proposed here is fundamentally different from the joint inversion scheme developed by Garofalo et al. (2015) where the Poisson's ratio is solely used as an interparameter constraint between  $v_p$  and  $v_s$  during the parameter estimation.

Future research activities aiming at the extension of the PJI scheme based on enhanced formulations for the seismic velocity need to take into account the associated increase of parameters in the underlying petrophysical model. Both the extension of the Wyllie equation proposed by Saleh and Castagna (2004) as well as the Hertz-Mindlin-based approach developed by Shen et al. (2016) rely on prior knowledge regarding certain petrophysical parameters, e.g., density or elastic moduli. Such information can be retrieved from literature or laboratory investigations, yet the obtained values might be associated to further uncertainties, and thus might affect the consistency in the resolved subsurface models. In this regard, approaches similar to the Shen et al. (2016) model are likely better suited as the associated incorporation of an additional input data set might be able to counterbalance the increased number of parameters in the petrophysical model, and thus reduce the ill-posedness of the inversion.

### 8.3 Concluding remarks

In this thesis, I presented the results of different self-contained studies addressing the application of innovative processing and inversion techniques to near-surface geophysical data collected in environmental and engineering investigations. Each of the conducted studies highlighted the applicability of the proposed methodologies and demonstrated the validity of the investigated approaches based on information from independent data sources. Yet, such comparison with direct information or results obtained from complementary geophysical methods also allowed for the identification of associated drawbacks or shortcomings. The critical assessment of the methods proposed in this thesis showed potential perspectives for future research activities related to combined applications of various complementary geophysical methods, the investigation of refined petrophysical relationships, or further developments of the processing and inversion algorithms. Hopefully, this thesis will be a valuable resource facilitating the application of the proposed techniques and might even lead to the development of novel solutions for the discussed problems related to the processing and inversion of near-surface geophysical data.

# List of Abbreviations, Acronyms and Symbols

## Abbreviations and Acronyms

<b>4PM</b>	Four-phase model	<b>GHG</b>	Greenhouse gas
<b>AC</b>	Alternating current	<b>GSD</b>	Grain size distribution
<b>ALS</b>	Airborne laser scanning	<b>HOAL</b>	Hydrological Open Air Laboratory
<b>ALT</b>	Active layer thickness	<b>IP</b>	Induced polarization
<b>bgs</b>	Below ground surface	<b>LFG</b>	Landfill gas
<b>CC</b>	Complex conductivity	<b>MASW</b>	Multi-channel analysis of surface waves
<b>CCI</b>	Complex conductivity inversion	<b>MSW</b>	Municipal solid waste
<b>CEC</b>	Cation exchange capacity	<b>PJI</b>	Petrophysical(lly-coupled) joint inversion
<b>CDW</b>	Construction and demolition waste	<b>RMS</b>	Root mean square
<b>CR</b>	Complex resistivity	<b>SIP</b>	Spectral induced polarization
<b>DC</b>	Direct current	<b>SRT</b>	Seismic refraction tomography
<b>DPH</b>	Dynamic probing heavy	<b>S/N</b>	Signal-to-noise ratio
<b>DSL</b>	Dynamic Stern layer model	<b>SWCC</b>	Soil-water characteristic curve
<b>EDL</b>	Electrical double layer	<b>TDIP</b>	Time-domain induced polarization
<b>EIT</b>	Electrical impedance tomography	<b>TOC</b>	Total organic carbon
<b>ER</b>	Electrical resistivity	<b>TLS</b>	Terrestrial laser scanning
<b>ERT</b>	Electrical resistivity tomography	<b>VCC</b>	Volume conservation constraint
<b>FDIP</b>	Frequency-domain induced polarization		

## Electrical methods

$I$	Current	$\rho_0$	Direct current or low frequency electrical resistivity
$U$	Voltage	$\rho_\infty$	Instantaneous or high frequency electrical resistivity
$R$	Resistance	$\rho^*$	Complex electrical resistivity
$\hat{n}_i$	Density of a single charge carrier	$\rho'$	Real component of the complex electrical resistivity
$\hat{Z}_i$	Valence of a single charge carrier	$\rho''$	Imaginary component of the complex electrical resistivity
$e$	Elementary charge	$\sigma$	Electrical conductivity
$r_i$	Radius of a hydrated ion	$\sigma_0$	Direct current or low frequency electrical conductivity
$\eta$	Fluid viscosity		
$\kappa$	Geometric factor		
$\rho$	Electrical resistivity		
$\rho_a$	Apparent electrical resistivity		

$\sigma_\infty$	Instantaneous or high frequency electrical conductivity	$\sigma_{EDL}$	Electrical conductivity of the electrical double layer
$\sigma^*$	Complex-valued electrical conductivity	$Z_e^*$	Complex-valued electrical impedance
$\sigma'$	Real component of the complex-valued electrical conductivity	$ Z_e $	Electrical impedance magnitude
$\sigma''$	Imaginary component of the complex-valued electrical conductivity	$\varphi_{Z_e}$	Electrical impedance phase shift
$ \sigma $	Magnitude of the complex-valued electrical conductivity	$\omega$	Angular frequency
$\varphi$	Phase of the complex-valued electrical conductivity	$\tau$	Characteristic relaxation time
$\sigma_s^*$	Complex-valued surface conductivity	$\tau_0$	Generalized relaxation time
$\sigma'_s$	Real component of the complex surface conductivity	$c$	Cole-Cole parameter
$\sigma''_s$	Imaginary component of the complex surface conductivity	$f_c$	Critical peak frequency in the polarization response
		$M$	Chargeability
		$M_n$	Normalized chargeability
		$M_{int}$	Integral chargeability
		$\epsilon$	Dielectric permittivity

## Seismic methods

$Z_a$	Acoustic impedance	$v_f$	Acoustic velocity of fluid medium
$v$	Bulk acoustic velocity of the medium	$K_m$	Bulk modulus
$s$	Seismic slowness (reciprocal of $v$ )	$\mu$	Shear modulus
$t$	Seismic (P-wave) travel time	$i_n$	Angle of incidence/reflection/refraction
$v_p$	P-wave velocity	$i_c$	Critical angle of incidence
$v_s$	S-wave velocity	$x_{crit}$	Critical distance
$\nu$	Poisson's ratio	$x_{cross}$	Crossover distance
$v_m$	Acoustic velocity of rock matrix	$t_i$	Intercept time

## Petrophysics

$\Phi$	Porosity	$\delta$	Density of medium
$\Phi_b$	Porosity from density-neutron logs	$\delta_b$	Bulk density
$\Phi_S$	Spherical porosity	$\delta_a$	Density of air
$f_w, \theta$	Fractional/volumetric water content	$\delta_w$	Density of water
$f_a$	Fractional air content	$\delta_r, \delta_g$	Rock or grain density
$f_i$	Fractional ice content	$m_w$	Mass of water in a sample
$f_r$	Fractional rock content	$m_s$	Mass of solids in a sample
$S_w$	Water saturation of the pore space	$F$	Formation factor
$S_a$	Air saturation of the pore space	$F_{EDL}$	Formation factor for the electrical double layer
$WC$	(Gravimetric) Water content	$F_s$	Formation factor for shaley sand

$a$	Tortuosity	$v_i$	Acoustic velocity of ice
$m$	Cementation exponent	$v_r$	Acoustic velocity of rock or more general the solid phase (i.e., minerals, grains)
$n$	Saturation exponent	$S$	Pore shape factor
$\sigma_m$	Matrix conductivity	$K_e$	Effective bulk modulus
$\sigma_f$	Electrolytic conductivity	$K_0$	Bulk modulus of rock-forming minerals
$\sigma_s$	Surface conductivity	$K_r$	Bulk modulus of rock matrix
$\sigma_w, \rho_w$	Fluid conductivity, fluid resistivity	$K_p$	Bulk modulus of pore space
$\sigma_o$	Bulk conductivity of fully saturated porous medium	$K_w$	Bulk modulus of water
$I_r$	Resistivity index	$K_a$	Bulk modulus of air
$B$	Apparent mobility of counterions for surface conduction	$\mu_e$	Effective shear modulus
$\Lambda$	Apparent mobility of counterions for polarization	$\mu_0$	Shear modulus of rock-forming minerals
$R$	Dimensionless ratio between $\Lambda$ and $B$	$\mu_r$	Shear modulus of rock matrix
$Q_v$	Volume concentration of the exchange cations	$n_{gc}$	Grain coordination number
$v_w$	Acoustic velocity of water	$P$	Total effective stress
$v_a$	Acoustic velocity of air	$k$	Hydraulic permeability
		$K$	Hydraulic conductivity
		$g$	Gravitational acceleration

## Inversion

$N$	Number of mesh/grid nodes	$\mathbf{m}$	Model vector
$C$	Number of mesh/grid cells	$\mathbf{m}_0$	Reference model vector
$B$	Number of mesh/grid boundaries	$\mathcal{F}(\mathbf{m})$	Model response
$D$	Number of data sets in PJI	$\Delta\mathbf{m}$	Model update
$U$	Number of target parameters in PJI	$p$	(Petrophysical) Target parameter
$\xi$	Physical property of subsurface medium	$\mathbf{p}$	(Petrophysical) Parameter vector
$\Psi$	Objective function	$\mathbf{p}_0$	Reference parameter vector
$\alpha, \beta, \gamma, \lambda$	Regularization parameter	$\mathbf{J}$	Jacobian matrix
$\Psi_d$	Data misfit	$\mathbf{W}_d$	Data weighting matrix
$\Psi_m$	Model roughness	$\mathbf{W}_m$	Model constraint matrix
$\mathbf{d}$	Data vector	$\mathbf{W}_p, \mathbf{W}_p^{sum}$	Model weighting matrix
$\Delta\mathbf{d}$	Difference between $\mathbf{d}$ and $\mathcal{F}(\mathbf{m})$	$\hat{\mathbf{W}}, \hat{\mathbf{J}}$	Scaled matrix in PJI
$\epsilon$	Error model	$\mathbf{C}$	First-order finite-difference roughness operator
$\epsilon_{abs}$	Absolute error	$z_{Weight}$	Ratio between horizontal and vertical smoothing
$\epsilon_{rel}$	Relative error	$\chi^2$	Error-weighted data misfit



# Bibliography

- Abdulsamad, F., A. Revil, A. S. Ahmed, A. Coperey, M. Karaoulis, S. Nicaise, and L. Peyras (2019). "Induced polarization tomography applied to the detection and the monitoring of leaks in embankments". In: *Engineering Geology* 254, pp. 89–101. DOI: 10.1016/j.enggeo.2019.04.001.
- Ahern, T., R. Casey, D. Barnes, R. Benson, T. Knight, and C. Trabant (2012). *SEED Reference Manual, Version 2.4*. URL: [http://www.fdsn.org/pdf/SEEDManual\\_V2.4.pdf](http://www.fdsn.org/pdf/SEEDManual_V2.4.pdf).
- Alston, J. M. and J. A. Rick (2021). "A Beginner's Guide to Conducting Reproducible Research". In: *The Bulletin of the Ecological Society of America* 102.2, e01801. DOI: 10.1002/bes2.1801.
- Annan, A. (2005). "Ground-penetrating radar". In: *Near-surface geophysics*. Society of Exploration Geophysicists, pp. 357–438. DOI: 10.1190/1.9781560801719.ch11.
- Aranda, N., V. R. Elis, R. L. Prado, M. G. Miguel, M. A. de Godoy Leme, B. Conicelli, and O. Guzmán (2021). "Electrical resistivity methods to characterize the moisture content in Brazilian sanitary landfill". In: *Environmental Monitoring and Assessment* 193.5, pp. 1–15. DOI: 10.1007/s10661-021-09050-w.
- Archie, G. E. (1942). "The electrical resistivity log as an aid in determining some reservoir characteristics". In: *Transactions of the AIME* 146.01, pp. 54–62. DOI: 10.2118/942054-g.
- Arrhenius, S. (1896). "XXXI. On the influence of carbonic acid in the air upon the temperature of the ground". In: *The London, Edinburgh, and Dublin Philosophical Magazine and Journal of Science* 41.251, pp. 237–276. DOI: 10.1080/14786449608620846.
- Arrhenius, S. (1908). *Worlds in the making: the evolution of the universe*. Harper & brothers.
- Bachrach, R., J. Dvorkin, and A. Nur (1998). "High-resolution shallow-seismic experiments in sand, Part II: Velocities in shallow unconsolidated sand". In: *Geophysics* 63.4, pp. 1234–1240. DOI: 10.1190/1.1444424.
- Bairlein, K., A. Hördt, and S. Nordsiek (2014). "The influence on sample preparation on spectral induced polarization of unconsolidated sediments". In: *Near Surface Geophysics* 12.5, pp. 667–678. DOI: 10.3997/1873-0604.2014023.
- Bairlein, K., M. Bucker, A. Hördt, and B. Hinze (Feb. 2016). "Temperature dependence of spectral induced polarization data: experimental results and membrane polarization theory". In: *Geophysical Journal International* 205.1, pp. 440–453. ISSN: 0956-540X. DOI: 10.1093/gji/ggw027.
- Barlaz, M. A., R. K. Ham, D. M. Schaefer, and R. Isaacson (1990). "Methane production from municipal refuse: a review of enhancement techniques and microbial dynamics". In: *Critical Reviews in Environmental Science and Technology* 19.6, pp. 557–584. DOI: 10.1080/10643389009388384.
- Barone, I., J. Boaga, A. Carrera, A. Flores-Orozco, and G. Casiani (2021). "Tackling Lateral Variability Using Surface Waves: A Tomography-Like Approach". In: *Surveys in Geophysics* 42.2, pp. 317–338. DOI: 10.1007/s10712-021-09631-x.
- Bell, R., T. Glade, K. Granica, G. Heiss, P. Leopold, H. Petschko, G. Pomaroli, H. Proske, and J. Schweigl (2013). "Landslide susceptibility maps for spatial planning in lower Austria". In: *Landslide science and practice*. Springer, pp. 467–472. DOI: 10.1007/978-3-642-31325-7\_60.
- Beniston, M., D. Farinotti, M. Stoffel, L. M. Andreassen, E. Coppola, N. Eckert, A. Fantini, F. Giacona, C. Hauck, M. Huss, H. Huwald, M. Lehning, J.-I. López-Moreno, J. Magnusson, C. Marty, E. Morán-Tejeda, S. Morin, M. Naaim, A. Provenzale, A. Rabatel, D. Six, J. Stötter, U. Strasser, S. Terzago, and C. Vincent (2018). "The European mountain cryosphere: a review of its current state, trends, and future challenges". In: *The Cryosphere* 12.2, pp. 759–794. DOI: 10.5194/tc-12-759-2018.
- Bergmann, P., M. Ivandic, B. Norden, C. Rücker, D. Kiessling, S. Luth, C. Schmidt-Hattenberger, and C. Juhlin (2014). "Combination of seismic reflection and constrained resistivity inversion with an application to 4D imaging of the CO<sub>2</sub> storage site, Ketzin, Germany". In: *Geophysics* 79.2, B37–B50. DOI: 10.1190/geo2013-0131.1.
- Beyreuther, M., R. Barsch, L. Krischer, T. Megies, Y. Behr, and J. Wassermann (2010). "ObsPy: A Python toolbox for seismology". In: *Seismological Research Letters* 81.3, pp. 530–533. DOI: 10.1785/gssrl.81.3.530.
- Bichet, V., E. Grisey, and L. Aleya (2016). "Spatial characterization of leachate plume using electrical resistivity tomography in a landfill composed of old and new cells (Belfort, France)". In: *Engineering Geology* 211, pp. 61–73. DOI: 10.1016/j.enggeo.2016.06.026.
- Bichler, A., P. Bobrowsky, M. Best, M. Douma, J. Hunter, T. Calvert, and R. Burns (2004). "Three-dimensional mapping of a landslide using a multi-geophysical approach: the Quesnel Forks landslide". In: *Landslides* 1.1, pp. 29–40. DOI: 10.1007/s10346-003-0008-7.
- Binley, A., S. S. Hubbard, J. A. Huisman, A. Revil, D. A. Robinson, K. Singha, and L. D. Slater (2015). "The emergence of hydrogeophysics for improved understanding of subsurface processes over multiple scales". In: *Water resources research* 51.6, pp. 3837–3866. DOI: 10.1002/2015wr017016.
- Binley, A., J. Keery, L. Slater, W. Barrash, and M. Cardiff (2016). "The hydrogeologic information in cross-borehole complex conductivity data from an unconsolidated conglomeratic sedimentary aquifer". In: *Geophysics* 81.6, E409–E421. DOI: 10.1190/geo2015-0608.1.
- Binley, A. and A. Kemna (2005). "DC Resistivity and Induced Polarization Methods". In: *Hydrogeophysics*. Ed. by Y. Rubin and S. S. Hubbard. Vol. 50. Springer Netherlands, pp. 129–156. ISBN: 978-1-4020-3102-1. DOI: 10.1007/1-4020-3102-5\_5.
- Binley, A., A. Ramirez, and W. Daily (1995). "Regularised image reconstruction of noisy electrical resistance tomography data". In: *Proceedings of the 4th Workshop of the European Concerted Action on Process Tomography, Bergen, Norway*. Ed. by M. S. Beck, pp. 401–410.
- Binley, A. and L. Slater (2020). *Resistivity and induced polarization: Theory and applications to the near-surface earth*. Cam-

bridge University Press. ISBN: 9781108492744. DOI: 10.1017/9781108685955.

- Binley, A., L. D. Slater, M. Fukes, and G. Cassiani (2005). "Relationship between spectral induced polarization and hydraulic properties of saturated and unsaturated sandstone". In: *Water resources research* 41.12. DOI: 10.1029/2005wr004202.
- Biot, M. A. (1956). "Theory of propagation of elastic waves in a fluid-saturated porous solid. II. Higher frequency range". In: *The Journal of the acoustical Society of America* 28.2, pp. 179–191. DOI: 10.1121/1.1908241.
- Biskaborn, B. K., J.-P. Lanckman, H. Lantuit, K. Elger, D. A. Streletskiy, W. L. Cable, and V. E. Romanovsky (2015). "The new database of the Global Terrestrial Network for Permafrost (GTN-P)". In: *Earth System Science Data* 7.2, pp. 245–259. DOI: 10.5194/essd-7-245-2015.
- Blanchy, G., S. Saneiyani, J. Boyd, P. McLachlan, and A. Binley (2020). "ResIPy, an intuitive open source software for complex geoelectrical inversion/modeling". In: *Computers & Geosciences* 137, p. 104423. ISSN: 0098-3004. DOI: 10.1016/j.cageo.2020.104423.
- Blazevic, L. A., L. Bodet, S. Pasquet, N. Linde, D. Jougnot, and L. Longuevergne (2020). "Time-lapse seismic and electrical monitoring of the vadose zone during a controlled infiltration experiment at the Ploemeur hydrological observatory, France". In: *Water* 12.5, p. 1230. DOI: 10.3390/w12051230.
- Blöschl, G., A. Blaschke, M. Broer, C. Bucher, G. Carr, X. Chen, A. Eder, M. Exner-Kittridge, A. Farnleitner, A. Flores Orozco, et al. (2016). "The hydrological open air laboratory (HOAL) in Petzenkirchen: A hypothesis-driven observatory". In: *Hydrology and Earth System Sciences* 20.1, pp. 227–255. DOI: 10.5194/hess-20-202-2016.
- Boeckli, L., A. Brenning, S. Gruber, and J. Noetzi (2012). "Permafrost distribution in the European Alps: calculation and evaluation of an index map and summary statistics". In: *The Cryosphere* 6.4, pp. 807–820. DOI: 10.5194/tc-6-807-2012.
- Böhm, R., I. Auer, M. Brunetti, M. Maugeri, T. Nanni, and W. Schöner (2001). "Regional temperature variability in the European Alps: 1760–1998 from homogenized instrumental time series". In: *International Journal of Climatology: A Journal of the Royal Meteorological Society* 21.14, pp. 1779–1801. DOI: 10.1002/joc.689.
- Börner, F., J. Schopper, and A. Weller (1996). "Evaluation of transport and storage properties in the soil and groundwater zone from induced polarization measurements<sup>1</sup>". In: *Geophysical prospecting* 44.4, pp. 583–601. DOI: 10.1111/j.1365-2478.1996.tb00167.x.
- Bourbié, T., O. Coussy, B. Zinszner, and M. C. Junger (1992). *Acoustics of porous media*. Acoustical Society of America.
- Brandstätter, C., D. Laner, and J. Fellner (2013). "Site specific in-situ aeration completion criteria: Case study 'Heferlbach'". In: *ISWA BEACON 2nd International Conference on Final Sinks, Espoo, Finland; 16.05.2013 - 18.05.2013*. Ed. by J. Heiskanen, pp. 220–227.
- Brandstätter, C., R. Prantl, and J. Fellner (2020). "Performance assessment of landfill in-situ aeration—A case study". In: *Waste Management* 101, pp. 231–240. DOI: 10.1016/j.wasman.2019.10.022.
- Brovelli, A. and G. Cassiani (2011). "Combined estimation of effective electrical conductivity and permittivity for soil monitoring". In: *Water Resources Research* 47.8. DOI: 10.1029/2011wr010487.
- Bücker, M., A. Flores Orozco, J. Gallistl, M. Steiner, L. Aigner, J. Hoppenbrock, R. Glebe, W. Morales Barrera, C. Pita de la Paz, C. E. García García, et al. (2021). "Integrated land and water-borne geophysical surveys shed light on the sudden drying of large karst lakes in southern Mexico". In: *Solid Earth* 12.2, pp. 439–461. DOI: 10.5194/se-12-439-2021.
- Bücker, M., A. Flores Orozco, S. Undorf, and A. Kemna (2019a). "On the role of stern-and diffuse-layer polarization mechanisms in porous media". In: *Journal of Geophysical Research: Solid Earth* 124.6, pp. 5656–5677. DOI: 10.1029/2019jb017679.
- Bücker, M., A. F. Orozco, and A. Kemna (2018). "Electrochemical polarization around metallic particles—Part 1: The role of diffuse-layer and volume-diffusion relaxation". In: *Geophysics* 83.4, E203–E217. DOI: 10.1190/geo2017-0401.1.
- Bücker, M., S. Undorf, A. Flores Orozco, and A. Kemna (2019b). "Electrochemical polarization around metallic particles—Part 2: The role of diffuse surface charge". In: *Geophysics* 84.2, E57–E73. DOI: 10.1190/geo2018-0150.1.
- Calvetti, D., S. Morigi, L. Reichel, and F. Sgallari (2000). "Tikhonov regularization and the L-curve for large discrete ill-posed problems". In: *Journal of computational and applied mathematics* 123.1-2, pp. 423–446. DOI: 10.1016/s0377-0427(00)00414-3.
- Carrier, A., P. Bottelin, L. Fabre, and A. Mathy (2022). "Damage Assessment of Supporting Pillars in an Underground Cave Using Joint Inversion of Electrical Resistivity and P-wave Velocity, Burgundy (France)". In: *Pure and Applied Geophysics* 179.1, pp. 45–67. DOI: 10.1007/s00024-021-02921-w.
- Carroll, D. (1959). "Ion exchange in clays and other minerals". In: *Geological Society of America Bulletin* 70.6, pp. 749–779. DOI: 10.1130/0016-7606(1959)70[749:ieicao]2.0.co;2.
- Cassiani, G., A. Kemna, A. Villa, and E. Zimmermann (2009). "Spectral induced polarization for the characterization of free-phase hydrocarbon contamination of sediments with low clay content". In: *Near Surface Geophysics* 7.5-6, pp. 547–562. DOI: 10.3997/1873-0604.2009028.
- Castaldi, P., G. Alberti, R. Merella, and P. Melis (2005). "Study of the organic matter evolution during municipal solid waste composting aimed at identifying suitable parameters for the evaluation of compost maturity". In: *Waste Management* 25.2, pp. 209–213. DOI: 10.1016/j.wasman.2004.12.011.
- Chambers, J., P. Wilkinson, O. Kuras, J. Ford, D. Gunn, P. Meldrum, C. Pennington, A. Weller, P. Hobbs, and R. Ogilvy (2011). "Three-dimensional geophysical anatomy of an active landslide in Lias Group mudrocks, Cleveland Basin, UK". In: *Geomorphology* 125.4, pp. 472–484. DOI: 10.1016/j.geomorph.2010.09.017.
- Chou, T.-K., M. Chouteau, and J.-S. Dubé (2016). "Intelligent meshing technique for 2D resistivity inverse problems". In: *Geophysics* 81.4, pp. IM45–IM56. DOI: 10.1190/geo2015-0177.1.
- Clément, R., M. Descloitres, T. Günther, L. Oxarango, C. Morra, J.-P. Laurent, and J.-P. Gourc (2010). "Improvement of electrical resistivity tomography for leachate injection monitoring". In: *Waste management* 30.3, pp. 452–464. DOI: 10.1016/j.wasman.2009.10.002.
- Cockett, R., S. Kang, L. J. Heagy, A. Pidlisecky, and D. W. Oldenburg (2015). "SimPEG: An open source framework for simulation and gradient based parameter estimation in geophysical applications". In: *Computers & Geosciences* 85, pp. 142–154. ISSN: 0098-3004. DOI: 10.1016/j.cageo.2015.09.015.
- Cole, K. S. and R. H. Cole (1941). "Dispersion and absorption in dielectrics I. Alternating current characteristics". In: *The Journal of chemical physics* 9.4, pp. 341–351. DOI: 10.1063/1.1750906.
- Dafflon, B., S. Hubbard, C. Ulrich, J. Peterson, Y. Wu, H. Wainwright, and T. J. Kneafsey (2016). "Geophysical estimation of shallow permafrost distribution and properties in an ice-wedge polygon-dominated Arctic tundra region". In: *Geophysics* 81.1, WA247–WA263. DOI: 10.1190/geo2015-0175.1.

- Dahlin, T. and V. Leroux (2012). "Improvement in time-domain induced polarization data quality with multi-electrode systems by separating current and potential cables". In: *Near Surface Geophysics* 10.6, pp. 545–565. DOI: 10.3997/1873-0604.2012028.
- Dahlin, T., H. Rosqvist, and V. Leroux (2010). "Resistivity-IP for landfill applications". In: *First Break* 28.8, pp. 101–105. DOI: 10.3997/1365-2397.28.8.40742.
- Damm, B. and B. Terhorst (2010). "A model of slope formation related to landslide activity in the Eastern Prealps, Austria". In: *Geomorphology* 122.3-4, pp. 338–350. DOI: 10.1016/j.geomorph.2009.11.001.
- Danielsen, J. E., E. Auken, F. Jørgensen, V. Søndergaard, and K. I. Sørensen (2003). "The application of the transient electromagnetic method in hydrogeophysical surveys". In: *Journal of applied geophysics* 53.4, pp. 181–198. DOI: 10.1016/j.jappgeo.2003.08.004.
- De Carlo, L., M. T. Perri, M. C. Caputo, R. Deiana, M. Vurro, and G. Cassiani (2013). "Characterization of a dismissed landfill via electrical resistivity tomography and mise-à-la-masse method". In: *Journal of Applied Geophysics* 98, pp. 1–10. DOI: 10.1016/j.jappgeo.2013.07.010.
- De Iaco, R., A. Green, H.-R. Maurer, and H. Horstmeyer (2003). "A combined seismic reflection and refraction study of a landfill and its host sediments". In: *Journal of Applied Geophysics* 52.4, pp. 139–156. DOI: 10.1016/s0926-9851(02)00255-0.
- Dhami, N. K., M. S. Reddy, and A. Mukherjee (2013). "Biomining of calcium carbonates and their engineered applications: a review". In: *Frontiers in microbiology* 4, p. 314. DOI: 10.3389/fmicb.2013.00314.
- Di Maio, R., S. Fais, P. Ligas, E. Piegari, R. Raga, and R. Cossu (2018). "3D geophysical imaging for site-specific characterization plan of an old landfill". In: *Waste Management* 76, pp. 629–642. DOI: 10.1016/j.wasman.2018.03.004.
- Doetsch, J., N. Linde, I. Coscia, S. A. Greenhalgh, and A. G. Green (2010). "Zonation for 3D aquifer characterization based on joint inversions of multimethod crosshole geophysical data". In: *Geophysics* 75.6, G53–G64. DOI: 10.1190/1.3496476.
- Doetsch, J., N. Linde, M. Pessognelli, A. G. Green, and T. Günther (2012). "Constraining 3-D electrical resistance tomography with GPR reflection data for improved aquifer characterization". In: *Journal of Applied Geophysics* 78. Developments in GPR and near-surface seismics - New applications and strategies for data integration, inversion, and modelling, pp. 68–76. ISSN: 0926-9851. DOI: 10.1016/j.jappgeo.2011.04.008.
- Draebing, D. (2016). "Application of refraction seismics in alpine permafrost studies: A review". In: *Earth-Science Reviews* 155, pp. 136–152. DOI: 10.1016/j.earscirev.2016.02.006.
- Dukhin, S. S., V. N. Shilov, and J. Bikerman (1974). "Dielectric phenomena and double layer in disperse systems and poly-electrolytes". In: *Journal of the Electrochemical Society* 121.4, p. 154C. DOI: 10.1149/1.2402374.
- Dumont, G., T. Pilawski, P. Dzaomhuo-Lenieregüe, S. Hiligsmann, F. Delvigne, P. Thonart, T. Robert, F. Nguyen, and T. Hermans (2016). "Gravimetric water distribution assessment from geoelectrical methods (ERT and EMI) in municipal solid waste landfill". In: *Waste management* 55, pp. 129–140. DOI: 10.1016/j.wasman.2016.02.013.
- Dumont, G., T. Robert, N. Marck, and F. Nguyen (2017). "Assessment of multiple geophysical techniques for the characterization of municipal waste deposit sites". In: *Journal of Applied Geophysics* 145, pp. 74–83. DOI: 10.1016/j.jappgeo.2017.07.013.
- Duvillard, P., A. Revil, Y. Qi, A. Soueid Ahmed, A. Coperey, and L. Ravel (2018). "Three-dimensional electrical conductivity and induced polarization tomography of a rock glacier". In: *Journal of Geophysical Research: Solid Earth* 123.11, pp. 9528–9554. DOI: 10.1029/2018jb015965.
- Duvillard, P.-A., L. Ravel, and P. Deline (2015). "Risk assessment of infrastructure destabilisation due to global warming in the high French Alps". In: *Journal of Alpine Research / Revue de géographie alpine* 103-2. DOI: 10.4000/rga.2896.
- Earle, P. S. and P. M. Shearer (1994). "Characterization of global seismograms using an automatic-picking algorithm". In: *Bulletin of the Seismological Society of America* 84.2, pp. 366–376. DOI: 10.1785/BSSA0840020366.
- Emmert, A. and C. Kneisel (2017). "Internal structure of two alpine rock glaciers investigated by quasi-3-D electrical resistivity imaging". In: *The Cryosphere* 11.2, pp. 841–855. DOI: 10.5194/tc-11-841-2017.
- Everett, M. E. (2013). *Near-surface applied geophysics*. Cambridge University Press.
- Exner, C. (1962). "Geologische Karte der Sonnblickgruppe 1:50.000". In: *Geologische Karte der Republik Österreich 1:50.000*. Geological Survey of Austria.
- Exner, C. (1964). *Erläuterungen zur geologischen Karte der Sonnblickgruppe 1: 50.000*. Tech. rep. Geological Survey of Austria.
- Farzamian, M., G. Vieira, F. A. Monteiro Santos, B. Yaghoobi Tabar, C. Hauck, M. C. Paz, I. Bernardo, M. Ramos, and M. A. de Pablo (2020). "Detailed detection of active layer freeze-thaw dynamics using quasi-continuous electrical resistivity tomography (Deception Island, Antarctica)". In: *The Cryosphere* 14.3, pp. 1105–1120. DOI: 10.5194/tc-14-1105-2020.
- Fellner, J., C. Brandstätter, and D. Laner (2015). "Landfill gas migration modelling - a prerequisite for determining environmentally compatible gas generation rates". In: *15th International Waste Management and Landfill Symposium, 5-9 Oct. 2015, S. Margherita diPula (Cagliari), Sardinia*. Ed. by R. Cossu, H. Pinjing, P. Kjeldsen, Y. Matsufuji, D. Reinhart, and R. Stegmann. CISA Publisher, pp. 1–11.
- Feng, S.-J., Z.-B. Bai, B.-Y. Cao, S.-F. Lu, and S.-G. Ai (2017). "The use of electrical resistivity tomography and borehole to characterize leachate distribution in Laogang landfill, China". In: *Environmental Science and Pollution Research* 24.25, pp. 20811–20817. DOI: 10.1007/s11356-017-9853-0.
- Flores Orozco, A., J. Gallistl, M. Steiner, C. Brandstätter, and J. Fellner (2020). "Mapping biogeochemically active zones in landfills with induced polarization imaging: The Hefelbach landfill". In: *Waste Management* 107, pp. 121–132. ISSN: 0956-053X. DOI: 10.1016/j.wasman.2020.04.001.
- Flores Orozco, A., L. Aigner, and J. Gallistl (2021). "Investigation of cable effects in spectral induced polarization imaging at the field scale using multicore and coaxial cables". In: *Geophysics* 86.1, E59–E75. DOI: 10.1190/geo2019-0552.1.
- Flores Orozco, A., J. Gallistl, M. Bucker, and K. H. Williams (2018a). "Decay curve analysis for data error quantification in time-domain induced polarization imaging". In: *Geophysics* 83.2, E75–E86. DOI: 10.1190/geo2016-0714.1.
- Flores Orozco, A., A. Kemna, A. Binley, and G. Cassiani (2019). "Analysis of time-lapse data error in complex conductivity imaging to alleviate anthropogenic noise for site characterization". In: *Geophysics* 84.2, B181–B193. DOI: 10.1190/geo2017-0755.1.
- Flores Orozco, A., M. Bucker, M. Steiner, and J.-P. Malet (2018b). "Complex-conductivity imaging for the understanding of landslide architecture". In: *Engineering Geology* 243, pp. 241–252. ISSN: 0013-7952. DOI: <https://doi.org/10.1016/j.enggeo.2018.07.009>.

- Flores Orozco, A., A. Kemna, C. Oberdörster, L. Zschornack, C. Leven, P. Dietrich, and H. Weiss (2012a). "Delineation of subsurface hydrocarbon contamination at a former hydrogenation plant using spectral induced polarization imaging". In: *Journal of contaminant hydrology* 136, pp. 131–144. DOI: 10.1016/j.jconhyd.2012.06.001.
- Flores Orozco, A., A. Kemna, and E. Zimmermann (2012b). "Data error quantification in spectral induced polarization imaging". In: *Geophysics* 77.3, E227–E237. DOI: 10.1190/geo2010-0194.1.
- Flores Orozco, A., M. Steiner, T. Katona, N. Roser, C. Moser, M. J. Stumvoll, and T. Glade (2022). "Application of induced polarization imaging across different scales to understand surface and groundwater flow at the Hofermuehle landslide". In: *CATENA* 219, p. 106612. ISSN: 0341-8162. DOI: 10.1016/j.catena.2022.106612.
- Flores Orozco, A., K. H. Williams, and A. Kemna (2013). "Time-lapse spectral induced polarization imaging of stimulated uranium bioremediation". In: *Near Surface Geophysics* 11.5, pp. 531–544. DOI: 10.3997/1873-0604.2013020.
- Fredlund, D. G., D. Sheng, and J. Zhao (2011). "Estimation of soil suction from the soil-water characteristic curve". In: *Canadian geotechnical journal* 48.2, pp. 186–198. DOI: 10.1139/t10-060.
- Frid, V., D. Doudkinski, G. Liskevich, E. Shafran, A. Averbakh, N. Korostishevsky, and L. Prihodko (2010). "Geophysical-geochemical investigation of fire-prone landfills". In: *Environmental Earth Sciences* 60.4, pp. 787–798. DOI: 10.1007/s12665-009-0216-0.
- Frid, V., I. Sharabi, M. Frid, and A. Averbakh (2017). "Leachate detection via statistical analysis of electrical resistivity and induced polarization data at a waste disposal site (Northern Israel)". In: *Environmental Earth Sciences* 76.6, p. 233. DOI: 10.1007/s12665-017-6554-4.
- Gallardo, L. A. and M. A. Meju (2003). "Characterization of heterogeneous near-surface materials by joint 2D inversion of dc resistivity and seismic data". In: *Geophysical Research Letters* 30.13. DOI: 10.1029/2003gl017370.
- Gallardo, L. A. and M. A. Meju (2004). "Joint two-dimensional DC resistivity and seismic travel time inversion with cross-gradients constraints". In: *Journal of Geophysical Research: Solid Earth* 109.B3. DOI: 10.1029/2003jb002716.
- Gallistl, J., M. Weigand, M. Stumvoll, D. Ottowitz, T. Glade, and A. F. Orozco (2018). "Delineation of subsurface variability in clay-rich landslides through spectral induced polarization imaging and electromagnetic methods". In: *Engineering Geology* 245, pp. 292–308. DOI: 10.1016/j.enggeo.2018.09.001.
- Gance, J., J.-P. Malet, R. Supper, P. Sailhac, D. Ottowitz, and B. Jochum (2016). "Permanent electrical resistivity measurements for monitoring water circulation in clayey landslides". In: *Journal of Applied Geophysics* 126, pp. 98–115. DOI: 10.1016/j.jappgeo.2016.01.011.
- Gao, G., A. Abubakar, and T. M. Habashy (2012). "Joint petrophysical inversion of electromagnetic and full-waveform seismic data". In: *Geophysics* 77.3, WA3–WA18. DOI: 10.1190/geo2011-0157.1.
- Garofalo, F., G. Sauvin, L. V. Socco, and I. Lecomte (2015). "Joint inversion of seismic and electric data applied to 2D media-seismic and electric data joint inversion". In: *Geophysics* 80.4, EN93–EN104. DOI: 10.1190/geo2014-0313.1.
- Garré, S., D. Hyndman, B. Mary, and U. Werban (2021). "Geophysics conquering new territories: The rise of "agrogeophysics". In: *Vadose Zone Journal* 20.4, e20115. DOI: 10.1002/vzj2.20115.
- Gassmann, F. (1951). "Elastic waves through a packing of spheres". In: *Geophysics* 16.4, pp. 673–685. DOI: 10.1190/1.1437718.
- Gazoty, A., G. Fiandaca, J. Pedersen, E. Auken, and A. V. Christiansen (2012a). "Mapping of landfills using time-domain spectral induced polarization data: the Eskelund case study". In: *Near Surface Geophysics* 10.6, pp. 575–586. DOI: 10.3997/1873-0604.2012046.
- Gazoty, A., G. Fiandaca, J. Pedersen, E. Auken, A. V. Christiansen, and J. Pedersen (2012b). "Application of time domain induced polarization to the mapping of lithotypes in a landfill site". In: *Hydrology and Earth System Sciences* 16.6, pp. 1793–1804. DOI: 10.5194/hess-16-1793-2012.
- Geuzaine, C. and J.-F. Remacle (2009). "Gmsh: A 3-D finite element mesh generator with built-in pre-and post-processing facilities". In: *International journal for numerical methods in engineering* 79.11, pp. 1309–1331. DOI: doi.org/10.1002/nme.2579.
- Glover, P. W. J. (2009). "What is the cementation exponent? A new interpretation". In: *The Leading Edge* 28.1, pp. 82–85. DOI: 10.1190/1.3064150.
- Glover, P. W. J. (2010). "A generalized Archie's law for n phases". In: *Geophysics* 75.6, E247–E265. DOI: 10.1190/1.3509781.
- Glover, P. W. J. (2015). "11.04 - Geophysical Properties of the Near Surface Earth: Electrical Properties". In: *Treatise on Geophysics (Second Edition)*. Ed. by G. Schubert. Second Edition. Oxford: Elsevier, pp. 89–137. ISBN: 978-0-444-53803-1. DOI: 10.1016/B978-0-444-53802-4.00189-5.
- Glover, P. W. J. (2017). "A new theoretical interpretation of Archie's saturation exponent". In: *Solid Earth* 8.4, pp. 805–816. DOI: 10.5194/se-8-805-2017.
- Gobiet, A., S. Kotlarski, M. Beniston, G. Heinrich, J. Rajczak, and M. Stoffel (2014). "21st century climate change in the European Alps—A review". In: *Science of The Total Environment* 493, pp. 1138–1151. ISSN: 0048-9697. DOI: 10.1016/j.scitotenv.2013.07.050.
- Grellier, S., K. Reddy, J. Gangathulasi, R. Adib, and C. Peters (2007). "Correlation between electrical resistivity and moisture content of municipal solid waste in bioreactor landfill". In: *Geoenvironmental Engineering*, pp. 1–14. DOI: 10.1061/40907(226)11.
- Grellier, S., H. Robain, G. Bellier, and N. Skhiri (2006). "Influence of temperature on the electrical conductivity of leachate from municipal solid waste". In: *Journal of Hazardous Materials* 137.1, pp. 612–617. DOI: 10.1016/j.jhazmat.2006.02.049.
- Gruber, S. and W. Haeberli (2009). "Mountain permafrost". In: *Permafrost soils*. Springer, pp. 33–44.
- Guedes, V. J. C. B., S. T. R. Maciel, and M. P. Rocha (2022). "Refrapy: A Python program for seismic refraction data analysis". In: *Computers & Geosciences* 159, p. 105020. ISSN: 0098-3004. DOI: 10.1016/j.cageo.2021.105020.
- Guérin, R., M. L. Munoz, C. Aran, C. Laperrelle, M. Hidra, E. Drouart, and S. Grellier (2004). "Leachate recirculation: moisture content assessment by means of a geophysical technique". In: *Waste Management* 24.8, pp. 785–794. ISSN: 0956-053X. DOI: 10.1016/j.wasman.2004.03.010.
- Günther, T., G. Schaumann, P. Musmann, and M. Grinat (2011). "Imaging of a Fault Zone by a Large-scale DC Resistivity Experiment and Seismic Structural Information". In: cp-253-00086. ISSN: 2214-4609. DOI: https://doi.org/10.3997/2214-4609.20144450.
- Günther, T. and C. Rücker (2015). *Boundless Electrical Resistivity Tomography BERT 2—The user tutorial*. URL: https://gitlab.com/resistivity-net/bert.
- Günther, T., C. Rücker, and K. Spitzer (2006). "Three-dimensional modelling and inversion of DC resistivity data incorporating topography—II. Inversion". In: *Geophysical Journal International* 166.2, pp. 506–517. DOI: 10.1111/j.1365-246x.2006.03011.x.

- Gurijala, K. R. and J. M. Sufliya (1993). "Environmental factors influencing methanogenesis from refuse in landfill samples". In: *Environmental Science & Technology* 27.6, pp. 1176–1181. DOI: 10.1021/es00043a018.
- Haber, E. and D. Oldenburg (1997). "Joint inversion: a structural approach". In: *Inverse problems* 13.1, pp. 63–77. DOI: 10.1088/0266-5611/13/1/006.
- Hagedoorn, J. (1959). "The plus-minus method of interpreting seismic refraction sections". In: *Geophysical prospecting* 7.2, pp. 158–182. DOI: 10.1111/j.1365-2478.1959.tb01460.x.
- Hallof, P. G. (1974). "The IP phase measurement and inductive coupling". In: *Geophysics* 39.5, pp. 650–665. DOI: 10.1190/1.1440455.
- Hansen, P. C. and D. P. O'Leary (1993). "The use of the L-curve in the regularization of discrete ill-posed problems". In: *SIAM journal on scientific computing* 14.6, pp. 1487–1503. DOI: 10.1137/0914086.
- Harris, C., D. Vonder Mühl, K. Isaksen, W. Haerberli, J. L. Sollid, L. King, P. Holmlund, F. Dramis, M. Guglielmin, and D. Palacios (2003). "Warming permafrost in European mountains". In: *Global and Planetary Change* 39.3, pp. 215–225. ISSN: 0921-8181. DOI: 10.1016/j.gloplacha.2003.04.001.
- Harris, C. R., K. J. Millman, S. J. van der Walt, R. Gommers, P. Virtanen, D. Cournapeau, E. Wieser, J. Taylor, S. Berg, N. J. Smith, R. Kern, M. Picus, S. Hoyer, M. H. van Kerkwijk, M. Brett, A. Haldane, J. F. del Río, M. Wiebe, P. Peterson, P. Gérard-Marchant, K. Sheppard, T. Reddy, W. Weckesser, H. Abbasi, C. Gohlke, and T. E. Oliphant (Sept. 2020). "Array programming with NumPy". In: *Nature* 585.7825, pp. 357–362. DOI: 10.1038/s41586-020-2649-2.
- Harris, S. A., H. M. French, J. A. Heginbottom, G. H. Johnston, B. Ladanyi, D. C. Sego, and R. O. van Everdingen (1988). *Glossary of permafrost and related ground-ice terms*. Associate Committee on Geotechnical Research, National Research Council of Canada. URL: [https://globalcryospherewatch.org/reference/glossary\\_docs/permafrost\\_and\\_ground\\_terms\\_canada.pdf](https://globalcryospherewatch.org/reference/glossary_docs/permafrost_and_ground_terms_canada.pdf).
- Hauck, C. (2002). "Frozen ground monitoring using DC resistivity tomography". In: *Geophysical research letters* 29.21, pp. 12–1. DOI: 10.1029/2002gl014995.
- Hauck, C., C. Hilbich, and C. Mollaret (2017). "A time-lapse geophysical model for detecting changes in ground ice content based on electrical and seismic mixing rules". In: *23rd European Meeting of Environmental and Engineering Geophysics*. Vol. 2017. 1. European Association of Geoscientists & Engineers, pp. 1–5. DOI: 10.3997/2214-4609.201702024.
- Hauck, C., M. Böttcher, and H. Maurer (2011). "A new model for estimating subsurface ice content based on combined electrical and seismic data sets". In: *Cryosphere* 5, pp. 453–468. ISSN: 1994-0424. DOI: 10.5194/tc-5-453-2011.
- Hauck, C. and C. Kneisel (2008). *Applied geophysics in periglacial environments*. Cambridge University Press.
- Hauck, C. and D. Vonder Mühl (2003). "Inversion and interpretation of two-dimensional geoelectrical measurements for detecting permafrost in mountainous regions". In: *Permafrost and periglacial processes* 14.4, pp. 305–318. DOI: 10.1002/ppp.462.
- Hausmann, H., K. Krainer, E. Brückl, and W. Mostler (2007). "Internal structure and ice content of Reichenkar rock glacier (Stubai Alps, Austria) assessed by geophysical investigations". In: *Permafrost and Periglacial Processes* 18.4, pp. 351–367. DOI: 10.1002/ppp.601.
- Heimann, S., M. Kriegerowski, M. Isken, S. Cesca, S. Daout, F. Grigoli, C. Juretzek, T. Megies, N. Nooshiri, A. Steinberg, H. Sudhaus, H. Vasyura-Bathke, T. Willey, and T. Dahm (2017). "Pyrocko - An open-source seismology toolbox and library". In: DOI: 10.5880/GFZ.2.1.2017.001.
- Hellman, K., M. Ronczka, T. Günther, M. Wennermark, C. Rücker, and T. Dahlin (2017). "Structurally coupled inversion of ERT and refraction seismic data combined with cluster-based model integration". In: *Journal of Applied Geophysics* 143, pp. 169–181. DOI: 10.1016/j.jappgeo.2017.06.008.
- Hertz, H. (1882). "On the Contact of Rigid Elastic Solids and on Hardness". In: *Ch 6: Assorted Papers*.
- Hibert, C., G. Grandjean, A. Bitri, J. Travelletti, and J.-P. Malet (2012). "Characterizing landslides through geophysical data fusion: Example of the La Valette landslide (France)". In: *Engineering Geology* 128, pp. 23–29. DOI: 10.1016/j.enggeo.2011.05.001.
- Hilbich, C. (2010). "Time-lapse refraction seismic tomography for the detection of ground ice degradation". In: *The Cryosphere* 4.3, pp. 243–259. DOI: 10.5194/tc-4-243-2010.
- Hilbich, C., C. Hauck, M. Hoelzle, M. Scherler, L. Schudel, I. Völsch, D. Vonder Mühl, and R. Mäusbacher (2008). "Monitoring mountain permafrost evolution using electrical resistivity tomography: A 7-year study of seasonal, annual, and long-term variations at Schilthorn, Swiss Alps". In: *Journal of Geophysical Research: Earth Surface* 113.F1. DOI: 10.1029/2007jf000799.
- Hinkel, K., J. Doolittle, J. Bockheim, F. Nelson, R. Paetzold, J. M. Kimble, and R. Travis (2001). "Detection of subsurface permafrost features with ground-penetrating radar, Barrow, Alaska". In: *Permafrost and Periglacial processes* 12.2, pp. 179–190. DOI: 10.1002/ppp.369.
- Holbrook, W. S., C. S. Riebe, M. Elwaseif, J. L. Hayes, K. Basler-Reeder, D. L. Harry, A. Malazian, A. Dosseto, P. C. Hartsough, and J. W. Hopmans (2014). "Geophysical constraints on deep weathering and water storage potential in the Southern Sierra Critical Zone Observatory". In: *Earth Surface Processes and Landforms* 39.3, pp. 366–380. DOI: 10.1002/esp.3502.
- Hördt, A., R. Blaschek, A. Kemna, and N. Zisser (2007). "Hydraulic conductivity estimation from induced polarisation data at the field scale—the Krauthausen case history". In: *Journal of Applied Geophysics* 62.1, pp. 33–46. DOI: 10.1016/j.jappgeo.2006.08.001.
- Hu, J., X. W. Wu, H. Ke, X. B. Xu, J. W. Lan, and L. T. Zhan (2019). "Application of electrical resistivity tomography to monitor the dewatering of vertical and horizontal wells in municipal solid waste landfills". In: *Engineering Geology* 254, pp. 1–12. DOI: 10.1016/j.enggeo.2019.03.021.
- Hubbard, S. S., C. Gangodagamage, B. Dafflon, H. Wainwright, J. Peterson, A. Gusmeroli, C. Ulrich, Y. Wu, C. Wilson, J. Rowland, et al. (2013). "Quantifying and relating land-surface and subsurface variability in permafrost environments using LiDAR and surface geophysical datasets". In: *Hydrogeology Journal* 21.1, pp. 149–169. DOI: 10.1007/s10040-012-0939-y.
- Hunter, J. D. (2007). "Matplotlib: A 2D graphics environment". In: *Computing in Science & Engineering* 9.3, pp. 90–95. DOI: 10.1109/MCSE.2007.55.
- IPCC (2022). *Climate change 2022: Impacts, adaptation and vulnerability*. Cambridge University Press. Cambridge, UK and New York, NY, USA. DOI: 10.1017/9781009325844.
- Jones, D. B., S. Harrison, K. Anderson, and W. B. Whalley (2019). "Rock glaciers and mountain hydrology: A review". In: *Earth-Science Reviews* 193, pp. 66–90. ISSN: 0012-8252. DOI: 10.1016/j.earscirev.2019.04.001.
- Jongmans, D. and S. Garambois (2007). "Geophysical investigation of landslides: a review". In: *Bulletin de la Société géologique de France* 178.2, pp. 101–112. DOI: 10.2113/gssgfbull.178.2.101.
- Jordi, C., J. Doetsch, T. Günther, C. Schmelzbach, H. Maurer, and J. O. Robertsson (2020). "Structural joint inversion on irregular

meshes". In: *Geophysical Journal International* 220.3, pp. 1995–2008. DOI: 10.1093/gji/ggz550.

Kamm, J., I. A. Lundin, M. Bastani, M. Sadeghi, and L. B. Pedersen (2015). "Joint inversion of gravity, magnetic, and petrophysical data—A case study from a gabbro intrusion in Boden, Sweden". In: *Geophysics* 80.5, B131–B152. DOI: 10.1190/geo2014-0122.1.

Karaoulis, M., J.-H. Kim, and P. Tsourlos (2011). "4D active time constrained resistivity inversion". In: *Journal of Applied Geophysics* 73.1, pp. 25–34. ISSN: 0926-9851. DOI: 10.1016/j.jappgeo.2010.11.002.

Kass, M. A., T. P. Irons, B. J. Minsley, N. J. Pastick, D. R. N. Brown, and B. K. Wylie (2017). "In situ nuclear magnetic resonance response of permafrost and active layer soil in boreal and tundra ecosystems". In: *The Cryosphere* 11.6, pp. 2943–2955. DOI: 10.5194/tc-11-2943-2017.

Katona, T., B. S. Gilfedder, S. Frei, M. Bucker, and A. Flores Orozco (2021). "High-resolution induced polarization imaging of biogeochemical carbon-turnover hot spots in a peatland". In: *Biogeosciences Discussions*, pp. 1–44. DOI: 10.5194/bg-18-4039-2021.

Kearey, P., M. Brooks, and I. Hill (2002). *An introduction to geophysical exploration*. Vol. 4. John Wiley & Sons.

Kemna, A. (2000). "Tomographic inversion of complex resistivity - Theory and application". PhD thesis. Ruhr-Universität Bochum.

Kemna, A., A. Binley, G. Cassiani, E. Niederleithinger, A. Revil, L. Slater, K. H. Williams, A. F. Orozco, F.-H. Haegel, A. Hördt, et al. (2012). "An overview of the spectral induced polarization method for near-surface applications". In: *Near Surface Geophysics* 10.6, pp. 453–468. DOI: 10.3997/1873-0604.2012027.

Kemna, A., A. Binley, A. Ramirez, and W. Daily (2000). "Complex resistivity tomography for environmental applications". In: *Chemical Engineering Journal* 77.1-2, pp. 11–18. DOI: 10.1016/S1385-8947(99)00135-7.

Kemna, A., A. Binley, and L. Slater (2004). "Crosshole IP imaging for engineering and environmental applications". In: *Geophysics* 69.1, pp. 97–107. DOI: 10.1190/1.1649379.

Kessouri, P., A. Furman, J. A. Huisman, T. Martin, A. Mellage, D. Ntarlagiannis, M. Bucker, S. Ehosioko, P. Fernandez, A. Flores-Orozco, A. Kemna, F. Nguyen, T. Pilawski, S. Saneiyani, M. Schmutz, N. Schwartz, M. Weigand, Y. Wu, C. Zhang, and E. Placencia-Gomez (2019). "Induced polarization applied to biogeophysics: recent advances and future prospects". In: *Near Surface Geophysics* 17.6-Recent Developments in Induced Polarization, pp. 595–621. DOI: 10.1002/nsg.12072.

Kim, H. J. and Y. Kim (2011). "A unified transformation function for lower and upper bounding constraints on model parameters in electrical and electromagnetic inversion". In: *Journal of Geophysics and Engineering* 8.1, pp. 21–26. DOI: 10.1088/1742-2132/8/1/004.

Kjeldsen, P. and E. V. Fischer (1995). "Landfill gas migration—Field investigations at Skellingsted landfill, Denmark". In: *Waste Management & Research* 13.5, pp. 467–484. DOI: 10.1016/S0734-242X(05)80025-4.

Kneisel, C., A. Emmert, and J. Kästl (2014). "Application of 3D electrical resistivity imaging for mapping frozen ground conditions exemplified by three case studies". In: *Geomorphology* 210, pp. 71–82. ISSN: 0169-555X. DOI: 10.1016/j.geomorph.2013.12.022.

Koch, K., A. Kemna, J. Irving, and K. Holliger (2011). "Impact of changes in grain size and pore space on the hydraulic conductivity and spectral induced polarization response of sand". In: *Hydrology and Earth System Sciences* 15.6, pp. 1785–1794. DOI: 10.5194/hess-15-1785-2011.

Kondracka, M., I. Stan-Kleczeck, S. Sitek, and D. Ignatiuk (2021). "Evaluation of geophysical methods for characterizing industrial and municipal waste dumps". In: *Waste Management* 125, pp. 27–39. DOI: 10.1016/j.wasman.2021.02.015.

Konstantaki, L. A., R. Ghose, D. Draganov, G. Diaferia, and T. Heimovaara (2015). "Characterization of a heterogeneous landfill using seismic and electrical resistivity data". In: *Geophysics* 80.1, EN13–EN25. DOI: 10.1190/geo2014-0263.1.

Konstantaki, L. A., R. Ghose, D. Draganov, and T. Heimovaara (2016). "Wet and gassy zones in a municipal landfill from P- and S-wave velocity fields". In: *Geophysics* 81.6, EN75–EN86. DOI: 10.1190/geo2015-0581.1.

Krautblatter, M. and D. Draebing (2014). "Pseudo 3-DP wave refraction seismic monitoring of permafrost in steep unstable bedrock". In: *Journal of Geophysical Research: Earth Surface* 119.2, pp. 287–299. DOI: 10.1002/2012JF002638.

Krautblatter, M., S. Verleysdonk, A. Flores Orozco, and A. Kemna (2010). "Temperature-calibrated imaging of seasonal changes in permafrost rock walls by quantitative electrical resistivity tomography (Zugspitze, German/Austrian Alps)". In: *Journal of Geophysical Research: Earth Surface* 115.F2. DOI: 10.1029/2008JF001209.

Kunz, J. and C. Kneisel (2020). "Glacier–Permafrost Interaction at a Thrust Moraine Complex in the Glacier Forefield Muragl, Swiss Alps". In: *Geosciences* 10.6. ISSN: 2076-3263. DOI: 10.3390/geosciences10060205.

LaBrecque, D. J., M. Miletto, W. Daily, A. Ramirez, and E. Owen (1996). "The effects of noise on Occam's inversion of resistivity tomography data". In: *Geophysics* 61.2, pp. 538–548. DOI: 10.1190/1.1443980.

Lacroix, P., A. L. Handwerker, and G. Bièvre (2020). "Life and death of slow-moving landslides". In: *Nature Reviews Earth & Environment* 1.8, pp. 404–419. DOI: 10.1038/s43017-020-0072-8.

Laner, D., M. Crest, H. Scharff, J. W. Morris, and M. A. Barlaz (2012). "A review of approaches for the long-term management of municipal solid waste landfills". In: *Waste management* 32.3, pp. 498–512. DOI: 10.1016/j.wasman.2011.11.010.

Lanz, E., H. Maurer, and A. G. Green (1998). "Refraction tomography over a buried waste disposal site". In: *Geophysics* 63.4, pp. 1414–1433. DOI: 10.1190/1.1444443.

Lapenna, V., P. Lorenzo, A. Perrone, S. Piscitelli, E. Rizzo, and F. Sdao (2005). "2D electrical resistivity imaging of some complex landslides in Lucanian Apennine chain, southern Italy". In: *Geophysics* 70.3, B11–B18. DOI: 10.1190/1.1926571.

Lapenna, V., P. Lorenzo, A. Perrone, S. Piscitelli, F. Sdao, and E. Rizzo (2003). "High-resolution geoelectrical tomographies in the study of Giarrossa landslide (southern Italy)". In: *Bulletin of Engineering Geology and the Environment* 62.3, pp. 259–268. DOI: 10.1007/s10064-002-0184-z.

Leroux, V., T. Dahlin, and M. Svensson (2007). "Dense resistivity and induced polarization profiling for a landfill restoration project at Härlöv, Southern Sweden". In: *Waste Management & Research* 25.1, pp. 49–60. DOI: 10.1177/0734242X07073668.

Leroy, P., A. Revil, A. Kemna, P. Cosenza, and A. Ghorbani (2008). "Complex conductivity of water-saturated packs of glass beads". In: *Journal of colloid and interface science* 321.1, pp. 103–117. DOI: 10.1016/j.jcis.2007.12.031.

Leroy, P. and A. Revil (2009). "A mechanistic model for the spectral induced polarization of clay materials". In: *Journal of Geophysical Research: solid earth* 114.B10. DOI: 10.1029/2008jb006114.

Lesmes, D. P. and S. P. Friedman (2005). "Relationships between the electrical and hydrogeological properties of rocks and soils".

In: *Hydrogeophysics*. Springer, pp. 87–128. DOI: 10.1007/1-4020-3102-5\_4.

- Lesmes, D. P. and K. M. Frye (2001). “Influence of pore fluid chemistry on the complex conductivity and induced polarization responses of Berea sandstone”. In: *Journal of Geophysical Research: Solid Earth* 106.B3, pp. 4079–4090. DOI: 10.1029/2000jb900392.
- Lesmes, D. P. and F. D. Morgan (2001). “Dielectric spectroscopy of sedimentary rocks”. In: *Journal of Geophysical Research: Solid Earth* 106.B7, pp. 13329–13346. DOI: 10.1029/2000jb900402.
- Lesparre, N., F. Nguyen, A. Kemna, T. Robert, T. Hermans, M. Daoudi, and A. Flores-Orozco (2017). “A new approach for time-lapse data weighting in electrical resistivity tomography”. In: *Geophysics* 82.6, E325–E333. DOI: 10.1190/geo2017-0024.1.
- Lima, P., S. Steger, T. Glade, N. Tilch, L. Schwarz, and A. Kociu (2017). “Landslide susceptibility mapping at national scale: a first attempt for Austria”. In: *Workshop on World Landslide Forum*. Springer, pp. 943–951. DOI: 10.1007/978-3-319-53498-5\_107.
- Linde, N., A. Binley, A. Tryggvason, L. B. Pedersen, and A. Revil (2006). “Improved hydrogeophysical characterization using joint inversion of cross-hole electrical resistance and ground-penetrating radar traveltime data”. In: *Water Resources Research* 42.12. DOI: 10.1029/2006wr005131.
- Linde, N. and J. Doetsch (2016). “Joint inversion in hydrogeophysics and near-surface geophysics”. In: vol. 218. John Wiley & Sons, Inc Hoboken, NJ, p. 119. DOI: 10.1002/9781118929063.ch7.
- Liu, X., L. Zhang, S. Wu, Y. Shao, X. Wu, and Z. Li (2020). “Changes in municipal solid waste pore structure during degradation: Analysis of synthetic waste using X-ray computed microtomography”. In: *Science of the Total Environment* 708, p. 135089. DOI: 10.1016/j.scitotenv.2019.135089.
- López-Sánchez, M., L. Mansilla-Plaza, et al. (2017). “Geometric factor and influence of sensors in the establishment of a resistivity-moisture relation in soil samples”. In: *Journal of Applied Geophysics* 145, pp. 1–11. DOI: 10.1016/j.jappgeo.2017.07.011.
- Lou, X. and J. Nair (2009). “The impact of landfilling and composting on greenhouse gas emissions—a review”. In: *Bioresourcetechnology* 100.16, pp. 3792–3798. DOI: 10.1016/j.biortech.2008.12.006.
- Lu, N. and W. J. Likos (2006). “Suction stress characteristic curve for unsaturated soil”. In: *Journal of geotechnical and geoenvironmental engineering* 132.2, pp. 131–142. DOI: 10.1061/(asce)1090-0241(2006)132:2(131).
- Maierhofer, T., C. Hauck, C. Hilbich, A. Kemna, and A. Flores Orozco (2022). “Spectral induced polarization imaging to investigate an ice-rich mountain permafrost site in Switzerland”. In: *The Cryosphere* 16.5, pp. 1903–1925. DOI: 10.5194/tc-16-1903-2022.
- Mao, D., A. Revil, and J. Hinton (2016). “Induced polarization response of porous media with metallic particles—Part 4: Detection of metallic and nonmetallic targets in time-domain induced polarization tomography”. In: *Geophysics* 81.4, pp. D359–D375. DOI: 10.1190/geo2015-0480.1.
- Marescot, L., R. Monnet, and D. Chapellier (2008). “Resistivity and induced polarization surveys for slope instability studies in the Swiss Alps”. In: *Engineering Geology* 98.1-2, pp. 18–28. DOI: 10.1016/j.enggeo.2008.01.010.
- Marshall, D. J. and T. R. Madden (1959). “Induced polarization, a study of its causes”. In: *Geophysics* 24.4, pp. 790–816. DOI: 10.1190/1.1438659.
- Martin, T., T. Günther, A. F. Orozco, and T. Dahlin (2020). “Evaluation of spectral induced polarization field measurements in time and frequency domain”. In: *Journal of Applied Geophysics* 180, p. 104141. DOI: 10.1016/j.jappgeo.2020.104141.
- Marzan, I., D. Martí, A. Lobo, J. Alcalde, M. Ruiz, J. Alvarez-Marron, and R. Carbonell (2021). “Joint interpretation of geophysical data: Applying machine learning to the modeling of an evaporitic sequence in Villar de Cañas (Spain)”. In: *Engineering Geology* 288, p. 106126. ISSN: 0013-7952. DOI: 10.1016/j.enggeo.2021.106126.
- Maurya, P. K., V. Rønde, G. Fiandaca, N. Balbarini, E. Auken, P. L. Bjerg, and A. V. Christiansen (2017). “Detailed landfill leachate plume mapping using 2D and 3D electrical resistivity tomography-with correlation to ionic strength measured in screens”. In: *Journal of Applied Geophysics* 138, pp. 1–8. DOI: 10.1016/j.jappgeo.2017.01.019.
- Mavko, G., T. Mukerji, and J. Dvorkin (2009). *The rock physics handbook*. Cambridge university press.
- McAnallen, L., R. Doherty, S. Donohue, P. Kirmizakis, and C. Mendonça (2018). “Combined use of geophysical and geochemical methods to assess areas of active, degrading and restored blanket bog”. In: *Science of the Total Environment* 621, pp. 762–771. DOI: 10.1016/j.scitotenv.2017.11.300.
- McKinney, W. (2010). “Data Structures for Statistical Computing in Python”. In: *Proceedings of the 9th Python in Science Conference*. Ed. by S. van der Walt and J. Millman, pp. 56–61. DOI: 10.25080/Majora-92bf1922-00a.
- Meju, M. A., L. A. Gallardo, and A. K. Mohamed (2003). “Evidence for correlation of electrical resistivity and seismic velocity in heterogeneous near-surface materials”. In: *Geophysical research letters* 30.7. DOI: 10.1029/2002gl016048.
- Mellage, A., A. B. Holmes, S. Linley, L. Vallée, F. Rezaeezhad, N. Thomson, F. Gu, and P. Van Cappellen (2018). “Sensing coated iron-oxide nanoparticles with spectral induced polarization (SIP): experiments in natural sand packed flow-through columns”. In: *Environmental science & technology* 52.24, pp. 14256–14265. DOI: 10.1021/acs.est.8b03686.
- Merz, K., H. Maurer, L. Rabenstein, T. Buchli, S. M. Springman, and M. Zweifel (2016). “Multidisciplinary geophysical investigations over an alpine rock glacier: Multigeophysics over a rock glacier”. In: *Geophysics* 81.1, WA1–WA11. DOI: 10.1190/geo2015-0157.1.
- Mewes, B., C. Hilbich, R. Delaloye, and C. Hauck (2017). “Resolution capacity of geophysical monitoring regarding permafrost degradation induced by hydrological processes”. In: *The Cryosphere* 11.6, pp. 2957–2974. DOI: 10.5194/tc-11-2957-2017.
- Michel, H., F. Nguyen, T. Kremer, A. Elen, and T. Hermans (2020). “1D geological imaging of the subsurface from geophysical data with Bayesian Evidential Learning”. In: *Computers & Geosciences* 138, p. 104456. ISSN: 0098-3004. DOI: 10.1016/j.cageo.2020.104456.
- Mindlin, R. D. (1949). “Compliance of elastic bodies in contact”. In: DOI: 10.1115/1.4009973.
- Mollaret, C., C. Hilbich, C. Pellet, A. Flores Orozco, R. Delaloye, and C. Hauck (2019). “Mountain permafrost degradation documented through a network of permanent electrical resistivity tomography sites”. In: *The Cryosphere* 13.10, pp. 2557–2578. DOI: 10.5194/tc-13-2557-2019.
- Mollaret, C., F. M. Wagner, C. Hilbich, C. Scapozza, and C. Hauck (2020). “Petrophysical joint inversion applied to alpine permafrost field sites to image subsurface ice, water, air, and rock contents”. In: *Frontiers in Earth Science* 8, p. 85. DOI: 10.3389/feart.2020.00085.
- Monnier, S. and C. Kinnard (2013). “Internal structure and composition of a rock glacier in the Andes (upper Choapa valley, Chile) using borehole information and ground-penetrating

- radar". In: *Annals of Glaciology* 54.64, pp. 61–72. DOI: 10.3189/2013AoG64A107.
- Moser, T. (1991). "Shortest path calculation of seismic rays". In: *Geophysics* 56.1, pp. 59–67. DOI: 10.1190/1.1442958.
- Nguyen, F., R. Ghose, I. Isunza Manrique, T. Robert, and G. Dumont (2018). "Managing past landfills for future site development: A review of the contribution of geophysical methods". In: *Proceedings of the 4th International Symposium on Enhanced Landfill Mining*, pp. 27–36.
- Noetzli, J. and S. Gruber (2009). "Transient thermal effects in Alpine permafrost". In: *The Cryosphere* 3.1, pp. 85–99. DOI: 10.5194/tc-3-85-2009.
- Ogilvy, R., P. Meldrum, J. Chambers, and G. Williams (2002). "The use of 3D electrical resistivity tomography to characterise waste and leachate distribution within a closed landfill, Thriplow, UK". In: *Journal of Environmental & Engineering Geophysics* 7.1, pp. 11–18. DOI: 10.4133/jee7.1.11.
- Oldenborger, G. A. and A.-M. LeBlanc (Aug. 2018). "Monitoring changes in unfrozen water content with electrical resistivity surveys in cold continuous permafrost". In: *Geophysical Journal International* 215.2, pp. 965–977. ISSN: 0956-540X. DOI: 10.1093/gji/ggy321.
- Palmer, D. (1980). *The generalized reciprocal method of seismic refraction interpretation*. Society of Exploration Geophysicists.
- Park, C. B., R. D. Miller, and J. Xia (1999). "Multichannel analysis of surface waves". In: *Geophysics* 64.3, pp. 800–808. DOI: 10.1190/1.1444590.
- Parsekian, A., K. Singha, B. J. Minsley, W. S. Holbrook, and L. Slater (2015). "Multiscale geophysical imaging of the critical zone". In: *Reviews of Geophysics* 53.1, pp. 1–26. DOI: 10.1002/2014RG000465.
- Parsekian, A. D., G. Grosse, J. O. Walbrecker, M. Müller-Petke, K. Keating, L. Liu, B. M. Jones, and R. Knight (2013). "Detecting unfrozen sediments below thermokarst lakes with surface nuclear magnetic resonance". In: *Geophysical Research Letters* 40.3, pp. 535–540. DOI: 10.1002/grl.50137.
- Pazzi, V., S. Morelli, and R. Fanti (2019). "A review of the advantages and limitations of geophysical investigations in landslide studies". In: *International Journal of Geophysics* 2019. DOI: 10.1155/2019/2983087.
- Pellet, C., C. Hilbich, A. Marmy, and C. Hauck (2016). "Soil Moisture Data for the Validation of Permafrost Models Using Direct and Indirect Measurement Approaches at Three Alpine Sites". In: *Frontiers in Earth Science* 3. ISSN: 2296-6463. DOI: 10.3389/feart.2015.00091.
- Pelton, W. H., S. Ward, P. Hallof, W. Sill, and P. H. Nelson (1978). "Mineral discrimination and removal of inductive coupling with multifrequency IP". In: *Geophysics* 43.3, pp. 588–609. DOI: 10.1190/1.1440839.
- Pepin, N., R. S. Bradley, H. F. Diaz, M. Baraer, E. B. Caceres, N. Forsythe, H. Fowler, G. Greenwood, M. Z. Hashmi, X. D. Liu, J. R. Miller, L. Ning, A. Ohmura, E. Palazzi, I. Rangwala, W. Schöner, I. Severskiy, M. Shahgedanova, M. B. Wang, S. N. Williamson, and D. Q. Yang (2015). "Elevation-dependent warming in mountain regions of the world". In: *Nature climate change* 5.5, pp. 424–430. DOI: 10.1038/nclimate2563.
- Pérez-Díaz, L., J. Alcalde, and C. E. Bond (2020). "Introduction: Handling uncertainty in the geosciences: identification, mitigation and communication". In: *Solid Earth* 11.3, pp. 889–897. DOI: 10.5194/se-11-889-2020.
- Perrone, A., V. Lapenna, and S. Piscitelli (2014). "Electrical resistivity tomography technique for landslide investigation: A review". In: *Earth-Science Reviews* 135, pp. 65–82. DOI: 10.1016/j.earscirev.2014.04.002.
- Petschko, H., R. Bell, P. Leopold, G. Heiss, and T. Glade (2013). "Landslide inventories for reliable susceptibility maps in Lower Austria". In: *Landslide science and practice*. Springer, pp. 281–286. DOI: 10.1007/978-3-642-31325-7\_37.
- Plattner, A. M. (2020). "GPRPy: Open-source ground-penetrating radar processing and visualization software". In: *The Leading Edge* 39.5, pp. 332–337. DOI: 10.1190/tle39050332.1.
- Pogliotti, P., M. Guglielmin, E. Cremonese, U. Morra di Cella, G. Filippa, C. Pellet, and C. Hauck (2015). "Warming permafrost and active layer variability at Cime Bianche, Western European Alps". In: *The Cryosphere* 9.2, pp. 647–661. DOI: 10.5194/tc-9-647-2015.
- Ponziani, M., E. Slob, H. Vanhala, and D. Ngan-Tillard (2012). "Influence of physical and chemical properties on the low-frequency complex conductivity of peat". In: *Near Surface Geophysics* 10.6, pp. 491–501. DOI: 10.3997/1873-0604.2011037.
- Powrie, W. (2018). *Soil mechanics: concepts and applications*. CRC Press.
- Promper, C. and T. Glade (2016). "Multilayer-exposure maps as a basis for a regional vulnerability assessment for landslides: applied in Waidhofen/Ybbs, Austria". In: *Natural Hazards* 82.1, pp. 111–127. DOI: 10.1007/s11069-016-2311-3.
- Raymer, L., E. Hunt, and J. S. Gardner (1980). "An improved sonic transit time-to-porosity transform". In: *SPWLA 21st annual logging symposium*. OnePetro.
- Revil, A. (2012). "Spectral induced polarization of shaly sands: Influence of the electrical double layer". In: *Water Resources Research* 48.2. DOI: 10.1029/2011wr011260.
- Revil, A. (2013a). "Effective conductivity and permittivity of unsaturated porous materials in the frequency range 1 mHz–1GHz". In: *Water resources research* 49.1, pp. 306–327. DOI: 10.1029/2012wr012700.
- Revil, A. (2013b). "On charge accumulation in heterogeneous porous rocks under the influence of an external electric field". In: *Geophysics* 78.4, pp. D271–D291. DOI: 10.1190/geo2012-0503.1.
- Revil, A., M. L. Breton, Q. Niu, E. Wallin, E. Haskins, and D. Thomas (2017a). "Induced polarization of volcanic rocks.–2. Influence of pore size and permeability". In: *Geophysical Journal International* 208.2, pp. 814–825. DOI: 10.1093/gji/ggw382.
- Revil, A. and N. Florsch (2010). "Determination of permeability from spectral induced polarization in granular media". In: *Geophysical Journal International* 181.3, pp. 1480–1498. DOI: 10.1111/j.1365-246x.2010.04573.x.
- Revil, A. and P. Glover (1998). "Nature of surface electrical conductivity in natural sands, sandstones, and clays". In: *Geophysical Research Letters* 25.5, pp. 691–694. DOI: 10.1029/98g100296.
- Revil, A., M. Schmutz, F. Abdulsamad, A. Balde, C. Beck, A. Ghorbani, and S. Hubbard (2021). "Field-scale estimation of soil properties from spectral induced polarization tomography". In: *Geoderma* 403, p. 115380. DOI: 10.1016/j.geoderma.2021.115380.
- Revil, A., A. S. Ahmed, A. Coperey, L. Ravanel, R. Sharma, and N. Panwar (2020). "Induced polarization as a tool to characterize shallow landslides". In: *Journal of Hydrology* 589, p. 125369. ISSN: 0022-1694. DOI: 10.1016/j.jhydrol.2020.125369.
- Revil, A., M. L. Breton, Q. Niu, E. Wallin, E. Haskins, and D. Thomas (2017b). "Induced polarization of volcanic rocks.–1. Surface versus quadrature conductivity". In: *Geophysical Journal International* 208.2, pp. 826–844. DOI: 10.1093/gji/ggw444.

- Revil, A., A. Coperey, Z. Shao, N. Florsch, I. L. Fabricius, Y. Deng, J. R. Delsman, P. S. Pauw, M. Karaoulis, P. G. B. de Louw, E. S. van Baaren, W. Dabekaussen, A. Menkovic, and J. L. Gunnink (2017c). "Complex conductivity of soils. COMPLEX CONDUCTIVITY OF SOILS". In: *Water Resources Research* 53, pp. 7121–7147. ISSN: 0043-1397. DOI: 10.1002/2017wr020655.
- Revil, A., A. Binley, L. Mejus, and P. Kessouri (2015a). "Predicting permeability from the characteristic relaxation time and intrinsic formation factor of complex conductivity spectra". In: *Water Resources Research* 51.8, pp. 6672–6700. DOI: 10.1002/2015wr017074.
- Revil, A., N. Florsch, and D. Mao (2015b). "Induced polarization response of porous media with metallic particles—Part 1: A theory for disseminated semiconductors". In: *Geophysics* 80.5, pp. D525–D538. DOI: 10.1190/geo2014-0577.1.
- Ringler, A. T. and J. R. Evans (2015). "A quick SEED tutorial". In: *Seismological Research Letters* 86.6, pp. 1717–1725. DOI: 10.1785/0220150043.
- Rittgers, J., A. Revil, M. Mooney, M. Karaoulis, L. Wodajo, and C. Hickey (2016). "Time-lapse joint inversion of geophysical data with automatic joint constraints and dynamic attributes". In: *Geophysical Journal International* 207.3, pp. 1401–1419. DOI: 10.1093/gji/ggw346.
- Robinson, J., T. Johnson, and L. Slater (2013). "Evaluation of known-boundary and resistivity constraints for improving cross-borehole DC electrical resistivity imaging of discrete fractures". In: *Geophysics* 78.3, pp. D115–D127. DOI: 10.1190/geo2012-0333.1.
- Rogger, M., G. Chirico, H. Hausmann, K. Krainer, E. Brückl, P. Stadler, and G. Blöschl (2017). "Impact of mountain permafrost on flow path and runoff response in a high alpine catchment". In: *Water Resources Research* 53.2, pp. 1288–1308. DOI: 10.1002/2016wr019341.
- Romero-Ruiz, A., N. Linde, T. Keller, and D. Or (2018). "A review of geophysical methods for soil structure characterization". In: *Reviews of Geophysics* 56.4, pp. 672–697. DOI: 10.1029/2018RG000611.
- Roncza, M., K. Hellman, T. Günther, R. Wisén, and T. Dahlin (2017). "Electric resistivity and seismic refraction tomography: a challenging joint underwater survey at Äspö Hard Rock Laboratory". In: *Solid Earth* 8.3, pp. 671–682. DOI: 10.5194/se-8-671-2017.
- Rücker, C., T. Günther, and F. M. Wagner (2017). "pyGIMLi: An open-source library for modelling and inversion in geophysics". In: *Computers & Geosciences* 109, pp. 106–123. DOI: 10.1016/j.cageo.2017.07.011.
- Saleh, A. A. and J. P. Castagna (2004). "Revisiting the Wyllie time average equation in the case of near-spherical pores". In: *Geophysics* 69.1, pp. 45–55. DOI: 10.1190/1.1649374.
- Sandmeier, K. J. (2020). *ReflexW. Program for the processing of seismic, acoustic or electromagnetic reflection, refraction and transmission data*. URL: <https://www.sandmeier-geo.de/download.html>.
- Saneiyani, S., D. Ntarlagiannis, D. D. Werkema Jr, and A. Ustra (2018). "Geophysical methods for monitoring soil stabilization processes". In: *Journal of applied geophysics* 148, pp. 234–244. DOI: 10.1016/j.jappgeo.2017.12.008.
- Sanphoti, N., S. Towprayoon, P. Chairasert, and A. Noparatana (2006). "The effects of leachate recirculation with supplemental water addition on methane production and waste decomposition in a simulated tropical landfill". In: *Journal of Environmental Management* 81.1, pp. 27–35. DOI: 10.1016/j.jenvman.2005.10.015.
- Schneider, S., S. Daengeli, C. Hauck, and M. Hoelzle (2013). "A spatial and temporal analysis of different periglacial materials by using geoelectrical, seismic and borehole temperature data at Murtèl-Corvatsch, Upper Engadin, Swiss Alps". In: *Geographica Helvetica* 68.4, pp. 265–280. DOI: 10.5194/gh-68-265-2013.
- Schöner, W., L. Boeckli, H. Hausmann, J.-C. Otto, S. Reisenhofer, C. Riedl, and S. Seren (2012a). "Spatial patterns of permafrost at Hoher Sonnblick (Austrian Alps)-extensive field-measurements and modelling approaches". In: *Austrian Journal of Earth Sciences* 105, pp. 154–168. DOI: 10.1007/s00704-012-0689-8.
- Schöner, W., R. Böhm, and I. Auer (2012b). "125 years of high-mountain research at Sonnblick Observatory (Austrian Alps)-from "the house above the clouds" to a unique research platform". In: *Theoretical and Applied Climatology* 110.4, pp. 491–498. DOI: 10.1007/s00704-012-0689-8.
- Schrott, L. (1998). "The hydrological significance of high mountain permafrost and its relation to solar radiation. A case study in the high Andes of San Juan, Argentina". In: *Bamberger Geographische Schriften* 15, pp. 71–84.
- Schwartz, N. and A. Furman (2014). "On the spectral induced polarization signature of soil organic matter". In: *Geophysical Journal International* 200.1, pp. 589–595. DOI: 10.1093/gji/ggu410.
- Schwarz, G. (1962). "A theory of the low-frequency dielectric dispersion of colloidal particles in electrolyte solution, 2". In: *The Journal of Physical Chemistry* 66.12, pp. 2636–2642. DOI: 10.1021/j100818a067.
- Sen, P., C. Scala, and M. Cohen (1981). "A self-similar model for sedimentary rocks with application to the dielectric constant of fused glass beads". In: *Geophysics* 46.5, pp. 781–795. DOI: 10.1190/1.1441215.
- Shen, J., J. M. Crane, J. M. Lorenzo, and C. D. White (2016). "Seismic velocity prediction in shallow (< 30 m) partially saturated, unconsolidated sediments using effective medium theory". In: *Journal of Environmental and Engineering Geophysics* 21.2, pp. 67–78. DOI: 10.2113/jseeg21.2.67.
- Sidle, R. and H. Ochiai (2006). "Processes, prediction, and land use". In: *Water resources monograph. American Geophysical Union, Washington* 525.
- Slater, L. and D. Glaser (2003). "Controls on induced polarization in sandy unconsolidated sediments and application to aquifer characterization". In: *Geophysics* 68.5, pp. 1547–1558. DOI: 10.1190/1.1620628.
- Slater, L. (2007). "Near surface electrical characterization of hydraulic conductivity: From petrophysical properties to aquifer geometries—A review". In: *Surveys in Geophysics* 28.2, pp. 169–197. DOI: 10.1007/s10712-007-9022-y.
- Slater, L., A. Binley, W. Daily, and R. Johnson (2000). "Cross-hole electrical imaging of a controlled saline tracer injection". In: *Journal of applied geophysics* 44.2-3, pp. 85–102. DOI: 10.1016/S0926-9851(00)00002-1.
- Slater, L. and D. P. Lesmes (2002a). "Electrical-hydraulic relationships observed for unconsolidated sediments". In: *Water resources research* 38.10, pp. 31–1. DOI: 10.1029/2001wr001075.
- Slater, L. D. and D. Lesmes (2002b). "IP interpretation in environmental investigations". In: *Geophysics* 67.1, pp. 77–88. DOI: 10.1190/1.1451353.
- Sloan, S. D., D. W. Steeples, and G. P. Tsoulias (2009). "Ultra-shallow imaging using 3D seismic-reflection methods". In: *Near Surface Geophysics* 7.5-6, pp. 307–314. DOI: 10.3997/1873-0604.2009015.
- Sokratov, S. A. and R. G. Barry (2002). "Intraseasonal variation in the thermoinsulation effect of snow cover on soil temperatures and energy balance". In: *Journal of Geophysical Research: Atmospheres* 107.D10, ACL–13. DOI: 10.1029/2001jd000489.

- Soueid Ahmed, A. and A. Revil (2018). "3-D time-domain induced polarization tomography: a new approach based on a source current density formulation". In: *Geophysical Journal International* 213.1, pp. 244–260. doi: 10.1093/gji/ggx547.
- Soupios, P. and D. Nturlagiannis (2017). "Characterization and monitoring of solid waste disposal sites using geophysical methods: current applications and novel trends". In: *Modelling trends in solid and hazardous waste management*. Springer, pp. 75–103. doi: 10.1007/978-981-10-2410-8\_5.
- Soupios, P., N. Papadopoulos, I. Papadopoulos, M. Kouli, F. Valianatos, A. Sarris, and T. Manios (2007). "Application of integrated methods in mapping waste disposal areas". In: *Environmental Geology* 53.3, pp. 661–675. doi: 10.1007/s00254-007-0681-2.
- Steger, S., A. Brenning, R. Bell, and T. Glade (2016). "The propagation of inventory-based positional errors into statistical landslide susceptibility models". In: *Natural Hazards and Earth System Sciences* 16.12, pp. 2729–2745. doi: 10.5194/nhess-16-2729-2016.
- Steiner, M., T. Katona, J. Fellner, and A. Flores Orozco (2022). "Quantitative water content estimation in landfills through joint inversion of seismic refraction and electrical resistivity data considering surface conduction". In: *Waste Management* 149, pp. 21–32. ISSN: 0956-053X. doi: 10.1016/j.wasman.2022.05.020.
- Steiner, M., F. M. Wagner, T. Maierhofer, W. Schöner, and A. Flores Orozco (2021). "Improved estimation of ice and water contents in Alpine permafrost through constrained petrophysical joint inversion: The Hoher Sonnblick case study". In: *Geophysics* 86.5, pp. 1–84. doi: 10.1190/geo2020-0592.1.
- Stockwell, J. W. (1999). "The CWP/SU: Seismic Unix package". In: *Computers & Geosciences* 25.4, pp. 415–419. ISSN: 0098-3004. doi: 10.1016/S0098-3004(98)00145-9.
- Stumvoll, M., E. Schmaltz, R. Kanta, H. Roth, B. Grall, J. Luhn, A. Flores Orozco, and T. Glade (2022). "Exploring the dynamics of a complex, slow-moving landslide in the Austrian Flysch Zone with 4D surface and subsurface information". In: *CATENA* 214, p. 106203. ISSN: 0341-8162. doi: 10.1016/j.catena.2022.106203.
- Stumvoll, M., E. Canli, A. Engels, B. Thiebes, B. Groiss, T. Glade, J. Schweigl, and M. Bertagnoli (2020). "The "Salcher" landslide observatory—experimental long-term monitoring in the Flysch Zone of Lower Austria". In: *Bulletin of Engineering Geology and the Environment* 79.4, pp. 1831–1848.
- Stumvoll, M., E. Schmaltz, and T. Glade (2021). "Dynamic characterization of a slow-moving landslide system—Assessing the challenges of small process scales utilizing multi-temporal TLS data". In: *Geomorphology* 389, p. 107803. doi: 10.1016/j.geomorph.2021.107803.
- Sullivan, C. B. and A. Kaszynski (2019). "PyVista: 3D plotting and mesh analysis through a streamlined interface for the Visualization Toolkit (VTK)". In: *Journal of Open Source Software* 4.37, p. 1450. doi: 10.21105/joss.01450.
- Sun, J. and Y. Li (2016). "Joint inversion of multiple geophysical data using guided fuzzy c-means clustering". In: *Geophysics* 81.3, pp. ID37–ID57. doi: 10.1190/geo2015-0457.1.
- Supper, R., D. Ottowitz, B. Jochum, J.-H. Kim, A. Römer, I. Baron, S. Pfeiler, M. Lovisolò, S. Gruber, and F. Vecchiotti (2014a). "Geoelectrical monitoring: an innovative method to supplement landslide surveillance and early warning". In: *Near Surface Geophysics* 12.1, pp. 133–150. doi: 10.3997/1873-0604.2013060.
- Supper, R., D. Ottowitz, B. Jochum, A. Römer, S. Pfeiler, S. Kauer, M. Keuschnig, and A. Ita (2014b). "Geoelectrical monitoring of frozen ground and permafrost in alpine areas: field studies and considerations towards an improved measuring technology". In: *Near Surface Geophysics* 12.1, pp. 93–115. doi: 10.3997/1873-0604.2013057.
- Tarasov, A. and K. Titov (2013). "On the use of the Cole–Cole equations in spectral induced polarization". In: *Geophysical Journal International* 195.1, pp. 352–356. doi: 10.1093/gji/ggt251.
- Tartrat, T., A. Revil, F. Abdulsamad, A. Ghorbani, D. Jougnot, A. Coperey, B. Yven, and R. de la Vaissiere (2019). "Induced polarization response of porous media with metallic particles—Part 10: Influence of desiccation". In: *Geophysics* 84.5, E357–E375. doi: 10.1190/geo2019-0048.1.
- Timur, A. (1968). "Velocity of compressional waves in porous media at permafrost temperatures". In: *Geophysics* 33.4, pp. 584–595. doi: 10.1190/1.1439954.
- Titov, K., V. Komarov, V. Tarasov, and A. Levitski (2002). "Theoretical and experimental study of time domain-induced polarization in water-saturated sands". In: *Journal of Applied Geophysics* 50.4, pp. 417–433. doi: 10.1016/s0926-9851(02)00168-4.
- Travelletti, J., P. Sailhac, J.-P. Malet, G. Grandjean, and J. Ponton (2012). "Hydrological response of weathered clay-shale slopes: Water infiltration monitoring with time-lapse electrical resistivity tomography". In: *Hydrological processes* 26.14, pp. 2106–2119. doi: 10.1002/hyp.7983.
- Tso, C.-H. M., O. Kuras, and A. Binley (2019). "On the field estimation of moisture content using electrical geophysics: The impact of petrophysical model uncertainty". In: *Water Resources Research* 55.8, pp. 7196–7211. doi: 10.1029/2019wr024964.
- Uhlemann, S., S. Hagedorn, B. Dashwood, H. Maurer, D. Gunn, T. Dijkstra, and J. Chambers (2016). "Landslide characterization using P- and S-wave seismic refraction tomography—The importance of elastic moduli". In: *Journal of Applied Geophysics* 134, pp. 64–76. ISSN: 0926-9851. doi: 10.1016/j.jappgeo.2016.08.014.
- Uieda, L., V. C. Oliveira Jr, and V. C. Barbosa (2013). "Modeling the earth with fatiando a terra". In: *Proceedings of the 12th Python in Science Conference*, pp. 96–103.
- Ustra, A. T., V. R. Elis, G. Mondelli, L. V. Zuquette, and H. L. Giacheti (2012). "Case study: a 3D resistivity and induced polarization imaging from downstream a waste disposal site in Brazil". In: *Environmental Earth Sciences* 66.3, pp. 763–772. doi: 10.1007/s12665-011-1284-5.
- van Genuchten, M. T. (1980). "A closed-form equation for predicting the hydraulic conductivity of unsaturated soils". In: *Soil science society of America journal* 44.5, pp. 892–898. doi: 10.2136/sssaj1980.03615995004400050002x.
- Vinegar, H. and M. Waxman (1984). "Induced polarization of shaly sands". In: *Geophysics* 49.8, pp. 1267–1287. doi: 10.1190/1.1441755.
- Wagner, F. M., C. Mollaret, T. Günther, A. Kemna, and C. Hauck (2019). "Quantitative imaging of water, ice and air in permafrost systems through petrophysical joint inversion of seismic refraction and electrical resistivity data". In: *Geophysical Journal International* 219.3, pp. 1866–1875. doi: 10.1093/gji/ggz402.
- Wagner, F. M., P. Bergmann, C. Rücker, B. Wiese, T. Labitzke, C. Schmidt-Hattenberger, and H. Maurer (2015). "Impact and mitigation of borehole related effects in permanent crosshole resistivity imaging: An example from the Ketzin CO2 storage site". In: *Journal of Applied Geophysics* 123, pp. 102–111. ISSN: 0926-9851. doi: 10.1016/j.jappgeo.2015.10.005.
- Ward, S. H. (1988). "The resistivity and induced polarization methods". In: *Symposium on the Application of Geophysics to Engineering and Environmental Problems 1988*. Society of Exploration Geophysicists, pp. 109–250. doi: 10.1190/1.9781560802785.ch6.

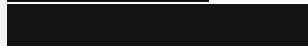
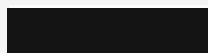
- Waxman, M. H. and L. Smits (1968). "Electrical conductivities in oil-bearing shaly sands". In: *Society of Petroleum Engineers Journal* 8.02, pp. 107–122. DOI: 10.2118/1863-a.
- Weigand, M. and A. Kemna (2016). "Relationship between Cole-Cole model parameters and spectral decomposition parameters derived from SIP data". In: *Geophysical Journal International* 205.3, pp. 1414–1419. DOI: 10.1093/gji/ggw099.
- Weller, A., L. Slater, A. Binley, S. Nordsiek, and S. Xu (2015). "Permeability prediction based on induced polarization: Insights from measurements on sandstone and unconsolidated samples spanning a wide permeability range". In: *Geophysics* 80.2, pp. D161–D173. DOI: 10.1190/geo2014-0368.1.
- Weller, A., L. Slater, and S. Nordsiek (2013). "On the relationship between induced polarization and surface conductivity: Implications for petrophysical interpretation of electrical measurements". In: *Geophysics* 78.5, pp. D315–D325. DOI: 10.1190/geo2013-0076.1.
- Whiteley, J., A. Watlet, S. Uhlemann, P. Wilkinson, J. Boyd, C. Jordan, J. Kendall, and J. Chambers (2021). "Rapid characterisation of landslide heterogeneity using unsupervised classification of electrical resistivity and seismic refraction surveys". In: *Engineering Geology* 290, p. 106189. ISSN: 0013-7952. DOI: 10.1016/j.enggeo.2021.106189.
- Whiteley, J., J. Chambers, S. Uhlemann, P. B. Wilkinson, and J. Kendall (2019). "Geophysical monitoring of moisture-induced landslides: a review". In: *Reviews of Geophysics* 57.1, pp. 106–145. DOI: 10.1029/2018rg000603.
- Williams, K. H., A. Kemna, M. J. Wilkins, J. Druhan, E. Arntzen, A. L. N'Guessan, P. E. Long, S. S. Hubbard, and J. F. Banfield (2009). "Geophysical monitoring of coupled microbial and geochemical processes during stimulated subsurface bioremediation". In: *Environmental science & technology* 43.17, pp. 6717–6723. DOI: 10.1021/es900855j.
- Williams, K. H., D. Ntarlagiannis, L. D. Slater, A. Dohnalkova, S. S. Hubbard, and J. F. Banfield (2005). "Geophysical imaging of stimulated microbial biomineralization". In: *Environmental science & technology* 39.19, pp. 7592–7600. DOI: 10.1021/es0504035.
- Wong, J. (1979). "An electrochemical model of the induced-polarization phenomenon in disseminated sulfide ores". In: *Geophysics* 44.7, pp. 1245–1265. DOI: 10.1190/1.1441005.
- Wu, Y., S. Hubbard, K. H. Williams, and J. Ajo-Franklin (2010). "On the complex conductivity signatures of calcite precipitation". In: *Journal of Geophysical Research: Biogeosciences* 115.G2. DOI: 10.1029/2009JG001129.
- Wyllie, M. R. J., A. R. Gregory, and L. W. Gardner (1956). "Elastic wave velocities in heterogeneous and porous media". In: *Geophysics* 21.1, pp. 41–70. DOI: 10.1190/1.1438217.
- Zhang, J. and A. Revil (2015). "2D joint inversion of geophysical data using petrophysical clustering and facies deformation". In: *Geophysics* 80.5, pp. M69–M88. DOI: 10.1190/geo2015-0147.1.
- Zhdanov, M. S. (2002). *Geophysical inverse theory and regularization problems*. Vol. 36. Elsevier.
- Zhdanov, M. S. and W. Lin (2017). "Adaptive multinary inversion of gravity and gravity gradiometry data Adaptive multinary inversion of gravity data". In: *Geophysics* 82.6, G101–G114. DOI: 10.1190/geo2016-0451.1.
- Zisser, N., A. Kemna, and G. Nover (2010). "Dependence of spectral-induced polarization response of sandstone on temperature and its relevance to permeability estimation". In: *Journal of Geophysical Research: Solid Earth* 115.B9. DOI: 10.1029/2010JB007526.
- Zonge, K., W. Sauck, and J. Sumner (1972). "Comparison of time, frequency, and phase measurements in induced polarization". In: *Geophysical Prospecting* 20.3, pp. 626–648. DOI: 10.1111/j.1365-2478.1972.tb00658.x.



# Curriculum vitae

## PERSONAL INFORMATION

NAME **Matthias Steiner**



<https://orcid.org/0000-0002-3595-3616>

## EDUCATION

PERIOD **October 2019 — October 2022**

**Doctoral program in Engineering Sciences**

INSTITUTION **TU Wien**

THESIS *The joint inversion of seismic refraction and electrical resistivity data: A quantitative approach to estimate hydrogeological parameters in an imaging framework*

PERIOD **October 2012 — May 2015**

**Master program in Geodesy and Geophysics**

INSTITUTION **TU Wien**

THESIS *Classification of signal sources based on seismic and acoustic measurements*

PERIOD **October 2008 — April 2012**

**Bachelor program in Geodesy and Geoinformation**

INSTITUTION **TU Wien**

THESIS *Geophysical exploration of the soil structure in the vicinity of the Schreierquelle (Austria) using ground-penetrating radar and electrical resistivity tomography*

PERIOD **September 2002 — June 2007**

INSTITUTION **Polytechnic Institute for Engineering**

Computing (Major) & Economics (Minor)

## WORK EXPERIENCE

PERIOD	October 2019 — Present
EMPLOYER	TU Wien Department of Geodesy and Geoinformation Research Unit of Geophysics
JOB TITLE	University assistant
PERIOD	October 2015 — December 2019
EMPLOYER	Univ. of Natural Resources and Life Sciences, Vienna Institute of Applied Geology
JOB TITLE	Research assistant
PERIOD	October 2013 — August 2015
EMPLOYER	Univ. of Natural Resources and Life Sciences, Vienna Institute of Applied Geology
JOB TITLE	Project assistant
PERIOD	October 2008 — September 2013
EMPLOYER	Various in public and private sector
JOB TITLE	Internships and part-time work (Geophysics, GIS, Remote Sensing, Engineering Geodesy, and Education)
PERIOD	April 2008 — September 2008
EMPLOYER	ETM professional control GmbH
JOB TITLE	Junior software developer